AD-A060 389 BOEING VERTOL CO PHILADELPHIA PA F/G 1/3
INTERACTIONAL AERODYNAMICS OF THE SINGLE-ROTOR HELICOPTER CONFI--ETC(U)
SEP 78 P F SHERIDAN DAAJ02-77-C-0020
UNCLASSIFIED USARTL-TR-78-23A NL

1 OF 4
AD A060389

LEVEL II

USARTL-TR-78-23A

INTERACTIONAL AERODYNAMICS OF THE SINGLE ROTOR HELICOPTER CONFIGURATION
VOLUME I - FINAL REPORT

Philip F. Sheridan
BOEING VERTOL COMPANY
P. O. BOX 16858
Philadelphia, Penn. 19142

September 1978

Final Report for Period 15 March 1977 - 13 February 1978

Approved for public release;
distribution unlimited.

Prepared for

APPLIED TECHNOLOGY LABORATORY
U. S. ARMY RESEARCH AND TECHNOLOGY LABORATORIES (AVRADCOM)
Fort Eustis, Va. 23604

APPLIED TECHNOLOGY LABORATORY POSITION STATEMENT

In 1975 a wind tunnel test program was conducted in the Boeing-Vertol 20-foot V/STOL Wind Tunnel on a 1/5th-scale UTTAS model to investigate and find solutions for several aerodynamic problems encountered during the UTTAS flight-testing. Specifically, these tests focused upon (a) the structure of the hub/rotor wake in the vicinity of the empennage, (b) the formulation of the ground vortex and its relation to hub loads and fuselage loads during transition, and (c) the occurrence of vibratory air pressures from the blade passing over the fuselage. Only portions of the above-mentioned wind tunnel test data were reduced and analyzed in addressing the flight-test problems of the UTTAS aircraft.

Under Contract DAAJ02-77-C-0020, Boeing-Vertol completed analyses on the data to understand more completely the aerodynamic interactions that are involved and to formulate instructions for the guidance of designers in these respects. The results of these studies are applicable to all existing and future single-rotor/tail rotor helicopters. The data have been segregated according to aerodynamic interactions and associated phenomena/problem areas. From this body of knowledge, a generalized set of design guidelines meaningful to the single-rotor helicopter design concept formulation were developed and are included in these reports.

Mr. Robert P. Smith of the Aeronautical Technology Division, Aeromechanics Technical Area, served as project engineer for this effort.

UNCLASSIFIED

SECURITY CLASSIFICATION OF THIS PAGE (When Data Entered)

REPORT DOCUMENTATION PAGE	READ INSTRUCTIONS BEFORE COMPLETING FORM
1. REPORT NUMBER: USARTL TR-78-23A	2. GOVT ACCESSION NO. / 3. RECIPIENT'S CATALOG NUMBER
4. TITLE (and Subtitle): INTERACTIONAL AERODYNAMICS OF THE SINGLE-ROTOR HELICOPTER CONFIGURATION, VOLUME I, FINAL REPORT	5. TYPE OF REPORT & PERIOD COVERED: Final Report, 15 Mar 1977–13 Feb 1978 / 6. PERFORMING ORG. REPORT NUMBER
7. AUTHOR(s): Philip F. Sheridan	8. CONTRACT OR GRANT NUMBER(s): DAAJ02-77-C-0020
9. PERFORMING ORGANIZATION NAME AND ADDRESS: Boeing Vertol Company, P.O. Box 16858, Philadelphia, Pennsylvania 19142	10. PROGRAM ELEMENT, PROJECT, TASK AREA & WORK UNIT NUMBERS: 62209A 1L262209AH76 00 189 EK
11. CONTROLLING OFFICE NAME AND ADDRESS: Applied Technology Laboratory, U. S. Army Research and Technology Laboratories (AVRADCOM), Fort Eustis, Virginia 23604	12. REPORT DATE: September 1978 / 13. NUMBER OF PAGES: 299
14. MONITORING AGENCY NAME & ADDRESS (if different from Controlling Office): 304p.	15. SECURITY CLASS. (of this report): Unclassified / 15a. DECLASSIFICATION/DOWNGRADING SCHEDULE

16. DISTRIBUTION STATEMENT (of this Report)

Approved for public release; distribution unlimited.

17. DISTRIBUTION STATEMENT (of the abstract entered in Block 20, if different from Report)

18. SUPPLEMENTARY NOTES

Volume I of an eight-volume report

19. KEY WORDS (Continue on reverse side if necessary and identify by block number)

Nap of the earth	Wake	Flow environment
Vortex	Configuration	Test
Ground vortex	Configuration aerodynamics	Wind tunnel
Ground effect	Interaction	Powered model
Downwash	Aerodynamic interaction	Hubcap

20. ABSTRACT (Continue on reverse side if necessary and identify by block number)

A study has been conducted to understand the interactional aerodynamics problems occurring during the UTTAS development. Powered wind tunnel model data were organized and analyzed in the following categories of interactions:

a. Rotor/ground,
b. Rotor/fuselage,
c. Rotor/fuselage/ground

→ over

DD FORM 1 JAN 73 1473 EDITION OF 1 NOV 65 IS OBSOLETE

UNCLASSIFIED

SECURITY CLASSIFICATION OF THIS PAGE (When Data Entered)

403 682

78 10 26 024 LB

19. Key Words (Continued)

Download	Interference	Air ejectors
Flow	Vibratory pressures	Flow modifiers
Rotor	Fuselage	Empennage
Trim change		

20. Abstract (Continued)

d. Rotor/empennage; and
e. Rotor/empennage/ground.

The following related problem areas are considered:

a. Severe lateral trim changes during transition close to the ground;
b. The occurrence of high vibratory aerodynamic loads on the airframe surfaces;
c. Turbulent flow on the airframe near the ground;
d. Excessive low-frequency unsteady loads on the empennage in forward flight due to the hub/rotor wake; and
e. Poor efficiency in tail rotor installations due to adverse fin loading.

The ground vortex is the cause of rapidly varying flow conditions at low speed. It has large unsteady elements in its structure and a significant mean part as well. These change rapidly with airspeed, resulting in the generation of highly nonlinear rotor and fuselage forces. This generally unstable environment may require special SCAS features for sustained operations.

Compact configurations with small clearances between rotor and fuselage can experience high vibratory airloads on the surface. Rotor blade-bending moments can be adversely affected and also can cause significant increases in vibratory hub loads. For high-disk-loading helicopters in the 8- to 10-psf range, it appears that at least two chord lengths should be maintained for the clearance distance.

Modern helicopters show a trend to large fins, mostly for directional trim in case the tail rotor is lost. This results in significantly larger adverse fin loads subtracting from the tail rotor thrust. Larger separations between tail rotor and fin will be required. The data seem to indicate that fin stall occurs in the normal tail rotor operating range. More investigation is needed to understand this phenomenon.

Tail buffeting is sometimes caused by the impingement of the lower frequency rotor/hub wake components on fin and tail rotor. This can be mitigated by the use of hub caps, by aft crown shaping to improve the gradients, or by offsetting the tail rotor and fin to the right side away from the wake.

It is recommended that more fundamental investigations be undertaken to understand the major flows of the helicopter and its environment and their mutual interactions.

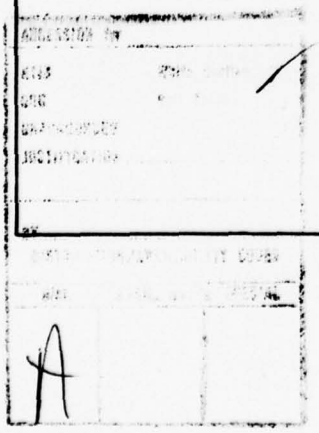

SUMMARY

A study was made of the experimental wind tunnel data obtained from powered model testing conducted during the UTTAS program. The model was equipped with extensive instrumentation and provided a comprehensive array of parametric data on rotor, fuselage, empennage and tail rotor loadings, and flow characteristics. The program was designed especially to provide information relative to aerodynamic interactions.

The data presented in this report were organized and analyzed according to the type of aerodynamic interaction. The following interactions were studied:

a. Rotor/ground
b. Rotor/fuselage
c. Rotor/fuselage/ground
d. Rotor/empennage
e. Rotor/empennage/ground

These are not all of the possible interactions. However, some very important problem areas fall under the five interactions above, including:

a. Severe trim changes during transition close to the ground.
b. The occurrence of high vibratory aerodynamic loads on the airframe surfaces.
c. Highly turbulent flow on the airframe near the ground which changes radically with airspeed.
d. Excessive low-frequency loads on the empennage due to wake impingement.
e. Poor efficiency in tail rotor installations due to adverse fin loading.

Requirements for sustained operation in the nap of the earth (NOE) will demand careful control system design, including an adequate lateral cyclic pitch range to accommodate the trim changes and a SCAS capable of corrective inputs to rapid trim change. These design requirements will depend upon the configuration and its design flight envelope. High-disk-loading machines will be prone to trim changes in cyclic pitch and power with speed close to the ground.

The demands for compactness of configuration for transportability or for minimum silhouette can result in a small gap between the rotor and fuselage. This will affect adversely the blade-bending moments, mechanical vibration, airframe surface vibratory pressures, or drive system vibratory torque to an intolerable degree. It is essential that future programs conduct tradeoff studies that consider the gap, blade strength, vibration isolation, panel design, and related parameters using realistic aerodynamic data obtained from suitable test programs.

The flow environment of the airframe near the ground is extremely unsteady because of the presence of the ground vortex and the mixing of the major flows and their reflections from the ground. The full energy of the rotor downwash is fed into this system, and a large low-frequency component to the flow contributes to violent upsets on all axes. This phenomenon affects the control of the aircraft and could cause pilot fatigue.

Systems that depend on steady fresh air for operation may face major redesign programs in order to cope with the complex flows of the NOE. These include powerplant air induction, cooling air induction systems, low airspeed instrumentation, and weapon launch equipment. External load pickup may also pose a problem in certain NOE situations.

The hub wake is entrained by the rotor wake, which determines its trajectory, and places it in the vicinity of the empennage. The forward flight regime, particularly in descents, is affected. The troublesome aspect of the wake impingement on the empennage is the low-frequency loading produced. The low-frequency flow elements result from not only the rotor and hub flow mixing, but also the low-frequency Karman vortex frequencies shed from elements of the airframe. These complexities have not been sorted out. Another complication in the mixing is an instability between the parallel flows behind the hub and over the aft crown. This seems to be a function of crown contouring, i.e., longitudinal pressure gradient and the rotor-to-fuselage gap.

In the investigation it was not possible to deflect the hub wake away from the empennage independent of the dominant rotor wake in any significant amount. The only way to effect a lateral separation between wake and empennage is to locate the fin and/or tail on the right side in an asymmetrical arrangement. The other approach is to reduce the low-frequency part of the wake spectrum, which has been accomplished in two ways. On the wind tunnel test of this report, the use of hubcaps proved successful when applied to a configuration with a rotor-to-fuselage gap equal to one chord length. On a subsequent wind tunnel test, reshaping of the aft crown provided a solution where the rotor-to-fuselage gap was two chord lengths. These are not necessarily exclusive solutions for each gap, i.e., reshaping was not seriously attempted for the low gap nor were hubcaps employed for the higher rotor case. Reshaping the crown is preferred as it is the lower drag solution.

The Army has had a requirement for maintenance of directional trim to permit return to base and a roll-on landing in the event of tail rotor loss. This requires a large fin compared to the tail rotor disk area. Such an empennage was tested in this program. With a 35-percent ratio of fin area (swept) to tail rotor disk area, it presented an adverse fin load of nearly 75 percent at 25 knots and 100 percent at 50 knots for 30 degrees of wind azimuth.

Fin load ratio was found to vary with thrust. More importantly, however, fin stall was found to occur at a relatively low value of tail rotor thrust ($C_T/\sigma = 0.07$). The stall suppresses the adverse fin force, and it will eventually decrease as the tail rotor thrust increases. The installation thus shows greater efficiency after stall. Some researchers, in an effort to be conservative, have set tail rotor thrust at a high value such as the maximum expected maneuver value. It now appears that this approach gave fin force ratio values one-half to one-third of the maximum to be found for the unstalled fin.

In all of the problem areas discussed above and in other interaction categories not investigated, considerably more study is needed to extend the data to other conditions and to understand better the physical mechanisms at work.

PREFACE

The entire report describing the investigation of INTERACTIONAL AERODYNAMICS OF THE SINGLE-ROTOR HELICOPTER CONFIGURATION comprises eight numbered volumes bound as 33 separate documents. The complete list of these documents is as follows:

This volume is

Volume I, Final Report

Volume II, Harmonic Analyses of Airframe Surface Pressure Data
- A – Runs 7-14, Forward Section
- B – Runs 7-14, Mid Section
- C – Runs 7-14, Aft Section
- D – Runs 15-22, Forward Section
- E – Runs 15-22, Mid Section
- F – Runs 15-22, Aft Section
- G – Runs 23-33, Forward Section
- H – Runs 23-33, Mid Section
- I – Runs 23-33, Aft Section

Volume III, Flow Angle and Velocity Wake Profiles in Low-Frequency Band
- A – Basic Investigations and Hubcap Variations
- B – Air Ejector Systems and Other Devices

Volume IV, One-Third Octave Band Spectrograms of Wake Split-Film Data
- A – Buildup to Baseline
- B – Basic Configuration Wake Explorations
- C – Solid Hubcaps
- D – Open Hubcaps
- E – Air Ejectors
- F – Air Ejectors With Hubcaps; Wings
- G – Fairings and Surface Devices

Volume V, Harmonic Analyses of Hub Wake

Volume VI, One-Third Octave Band Spectrograms of Wake Single Film Data
- A – Buildup to Baseline
- B – Basic Configuration Wake Exploration
- C – Hubcaps and Air Ejectors

Volume VII, Frequency Analyses of Wake Split-Film Data
- A – Buildup to Baseline
- B – Basic Configuration Wake Explorations
- C – Solid Hubcaps

D – Open Hubcaps
E – Air Ejectors
F – Air Ejectors With Hubcaps; Wings
G – Fairings and Surface Devices

Volume VIII, Frequency Analyses of Wake Single Film Data
A – Buildup to Baseline
B – Basic Configuration Wake Exploration
C – Hubcaps and Air Ejectors

TABLE OF CONTENTS

Page

APPENDIXES

LIST OF ILLUSTRATIONS

LIST OF TABLES

INTRODUCTION

BACKGROUND

During the late summer of 1975, Boeing Vertol conducted a test program in its 20-foot V/STOL wind tunnel to investigate and find solutions for several aerodynamics problems encountered during the UTTAS flight testing. Specifically, these tests focused upon the following areas:

a. The structure of the hub/rotor wake in the vicinity of the empennage.

b. The formation of the ground vortex and its relation to hub loads and fuselage during transition.

c. The occurrence of vibratory air pressures from the blade passing over the fuselage.

The wake was measured by a rake-mounted array of hot film anemometers from which time histories were obtained of flow velocity and direction. These measurements were made for a variety of locations near the empennage, which were mostly in a vertical sweep just aft of the main rotor. The wake was altered by many devices such as hub covers, wings, air injection, and fairings, and the changes to the wake dynamics were verified by the hot film anemometer measurements. This was probably the most extensive treatment of hub/rotor wake ever undertaken in terms of the detail of the measurements and the number of variations considered.

In the studies of the ground vortex, load measurements were made on the rotor, fuselage, empennage, tail rotor, and total load balances. Variations were made in height from ground, disk loading, pitch attitude, sideslip, and speed. For many of these test conditions, smoke was employed to define the vortex core and its location with respect to the rotor. This technique provided visual correlation to the force variations. These data were applied to analyze the variations in trim experienced by the YUH-61A in transition near the ground. A very comprehensive picture of the variations in the forces on the helicopter in the nap-of-the-earth regime was established.

A third area of investigation was the time history of vibratory components of pressure on the airframe surfaces. This area is of principal interest as an input to the aircraft vibration separate from the normal transmissions through the hub. Measurements were made at 53 locations with interest focused on the crown, nacelle area, boom, fin, and stabilizer. Test conditions included level flight from 20 to 160 knots, climb and autorotation for two speeds, and several disk loadings, each at two speeds. The principal finding was that the vibratory pressures on the crown above the pilot compartment are high (approximately 0.1 psi) and could be significant in producing excessive vibration levels at high speed. The variable pressures are in phase with blade passage and therefore occur four times per revolution. These findings were an important consideration in the subsequent decision to raise the rotor.

The purpose of the effort performed under this contract is to extend the analysis of the data toward a more complete examination and understanding of the aerodynamic interactions that are involved, and to formulate instructions for the guidance of designers in these respects. The results of these studies in the form of graphs, tables, charts, and guideline statements are generally applicable to existing and future single-rotor/tail rotor helicopters. The general objectives are as follows:

1. Understanding the effect of the ground boundary on performance, stability and control, and loads on the aircraft.

2. More detailed understanding of the rotor flow field, which will help in predicting vibratory loads and flight stability and thus save the costs of corrective design and flight tests.

3. Understanding the flow environment and related problem areas in the NOE flight regime.

4. Documenting the data base for future reference.

BASIC DEFINITIONS

This wind tunnel test was an effort in the field of Configuration Aerodynamics, which is a study of the flow patterns that prevail and the forces that are produced on the body when the configuration elements are brought together. This is distinctly different from the more familiar rotor aerodynamics, fuselage aerodynamics, tail rotor aerodynamics, and other categories most often treated separately within the broad scope of Helicopter Aerodynamics.

Interactional Aerodynamics is almost synonymous with Configuration Aerodynamics. It is a study specifically of the flow mechanisms and the incremental forces produced as a result of combining elements and their associated flows or flow influences. The interaction mechanism is normally some kind of flow anomaly such as a supervelocity region, a pressure field distortion, a separated area, a wake, a vortex, a flow redirection, or combinations of these. These are inherently related to the geometry of the configuration, the physical relationships between the elements, the relative wind direction and magnitude, the rotor downwash velocity, and the proximity of the rotor and other elements to the ground or other objects.

Generally speaking, aircraft whose elements are widely separated with simple connection geometry will exhibit fewer and smaller interactions and offer a higher overall aerodynamic efficiency. The fixed-wing airplane is the obvious example here; at the opposite pole is the helicopter, which fundamentally possesses a high degree of aerodynamic coupling in its system elements. Moreover, the interactional activity is accentuated by the relative position of the rotor and the dominating and pervasive influence of its wake in all flight regimes. Beyond this, the flow complexity is heightened in the helicopter's unique operational capability at very low speeds near the ground which is the theater of NOE operations.

TRENDS IN INTERACTIONAL AERODYNAMICS

A number of factors have been at work in recent years leading to a renewed interest in helicopter interactional aerodynamics. One of these has been the Army's NOE concept, which has been extensively promulgated as an operational doctrine for all helicopters. The aerodynamics implications of flying low and slow have been dealt with extensively in Reference 1, with additional insights provided in this report. The necessity for extended flight durations in the NOE to avoid the mounting threat is causing a shift in emphasis from the high-performance, high-speed area of research and development.

---

1. Sheridan, Philip F., and Wiesner, Wayne, AERODYNAMICS OF HELICOPTER FLIGHT NEAR THE GROUND, American Helicopter Society 33rd Annual National Forum, Preprint No. 77.33-04, Washington, D.C., May 1977.

The UTTAS programs have directed attention to flow conditions near the ground, between the rotor and fuselage and in the vicinity of the tail rotor and empennage. These problems have been aggravated because of the higher disk loadings and closer proximity to the ground of the main rotors of these aircraft.

Transportability has required that the helicopter dimensions match the cargo compartments of military transport airplanes with minimal disassembly, resulting in an overall height that is small for the size of the aircraft. One significant aerodynamic configuration characteristic that results from that requirement has been a narrow gap between the blades and the top of the airframe. This is of the order of one blade chord in magnitude. Because of this, the surface pressures due to blade proximity can be considerably higher than they are with more conventional separation distances. Another important effect is the closer rotor proximity to the ground.

A significant trend is higher disk loading, which produces greater downwash velocities. In combination with low rotor height this produces greater disturbance at the ground and a higher consequent reflection back to the rotor. Hence there is greater aerodynamic interaction between ground and rotor and other configuration elements in the emerging new aircraft.

Similarly, the low placement of the rotor with essentially no pylon aggravates the rotor/hub/fuselage interaction, which seems to be manifested by a more irregular wake behind the hub with a deep depression in the vertical velocity profile. A strong imprint of the rotor blade passage frequencies is also evident in the wake spectral profile.

Another requirement drawing attention to the aerodynamic interactions is the need to sustain directional trim in the event of tail rotor loss at minimum power speed. This results in large vertical tail area relative to tail rotor disk area, and in the conventional fin/tail rotor configuration large fin losses can result. Their effect is addressed in considerable depth in a subsequent section of this report.

THE AERODYNAMIC SYSTEM CONCEPT

In order to exercise the configuration aerodynamics discipline in its rightful scope and depth, it is desirable to be able to consider the many interactional aerodynamics areas in a comprehensive and related manner. To accomplish this, the whole entity may be viewed as an aerodynamic system whose elements are interactively coupled by the air. This concept is depicted in Figure 1. The principal configuration elements are shown in the blocks and their mutual interactions (often called "interferences") as dotted lines. In general, the vertical dotted lines are associated with hover and low-speed flight and the horizontally oriented lines denote wake-related interactions of forward flight. These are, of course, intimately associated with the principal flows, which are the relative wind, the main rotor wake and the associated complex vortex geometry, the tail rotor downwash, the engine exhaust, and the ground flow.

The system described is applicable to any aircraft if we suitably reassign the lift, propulsion, and other elements. It is most highly coupled in the helicopter because of the dominating influence and relative position of the rotor plus the helicopter's natural operating environment near the ground. A basis is formed here for systematically addressing the associated problems in a coordinated and comprehensive way.

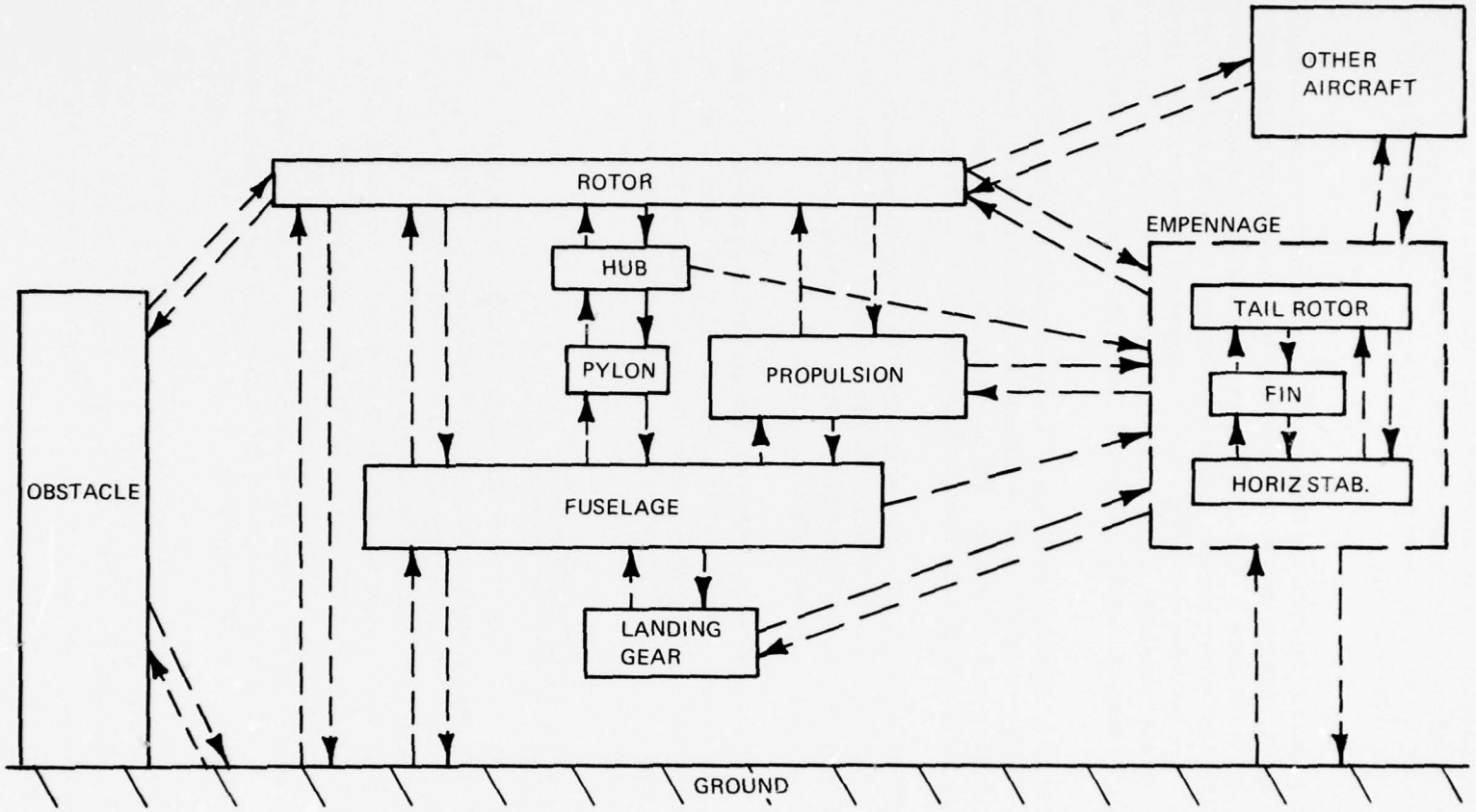

Figure 1. Aerodynamic Interactions of the Single-Rotor Helicopter Configuration.

CLASSIFICATION OF PROBLEMS

The framework of Figure 1 presents a logical basis for the classification of interactional problems in Configuration Aerodynamics. Each problem will be associated with one or more of the interactions denoted by the dotted lines in Figure 1. Such a classification is presented in Table 1. A list of the interactions is presented in the first column. Next to this are the associated problems stated in familiar terms. A third column lists the key design and flight variables that are involved. Use of this unifying philosophy will make it easier to cope with the many and various interactional aerodynamics problems in any phase of the design cycle. Specific advantages of the system approach are as follows:

1. It adequately describes the total Configuration Aerodynamics problem areas for the first time.
2. The individual problems are related where they share the same flows. Thus test and analysis of any specific problem will also demand consideration of the associated problems so that solutions for the one will not create new problems elsewhere. This consideration is facilitated by the problem identification of the system approach.
3. By the same token, although the number of related problems is large, they are functions of similar parameters so that the exercise of these variables can cause flow changes favorably impacting other problems, resulting in a more optimum system.
4. The system definition and the related classification of problems provide a checklist for scorekeeping in assessing our understanding and handling of configuration aerodynamics in design, development, test, and operations.
5. A tool is provided both for evaluating current knowledge and for planning required work to advance understanding and more efficient solutions.

ORGANIZATION OF WORK FOR THIS REPORT

The problem classification chart of Table 1 has been employed conveniently to organize the work of this report in the same format as shown in Table 2. These are the interactions and related problems discussed in the subsequent sections.

TEST CONDITIONS

The test runs are grouped and tabulated according to interaction category. These tables are placed in the report with the appropriate section of analysis. Presented information includes the run numbers, configuration code, test condition and purpose, speed, main and tail rotor rpm, disk loading, model angles of attack and yaw, nondimensional rotor height, and tail rotor on or off. These data are derived from the official log of the test in the file of the Boeing Vertol wind tunnel.

Only those runs are shown that form the basis for the studies of this contract. Omitted are runs for such purposes as equipment functional checks, certain tests not relevant to the scope of the contracted work, runs which were repeated due to malfunctioning equipment, and so forth.

TABLE 1. CLASSIFICATION OF AERODYNAMIC INTERACTIONS AND RELATED PROBLEMS

Aerodynamic Interaction	Problems or Phenomena	Key Variables
Rotor/Fuselage	High vibratory fuselage pressures Steady fuselage loads Higher rotor power Vibratory blade loads Vibratory drive system torque	V (α, β), w, rotor-to-fuselage distance Δh
Rotor/Hub/Fuselage	Flow environment at hub Hub drag	V (α, β), size and shape of hub, size and shape of fuselage Δh, w
Rotor/Ground	Size, strength, and structure of ground vortex Vibratory blade loads Rapid changes in power and hub moments Pilot workload Dust ingestion Dust cloud Debris entrainment	V (α, β), w, height-to-diameter ratio h/d, root cutout
Rotor/Fuselage/Ground	Rotor power IGE fuselage download IGE steady and vibratory fuselage pressures Low airspeed measurement Cooling air availability Weapons launch Fluctuating fuselage loads (skittishness) Pilot workload	V (α, β), w, h/d, root cutout, fuselage shape
Rotor/Empennage Hub/Empennage	Trim loads and flow angles on stabilizer and fin, load sharing, T/R vs fin Flow environment (wake) Wake-induced vibratory loads on T/R, stabilizer and fin	V (α, β), hub covers, wings, fairings, air injection, stabilizer settings, empennage locations and geometries
Fuselage/Empennage	Yaw kick	V (α, β), fuselage afterbody shape
Rotor/Wing	Download on wing Blade loads Induced flow field Trim change on wing	V (α, β), w, wing loading, wing/rotor area ratio, load sharing ratio, gap, aspect ratio
Rotor/Wing/Ground	Download on wing Pitching upset Rolling upset Skittishness Trim change Vibr wing loads in transition	V (α, β), w, gap, h/d, h/b wing/rotor swept area ratio

TABLE 1 - Continued

Aerodynamic Interaction	Problems or Phenomena	Key Variables
Rotor/Wing/Fuselage	Fuselage moments Fuselage download Induced flow field Induced drag Afterbody flow separation	V (α, β), w, gap, wing placement, wing loading, wing/rotor area ratio, load sharing, aspect ratio
Rotor/Wing/Empennage	Trim changes at tail Wake structure at tail Induced flow angles at tail Wake-induced vibratory loads	V (α, β), w, tail placement, rotor and wing parameters
Rotor/Empennage/Ground	Trim changes on T/R, fin and stabilizer forces and flow angle near ground	V (α, β), h/d, w, T/R induced flows
Main/Tail Rotor/Ground	Effect of T/R on main rotor power and trim Effect of M/R on tail rotor power and trim	V (α, β), h/d, w, T/R location, T/R disk loading
Main/Tail Rotor/Fin/Ground	Adverse fin load Fin stall Low-speed buffet	V (α, β), fin area/disk area, tractor vs pusher, fin-to-T/R gap, M/R and T/R w, h/d, main/tail rotor proximity
Main/Tail Rotor/Stabilizer/Ground	Rapid changes in stabilizer load and flow angle	V (α, β), w, h/d, T/R height, stabilizer position and geometry, W_{TR}
Rotor/Powerplant/Ground	Engine surge due to high exhaust gas reingestion Engine cooling air availability	V (α, β), w, h/d, nacelle geometry, nacelle-to-rotor distance, inlet and exhaust pipe geometries, gas temperature and velocity
Rotor/Rotor (Multi-Helicopter Op)	Upset loads on all axes	V (α, β), w
Rotor/Ground/Rotor	Upset loads on all axes	V (α, β), w, h/d
Rotor/Ground/Obstacle	Upset loads on all axes	V (α, β), w, h/d, obstacle size and location
Powerplant/Nacelle	Inlet distortion Engine cooling IR signature	Nacelle/inlet geometry P/P heat rejection Exhaust temperature
Fan-in-Fin	Thrust vs power Blade cyclic loads Noise Fin loads	Disk loading Disk/fin area Duct shaping Blade/duct gap Cross flow

TABLE 2. SPECIFIC AERODYNAMIC INTERACTIONS AND RELATED PROBLEMS OR PHENOMENA ANALYZED IN THIS REPORT

Aerodynamic Interaction	Problems or Phenomena	Key Variables
Rotor/Ground	Formation of ground vortex Rapid changes in power and hub moments	Speed magnitude in direction V (α, β), rotor-to-ground height (h/d), disk loading (w)
Rotor/Fuselage	Vibratory pressures Fuselage loads Rotor power	V (α, β) rotor-to-fuselage height
Rotor/Fuselage/Ground	IGE fuselage download IGE fuselage pressure	V (α, β), h/d, w
Rotor/Empennage (Tail Rotor, Pylon, and Stabilizer)	Wake structure Wake-induced loads Tail rotor/main rotor blade proximity effects Pressures on stabilizer and pylon	Trim (α, β) hubcaps, wings, fairings, air injection, stabilizer settings
Rotor/Empennage/Ground	IGE trim change Tail rotor/main rotor mutual interaction on power, loads, etc. Adverse fin load Fin stall	V (α, β), h/d, w, T/R on and off

The basic configuration summary codes are given in Table B-5 and the codings for the individual test pieces are defined in the Model Test Component section of Appendix B.

TEST FACILITIES AND EQUIPMENT

This section consists of general descriptions of the wind tunnel, the model and its test configurations, and the instrumentation and data systems. More detailed discussions of the model system, the test pieces, instrumentation, data acquisition and processing, calibrations, and equipment checkout may be found in Appendix B.

WIND TUNNEL DESCRIPTION

The testing was conducted at the Boeing V/STOL wind tunnel, which is located at the Boeing Vertol plant in Delaware County, Pennsylvania. The complex includes the wind tunnel itself, an engineering support building, and a model fabrication shop. A cutaway perspective view of the tunnel is presented in Figure 2 and a circuit diagram in Figure 3. The basic dimensions of the closed test section are 20-by-20 feet square and 45 feet long. Excellent flow quality exists over an 18-foot-square by 25-foot-long volume of the test section.

For low-speed work the tunnel is usually converted to the open-throat configuration by removal and nearby storage of the aft 29 feet of test section ceiling, walls, and floor. For ground effect studies, the floor is left in place to receive the ground board.

The wind tunnel is powered by a 15,000-hp package comprising two motors located inside the fan nacelle. A 1,500-hp dc motor powers the fan at low speed. A 13,500-hp ac motor with a liquid rheostat drives the tunnel at medium speeds with the dc motor in a motor/generator mode acting as a speed control. At the highest speeds both motors will share the load. This system provides excellent speed control through the test section speed range of zero to 235 knots. For cooling, an air exchange inlet is located just downstream of the test section and the exit, upstream of the contraction cone. With the maximum purge rate of 10 percent exchange per circuit, tunnel air temperature rise at maximum speed can be maintained to approximately 20°F with respect to the ambient value.

Because of the exhaust location the tunnel becomes vented in a low-velocity high-pressure region. Thus the test section will carry a pressure lower than atmospheric and must be contained within a plenum structure. The large volume of the plenum provides a commodious chamber for hover testing a model in the test section in the open jet configuration with the sides removed.

The ground board measures 20 feet square, as wide as the test section and centered longitudinally about the model axis of rotation. Physically separate from the model, the ground board may be fixed with the model moving to vary rotor-to-ground height or the model may be maintained fixed in the airstream with the floor dropping down to vary the height.

A moving-belt ground plane is available, capable of speeds as high as 100 knots. This is usable, however, only with models that are sting-mounted in such a way as to freely overhang the moving belt.

The control room and the on-line computer room are situated adjacent to and on the same level as the test section. Here are housed the tunnel speed and equipment controls, model condition controls, safety-of-flight monitor equipment, and the tunnel data system based upon

the IBM 1800 computer. In addition to displays of all the pertinent input and output values, there are data output devices like the printer that gives final processed information for each test point. There are also analog (CEC) recorders, X-Y plotters, and a power spectral density analyzer. This last item is used to make spectral analysis of any dynamic parameter that is either available instantly on-line or may be derived subsequently from tape. Spectrographs may be obtained either photographically (Polaroid camera on scope) or from a special integral analog plotter.

Adjacent to the control room on the second floor of the engineering building are a model hardware preparation area, instrumentation lab, and office space for engineers of the test disciplines.

The shop is large and well equipped, having the tools and staff to do machining, woodworking, composite material bonding, instrumentation work, and model assembly and inspection. This capability can produce 85 to 90 percent of the models, most of which are powered and dynamically scaled. This output includes drive systems, rotor blades, balances, and instrumentation and control systems.

MODEL DESCRIPTION

The Single-Rotor Helicopter (SRH) model system was employed for the testing described in this report. The SRH system consists of a power pod, main rotor and control drive system, and a frame to receive the nonrotor items of the test configuration. The system may be used to support tests of main rotor alone, tail rotor alone, fuselage alone, or any combination. Figures 4 and 5 show exterior views of the SRH installed in the test section and configured as the YUH-61A UTTAS helicopter at a scale of 1/4.85. The system elements are depicted schematically in Figure 6. Key model parameters are listed in Table 3.

TABLE 3. MODEL PARAMETERS

Rotor Radius – Main/Tail	60.62/12.37 inches
Reference Chord – Main/Tail	4.74/1.812 inches
Blade Number – Main/Tail	4/4
RPM – Main/Tail	1,433/4,500
Tip Speed – Main/Tail	768/486 fps
Main Rotor Shaft Incidence to WL	4 degrees
Main Rotor Center Station/Waterline	41.6/43.6
Tail Rotor Center Station/Waterline	115.7/48.6
Horizontal Stabilizer Span	37.36 inches
Mean Aerodynamic Chord (MAC)	6.87 inches
Root Chord (Extended)	8.22 inches
Tip Chord	5.32 inches
1/4-Chord Sweep	6.8 degrees
Tail Arm (25% MAC to STA 44.3)	63 inches
Incidence Range	−5 to + 50 degrees
Vertical Tail Height (Tip to WL 37.5)	16.25 inches
Root Chord	15.2 inches
Tip Chord	6.4 inches
Mean Aerodynamic Chord (MAC)	11.4 inches
1/4-Chord Sweep	37.5 degrees
Incidence	0 degrees
Tail Arm (25% MAC to STA 44.3)	66.9 inches

The power pod contains three air motors with a total output capability of 400 hp into the gear train, whose output shaft to the main rotor rotates at 1,600 rpm. The vertically oriented shaft is contained within the faired hollow strut and extends upward to connect with the rotor head.

The tail rotor is driven by its own 15-hp air motor, mounted underneath it, which drives bevel reduction gearing connected to the rotor shaft. The air supply is ducted up from the power pod through the hollow support strut using flexible hose.

The model pitch attitude is varied through a knuckle joint in the main support. Its yawing angle is achieved by rotation of the vertical support strut by a mechanism within the power pod.

The fuselage comprises 1/4-inch-thick left and right fiberglass shells. These are bolted together and the combination is attached to the fuselage balance, which is forward of the rotor. This is the only support point, thus assuring the isolation necessary for fuselage load measurement. The shells came in two versions; one plain and one instrumented with Kulite pressure transducers for obtaining vibratory pressures.

The horizontal stabilizer of 5.5 aspect ratio is pivot-mounted at 25 percent of the mean aerodynamic chord and is remotely positioned through a range of -5 to +50 degrees. The vertical tail (fin) is made in two shell halves like the fuselage. Both the stabilizer and fin along with the tail rotor are mounted off the empennage balance, which senses the loadings on the model aft of a demarcation line at approximately model station 100. The tail rotor also has its own separate balance.

The variations in model parameters fall into three categories associated with the requirements of the program objectives:

1. Understanding the Vibratory Pressures. Here test pieces were created to reduce the vibratory pressures on the upper surfaces of the fuselage. These included various strake configurations, vortex generators, and drive shaft plugs to raise the rotor.

2. Understanding the Ground Vortex. The only model variation exercised was removal of the tail rotor for one run.

3. Reducing the Wake Impingement on the Empennage. Many pieces were created to alter the wake so as to reduce the low-frequency turbulence at the empennage. These devices were intended to deflect the flow downward to lessen its impingement, to mix fresher (less turbulent) air into the wake to reduce the dynamic activity, or to achieve a combination of these effects. Examples of the deflection devices included principally wings of various shapes and locations. The freshening devices included a variety of air ejector systems installed just aft of the hub on the aft crown. In this category also are a number of fairings designed to bring the air smoothly around and past the hub, which was situated almost on top of the fuselage; i.e., there was no pylon. A variety of hubcaps differing in size, shape, and arrangement was evaluated. These generally seemed to effect both a deflection and a low-frequency attenuation, apparently by covering the hub and entraining fresh air from in front.

These devices and their effects are discussed in detail in this data analysis section. Dimensioned sketches of each are presented in Appendix B.

INSTRUMENTATION

The basic model instrumentation is shown schematically in Figure 7. This includes the basic package of five balances, main and tail rotor control systems, model orientation (pitch and yaw angles), lubrication system temperatures and flow rates, tail angles, and blade stresses. Many of these were safety-of-flight parameters and were monitored on the on-line displays such as digital meters, scopes, peak-to-peak meters, and analog meters.

The SRH system contains four balances on the model chassis within the shell and a total loads balance in the strut fairing below the model. The four include rotor, fuselage, empennage, and tail rotor balances. All are the six-component type except the empennage balance, which omits the drag force. Data from these balances are available for every test point of each run. A location drawing of the balance is shown in Figure 8.

Fifty-three 0.1-psi pressure transducers were fitted to one of the fuselage shells and to the empennage. Figure 9 shows the deployment of the transducers over the surface. They are concentrated on the upper surfaces and the empennage to sense the effect of rotor proximity or wake passage. A tabulation of their precise coordinates in the model reference system may be found in Appendix B.

The greater number of test runs were concerned with measurement of the wake. The apparatus employed for this purpose consisted of a remotely actuated rake on which were mounted TSI hot film flow sensors. Two such devices of the split-film type were installed at the center of the rake bar at 90 degrees to one another to sense lateral and longitudinal flow angles (α and β) and associated velocities. Three single film transducers sensing only velocity were located outboard along the bar on each side. The rake could be moved longitudinally and vertically by remotely actuated screwjack traversing mechanisms. Figure 10 illustrates the rake as it was positioned just in front of the empennage.

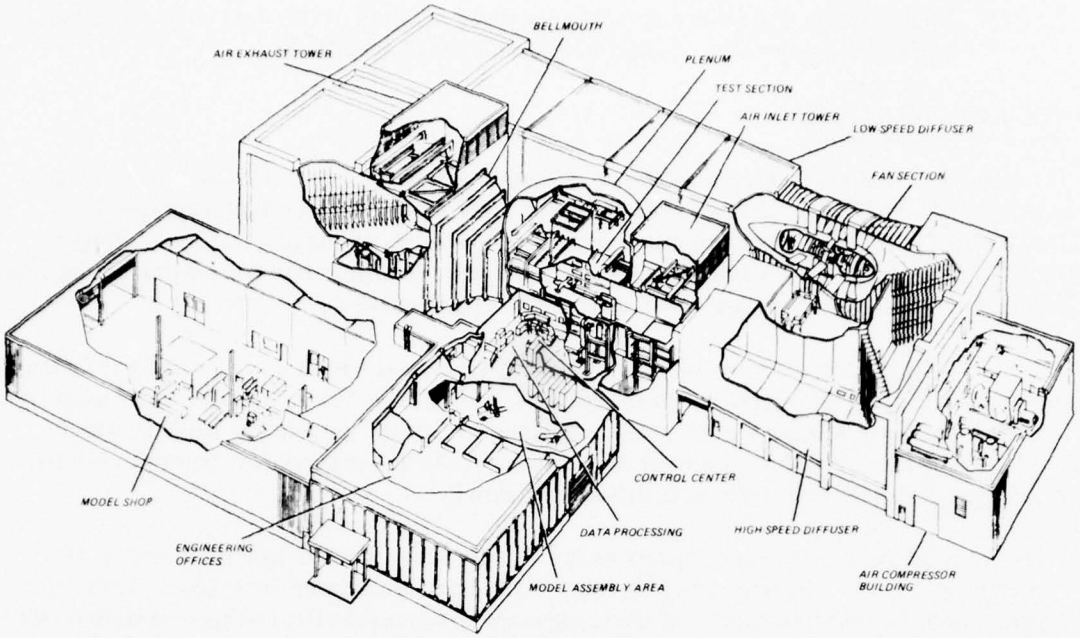

Figure 2. Overview of Boeing V/STOL Wind Tunnel.

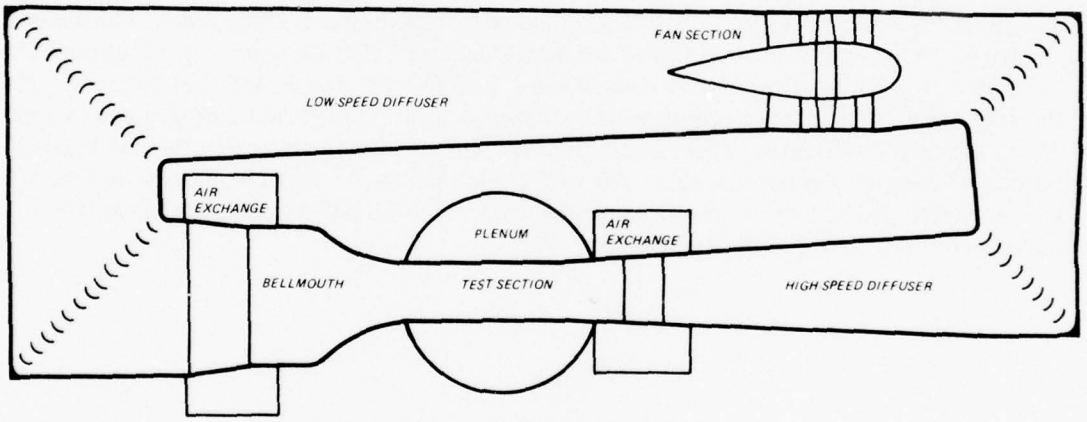

TEST SECTION FEATURES

- 20x20-FT CROSS SECTION
- 45 FT LONG
- CONTRACTION RATIO = 6.0
- DIFFUSER ANGLE = 6^{o} EQUIV CONE
- MAXIMUM TUNNEL VELOCITY
  v = 240 KNOTS

Figure 3. Boeing V/STOL Wind Tunnel Circuit Layout.

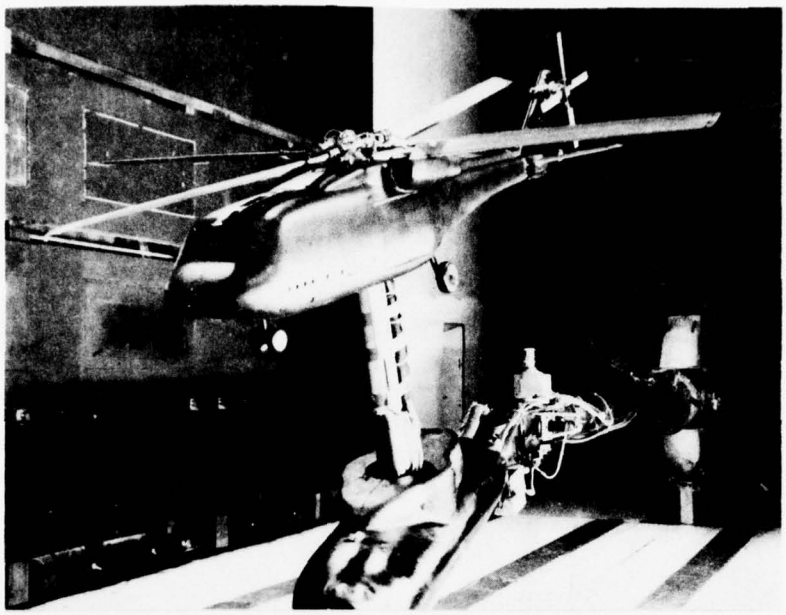

Figure 4. SRH Model in YUH-61A Configuration (Front View).

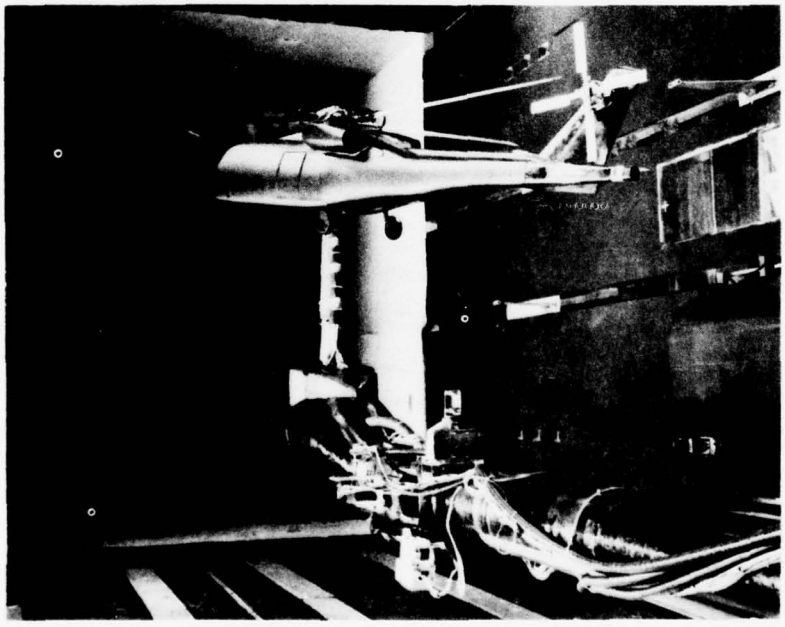

Figure 5. SRH Model in YUH-61A Configuration (Rear View).

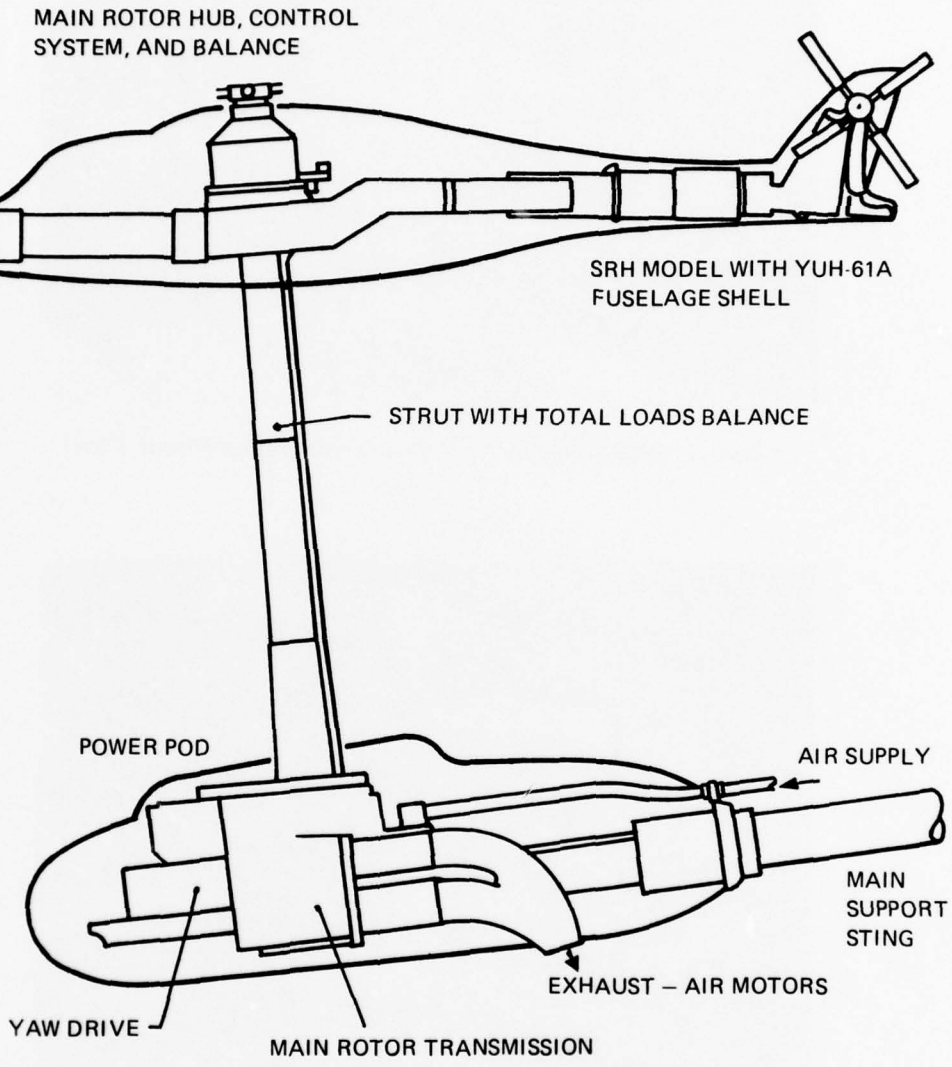

Figure 6. SRH Model Arrangement.

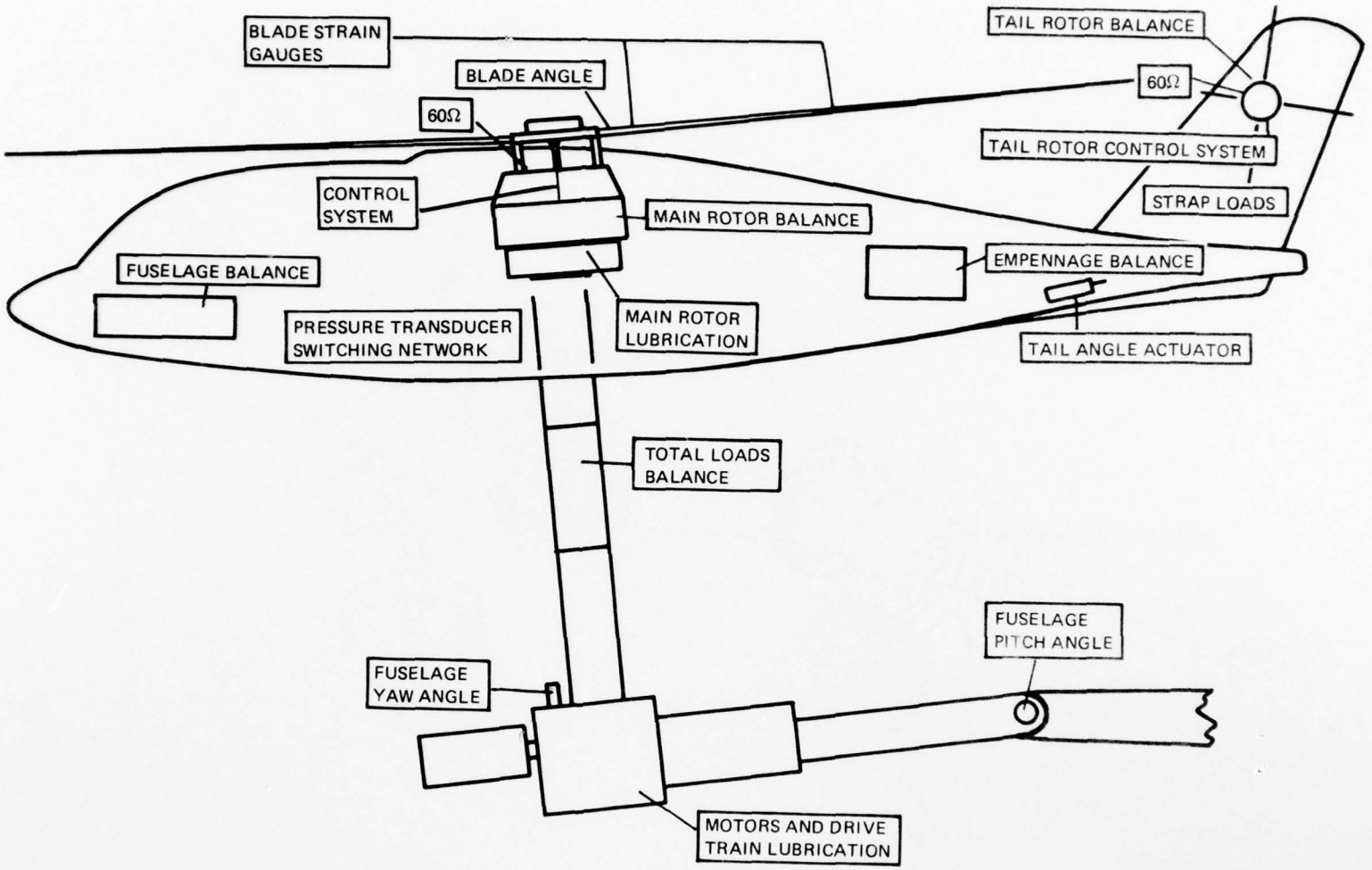

Figure 7. Basic Instrumented Model Parameters.

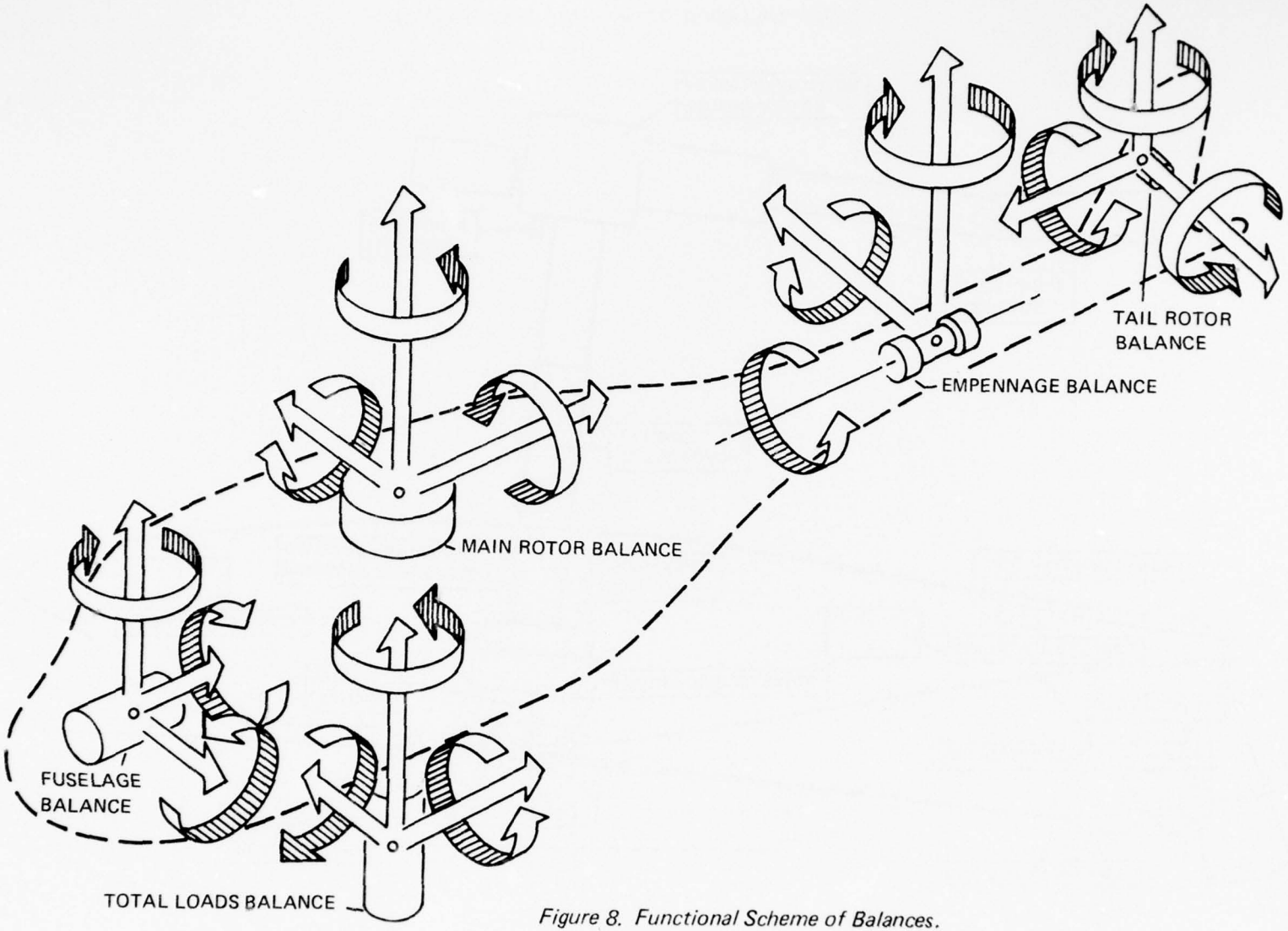

Figure 8. Functional Scheme of Balances.

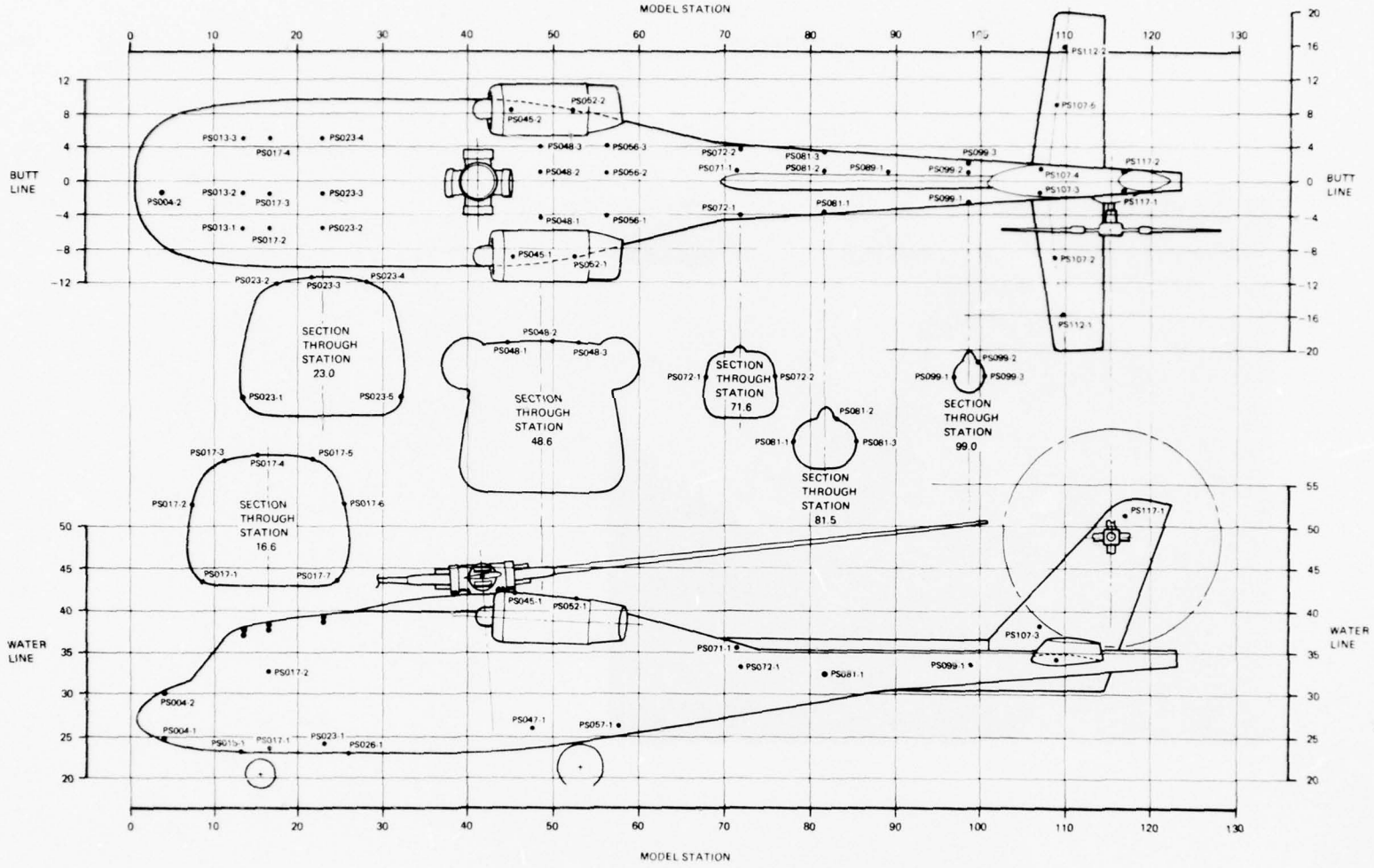

Figure 9. UTTAS 1/4.85-Scale Model Geometry and Surface Pressure Transducer Locations.

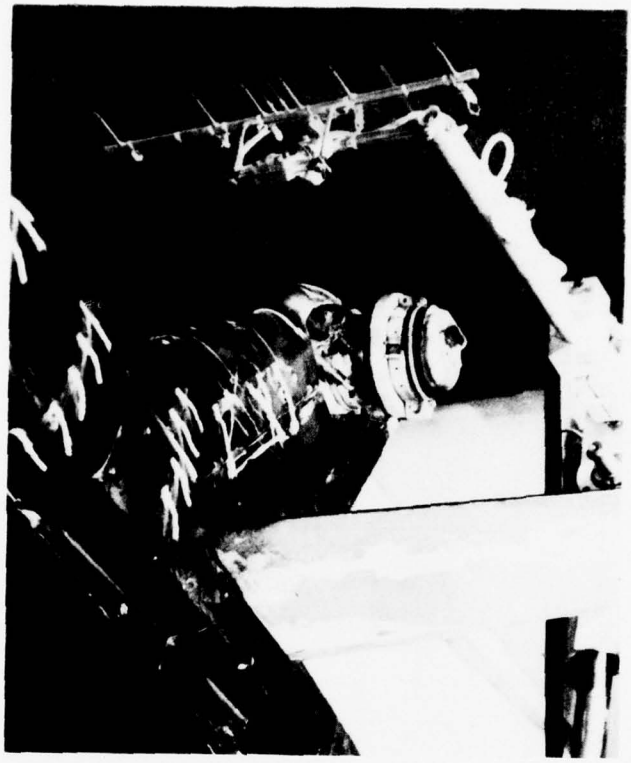

Figure 10. Hot Film Probe Rake Installation.

ROTOR/GROUND INTERACTION

A large and significant interaction occurs between the rotor and the ground at height-to-diameter ratios below about 0.5 and at speeds from zero to 50 knots. It affects power required and hub forces and moments in a nonlinear manner, and will occur with the wind from any azimuth. The principal agency of interaction is the ground vortex, a large and powerful aerodynamic entity generated by the interaction of the main rotor downwash and the relative wind in the presence of the ground.

A number of investigators have studied the ground vortex in connection with directional control problems in rearward flight. Here the interactions at work involved the tail rotor and fin with the ground vortex and with a secondary influence from the main rotor. References 2, 3, 4, and 5 are cited in this regard.

In contrast, the wind tunnel tests described in this report are the first, apparently, to address the influence of the ground vortex on main rotor and fuselage parameters. Some of this has been presented to the technical community in Reference 1. There and here, the flight condition of interest was forward flight with the exception of two runs at ψ = -30 and +30 degrees. Table 4 lists the runs of the test program devoted to ground proximity studies.

The motivation for this phase of the work was the need to understand the nonlinear variations in lateral stick trim that occurred in transition when translating parallel and close to the ground either in takeoff or landing. When accelerating, the aircraft required a very sharp increase in left lateral stick at about 20 knots. In the deceleration, similar action was required except that the stick had to be moved to the right to maintain lateral equilibrium. Typically, this would occur with a wheel height of 10 to 15 feet. Since it occurred for very high and low magnitudes of acceleration, it was believed to be a steady state phenomenon. It was also repeatable, which ruled out a wind-turbulence-induced upset. Precise means to measure airspeed and wheel height were not available at the time, so a wind tunnel program was initiated and conducted.

THE GROUND VORTEX

The aerodynamics of the helicopter in ground proximity are extremely complex. All of the major flows play a role and interact with one another, i.e., the relative wind, the main rotor wake, the tail rotor wake, the engine exhaust, and the ground flow, which results from the interaction of the previous flows and the ground boundary.

---

2. Huston, Robert J., and Morris, Charles E.K., Jr., A WIND TUNNEL INVESTIGATION OF HELICOPTER DIRECTIONAL CONTROL IN REARWARD FLIGHT IN GROUND EFFECT, NASA Technical Note D-6118, National Aeronautics and Space Administration, Langley Research Center, Hampton, Virginia, March 1971.

3. Wiesner, W., and Kohler, G., TAIL ROTOR PERFORMANCE IN PRESENCE OF MAIN ROTOR, GROUND AND WINDS, Journal of the American Helicopter Society, Vol. 19, No. 3, Washington, D.C., July 1974.

4. Yeager, William T., Jr., Young, Warren H., Jr., and Mantay, Wayne R., A WIND TUNNEL INVESTIGATION OF PARAMETERS AFFECTING HELICOPTER DIRECTIONAL CONTROL AT LOW SPEEDS IN GROUND EFFECT, NASA Technical Note D-7694, Langley Directorate, U.S. Army Air Mobility Research and Development Laboratory, Langley Research Center, Hampton, Virginia, November 1974.

5. Empey, R. W., and Ormiston, R.A., TAIL ROTOR THRUST ON A 5.5 FOOT HELICOPTER MODEL IN GROUND EFFECT, Technical Paper, Ames Directorate, U.S. Army Air Mobility Research and Development Laboratory, Moffett Field, California, 1975.

TABLE 4. TEST RUNS FOR THE EFFECTS OF GROUND PROXIMITY

Run No.	Configuration	V_{TUN} (kn)	MR/TR Speed (rpm)	Disk Ldg (psf)	Model Angles α (deg)	Model Angles ψ (deg)	MR Ht (h/d)	Tail Rotor
83	K_9/Baseline for D.L. variation	◇11	1,433/ 4,500	8	0	0	0.4	On
84	K_9/Added detail to 83	10↔20 /2's	1,433/ 4,500	8	0	0	0.4	On
85	K_9/Increased D.L.	◇11	1,433/ 4,500	10	0	0	0.4	On
86	K_9/Added detail to 85	20↔26 /2's	1,433/ 4,500	10	0	0	0.4	On
87	K_9/Reduced D.L.	◇11	1,433/ 4,500	6	0	0	0.4	On
88	K_9/Added detail to 87	12↔18 /2's	1,433 4,500	6	0	0	0.4	On
89	K_9/Reduced D.L.	◇11	1,433/ 4,500	4	0	0	0.4	On
90	K_9/Effect of pos yaw	◇11	1,433/ 4,500	8	0	+30	0.4	On
91	K_9/Effect of neg yaw	◇11	1,433/ 4,500	8	0	-30	0.4	On
92	K_9/Effect of neg angle of attack	◇11	1,433/ 4,500	8	-6.6	0	0.4	On
93	K_9/Effect of pos angle of attack	◇11	1,433/ 4,500	8	+10	0	0.4	On
94	K_9/Reset α to mean value over transition	◇11	1,433/ 4,500	8	5	0	0.4	On
95	K_9/Added detail to 94	12↔20 /2's	1,433/ 4,500	8	5	0	0.4	On
96	K_9/Added detail to 94	10↔30 /2's	1,433/ 4,500	8	5	0	0.4	On
97	K_9/Added detail to 94	10↔30 /2's	1,433/ 4,500	8	5	0	0.4	On
98	K_9/Reduced D.L.	10↔30 /2's	1,433/ 4,500	6	5	0	0.4	On
99	K_9/Increased rotor height	10↔30 /2's	1,433/ 4,500	8	5	0	0.475	On
100	K_9/Increased rotor height	◇11	1,433/ 4,500	8	5	0	0.475	On
101	K_9/Effect of tail rotor stopped	◇11	1,433/0	8	5	0	0.4	Stopped
102	K_9/Increased rotor to ground height	◇11	1,433/ 4,500	8	5	0	0.6	On
103	K_9/Increased rotor to ground height	◇11	1,433/ 4,500	8	5	0	0.7	On
104	K_9/Increased rotor to ground height	◇11	1,433/ 4,500	8	5	0	0.8	On
105	K_9/Increased rotor to ground height	◇11	1,433/ 4,500	8	5	0	1.0	On

NOTE: ◇11 for V_{TUN} = 0, 10 to 40 knots by 5's, then 50 kn

The earliest identification of the ground vortex appeared in Reference 6 during tuft grid studies incidental to an investigation of transition aerodynamics out of ground effect. The first work to clearly identify the ground vortex as the product of the interaction of the relative wind and the main rotor wake in ground effect was Reference 5. This work also was the first to consider the vortex as the influential element in a real world problem and to exercise some of the variables that affect it. The problem, as reported in Reference 7, was the inadequacy of the AH-1G helicopter directional control in left-quartering low-velocity tail winds when operating at high gross weights in ground effect with the original pusher tail rotor. The AH-1G also suffered from marginal directional control in right sideward flight above 12 knots, according to Reference 8.

The Huey Cobra problem instigated the series of investigations that were reported in References 2, 3, 4, and 5. Reflecting tail rotor interest, these experiments emphasized the tailwind-rearward flight situation and low rotor heights, with h/d of 0.355 for References 2 and 4, 0.3 for Reference 3, and 0.265 for Reference 5.

In contrast, the wind tunnel tests of this report emphasized forward flight, h/d of 0.4, and the effects on the main rotor.

As the tunnel speed is increased from zero, the ground vortex, as delineated by smoke released at the edge of the ground, is seen to appear at the edge of the wind tunnel ground board with the oncoming air coming up and over the vortex. Some air is entrained in the vortex and the rest moves up and then down as entrainment in the rotor inflow takes place. This is illustrated by Figure 11, which idealizes the flow by a static representation of an extremely unsteady flow state. The entire flow is randomly oscillating in all directions, a characteristic that persists with increasing speeds.

As the vortex approaches the rotor, the negative inflow at the rotor leading edge appears to increase as shown by the smoke flow patterns. The vortex becomes more identifiable and the velocities seem greater, which is logical with the vortex receiving a greater concentration of rotor energy.

The ground vortex comes abreast of the rotor and passes beneath it at a speed of about 17 knots for 0.4 h/d and a disk loading of 8 psf. As this occurs, the inflow at the front of the rotor changes from a high downflow to a high upflow. This is evident in the smoke patterns, and also in the rotor hub moment data discussed later. This process is diagrammed in Figure 12, which compares the flow pattern before and after the vortex moves under the rotor.

Following soon after this, the high vortex velocities near the vortex center will impact on the fuselage and cause sharp changes to be evident in the force and moment variations with speed. Evidently, when the vortex moves under the rotor, the resulting containment causes an increase

---

6. Jenkins, Julian L., Jr., TRIM REQUIREMENTS AND STATIC STABILITY DERIVATIVES FROM A WIND TUNNEL INVESTIGATION OF LIFTING ROTORS IN TRANSITION, NASA Technical Note D-2655, National Aeronautics and Space Administration, Langley Research Center, Hampton, Virginia, February 1965.

7. Conner, William J., THE HUEY COBRA IN VIETNAM, Technical Review, Vol. 9, No. 2, Society of Experimental Test Pilots, 1968.

8. Lewis II, Richard B., ARMY HELICOPTER PERFORMANCE TRENDS, Journal of the American Helicopter Society, Vol. 17, No. 2, Washington, D.C., April 1972.

in strength and dynamic activity. The noise level is noticeably high and the rotor tip path moves erratically under the influence of the unsteady inflow.

Figures 13a and 13b compare the vortex flow for rotor heights of h/d 0.48 and 1.0. The smoke was introduced at the edge of the ground board and just to the right of center. There were two smoke jets – one just above the board and one higher. Despite the large difference in height, the vortex retains the same location at approximately 20-percent diameter above the board and seems to have similar strength. Although the horizontal position of the vortex changes considerably with speed, and to some degree with the other variables, its core was observed to stay within 20-percent diameter distance off the floor for all cases. Although the vortex is no longer seriously influencing aircraft or rotor loadings at h/d of 1.0, the high winds at the ground must still be reckoned with.

In the test that is being reported, no measurements were made of the velocities in or near the vortex. However, a year later, during exhaust ingestion investigations in the wind tunnel, a vertical traverse with hot film anemometer equipment was made. The results are shown in Figure 14, and although the measurement period is too brief to acquire the lowest frequency material, evidence of high mean velocities with wide fluctuations is clear. This modest effort just scratches the surface, and it remains to define accurately the flow field in its steady and unsteady aspects.

The results of the flow observations and measurements underscore the unsteady nature of the helicopter aerodynamic environment near the ground and the need to approach it with the most sophisticated tools and techniques.

One problem that has emerged in studying the data is the need for special consideration of boundary corrections when varying rotor height from the ground board in the transition speed range. This is not important when the presence of the board is a dominating factor as it is with the very low rotor heights that were the principal interest in this wind tunnel test. However, as the rotor is raised away from the board and closer to the open jet boundary, it will begin to interact with the tunnel jet. Corrections to flow angles will then be necessary to insure that the data properly approaches the out-of-ground-effect value for the high h/d values beyond 1.0. This is quite a complex matter requiring different corrections for each h/d and $\mu\sqrt{C_T/2}$. Having a relatively low priority, it was not attempted for the reported program. In discussing the data in this report, the practice will be to compare the case for h/d equal 0.4 – occasionally 0.6 as well – to out-of-ground data obtained in the closed tunnel with boundary effects applied.

EFFECTS ON POWER REQUIRED

Effect of Height

The variation of power required by the main rotor versus speed is shown in Figure 15 (h/d of 0.4 and OGE). The hover values indicate the familiar reduction in power due to ground proximity. A smaller power differential remains at the higher speed, which would vanish for equal trim on the two curves. The interesting feature in the comparison is the increasing power required as speed increases from the hover point. This is attributed to the ground-vortex-induced downflow into the rotor, which goes away at about 0.8 (approximately 20 knots) as the vortex moves under the rotor.

Effect of Model Pitch Attitude

The manner in which the data varies as model pitch attitude changes is shown in Figure 16. The data of Figure 15 were shown for 5 degrees attitude and are repeated in Figure 16 for comparison to zero, 10, and -6.6 degrees. The odd negative angle of -6.6 resulted from a limitation in the mechanism at that time. The hill created by the power-required increase at low speed is evident in the carpet plot topography and has greatest eminence for zero degrees. The other three cases, however, have fewer points in this regime and the power rise could be more severe than Figure 16 indicates.

Effect of Disk Loading

Figure 17 shows power required versus nondimensional speed for 4, 6, 8, and 10 pounds per square foot disk loading. The effect of the vortex as indicated by the shaded area is only approximate, since we can only guess at the zero vortex baseline. However, an effect proportional to disk loading is clearly in evidence, and it is possible that high-disk-loading helicopters may have a greater power management problem when operating in the NOE.

Effect of Yaw Angle

The power-required data are carpet plotted against speed and yaw angle, i.e., wind direction, in Figure 18. Power is significantly less for plus 30 degrees at all speeds, and the hill is less prominent. Presumably the lack of symmetry with yaw is related to one or more of the nonsymmetric elements such as rotor swirl, the tail rotor flow, or a lateral dissymmetry in the induced velocity pattern. More investigation is needed here.

EFFECTS ON ROLLING MOMENT

As was mentioned in the introductory discussion of this section, a sudden and large rolling moment change in transition close to the ground was encountered in the UTTAS program. This was present for large and small amounts of deceleration and acceleration which suggested it probably existed for steady flight as well, and would be measurable in the wind tunnel. The tests proved it to be reproducible provided care was taken to obtain a sufficient number of data points. Rather than trim to zero hub moment for each point, cyclic pitch is held constant and the moment change recorded.

The baseline curve for the roll hub moment is plotted in Figure 19 for an h/d of 0.4. The delay in the moment rise with speed is evident, followed by a sharp rise. On the aircraft, if the pilot trims the moment to zero just above a speed of 0.82, a small reduction in speed will result in a sharp roll to the left. This was observed in flares. Similarly, if trimmed at zero at 0.4, the aircraft would roll slightly, then sharply, to the right if speed were increased to about 0.65 and no correction was made. This was observed in level accelerations.

As explained previously, there is apparent from the flow visualization a reversal in the inflow at the forward edge of the rotor disk as the ground vortex moves aft under the rotor. This explains the moment behavior observed in the data of Figure 19. Relatively high negative inflow at the front initially suppresses the lateral flapping, which is high at $\psi = 270$ degrees and hence retards the normal buildup in positive rolling moment. When the inflow induced by the

vortex suddenly becomes positive at the rotor edge, a corresponding increase in lateral flapping occurs with an associated sudden buildup in moment in the positive roll in the right sense.

Effect of Height

Figure 19 presents roll moment variation for an h/d of 0.6 and the OGE case as well as the baseline IGE case discussed above. The 50-percent change in rotor height from 0.4 to 0.6 greatly reduces the vortex effect. This corresponds to a full-scale height change from about 20 feet to 30 feet for the rotor and from about 10 feet to 20 feet in terms of wheel height.

Another feature, which is not related to the ground vortex but rather to the general modification of the rotor flow field by the ground, is the reduction in the rolling moment peak value as height is reduced. As this reflects lateral flapping, it is concluded that the ground proximity suppresses the fore-and-aft variation of induced velocity.

Also noteworthy is the discontinuity in the curves at the peak value, which occurs at a speed point just past 1.2. This also will be noticed in other data taken in the ground effect testing. Only a large and fundamental change in the induced flow field could have caused a sudden change like those observed, and it is suggested that the rotary-wing tip vortices suddenly form at full strength and dominate the flow field above a nondimensional speed of 1.2. In other words, we are seeing data characteristic of a rotor wake below 1.2 and like a wing wake above 1.2. This is an area that must be worked extensively if we are to understand transition aerodynamics.

Effect of Disk Loading

The variation of hub rolling moment with speed is shown in Figure 20 for four-disk loadings. No precise trend is defined, but the ground vortex effect is larger at the higher disk loadings. Also, the peak moments, i.e., lateral flapping, increase with disk loading, supporting the notion that the fore-and-aft ($\cos \psi$) variation of induced velocity is proportional to the mean value.

Effect of Pitch Attitude

Figure 21 shows the effect of model pitch attitude on the rolling moment/speed relationship. Although the carpet plot is quite erratic with attitude, two points are noted. The first is a relatively small ground vortex effect at the negative angle. The mechanism here is not easily interpreted, but it could be that, with the rotor directing its wake rearward due to the forward tip path plane inclination, a significantly smaller portion of the wake energy is deflected forward by the ground to feed the vortex. It is suggested, therefore, that high initial linear accelerations in level takeoffs may mitigate the adverse roll due to the vortex.

The other notable feature is the steady rise in peak moment, i.e., peak flapping, as attitude becomes more positive. The front of the rotor is getting higher and presumably the induced velocities here are not experiencing as much reduction due to ground proximity. This is consistent with the trend noticed in the height variation of Figure 19.

Effect of Wind Azimuth

Azimuth changes cause large changes in rolling moments, as shown in Figure 22, mainly due to a different resolution of the resultant moment vector as the body axis moves with respect to the wind axis. This explanation is given credence by the opposite trend with wind azimuth for the pitching moment as seen in Figure 23.

Not only do the existing moments change their phasing with respect to the axes, but also the cyclic pitch with respect to the wind axis goes through a rephasing. There is approximately 1/2 degree less cyclic pitch at $\psi = 30$ degrees referred to the wind axis than at $\psi = 0$, and 1/2 degree more at $\psi = -30$ degrees. This cyclic difference is equivalent to an increment in C_{RM} of about 1.5×10^{-4}.

The large reduction in both the ground-vortex-induced discontinuity and the peak moment/flapping at $\psi = -30$ degrees suggests a flight path to minimize rapid control change. Although the pitching moment is higher here, it is easier to handle because of the much higher inertia compared to that of roll.

Cyclic Pitch Required

Figure 24 depicts the longitudinal and lateral cyclic pitch required to trim out the pitching and rolling moment. The effect of the ground vortex is apparent in both curves.

These are calculated values using measured control rates to reduce measured moments to zero. The coupling terms were employed as well as the direct, i.e., $\frac{\partial \mathcal{L}}{\partial B_1}$ and $\frac{\partial M}{\partial A_1}$ as well as $\frac{\partial \mathcal{L}}{\partial A_1}$ and $\frac{\partial M}{\partial B_1}$.

ADDITIONAL WORK REQUIRED

Study of the effects of the ground vortex and the nonlinear variations of power and hub moments (flapping) indicates the need for a deeper understanding of the complex aerodynamics of the helicopter in the ground environment.

The ground vortex pattern should be defined in terms of actual mean and unsteady velocities at various speeds for the ranges of variables considered here in a completely generalized treatment.

The following additional areas need further investigation:

1. Better definition of most relationships, i.e., closer spaced data points.
2. Extension of this work to the complete yaw range.
3. Accurate trends with rotor height. This may require detailed tunnel boundary correction determinations.
4. Averaging techniques to best suit the environment.

5. Effect of fuselage presence.

6. Detailed study of induced flow field changes through transition such as the formation of the rotary-wing tip vortices.

7. The unsteadiness of the flow in the helicopter airspace near the ground, as determined by spectral analysis.

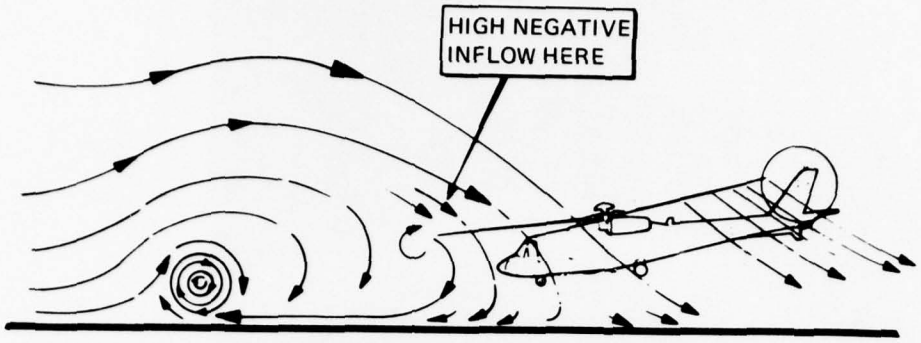

Figure 11. Ground Vortex Between 5 and 10 Knots.

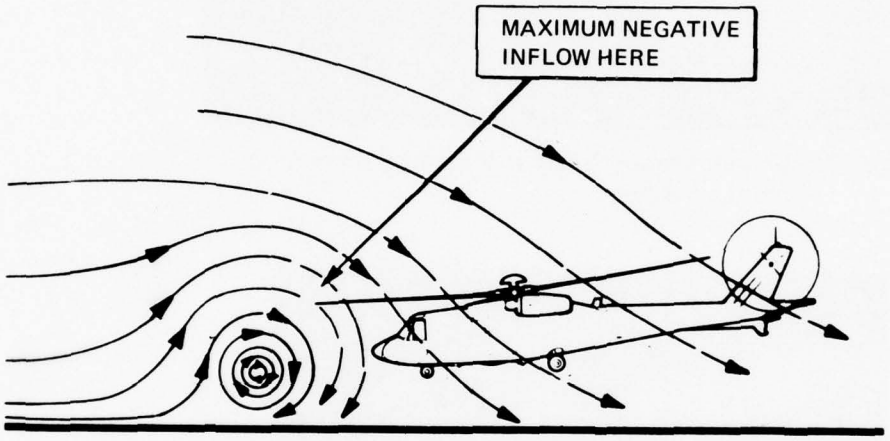

Figure 12a. Ground Vortex at 16 to 18 Knots.

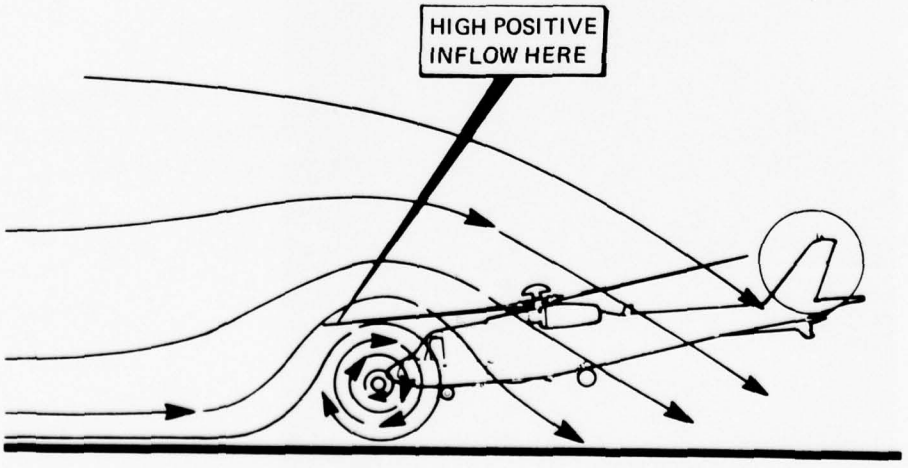

Figure 12b. Ground Vortex at 18 to 20 Knots.

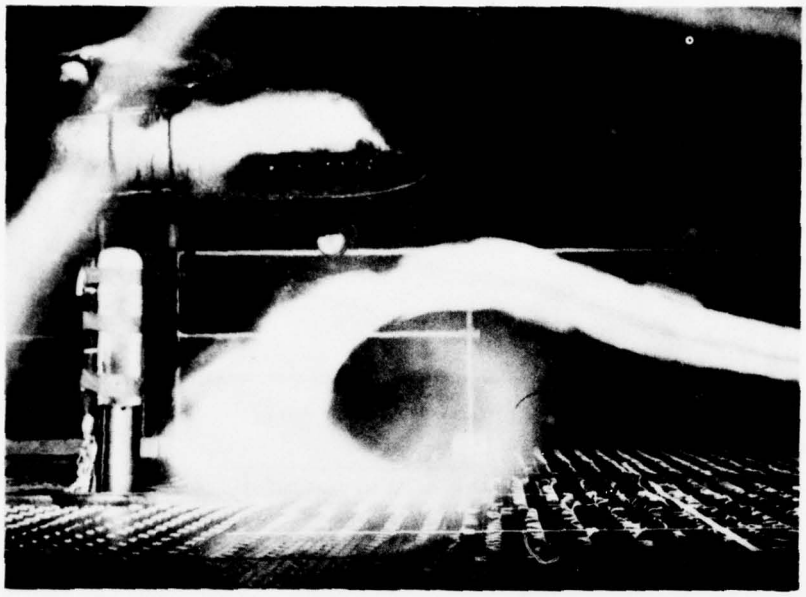

Figure 13a. Ground Vortex Center at V = 20 kn, h/d = 0.48, and DL = 8 psf.

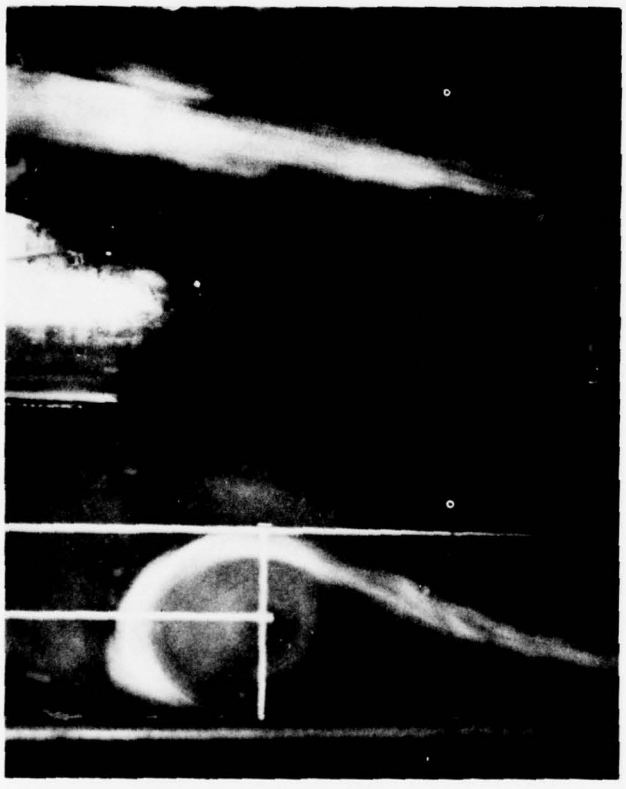

Figure 13b. Ground Vortex Center at V = 20 kn, h/d = 1.0, and DL = 8 psf.

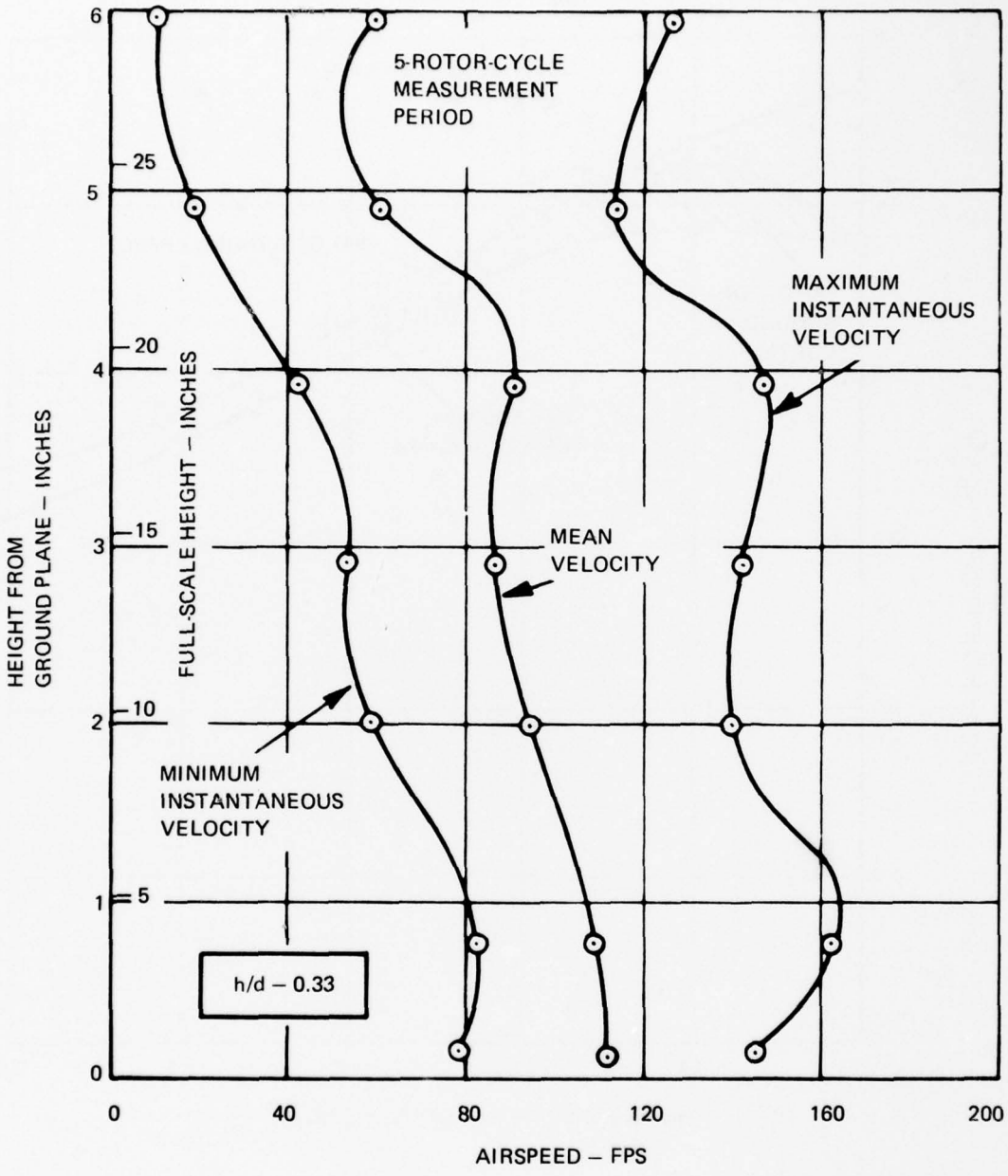

Figure 14. Velocities Measured Near Ground Vortex at 32 Knots.

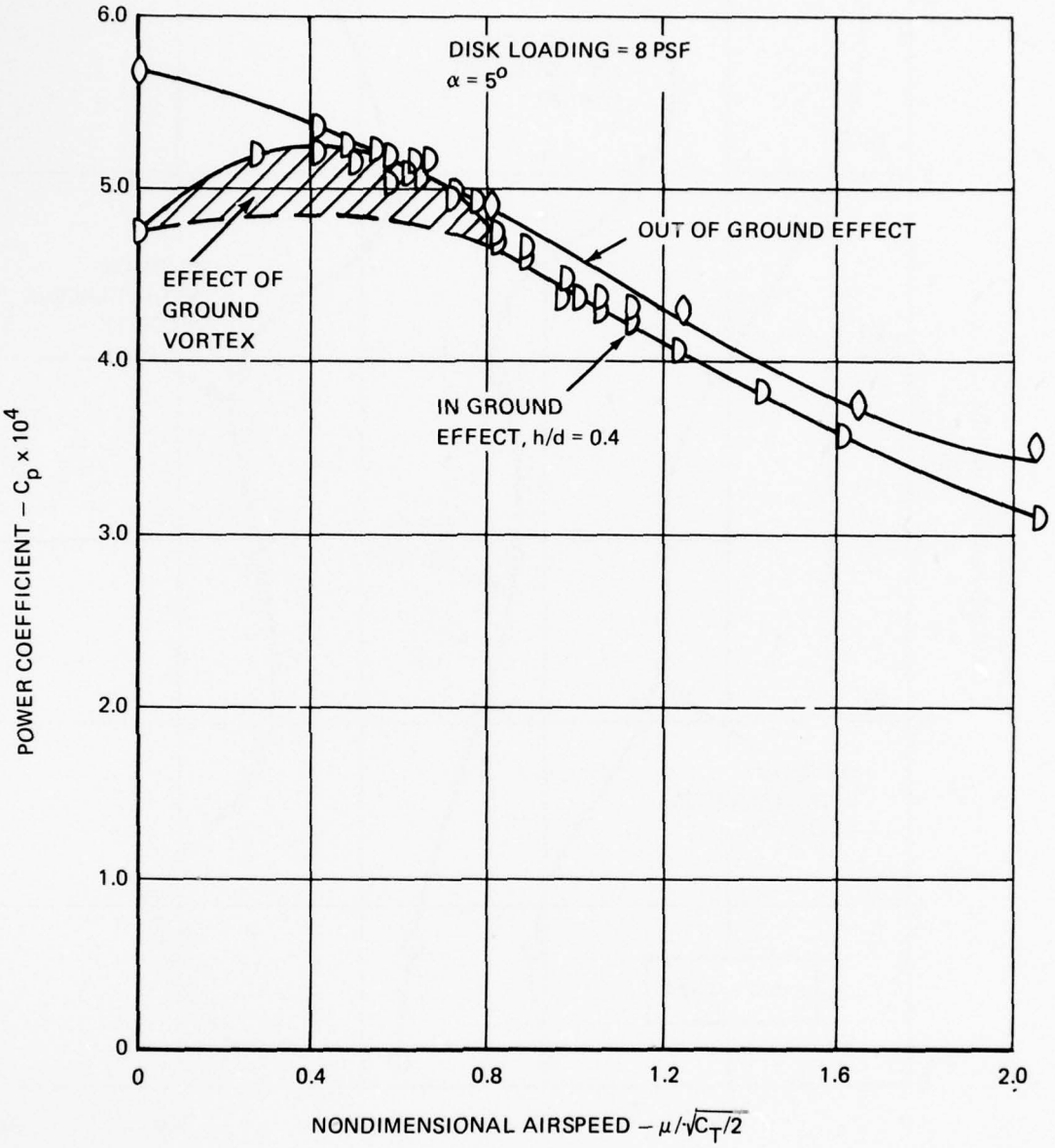

Figure 15. Power Required as a Function of Airspeed In and Out of Ground Effect.

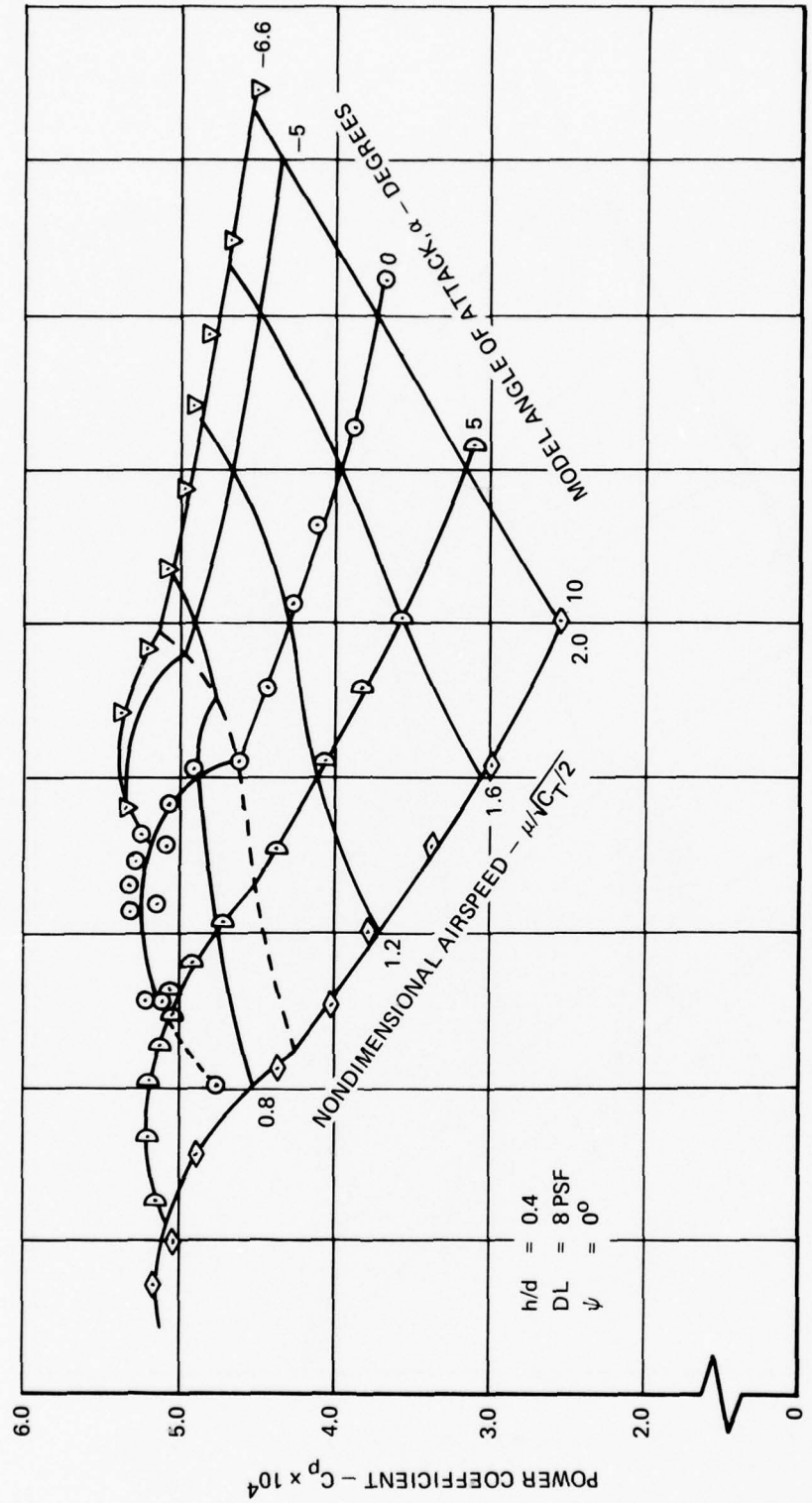

Figure 16. Power Required In Ground Effect as a Function of Airspeed and Angle of Attack.

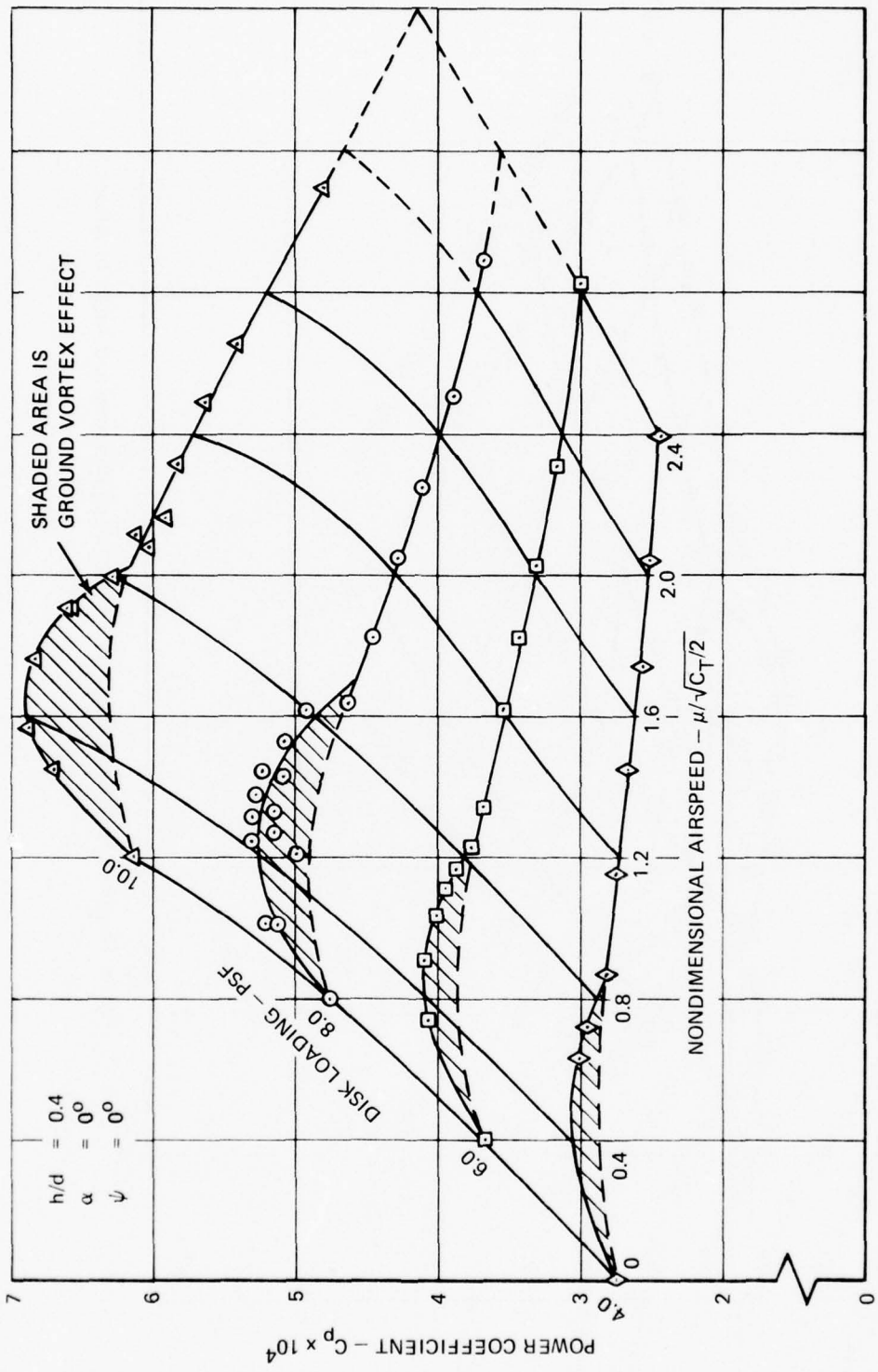

Figure 17. Power Required in Ground Effect as a Function of Airspeed and Disk Loading.

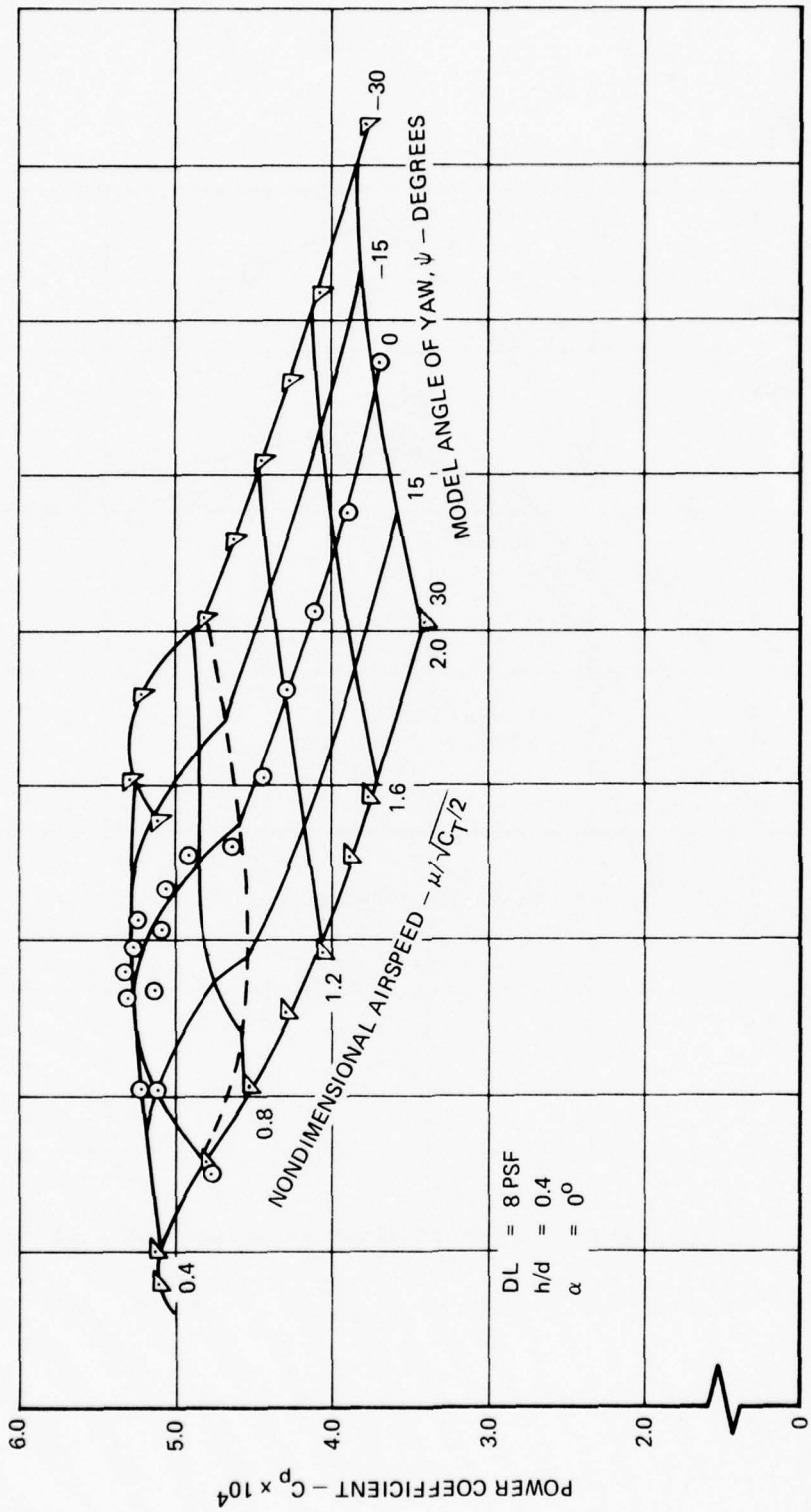

Figure 18. Power Required In Ground Effect as a Function of Airspeed and Yaw Angle.

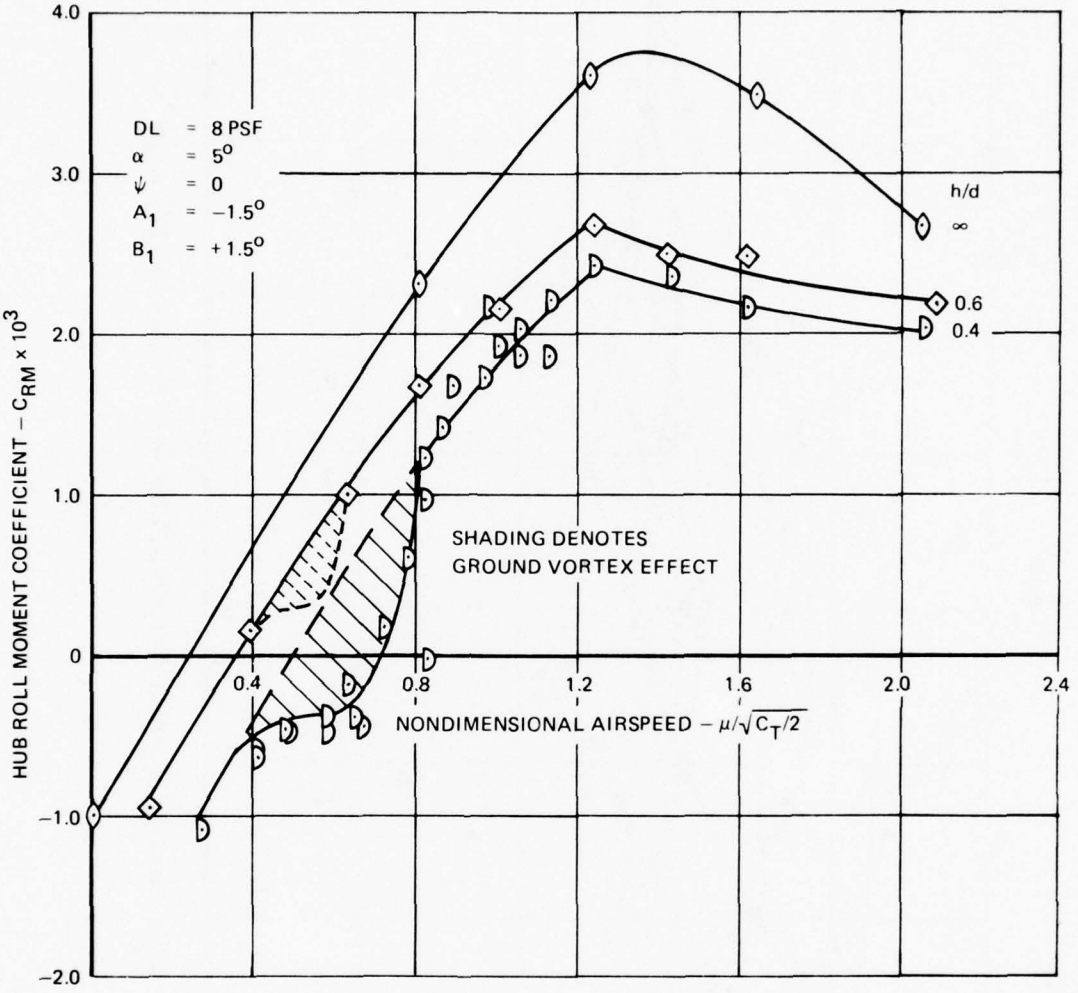

Figure 19. Hub Rolling Moment Coefficient In Ground Effect as a Function of Airspeed.

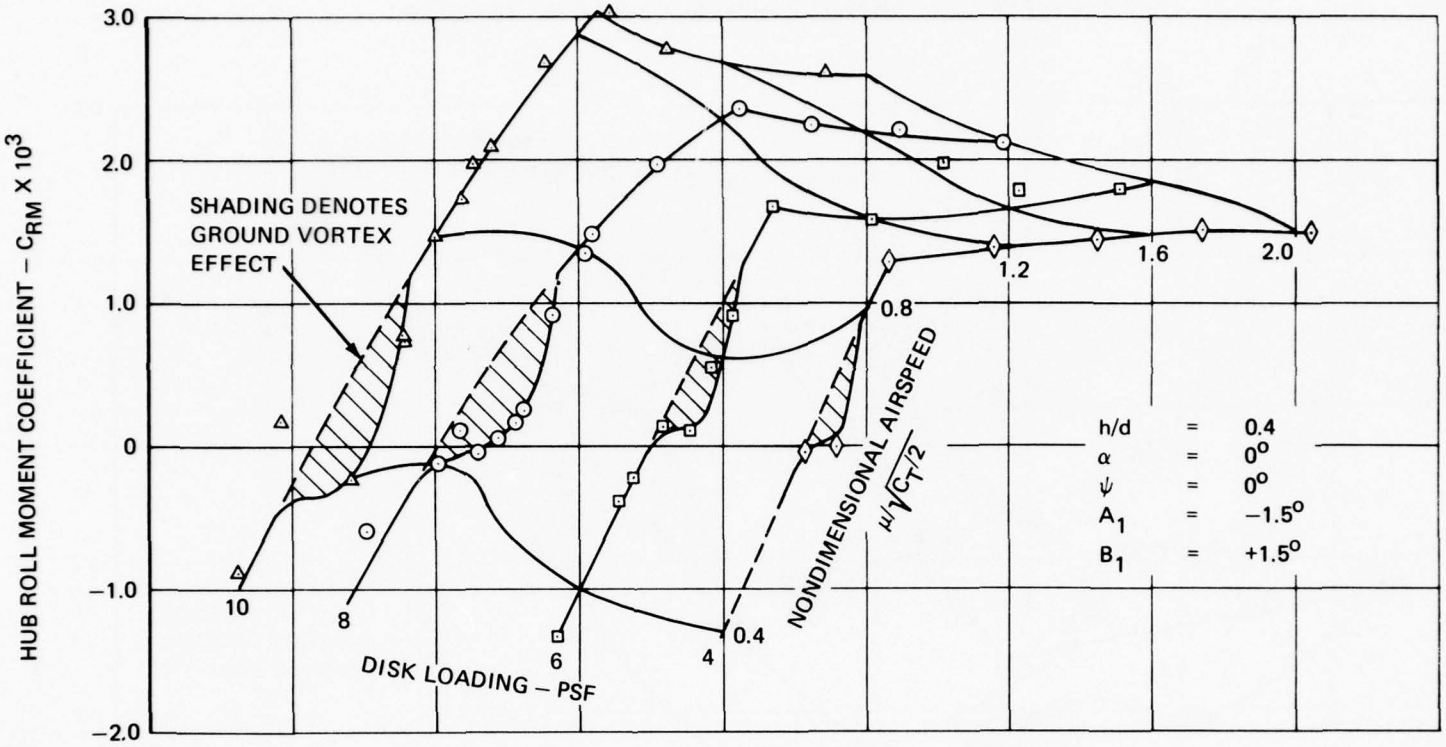

Figure 20. Hub Rolling Moment Coefficient In Ground Effect as a Function of Airspeed and Disk Loading.

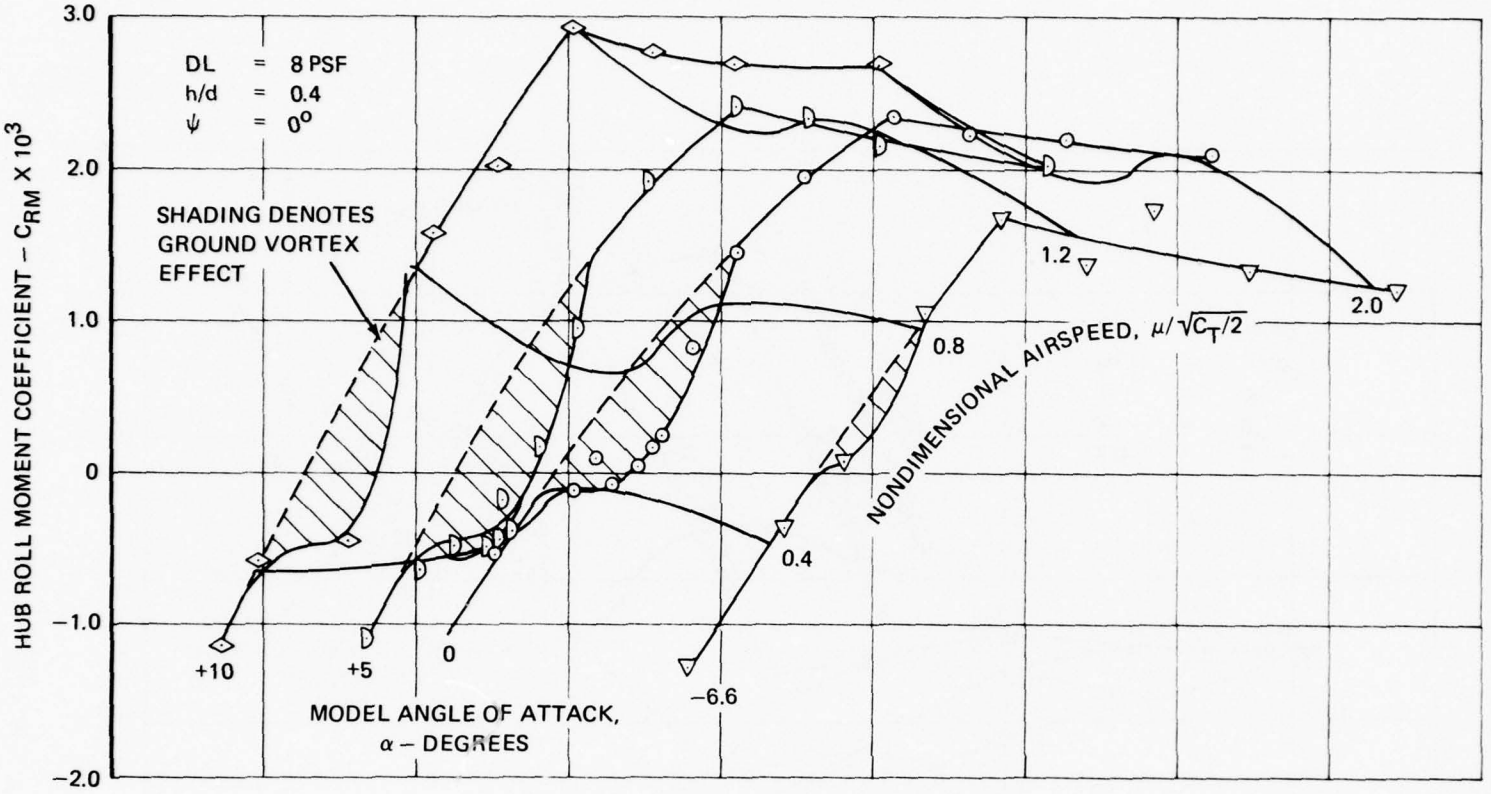

Figure 21. Hub Rolling Moment Coefficient In Ground Effect as a Function of Airspeed and Angle of Attack.

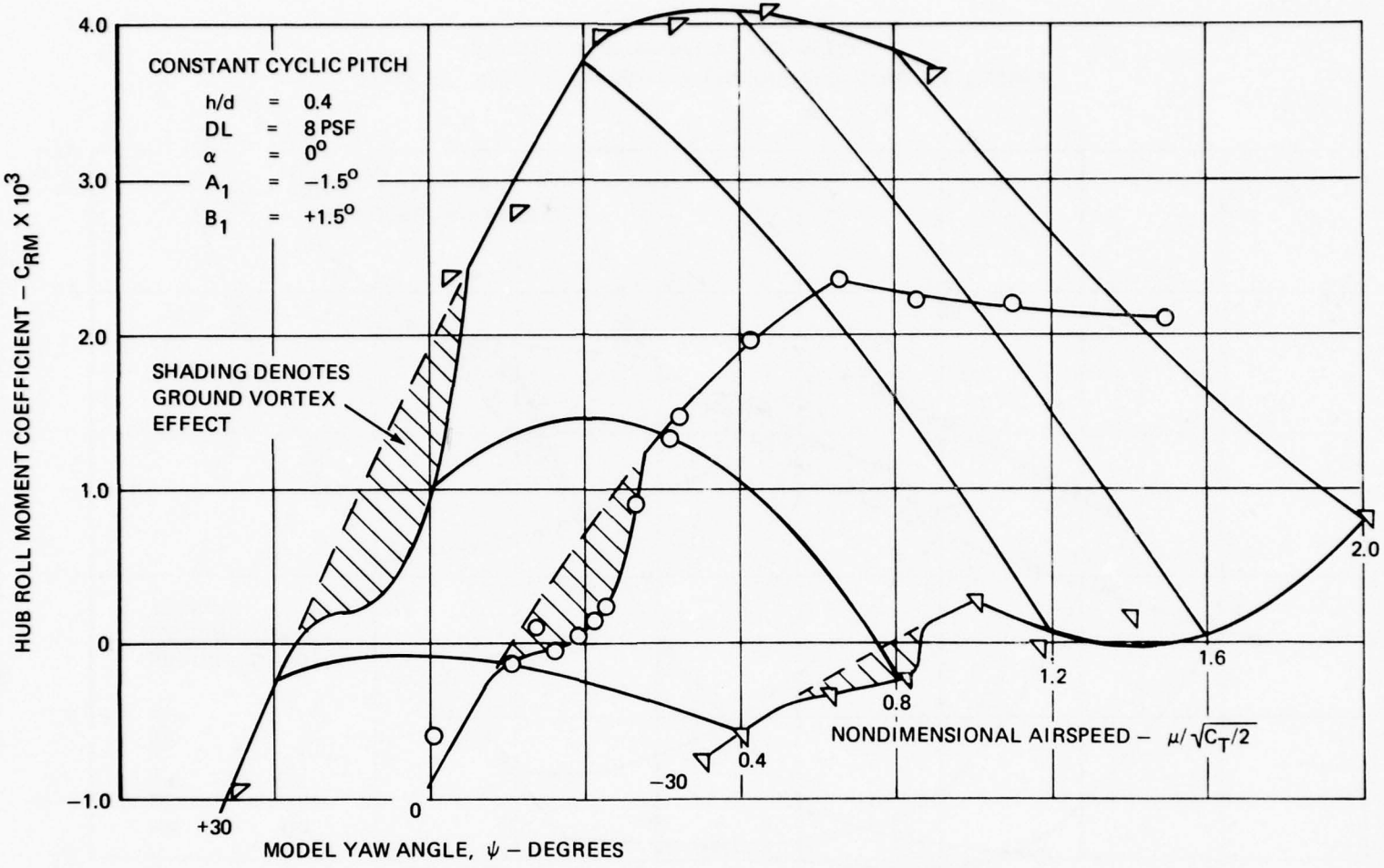

Figure 22. Hub Rolling Moment Coefficient In Ground Effect as a Function of Airspeed and Yaw Angle.

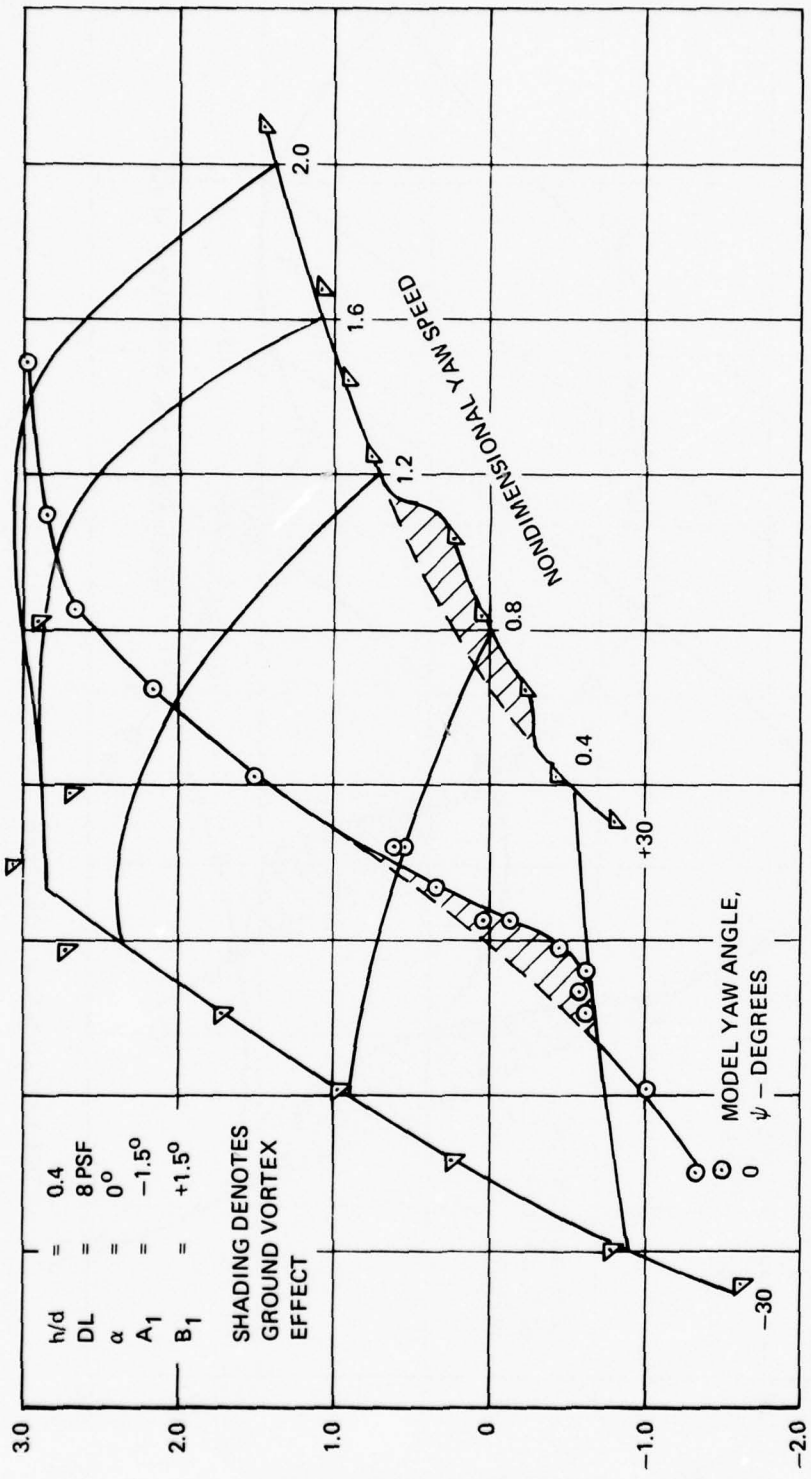

Figure 23. Hub Pitching Moment Coefficient In Ground Effect as a Function of Airspeed and Yaw Angle.

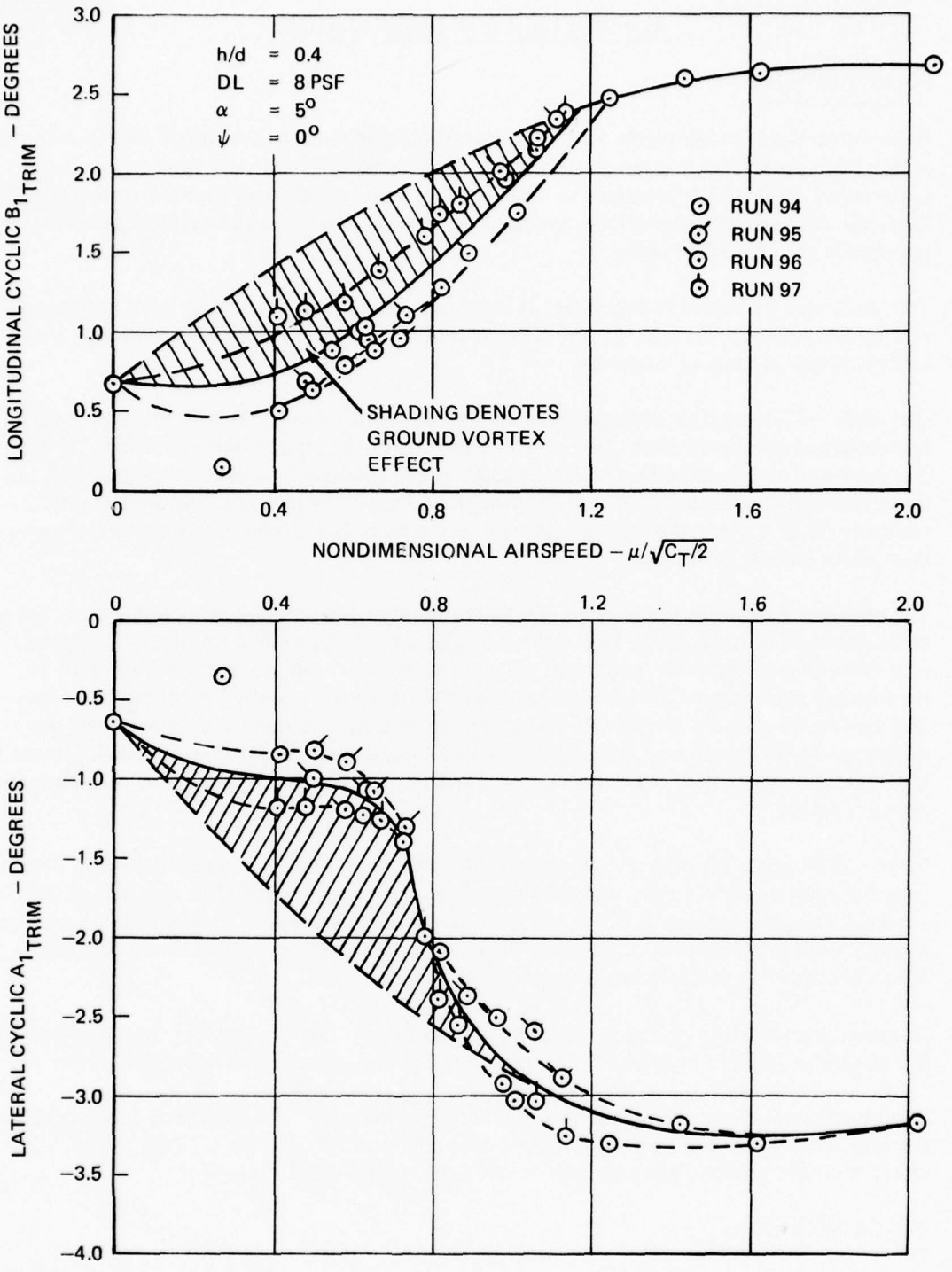

Figure 24. Cyclic Pitch Required in Transition for Zero Hub Moments.

ROTOR/FUSELAGE INTERACTIONS

INTRODUCTION

Helicopters designed compactly with the rotor positioned close to the top of the fuselage exhibit a large aerodynamic interaction between the overpassing blade and fuselage surfaces underneath. This results in impulsive blade loading with each passage over the closest surfaces. Similarly, blade overpassage effects an impulsive imprint locally on the airframe pressure patterns in the proximate areas.

The blade may be pulsed in two ways. It receives a general interruption to its own flow pattern by the adjacent fuselage. It may also cut through a local pressure peak occurring at an abrupt change in fuselage curvature.

The blade will respond predominantly in the first harmonic due to the once-per-revolution occurrence of the disturbance. However, the shaping of the input is nonsinusoidal. In fact, it is pulse-like and the resulting impactive loading will produce significant response in all the lower flap and chord-bending modes. Consideration has to be given both to incremental vibratory blade stresses so produced and also to the incremental hub shears and moments as they affect aircraft vibration.

The pressure changes on the fuselage will be felt as vibratory loadings predominantly equal to blade number per revolution. Thus a three-bladed rotor will produce a 3-per-rev change; a four-bladed rotor, 4 per rev, and so on. These will be translated into mechanical inputs to the fuselage according to the structural dynamic characteristics at the area of impact. They will then be transmitted through the structure and produce vibration according to the prevailing mechanical paths and the susceptibility of the major fuselage vibratory modes to the transmitted frequencies. They may also be transmitted through the cabin air space as audible pressure waves.

On the YUH-61A with original low rotor height, this was a pilot annoyance problem. The most bothersome aspect was a high-frequency noise caused by flexing (oil canning) of the overhead skin panel under the influence of the oscillating airloads. This was largely cured by acoustic damping treatment of the skin. However, a low-frequency component, probably 4Ω or 8Ω, was relieved only when the rotor was raised.

Another area deserving attention under these conditions is the drive system, which will receive inputs proportional to incremental loadings in the chordwise and, hence, torque sense.

Wind tunnel tests were conducted to evaluate the aerodynamic vibratory pressures on the fuselage at the low rotor-to-fuselage height originally prevailing on the UTTAS aircraft. The effect of height increase was also investigated for the high-speed case.

TEST CONDITIONS

The test conditions are listed in Table 5 and feature envelope exploration in terms of a speed sweep, rate of climb variation, and a check at higher disk loading; the effect of surface devices such as strakes and vortex generators; and, finally, the effect of raising the rotor to two

TABLE 5. TEST RUNS FOR THE MEASUREMENT OF VIBRATORY SURFACE PRESSURES

Run No.	Configuration	V_{TUN} (kn)	MR/TR Speed (rpm)	Disk Ldg (psf)	Model Angles α (deg)	Model Angles ϕ (deg)	MR Ht (h/d)	Tail Rotor
7	K_1/(a) Level flight baseline	60	1,433/ 4,500	8	2.2	- 6.5	∞	On
7	K_1/(b) Max gross weight level flt baseline	60	1,433/ 4,500	10	3.3	- 6.5	∞	On
8	K_1/(a) Repeat 7(a)	60	1,433/ 4,500	8	2.2	- 6.5	∞	On
8	K_1/(b) Increase speed to maximum	160	1,433/ 4,500	8	- 3.5	- 2.0	∞	On
9	K_2/Repeat high-speed baseline with TR off	160	1,433/0	8	- 3.5	- 2.0	∞	Off
10	K_2/Max climb at low speed	60	1,433/0	8	-26.5	-15	∞	Off
11	K_2/(a) Repeat 10; T.P. 2,3,4,5	60	1,433/0	8	-26.5	-15	∞	Off
11	K_2/(b) Repeat 7(a) with TR off, T.P. 6,7, 8, 9	60	1,433/0	8	2.2	- 6.5	∞	Off
12	K_2/(a) Repeat 7(b) with TR off	60	1,433/0	10	3.3	- 6.5	∞	Off
12	K_2/(b) Max GW at max speed with TR off	160	1,433/0	10	- 2.0	- 2.0	∞	Off
13	K_2+S_1/Check longitudinal strakes	160	1,433/0	8	- 3.5	- 2.0	∞	Off
14	K_2+S_2/Check lateral strakes	160	1,433/0	8	- 3.5	- 2.0	∞	Off
15	K_3/Effect of 45° tapered blade root cutout	160	1,433/0	8	- 3.5	- 2.0	∞	Off
16	K_2+VG_1/Effect of vortex generators on forward crown	160	1,433/0	8	- 3.5	- 2.0	∞	Off
17	K_2/Autorotation	60	1,433/0	8	21	0	∞	Off
18	K_2+S_3/Effect of lower longitudinal strakes	160	1,433/0	8	- 3.5	- 2.0	∞	Off
19	K_4/Rotor raised 2.5 inches	160	1,433/0	8	- 3.5	- 2.0	∞	Off
20	K_4+S_3/Lower strakes added to raised rotor	160	1,433/0	8	- 3.5	- 2.0	∞	Off
21	K_5/Rotor raised 5.0 inches	160	1,433/0	8	- 3.5	- 2.0	∞	Off
22	K_5+S_3/Lower strakes with rotor in highest position	160	1,433/0	8	- 3.5	- 2.0	∞	Off
23	K_2/Autorotation at maximum speed	160	1,433/0	8	- 3.5	- 2.0	∞	Off
24	K_2/Level flight speed sweep	20	1,433/0	8	5.3	0	∞	Off
25	K_2/Level flight speed sweep	30	1,433/0	8	5.0	0	∞	Off
26	K_2/Level flight speed sweep	40	1,433/0	8	4.4	0	∞	Off
27	K_2/Level flight speed sweep	50	1,433/0	8	3.5	0	∞	Off
28	K_2/Level flight speed sweep	60	1,433/0	8	2.2	- 6.5	∞	Off
29	K_2/Level flight speed sweep	80	1,433/0	8	0.2	- 3.2	∞	Off
30	K_2/Level flight speed sweep	100	1,433/0	8	- 0.6	- 2.3	∞	Off
31	K_2/Level flight speed sweep	120	1,433/0	8	- 1.6	- 2.2	∞	Off
32	K_2/Level flight speed sweep	140	1,433/0	8	- 2.7	- 2.1	∞	Off
33	K_2/Level flight speed sweep	160	1,433/0	8	- 3.5	- 1.9	∞	Off

higher positions. The only blade variation was a change in the standard inboard termination of the blade working section from rectangular cutout to a 45-degree taper.

For each test condition, time histories of pressure were obtained at the 53 locations portrayed in Figure 25. Twenty-three are on the upper surfaces and 10 on the empennage, reflecting a primary interest in the effects of the rotor on the surface pressures of the most proximate airframe areas.

For each case, the time history was digitized and harmonic analysis made. These results are the basis for the analysis of the following sections. Additionally, computer printout sheets for all cases are available for further study in Volume II. These present the steady value and the harmonic values up to the tenth, both as resultant with phase angle and as sine and cosine components.

CRITICAL AREAS OF THE AIRFRAME

Referring to the sketch of the model in Figure 25, it is evident that certain areas of the fuselage and other configuration elements are especially vulnerable to aerodynamic flow interactions occasioned by blade proximity.

Table 6 shows the maximum vibratory surface pressures measured at various locations with the forward crown and the right nacelle as the outstanding features. The high values on the crown are expected, but the right nacelle shows surprisingly high values compared to the left nacelle. The crown will be emphasized in subsequent sections, as it was the problem area in the flight testing.

PRESSURES ON THE FORWARD CROWN

The 4Ω pressures on the forward crown resulting from the four-times-per-revolution passage of the blades are plotted in Figure 26. The carpet plot indicates values on a section of approximately 10 by 10 inches. The right side (positive buttline 5.2) receives the maximum pressures, and they steadily decrease across the fuselage from right to left. The highest pressures are forward and the trend in this direction probably reflects proximity to the fuselage pressure peak aft of the windscreen. Repeated interaction with this peak as each blade passes will cause the highest pressure perturbations along the longitudinal axis.

Values of these magnitudes are considered high enough for concern about the effects on aircraft vibration. For example, if an average 4Ω pressure of 0.1 psi prevailed over the entire forward crown area the resultant would be an integrated loading approaching one-tenth of the model's steady lift.

EFFECT OF GAP INCREASE ON CROWN PRESSURES

Raising the rotor to increase the rotor-to-fuselage gap proved to be a powerful means of reducing the 4Ω pressures on the forward crown. Figure 27 shows the effect on the pressures of the right side (which were the highest) of rotor height increases of 2.5 and 5 inches. The pressure change is almost linear, and reductions of approximately 50 percent are effected by the 5-inch change in height. Five inches is approximately one blade chord length. The UTTAS

TABLE 6. MAXIMUM VIBRATORY SURFACE PRESSURES FOR VARIOUS LOCATIONS

	Pressure (psi)/Speed (kn)		
	1Ω	4Ω	8Ω
Forward Crown	0.023/140	0.144/160	0.098/160
Right Nacelle	0.023/120	0.063/160	0.080/160
Left Nacelle	0.024/80	0.045/160	0.043/160
Aft Crown	0.028/160	0.052/160	0.018/160
Tailboom	0.044/160	0.057/80	0.031/80
Fin Right Side	0.020/140	0.009/140	0.012/140
Fin Left Side	0.028/140	0.063/160	0.023/160
Right Stabilizer	0.026/140	0.015/160	0.011/140
Left Stabilizer	0.024/160	0.051/140	0.018/160
Level flight Disk loading 8 psf			

aircraft ultimately incorporated a proportionate change (2 feet), and with a highly sophisticated isolation system also installed, enjoyed excellent vibration characteristics.

EFFECT OF GAP INCREASE ON EMPENNAGE

An interesting result of rotor height increase is portrayed in Figure 28. Here the changes in both 1Ω and 4Ω pressures at various points on the fin and stabilizer are plotted against rotor height. These measurements reflect changes in the hub wake frequency content as the center of the wake in forward flight passes just above the stabilizer and to the left of the fin.

Figure 28 generally indicates that a reduction in 4Ω and a large increase in 1Ω pressure result from raising the rotor. The favorable effect on the 4Ω probably is due simply to the lower 4Ω imprint noted early in the pressures on the forward crown, which would be felt generally in the flow along the top of the fuselage. This would be entrained in the hub wake and transported back to the empennage.

The 1Ω pressure increase was puzzling but significant in that it foretold another problem. It is bad to have disturbances near this frequency, as it is close to structural natural frequencies. When the YUH-61A rotor was raised, the shuffle (random lateral disturbance) that had been quelled by a hubcap with the rotor in low position emerged in full bloom again as a major problem.

This necessitated another wind tunnel test program that will not be discussed here in detail, but it was found that raising the rotor aggravated an instability between the adjacent flows on the fuselage and off the hub. This instability is characterized by vertical unsteadiness with air surging in and out of the rotor. Such a process can generate a large low-frequency content. A slug of air can be interacted by one, two, three, or four blades, depending on the duration of its stay in the rotor plane, or it can be interacted once every other revolution and so on. The basic instability was cured by achieving more stable pressure gradients on the fuselage flow through refairing. Simultaneously, the wake low-frequency content (1Ω to 2Ω) dropped significantly. It is very likely that such a modification would offer an acceptable alternative to the hubcap for the low rotor case.

EFFECT OF FORWARD SPEED

Figure 29 shows the effect of speed on the right row of pressure transducers from 20 to 160 knots – the conversion factor from nondimensional to dimensional airspeed is approximately 25. The pressure appears to be closer to a linear function of speed rather than the typical square function. Functionally it appears to involve the product of dynamic pressure and a 4Ω angle of attack increment, i.e., velocity squared times v_4/V, resulting in a v_4V term. A slight rise occurs on the low-speed end that may or may not be a transition peak.

EFFECT OF RATE OF CLIMB

Figure 30 is a carpet plot showing the variation of 4Ω pressure across the crown at station 16.6 for climb, level flight, and descent at 60 knots. Pressures are somewhat higher in descent, particularly on the left side.

EFFECT OF DISK LOADING

Most of the data was run at a model disk loading of 8 psf. One run was made at 10 psf to study that variation. The comparison of 8- and 10-psf disk loading is shown on the carpet plot of Figure 31, which indicates that, for the 160-knot condition, the 4Ω crown pressures varied approximately as the square root of disk loading.

EFFECT OF SURFACE FLOW MODIFIERS

The conventional surface flow devices were applied to the crown to determine their effect on the 4Ω pressures. These included longitudinal and lateral strakes and vortex generators. Pressures for these configurations are plotted on Figure 32. Rather predictably, these devices made the pressures slightly worse to much worse, thus confirming the three-dimensional nature of the phenomenon. The high vibratory pressures on the surface have little to do with the surface gradients or contour but are due to interaction of rotor, hub, and fuselage flow fields.

EFFECT OF BLADE ROOT TAPER

Two different root cutout geometries were considered in the testing in order to modify the blade root vorticity adjacent to the crown. The results as plotted in Figure 33 show that the 4Ω crown pressures are approximately 10 percent higher for the 45-degree root taper compared to the square cut.

BLADE BENDING MOMENTS

Model blade flap, chord, and torsion bending moments were measured during these tests from the safety gages. The bending moments due to proximity to the fuselage are not a blade strength consideration on the hingeless rotor. Indeed, the blade is extremely strong in the root area where the close proximity occurs.

Rather, the concern was the generation of vibratory hub loadings due to blade excitations in relevant frequencies. Data for two different speeds, 35 knots and 160 knots, are examined here in this context. Two rotor heights are considered: baseline and a 5-inch increase. The 35-knot data are taken from another test, but the model configuration is identical to the test of this report.

The blade flap bending moment time histories are plotted for one cycle in Figure 34 for the 35-knot case and in Figure 35 for the 160-knot case. Configurations with both standard and 5-inch additional rotor height are indicated. The effects of blade-to-fuselage interaction are more clearly delineated in Figure 35. The effect of blade passage over the crown is evident near ψ = 180 degrees. The blade's proximity to the right nacelle may be the cause of the difference seen between zero and 45 degrees.

The harmonic components up to the fifth are tabulated in Table 7 for flap, chord, and torsion bending moments for these cases. The flap values are also repeated in Figures 34 and 35.

TABLE 7. EFFECT OF ROTOR-FUSELAGE GAP ON BLADE BENDING MOMENTS

		35 Knots		160 Knots	
	Ω	Basic	Extended	Basic	Extended
Blade Flap Bending 0.11 Span	1	50 at 336°	23 at 294°	111 at 53°	128 at 33°
	2	27 at 53°	26 at 48°	75 at 246°	90 at 244°
	3	83 at 321°	89 at 316°	92 at 294°	82 at 290°
	4	26 at 358°	25 at 353°	23 at 238°	13 at 199°
	5	20 at 47°	18 at 25°	24 at 221°	24 at 118°
		(Average of 15 rotor cycles)		(Average of 45 rotor cycles)	
	Ω	Basic	Extended	Basic	Extended
Blade Chord Bending 0.11 Span	1	970 at 287°	667 at 290°	945 at 320°	920 at 323°
	2	152 at 121°	74 at 134°	95 at 65°	110 at 47°
	3	60 at 113°	30 at 85°	18 at 149°	16 at 111°
	4	84 at 314°	14 at 299°	38 at 250°	23 at 239°
	5	100 at 144°	36 at 123°	55 at 273°	40 at 314°
		(1 rotor cycle)		(Average of 3 rotor cycles)	
	Ω	Basic	Extended	Basic	Extended
Blade Torsion Bending 0.11 Span	1	11 at 55°	10 at 69°	37 at 112°	38 at 112°
	2	3 at 114°	3 at 122°	26 at 320°	26 at 320°
	3	4 at 296°	4 at 299°	6 at 18°	9 at 57°
	4	3 at 10°	3 at 27°	6 at 176°	6 at 277°
	5	6 at 109°	6 at 111°	4 at 207°	4 at 107°
		(Average of 15 rotor cycles)		(Average of 3 rotor cycles)	

The relief of vibration levels by raising the rotor was experienced in flight testing of the YUH-61A. The pattern of the force and moment changes unfortunately is not clear from the data of Table 7. Contributing to vibratory hub moments in a hingeless rotor system are 4Ω flap bending (vertical hub shear), 3Ω and 5Ω flap bending (roll and pitch hub moments), and 3Ω and 5Ω chord bending (lateral and longitudinal shear and roll and pitch hub moments).

The 4Ω flap bending is reduced by 50 percent at 160 knots but negligibly at 35 knots. This latter may be due to inadequate cycle number in the averaging at the extremely turbulent low-speed condition.

For the 160-knot case, raising the rotor results in an 11-percent reduction in 3Ω flap bending with no phase change and no reduction in 5Ω flap bending with a 103-degree phase change.

3Ω bending is not changed at 160 knots and the 5Ω value is only slightly reduced. On the other hand, very large changes in both 3Ω and 5Ω chord bending are evident.

The chord bending data must be viewed with caution, however, because of the low cycle count. Also, the 5Ω chord bending response will be aggravated by the close proximity of the second chord bending mode to that frequency.

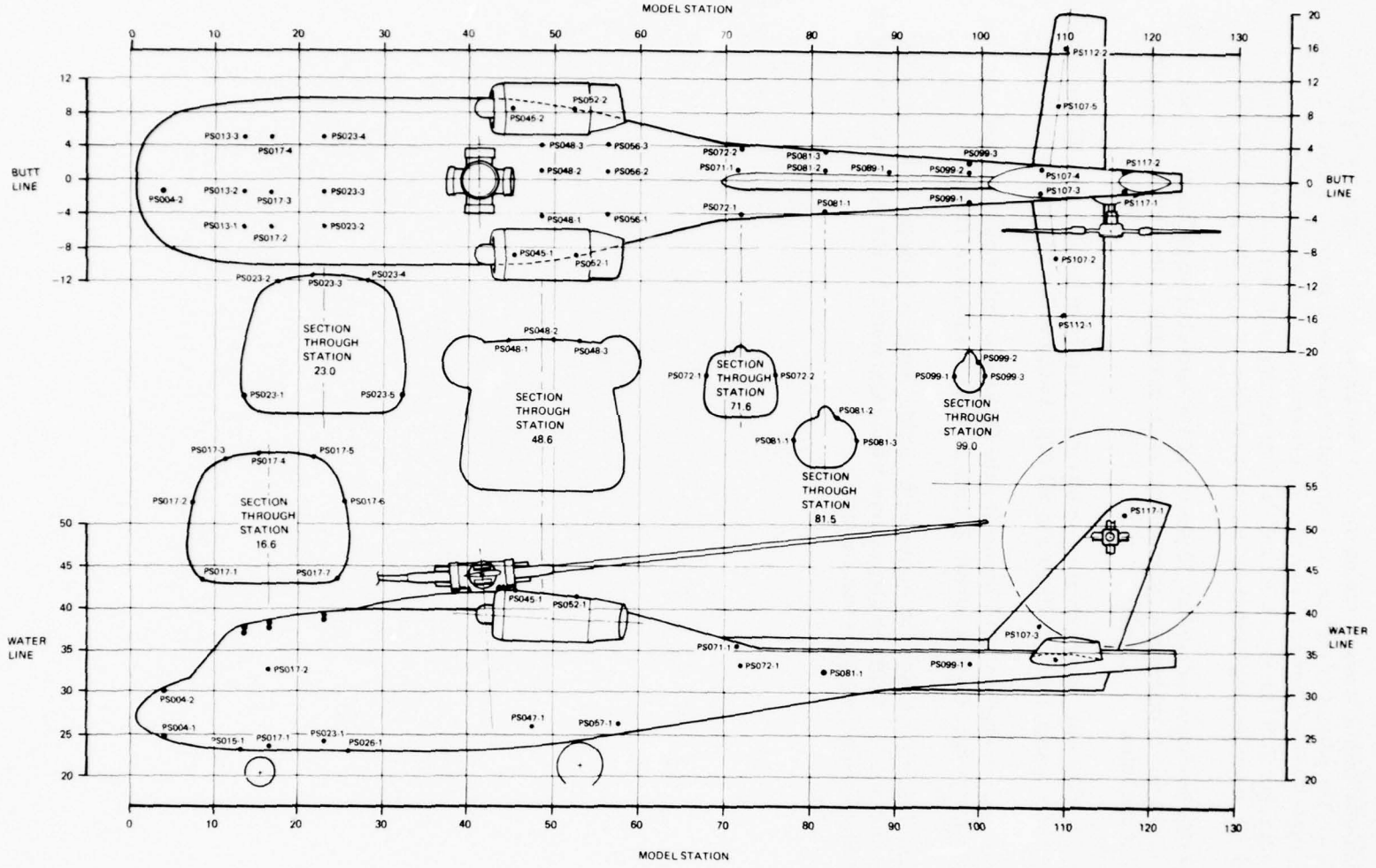

Figure 25. UTTAS 1/4.85-Scale Model Geometry and Surface Pressure Transducer Locations.

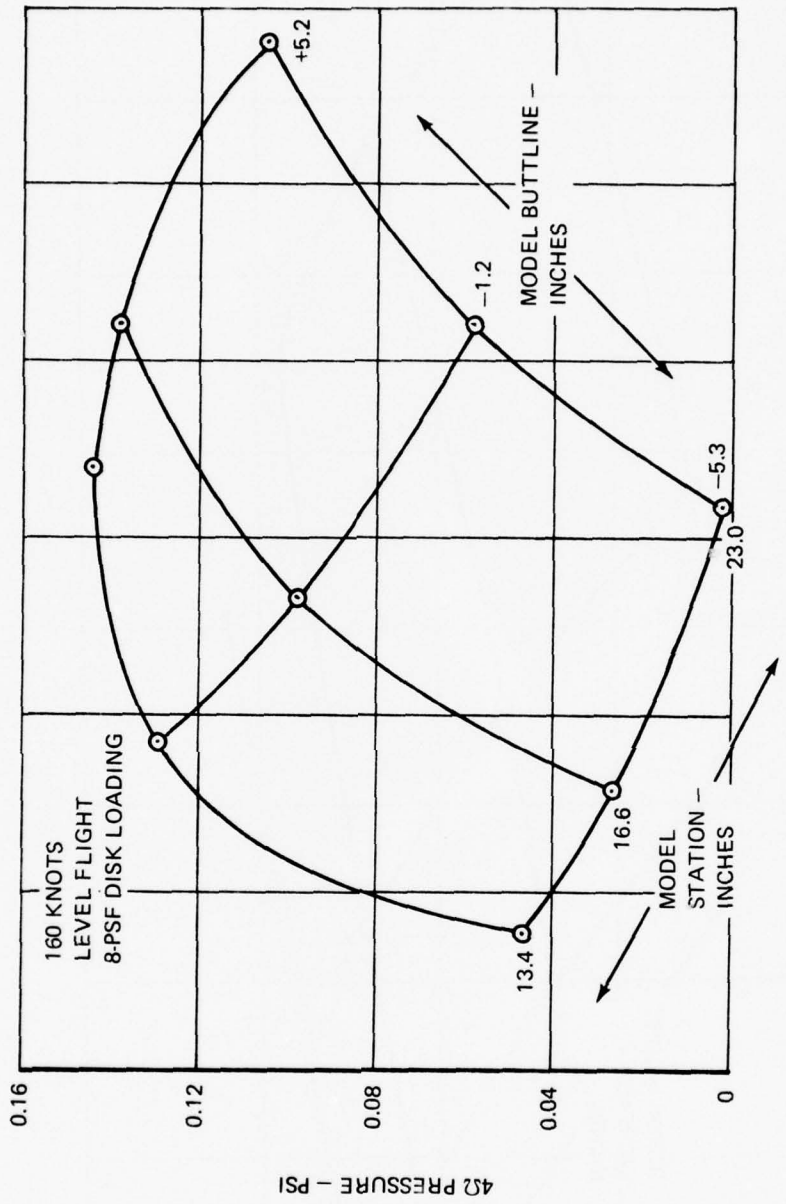

Figure 26. 4Ω Pressure Amplitudes on Forward Crown.

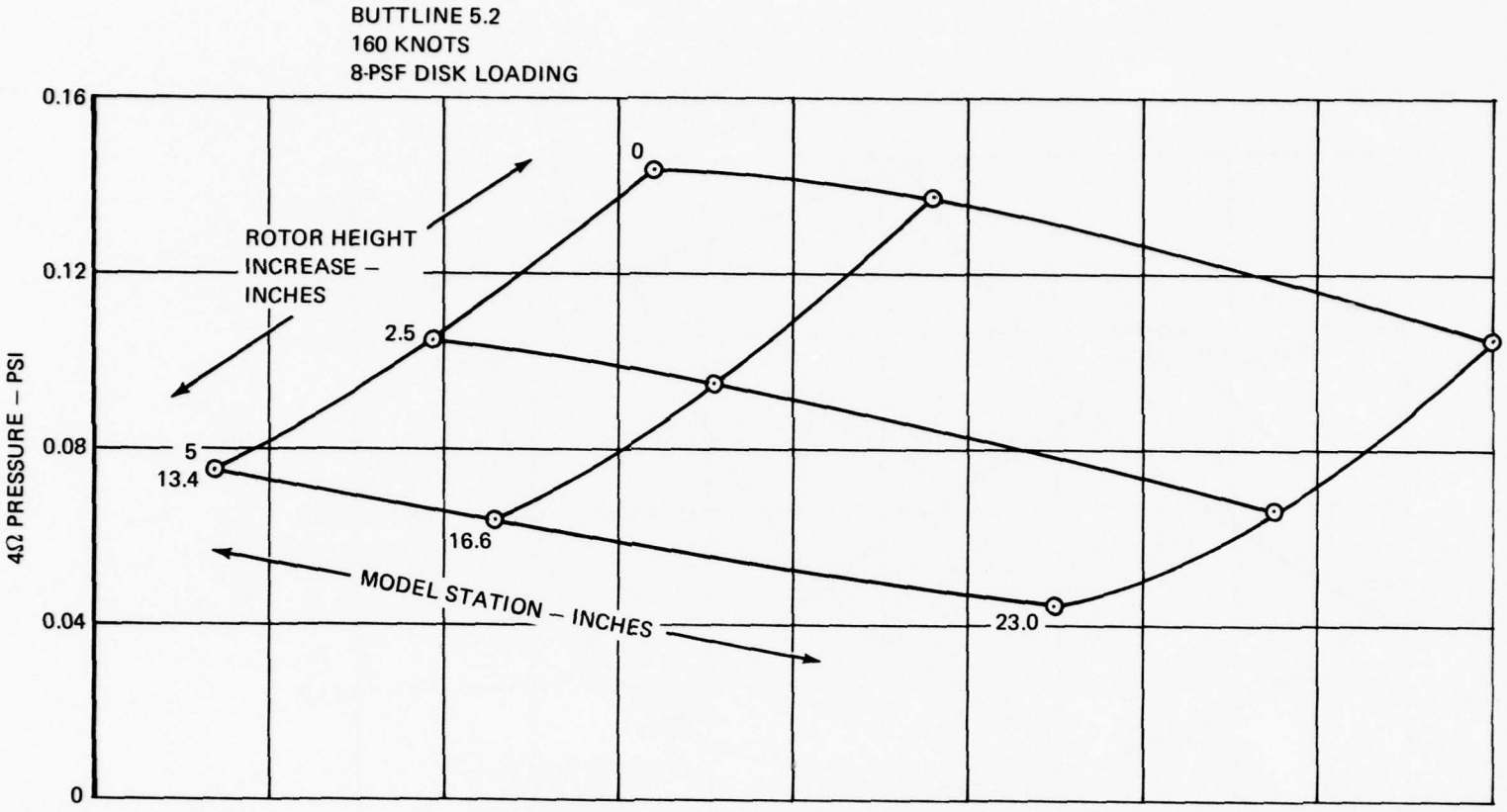

Figure 27. Variation of 4Ω Crown Pressures With Rotor/Fuselage Gap Increase.

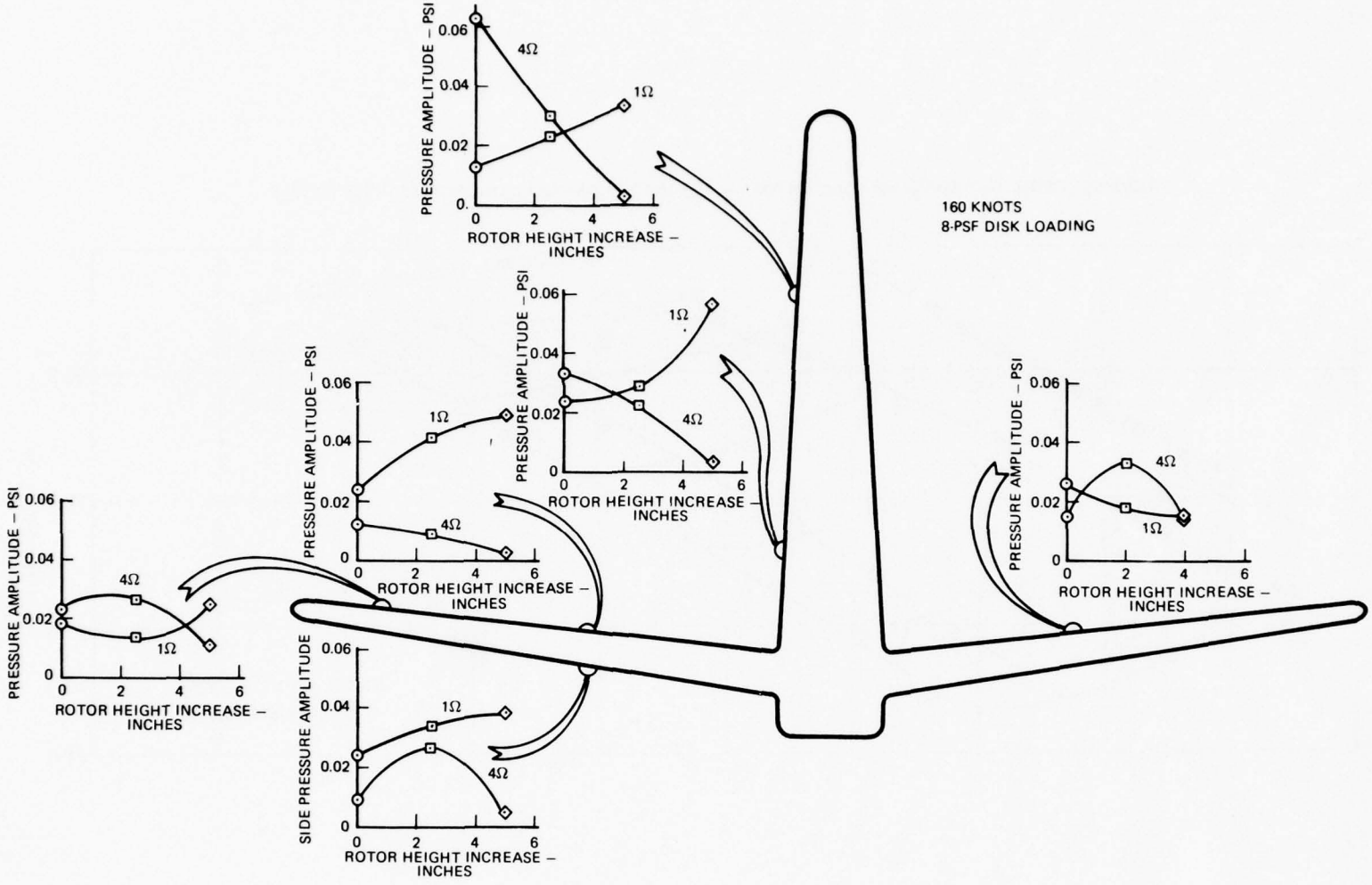

Figure 28. Alternating Empennage Pressure Changes Due to Rotor Height Increase.

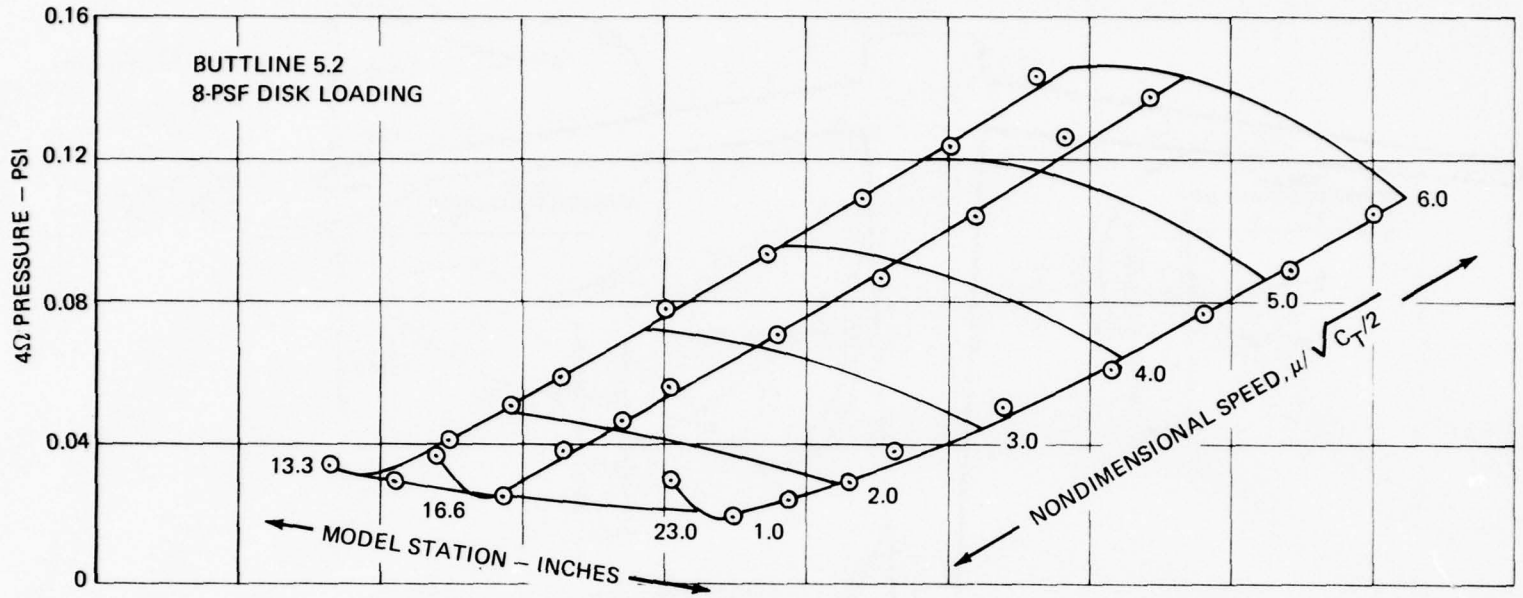

Figure 29. Variation of Forward Crown 4Ω Pressures With Airspeed and Model Station.

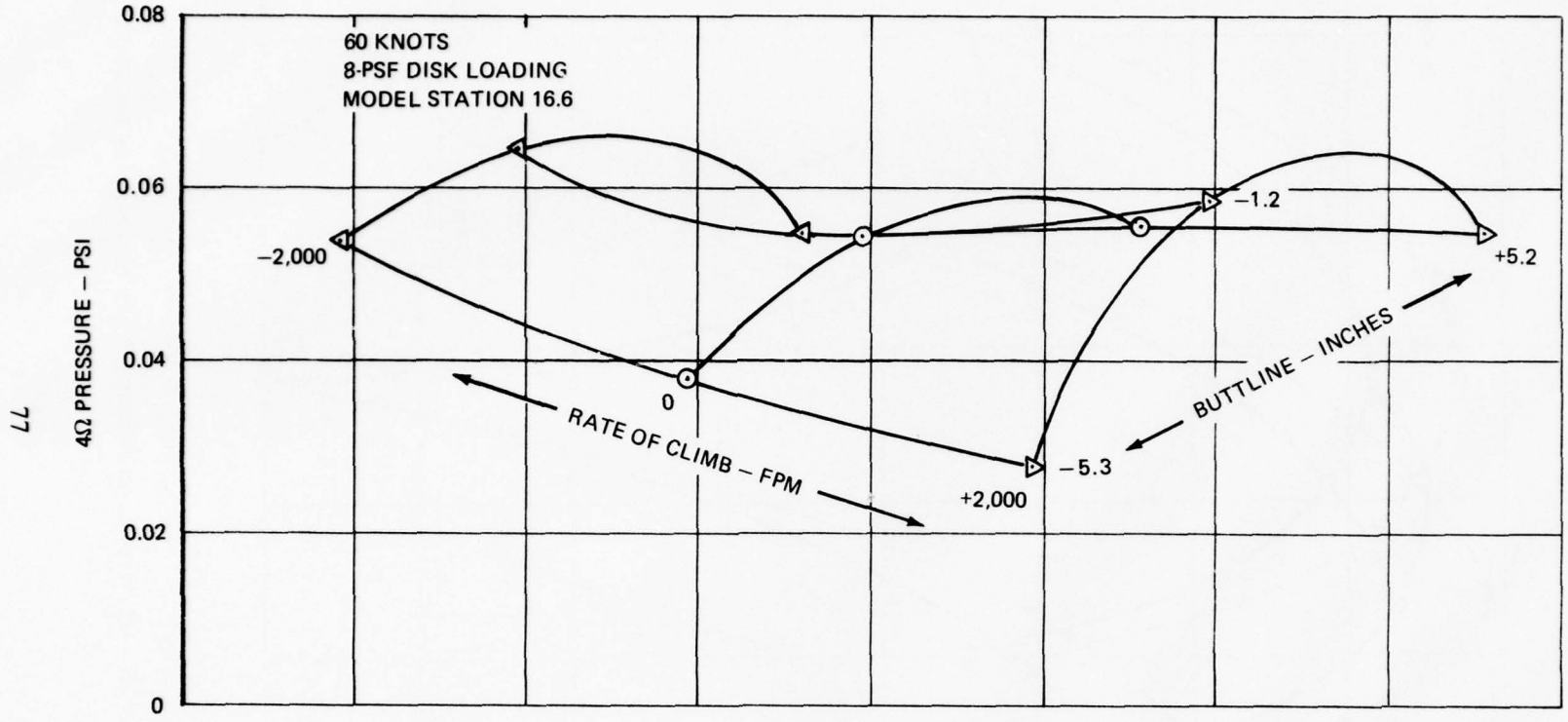

Figure 30. Variation of 4Ω Pressures Across the Forward Crown as Affected by Rate of Climb.

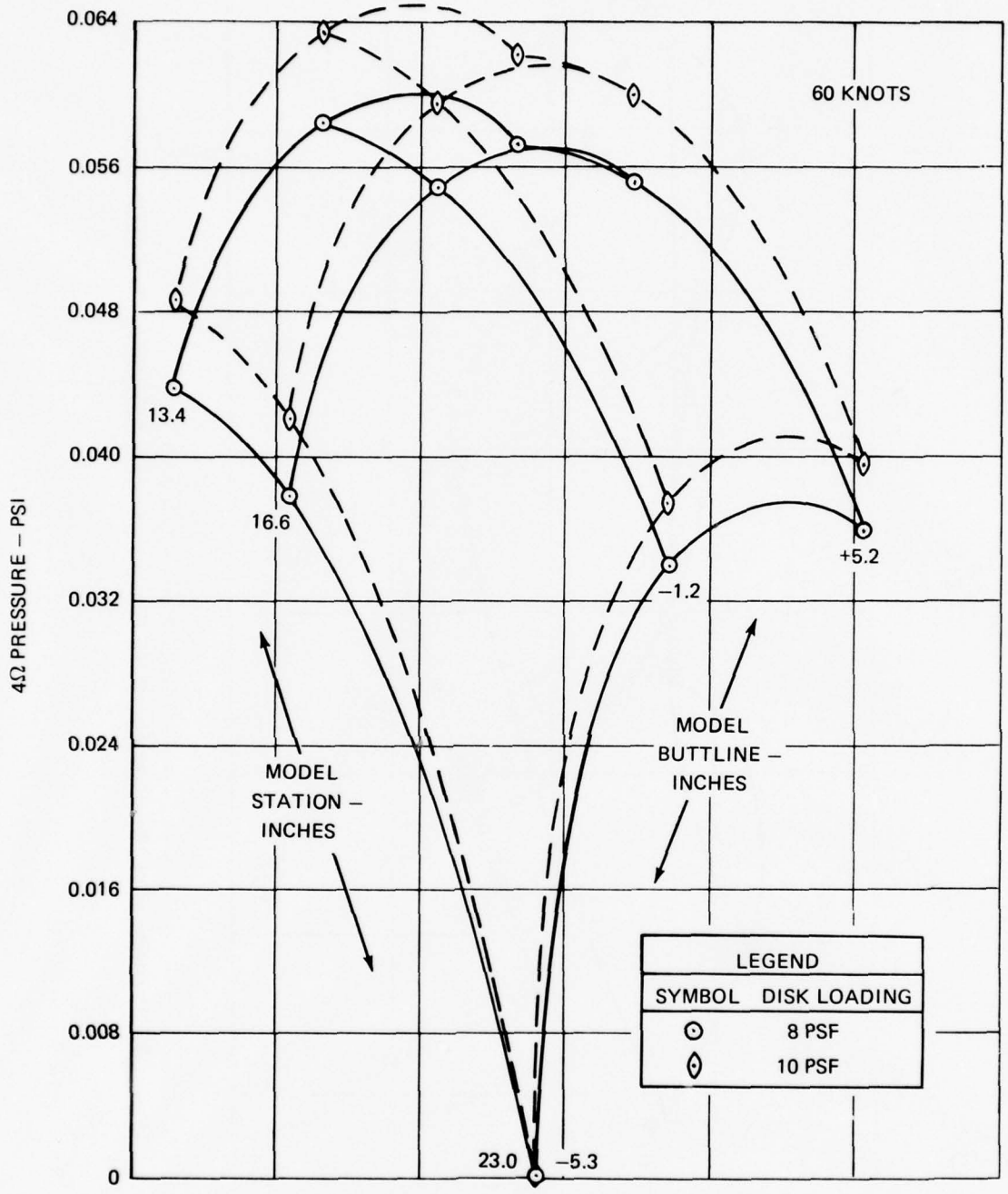

Figure 31. 4Ω Pressures on Forward Crown for Two Disk Loadings.

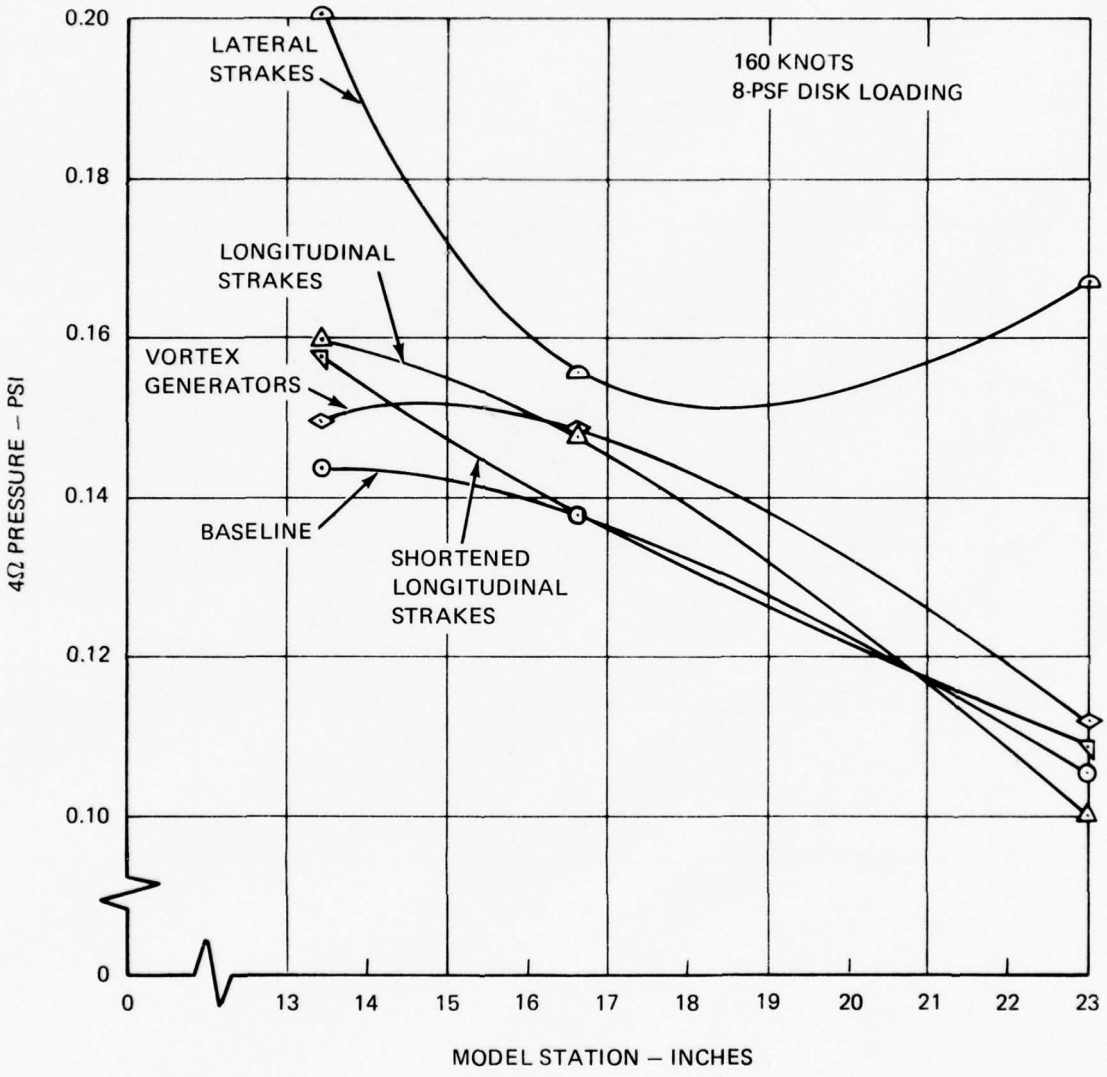

Figure 32. Variation of 4Ω Forward Crown Pressures Along Buttline 5.2 as Affected by Surface Flow Modifiers.

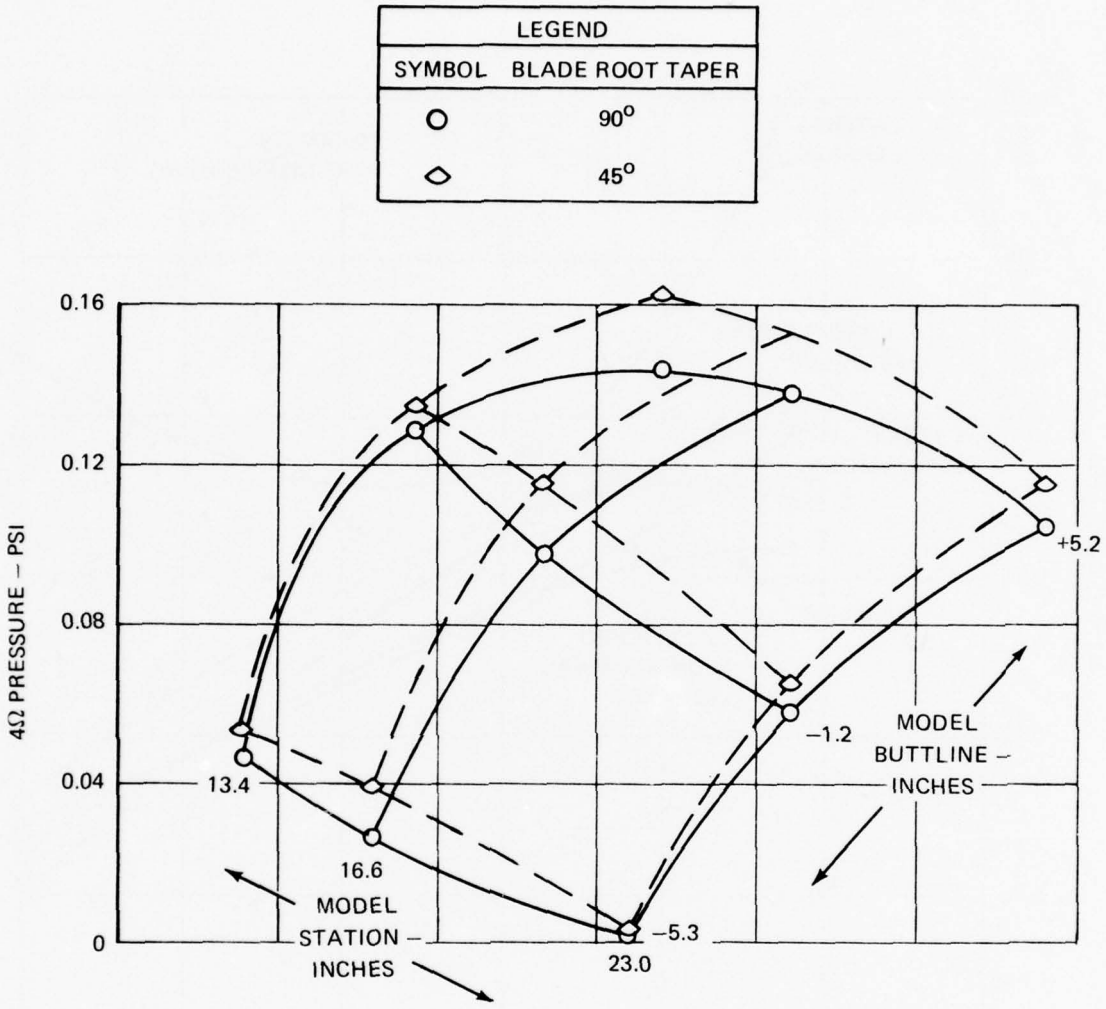

Figure 33. 4Ω Pressure Amplitudes on Forward Crown at 160 Knots for Two Blade Root Tapers.

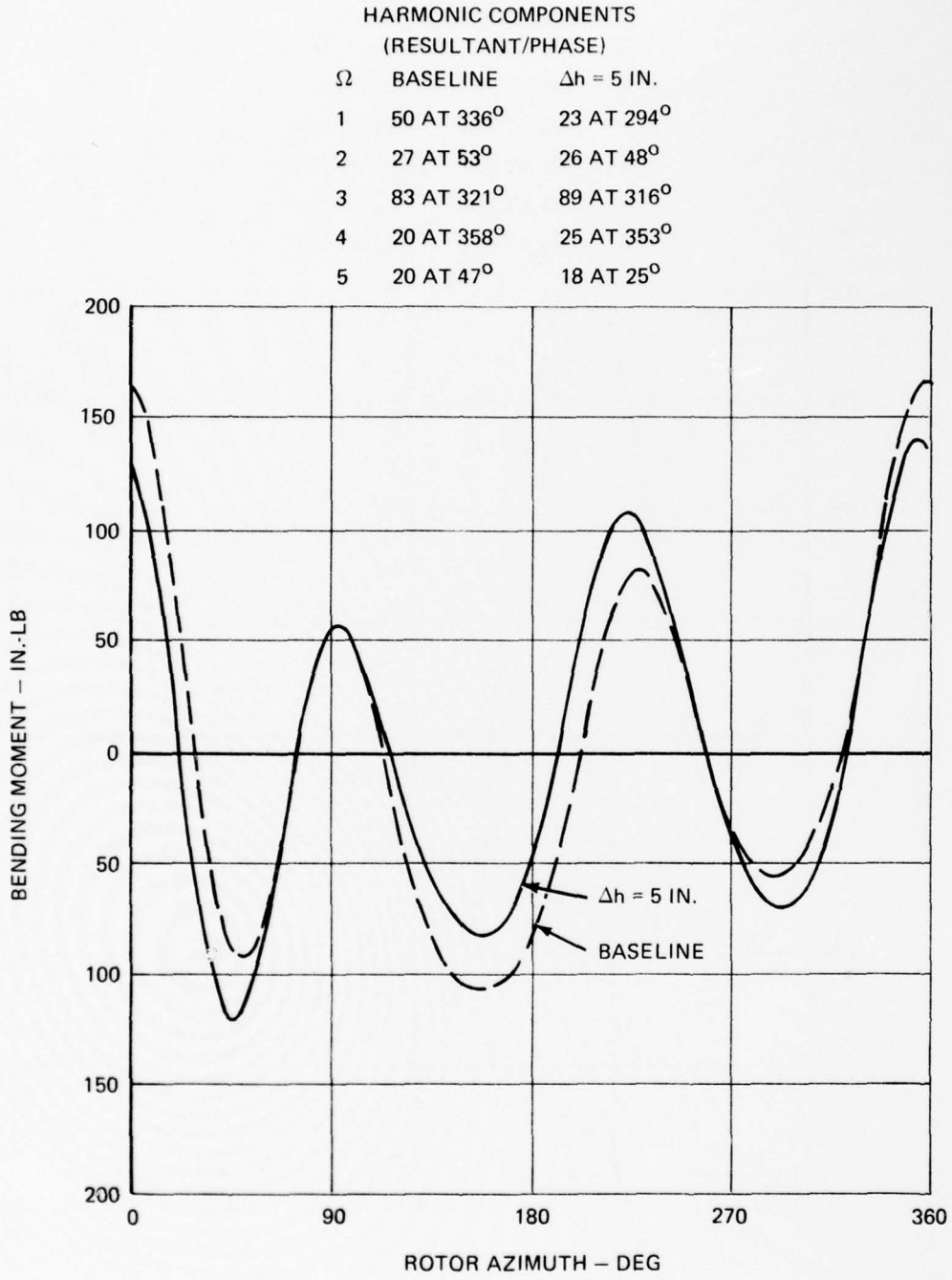

Figure 34. Effect of Rotor/Fuselage Gap Increase on Blade Flap-Bending Moments at 35 Knots.

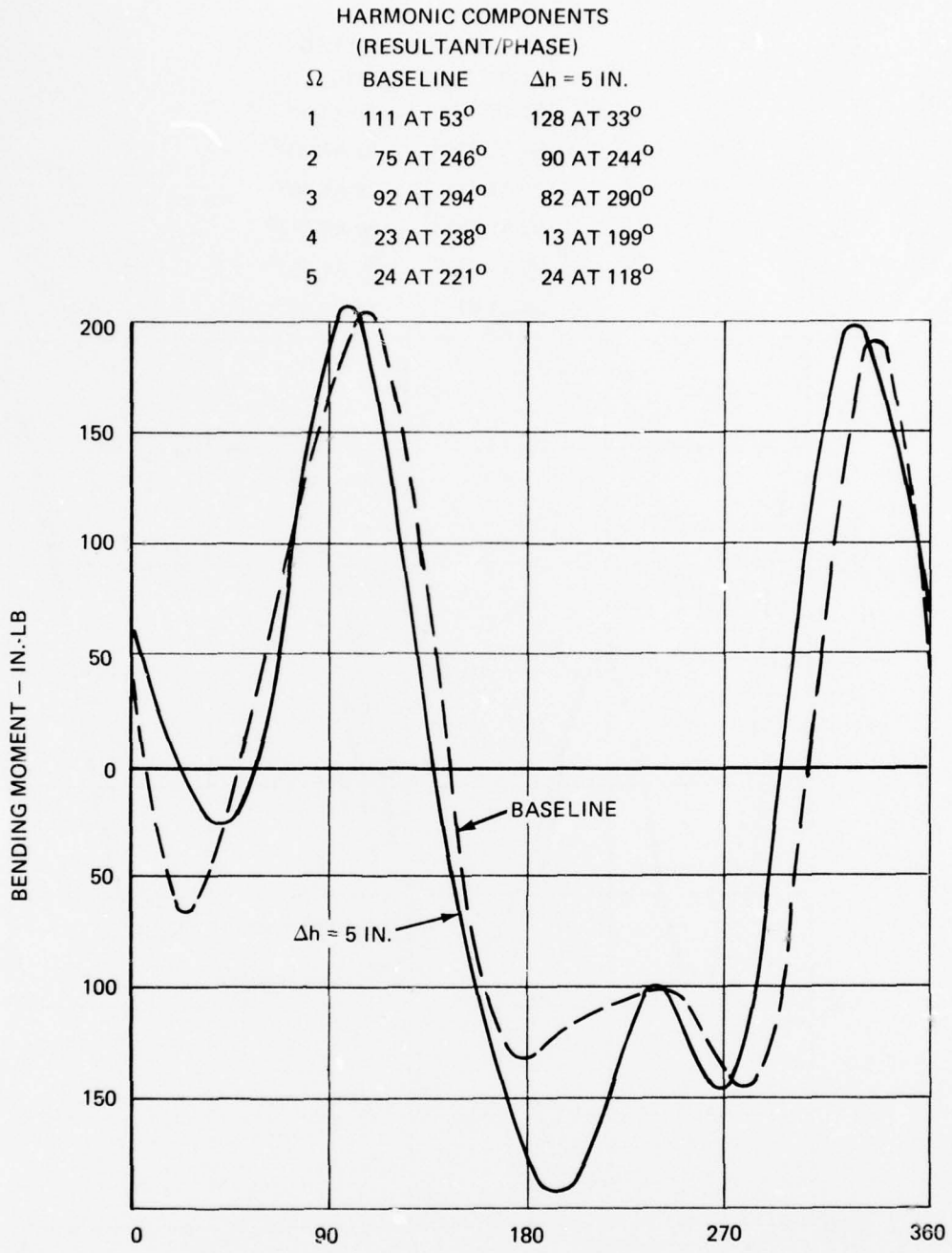

Figure 35. Effect of Rotor/Fuselage Gap Increase on Blade Flap-Bending Moments at 160 Knots.

ROTOR/FUSELAGE/GROUND INTERACTIONS

GENERAL

The interactions between the rotor, fuselage, and ground that are discussed in this section are the effects of the ground vortex on the fuselage forces and moments, specifically the fuselage lift and the fuselage pitching, yawing, and rolling moments. The effect of the fuselage presence on rotor loads was considered to be of secondary importance and was not obtained because of the time necessary to remove the shells.

The principal reason for examining these aerodynamic effects is the direct effect of fuselage download on performance capability. It is important also to study the moment variations for their relevance to pilot workload in NOE operations and for their indications of flow changes.

The loads and moments discussed here are obtained from the fuselage balance, which receives loadings of the body, the nacelles, and the tailboom, but not the empennage, which has its own balance. Because of the generally unsteady environment of helicopter models, the data handling system is designed to average the data over a prescribed time period. This period should probably have been longer for the ground-vortex-induced loadings, but the trends in most cases are clearly evident.

TEST CONDITIONS

The test conditions encompass the same runs as those listed for the section on the Rotor/Ground Interactions. The same variations in rotor height, disk loading, model pitch attitude, and yaw angle were made. The particulars of the runs are listed in Table 8.

FUSELAGE LIFT

The fuselage lift variation with speed for the out-of-ground-effect case has the general characteristic of rising with speed from its negative value at hover until the end of transition, where it reverses and assumes a gradual negative trend as shown in Figure 36. Near the ground, however, the download in hover is reduced because of aerodynamic flow between the ground and the undersurface. This effect is well known and is strongest for flat-bottomed bodies as was the one under test. When the model is sufficiently close to the ground board, the download can actually change sign and become an upload as can be seen in Figure 36 for an h/d of 0.4. Extrapolation to zero speed indicates the probability of an upload approaching 2 percent of lift.

The trend of the IGE line is to the negative side, which it attains at about $0.32\ \mu/\sqrt{C_T/2}$, which is about 8 knots. This continues until a nondimensional speed of 0.7 is reached. Here the curve forms an elbow and turns sharply upwards, paralleling the OGE curve. This is the speed where the ground vortex is observed to move under the rotor and induces a heavy downflow on the fuselage nose.

With the rotor 50 percent higher at 0.6 h/d, the curve at the low speed is displaced away from the positive lift side and appears to join the OGE line at about 0.4, or a dimensional

TABLE 8. TEST RUNS FOR THE EFFECTS OF GROUND PROXIMITY

Run No.	Configuration	V_{TUN} (kn)	MR/TR Speed (rpm)	Disk Ldg (psf)	Model Angles α (deg)	Model Angles ψ (deg)	MR Ht (h/d)	Tail Rotor
83	K_9/Baseline for D.L. variation	⟨11⟩	1,433/ 4,500	8	0	0	0.4	On
84	K_9/Added detail to 83	10↔20 /2's	1,433/ 4,500	8	0	0	0.4	On
85	K_9/Increased D.L.	⟨11⟩	1,433/ 4,500	10	0	0	0.4	On
86	K_9/Added detail to 85	20↔26 /2's	1,433/ 4,500	10	0	0	0.4	On
87	K_9/Reduced D.L.	⟨11⟩	1,433/ 4,500	6	0	0	0.4	On
88	K_9/Added detail to 87	12↔18 /2's	1,433 4,500	6	0	0	0.4	On
89	K_9/Reduced D.L.	⟨11⟩	1,433/ 4,500	4	0	0	0.4	On
90	K_9/Effect of pos yaw	⟨11⟩	1,433/ 4,500	8	0	+30	0.4	On
91	K_9/Effect of neg yaw	⟨11⟩	1,433/ 4,500	8	0	-30	0.4	On
92	K_9/Effect of neg angle of attack	⟨11⟩	1,433/ 4,500	8	-6.6	0	0.4	On
93	K_9/Effect of pos angle of attack	⟨11⟩	1,433/ 4,500	8	+10	0	0.4	On
94	K_9/Reset α to mean value over transition	⟨11⟩	1,433/ 4,500	8	5	0	0.4	On
95	K_9/Added detail to 94	12↔20 /2's	1,433/ 4,500	8	5	0	0.4	On
96	K_9/Added detail to 94	10↔30 /2's	1,433/ 4,500	8	5	0	0.4	On
97	K_9/Added detail to 94	10↔30 /2's	1,433/ 4,500	8	5	0	0.4	On
98	K_9/Reduced D.L.	10↔30 /2's	1,433/ 4,500	6	5	0	0.4	On
99	K_9/Increased rotor height	10↔30 /2's	1,433/ 4,500	8	5	0	0.475	On
100	K_9/Increased rotor height	⟨11⟩	1,433/ 4,500	8	5	0	0.475	On
101	K_9/Effect of tail rotor stopped	⟨11⟩	1,433/0	8	5	0	0.4	Stopped
102	K_9/Increased rotor to ground height	⟨11⟩	1,433/ 4,500	8	5	0	0.6	On
103	K_9/Increased rotor to ground height	⟨11⟩	1,433/ 4,500	8	5	0	0.7	On
104	K_9/Increased rotor to ground height	⟨11⟩	1,433/ 4,500	8	5	0	0.8	On
105	K_9/Increased rotor to ground height	⟨11⟩	1,433/ 4,500	8	5	0	1.0	On

NOTE: ⟨11⟩ for V_{TUN} = 0, 10 to 40 knots by 5's, then 50 kn

speed of 10 knots. As with power required, the ground vortex effect comes into play at a lower speed when the rotor is farther off the ground than 0.4.

EFFECT OF ANGLE OF ATTACK ON LIFT

Figure 37 shows the lift variation with speed for three angles of attack at h/d equal to 0.4, and the disk loading at 8 psf. Generally the data follow the same curve up to 0.7 airspeed where the elbow forms, as on the previous figure where α was set at 5 degrees. From that point on the variations are quite different.

All curves, however, exhibit a second break just above $\mu/\sqrt{C_T/2} = 0.8$, beyond which they transition to their forward flight pattern. Additional flow studies are required to explain these nonlinearities. Interestingly, the second break did not appear in the previous graph for $\alpha = 5$ degrees, in all likelihood due to the absence of a point near 0.9.

EFFECT OF DISK LOADING ON LIFT

The lift variation with speed is shown in Figure 38, for four disk loadings. These are plotted for clarity on separate coordinates, since they are so similar. The first break occurs close to 0.7 with a maximum negative value of about 2 percent of lift for all four disk loadings. At the higher speeds, the pattern shows the higher disk loadings with more upload, which seems contradictory to the higher mean downwash angles known to exist. The explanation probably lies in the fore-and-aft variation of downwash typical of forward flight. An upwash at the front of the rotor relative to the rear, which is proportional to disk loading, would give more positive flow angles on the forward (lifting) portion of the fuselage.

EFFECT OF WIND AZIMUTH

Figure 39 compares lift/speed variations for plus and minus 30 degrees and zero degrees of yaw. The curves for zero and +30 degrees are similar but with a delay in the "elbow-formation" speed for the latter case. This would be expected, since the vortex (in plan view) is farther away from the nose at a given forward speed.

The lack of symmetry of the fuselage lift in yaw suggests that there is strong lateral dissymmetry in the induced flow field, i.e., more negative flow on the left side. This implies that the left rotary-wing tip vortex is stronger than the right, i.e., that vorticity is piled up by the blades coming around the front of the rotor, but not to the right side as the blade sweeps the downstream side of the rotor. This is not inconsistent with the flow visualization pictures of the vortex pattern in forward flight, as shown in Figure 40.

Two features in this photograph are significant. First of all, the vortex trails on the aft portion retain their identity and are carried downstream as segments forming the necklace pattern. The vortex trails originating on the forward portion are not in evidence downstream, and it is probable that they are drawn in to the rollup of the left rotary-wing vortex. If this happens, a greater strength results on the left vortex and, significantly, the necklaces are seen (with some difficulty) to be warped laterally downward more on the left side as they move aft. Again, this entire area of understanding the low-speed flow field requires much research.

FUSELAGE PITCHING MOMENT

A sharp reversal in the fuselage pitching moment variation with speed occurs as a result of ground vortex passage similar to the trend already noted in the fuselage lift data. The effect of this reversal on aircraft handling qualities is not certain. No pilot reports are in evidence, and it may well be that any jolt is lost in the general unsteadiness that prevails.

The fuselage moments are nondimensionalized simply by dividing by model lift times rotor radius, since the moment is a function mainly of downwash and length. This approach is agreeable and it does have the result of making the curves of the lift (disk loading) variation almost identical. Ideally, perhaps the moments should be nondimensionalized by a dynamic pressure term reflecting the downwash velocity and the forward speed, such as the "double prime" terminology introduced by NASA for use with the forces on tilt-wing and other V/STOL's with propwash-energized wings.

Effect of Height

Figure 41 presents the variation of pitching moment with speed for 0.4 and 0.6 height-to-diameter ratios, compared to the out-of-ground-effect case. The effect of the ground vortex is equally strong at h/d 0.4 and 0.6. Apparently, its effect on the fuselage persists more than its effect on the rotor as height is increased. In and out of ground effect, the sharp break is evident at 1.2 nondimensional speed, supporting again the suggestion of a sudden change in the flow field.

Effect of Disk Loading

Disk loading effects are shown in Figure 42. The pitching moment curves versus speed are plotted separately, since they are so similar and make a confused presentation on the same grid. Thus the ground vortex effect on the moment is proportional to disk loading. The moment change involved in the dip to the negative value around −12.0 is not small (approximately −0.0006 in C_{RM}), so it will tend to aggravate the discontinuity in the aircraft pitching moment already present due to the hub moment. This is not serious, as the pitch axis is not sensitive because of high inertia.

Effect of Model Pitch Attitude

The ground vortex effect is very similar for all angles at the low-speed end of the curves of Figure 43. Beyond this, all curves peak near 1.2 and the variation with attitude is similar to that observed earlier for the lift in Figure 37. The curve for the negative angle experiences a disproportionate vertical displacement, doubtless because the induced upflow is least with the nose closest to the ground as it is with a negative attitude.

Effect of Wind Azimuth

Figure 44 shows the effects of right and left yaw angles on pitching moment. The ground vortex effect in the speed regime 0.6 to 0.8 appears less for −30 and +30 degrees compared to zero degrees as expected. However, the trend versus yaw at the higher speeds is puzzling as it is opposite to that exhibited by the lift data.

FUSELAGE YAWING MOMENT

A significant negative yawing moment exists in or out of ground proximity probably due to side forces on the boom created by rotor swirl. These are maximum for the OGE case at zero speed and gradually become more positive with increasing forward speed, as shown in Figure 45. By a mechanism not evident, the two IGE curves apparently start out at small negative values, plunge steeply under the influence of the ground vortex flow, then reverse and finally line up with the OGE past a speed of 1.2.

Effect of Disk Loading

The fuselage yawing moment is shown in Figure 46 for four disk loadings. Unlike the case of the pitching moments, the selected nondimensionalization did not collapse all the lines on top of one another. Dimensionally, as moments in ft/lb, the curves would be quite close. This seems to be telling us that the swirl velocity is not a function of disk loading, but perhaps is more directly related to rotor angular velocity, which is held constant in these tests.

Effect of Model Pitch Attitude

The effects of angle of attack variation are presented in Figure 47. The four curves are variously shaped in the trend with speed. Generally, the cases with the tailboom highest in the air, i.e., zero and −6.6 degrees, show the least effect from the vortex as would be expected, as well as the smoothest variation. Thus in the acceleration case the yaw upset will be the least and in deceleration, the most.

Effect of Wind Azimuth

The yawing moment trend with speed is shown in Figure 48 for plus and minus 30 degrees of yaw. The position of the minus 30-degree curve is surprising. It should be exhibiting a more negative moment compared to zero yaw, and yet it is considerably more positive.

FUSELAGE ROLLING MOMENT

The fuselage rolling moment variation with speed exhibits very small values and is certainly of no consequence in the handling of the aircraft. Figure 49 shows this trend for a h/d of 0.4 and infinity. Figure 50 is interesting in its consistency with the sign of the fuselage side force, i.e., for right yaw a side force to the right produces a roll to the right.

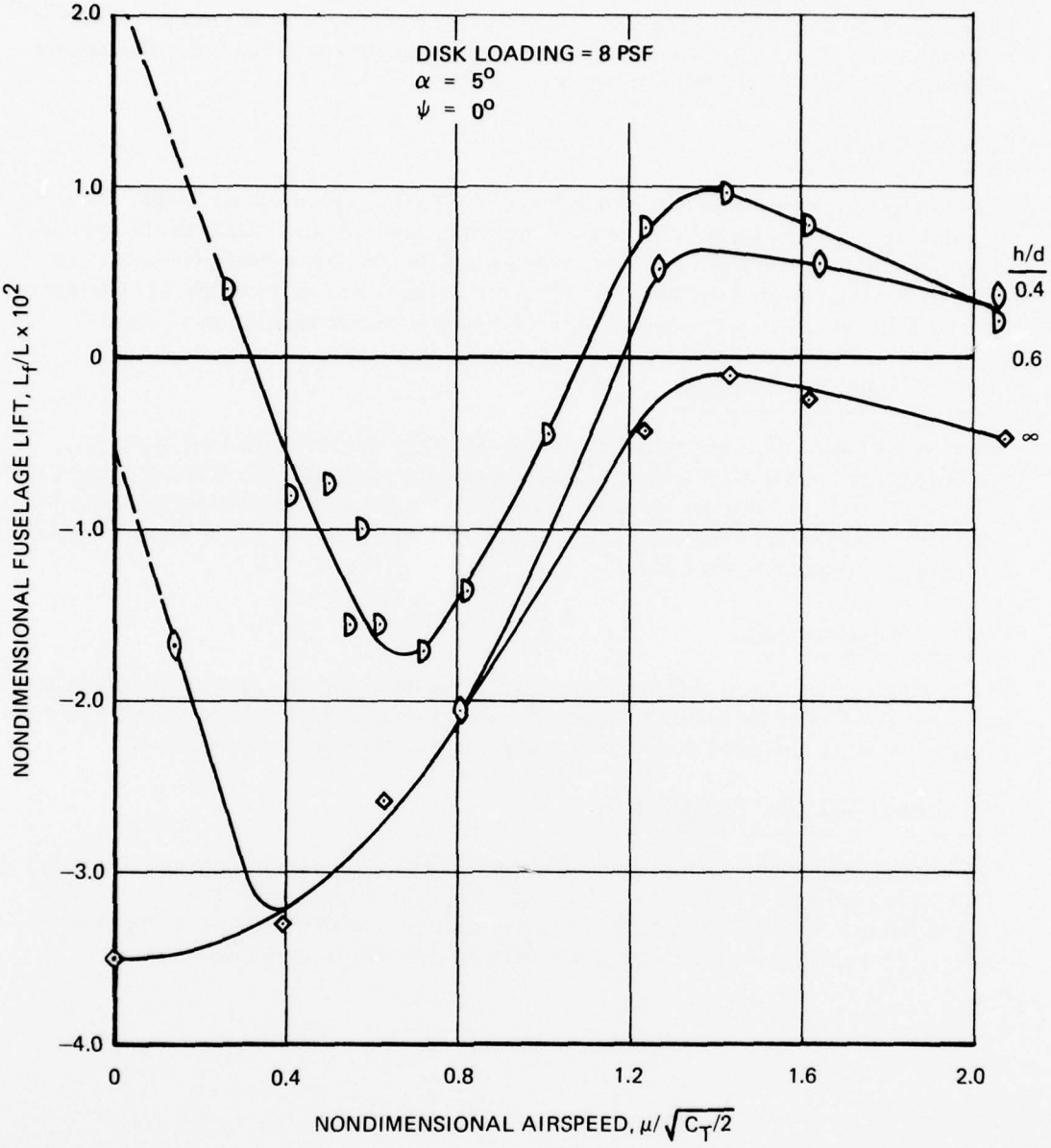

Figure 36. Fuselage Lift as a Function of Airspeed for Selected Rotor-to-Ground Heights.

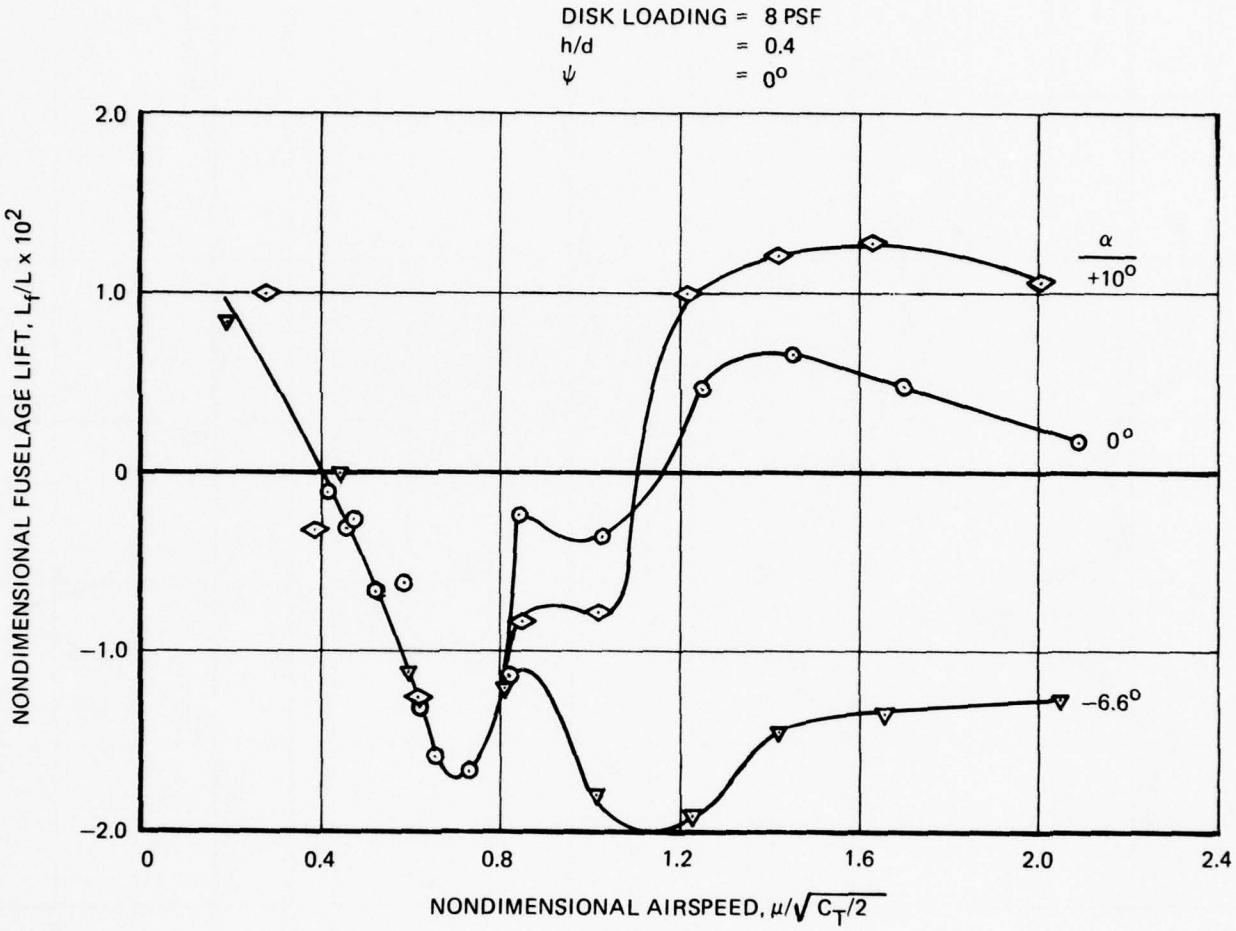

Figure 37. Fuselage Lift in Ground Proximity as a Function of Airspeed for Three Model Attitudes.

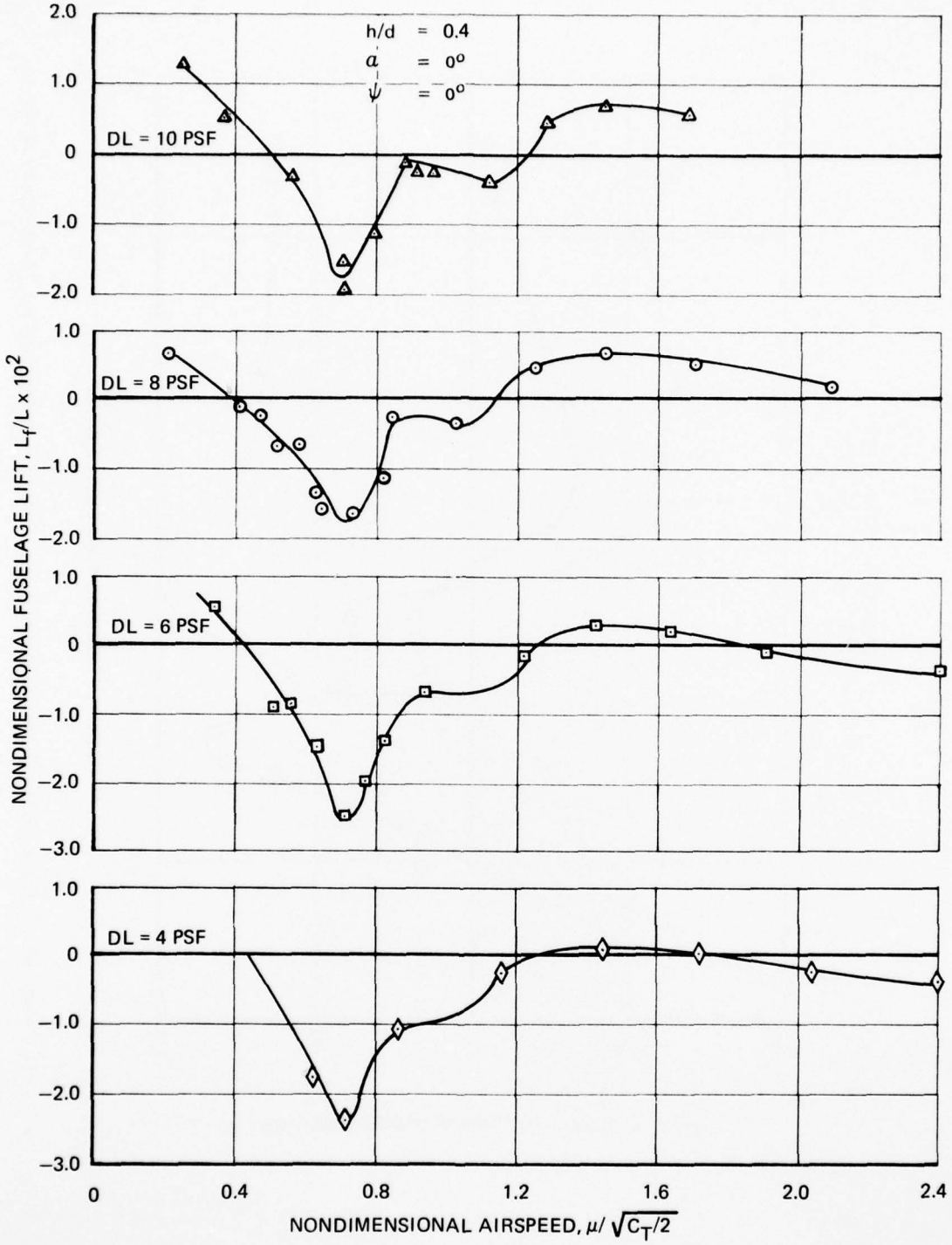

Figure 38. Fuselage Lift in Ground Proximity as a Function of Airspeed for Four Disk Loadings.

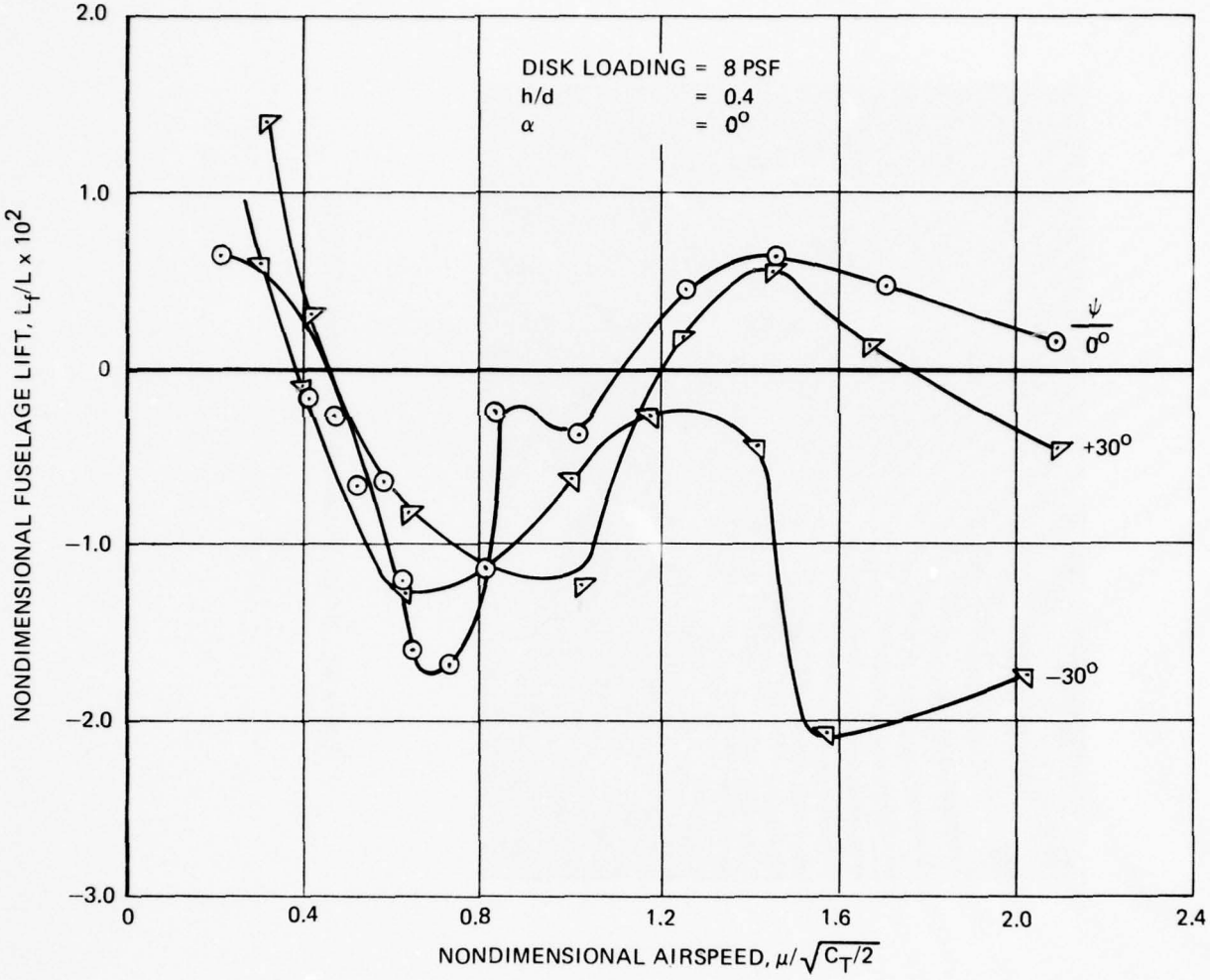

Figure 39. Fuselage Lift as a Function of Airspeed for Right and Left Wind Azimuth.

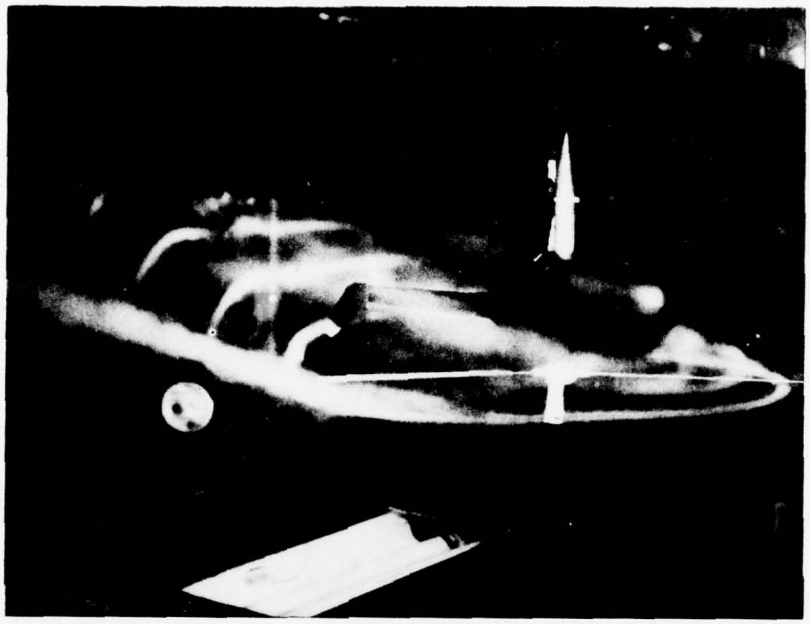

Figure 40. Rotor Vortex Wake in Forward Flight.

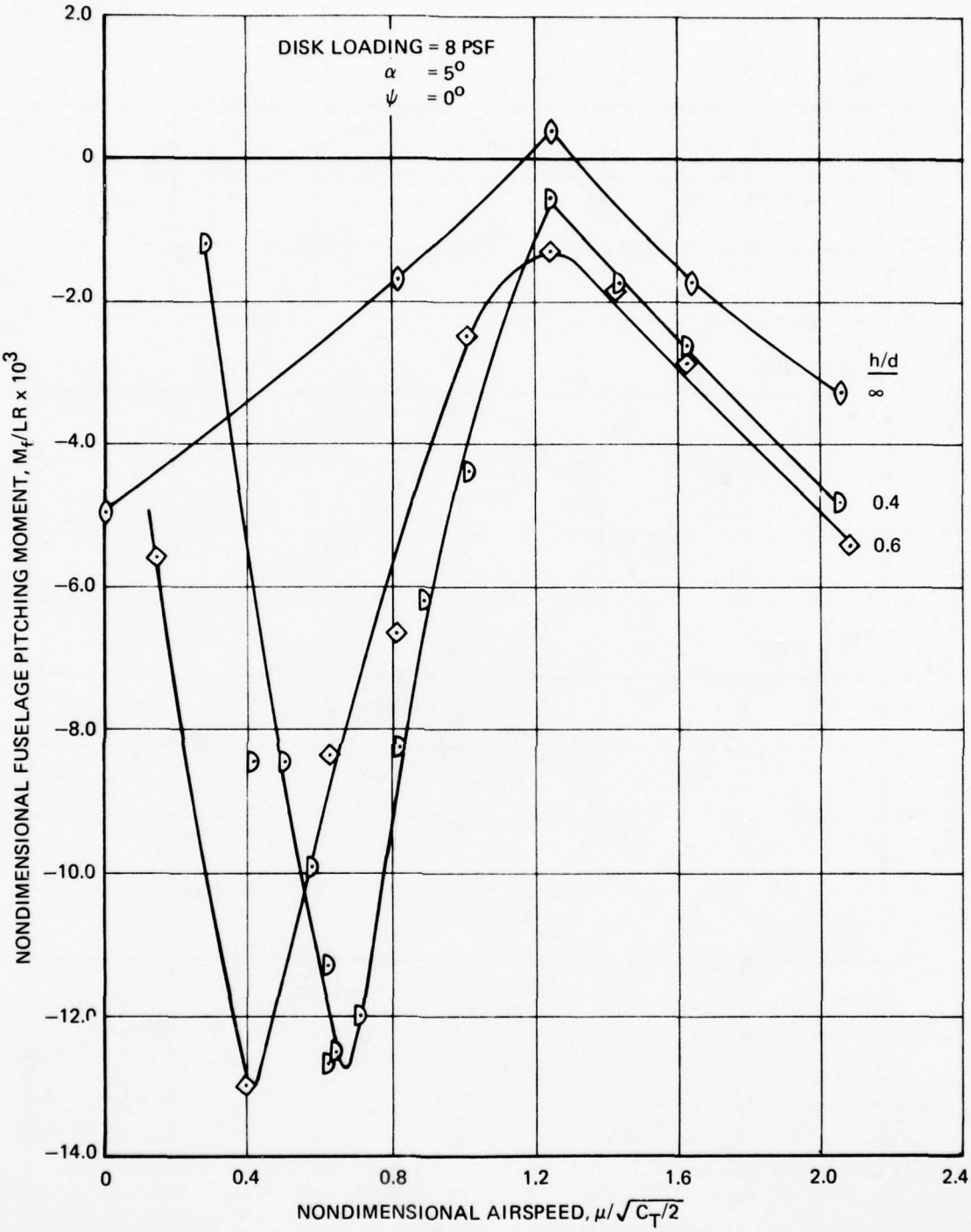

Figure 41. Variation of Fuselage Pitching Moment With Airspeed In and Out of Ground Effect.

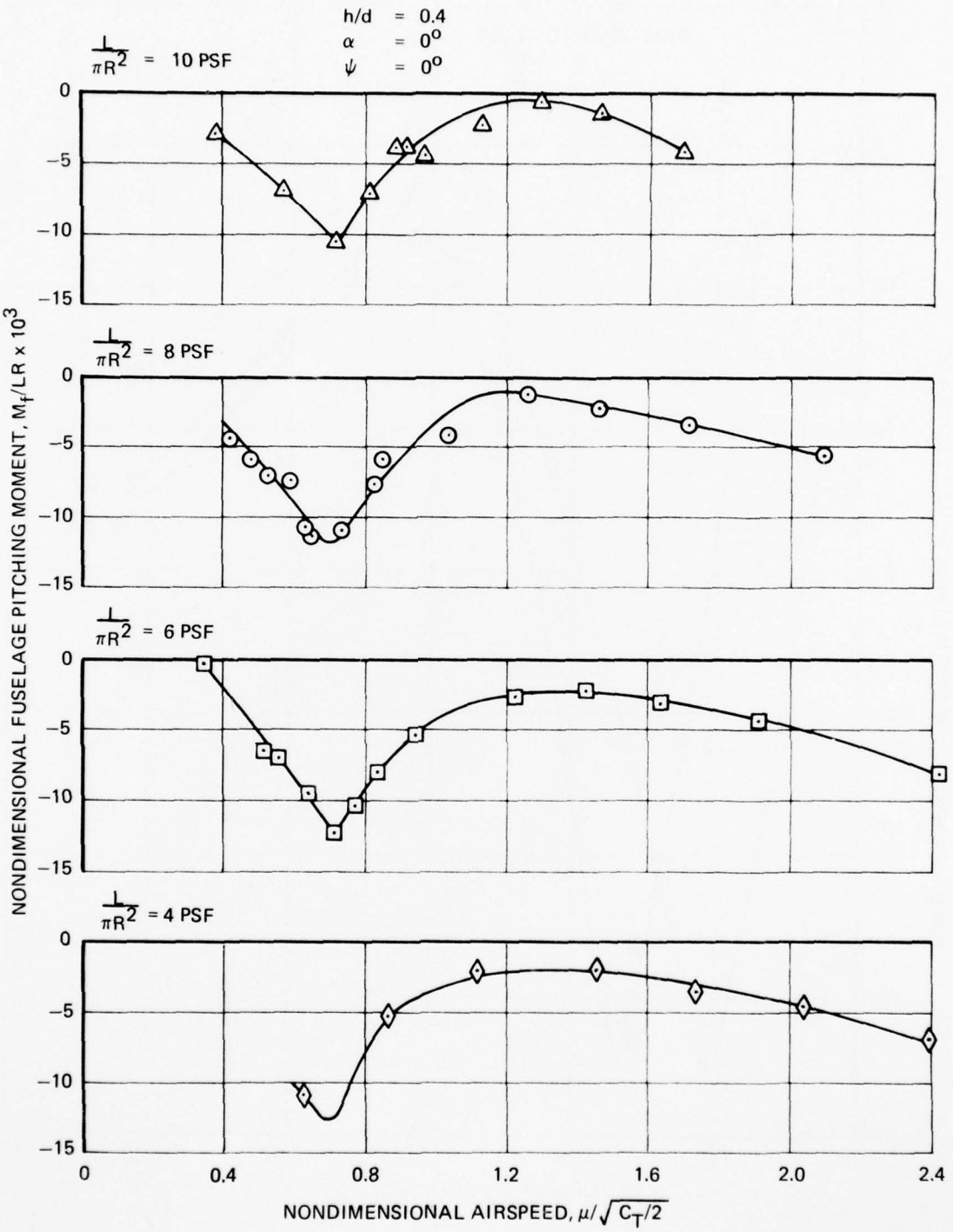

Figure 42. Variation of Fuselage Pitching Moment With Airspeed Showing the Effects of Disk Loading.

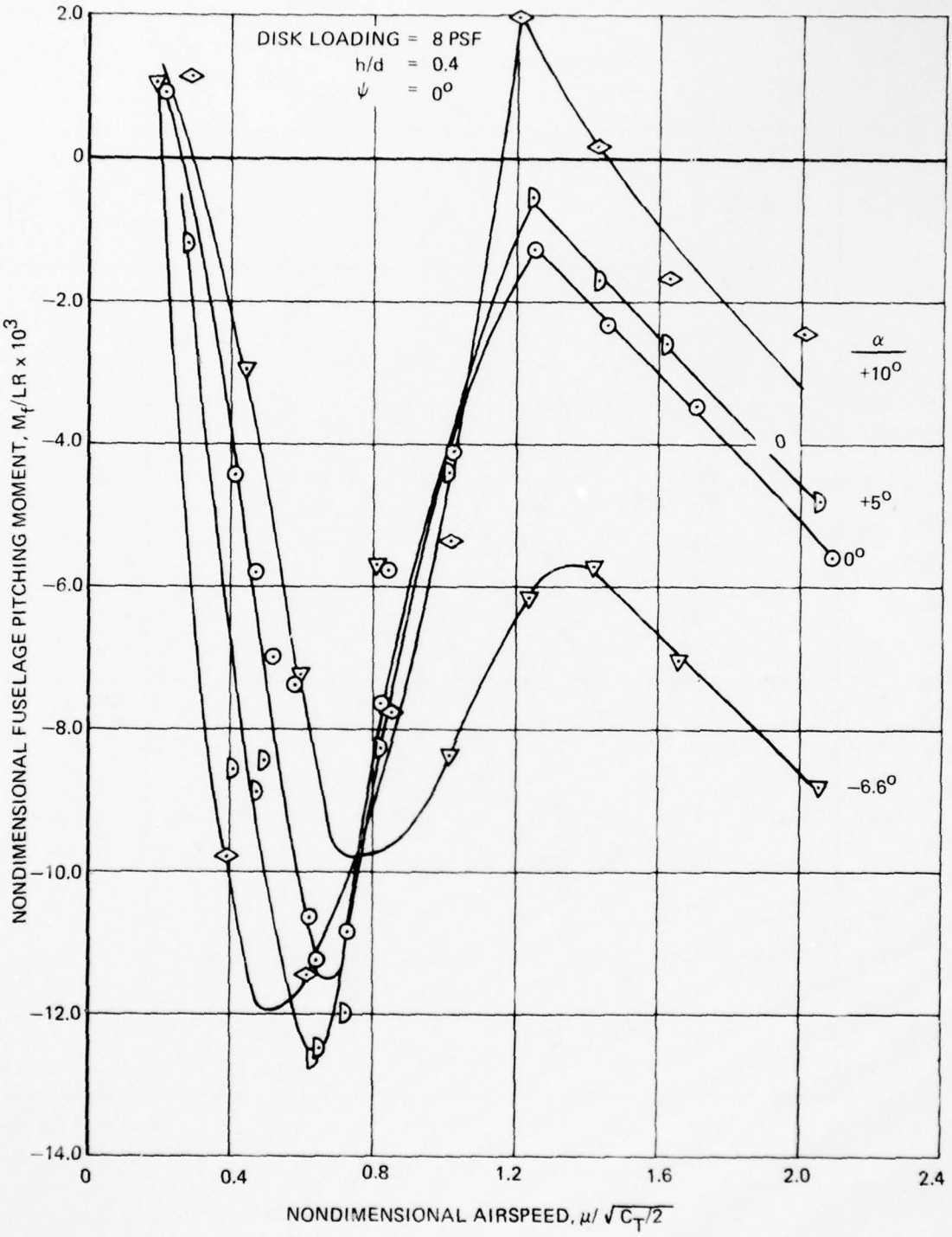

Figure 43. Variation of Fuselage Pitching Moment With Airspeed Showing Effect of Model Attitude.

AD-A060 389 BOEING VERTOL CO PHILADELPHIA PA F/G 1/3
INTERACTIONAL AERODYNAMICS OF THE SINGLE-ROTOR HELICOPTER CONFI--ETC(U)
SEP 78 P F SHERIDAN DAAJ02-77-C-0020
UNCLASSIFIED USARTL-TR-78-23A NL

2 OF 4
AD
AO 60389

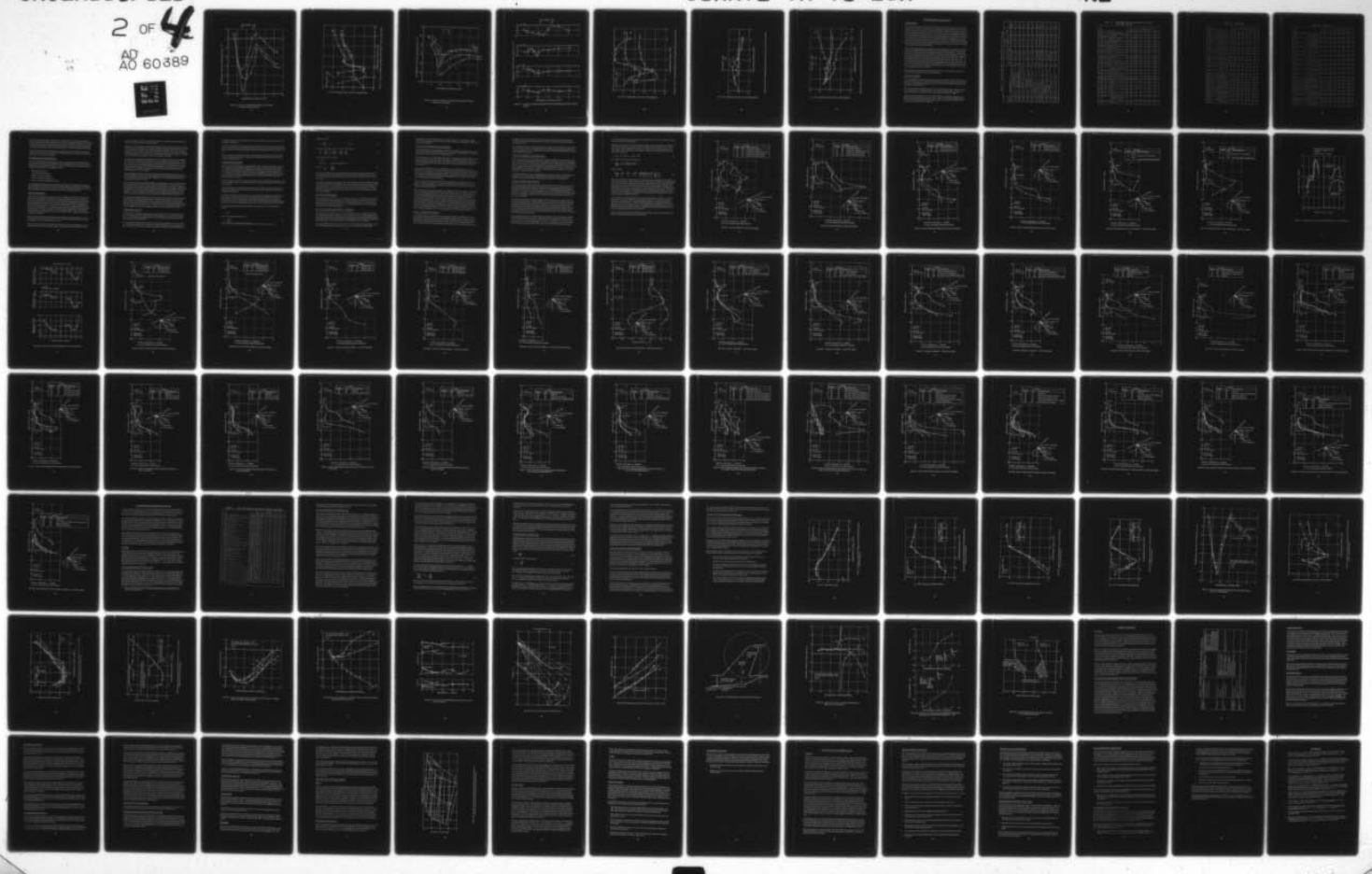

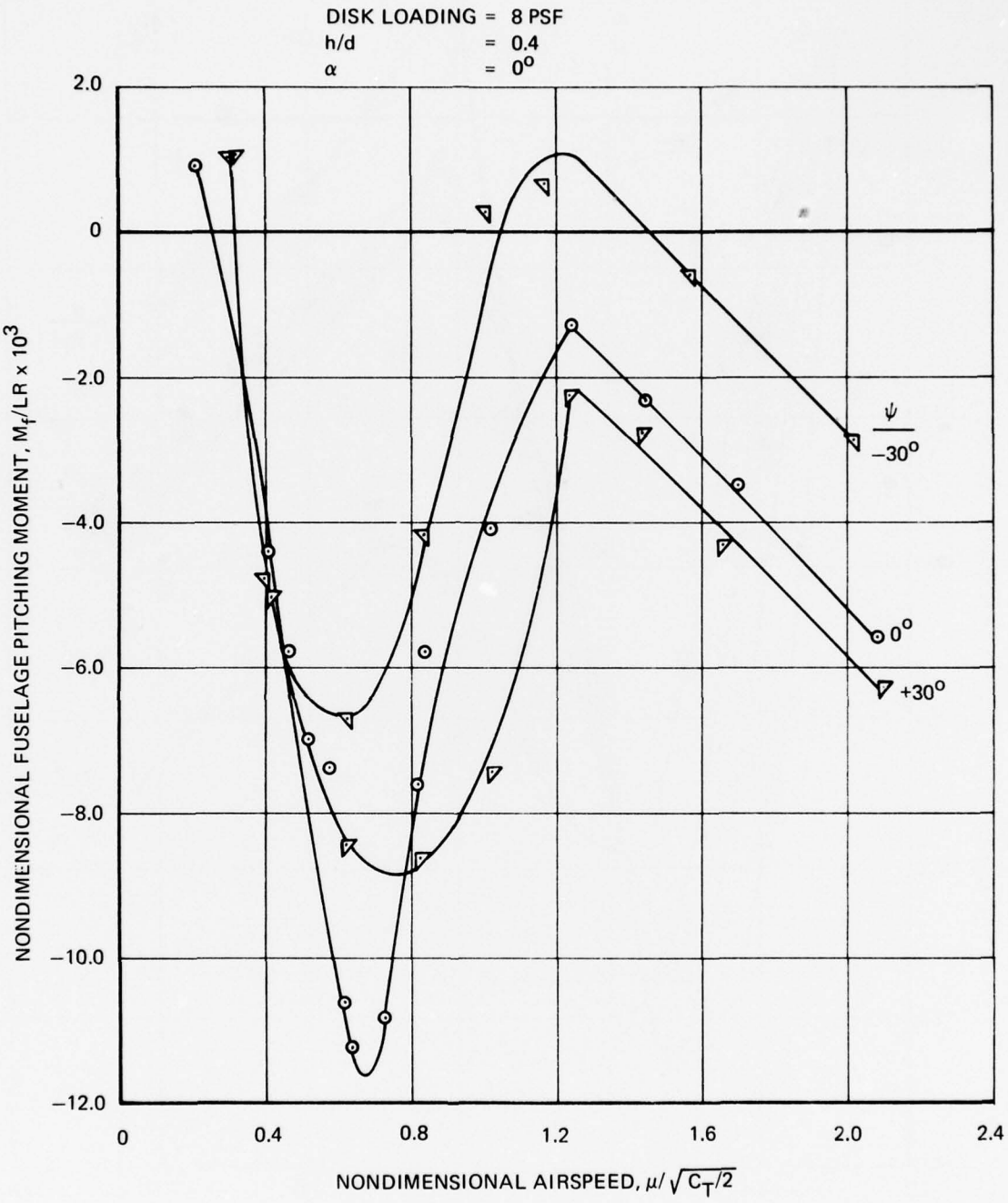

Figure 44. Variation of Fuselage Pitching Moment With Airspeed for Right and Left Wind Azimuth.

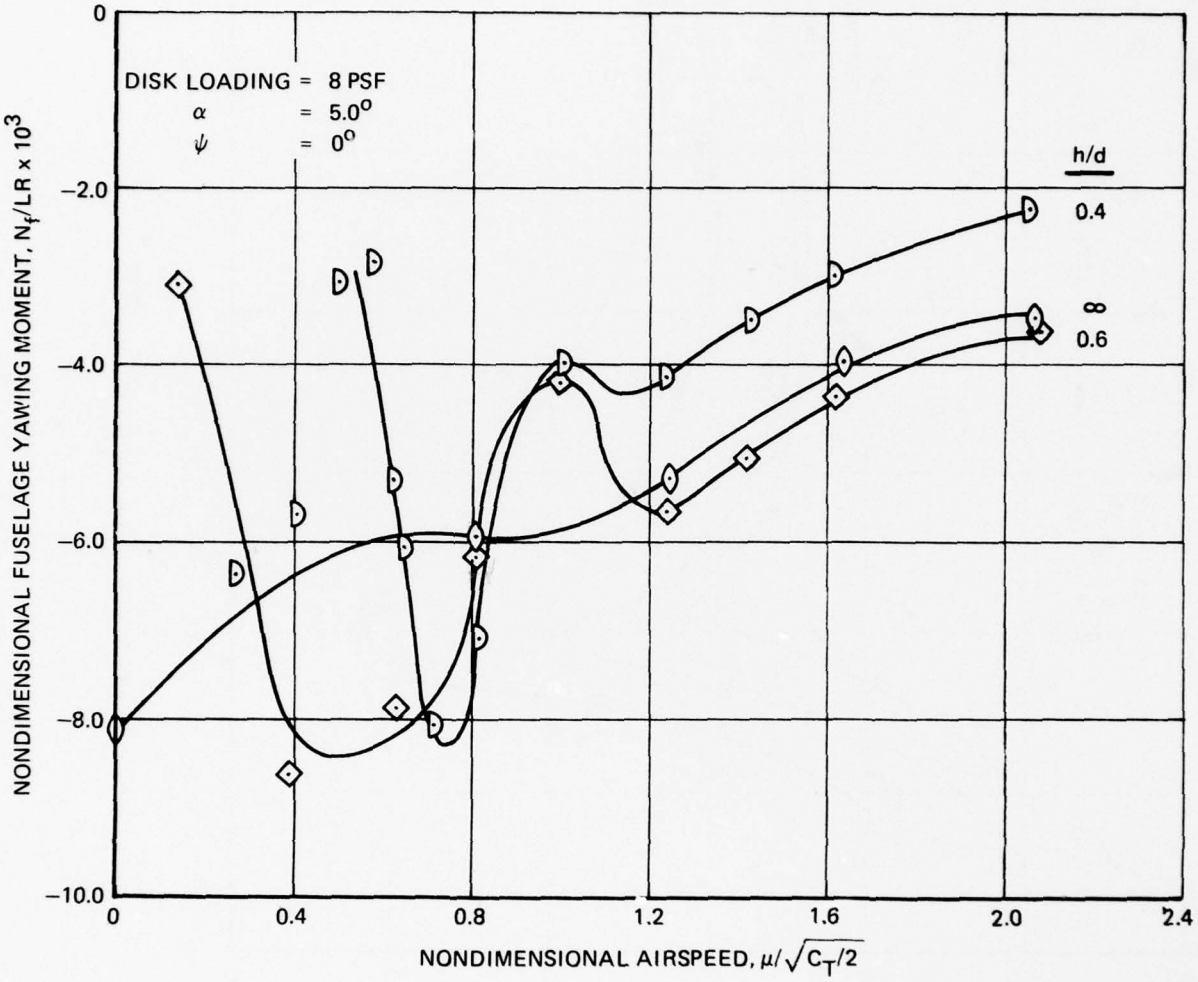

Figure 45. Variation of Fuselage Yawing Moment With Airspeed In and Out of Ground Effect.

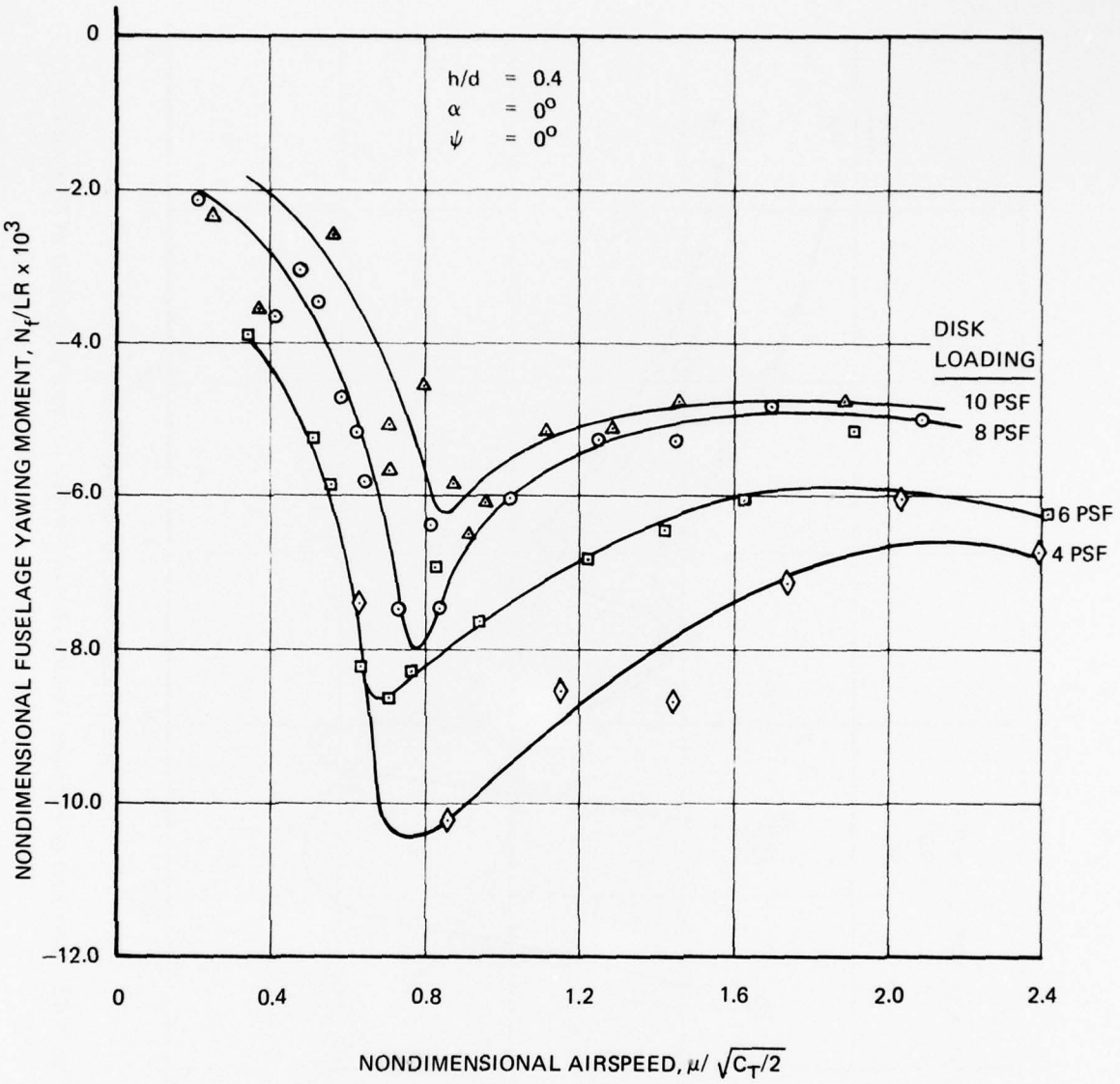

Figure 46. Variation of Fuselage Yawing Moment With Airspeed Showing the Effect of Disk Loading.

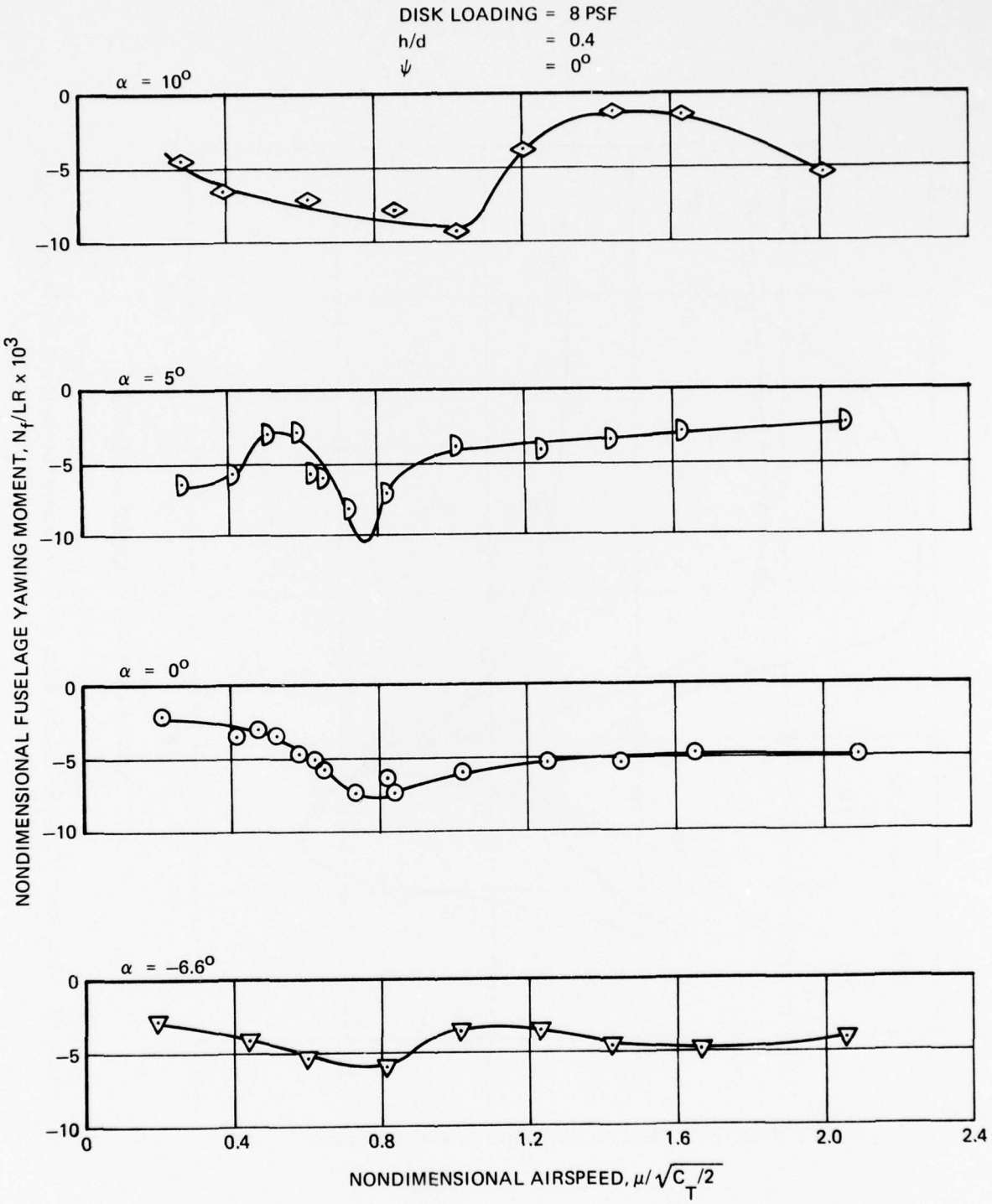

Figure 47. Variation of Fuselage Yawing Moment With Airspeed Showing the Effect of Model Attitude.

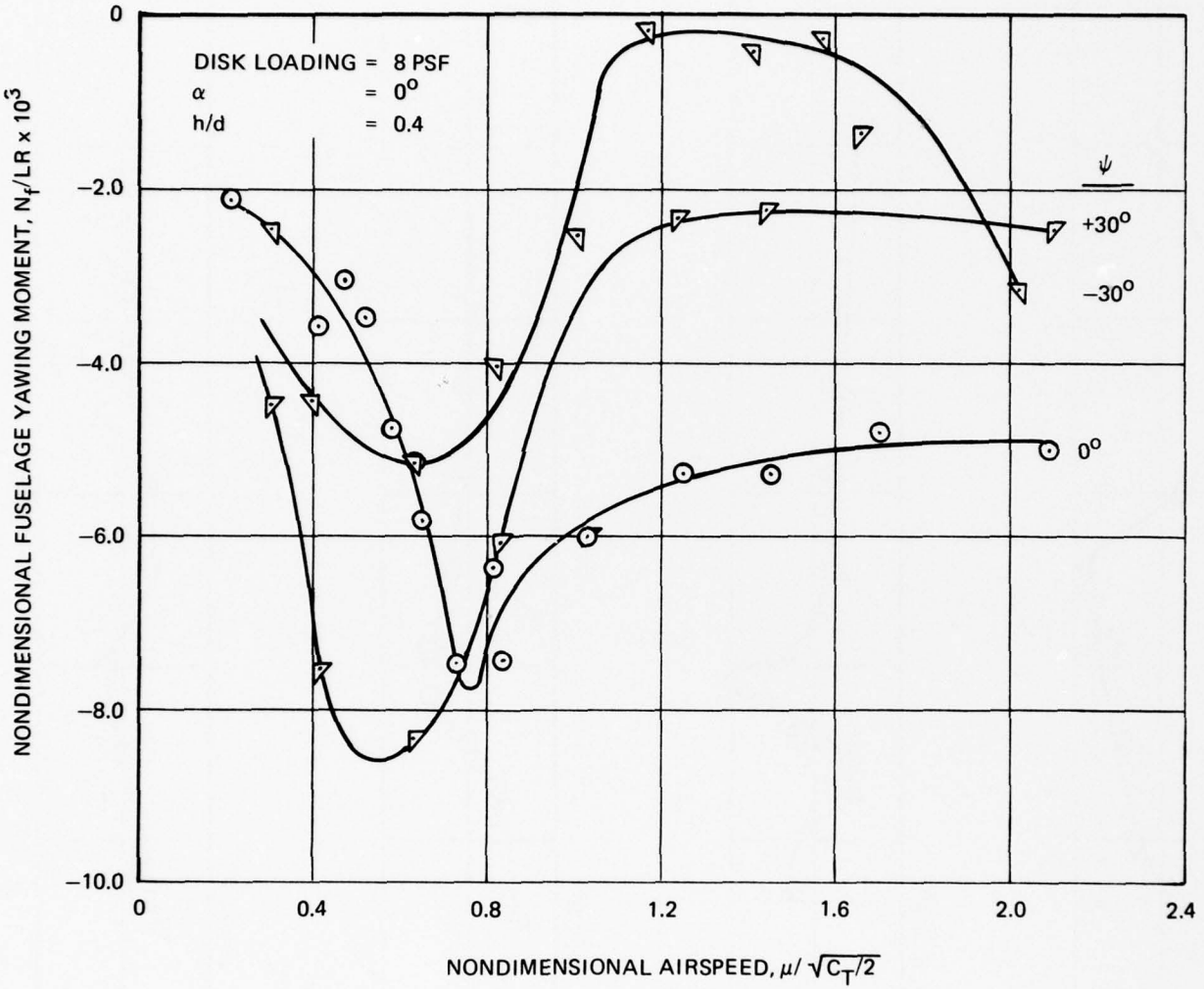

Figure 48. Variation of Fuselage Yawing Moment With Airspeed for Right and Left Wind Azimuth.

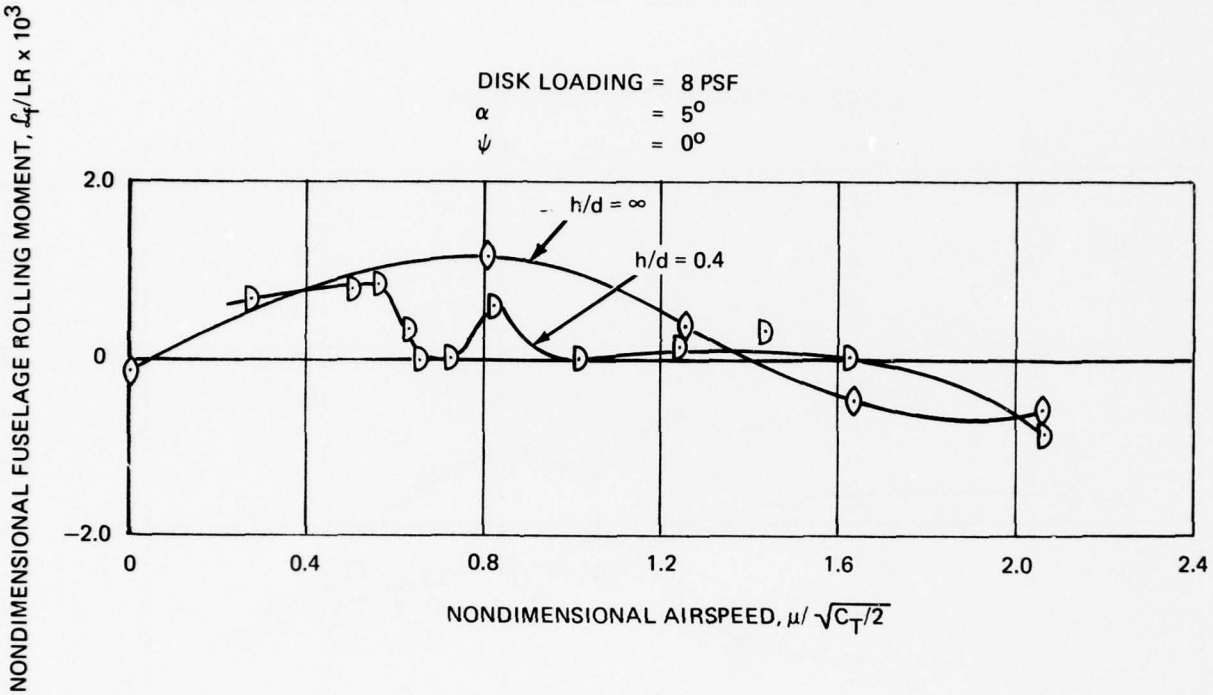

Figure 49. Variation of Fuselage Rolling Moment With Airspeed In and Out of Ground Effect.

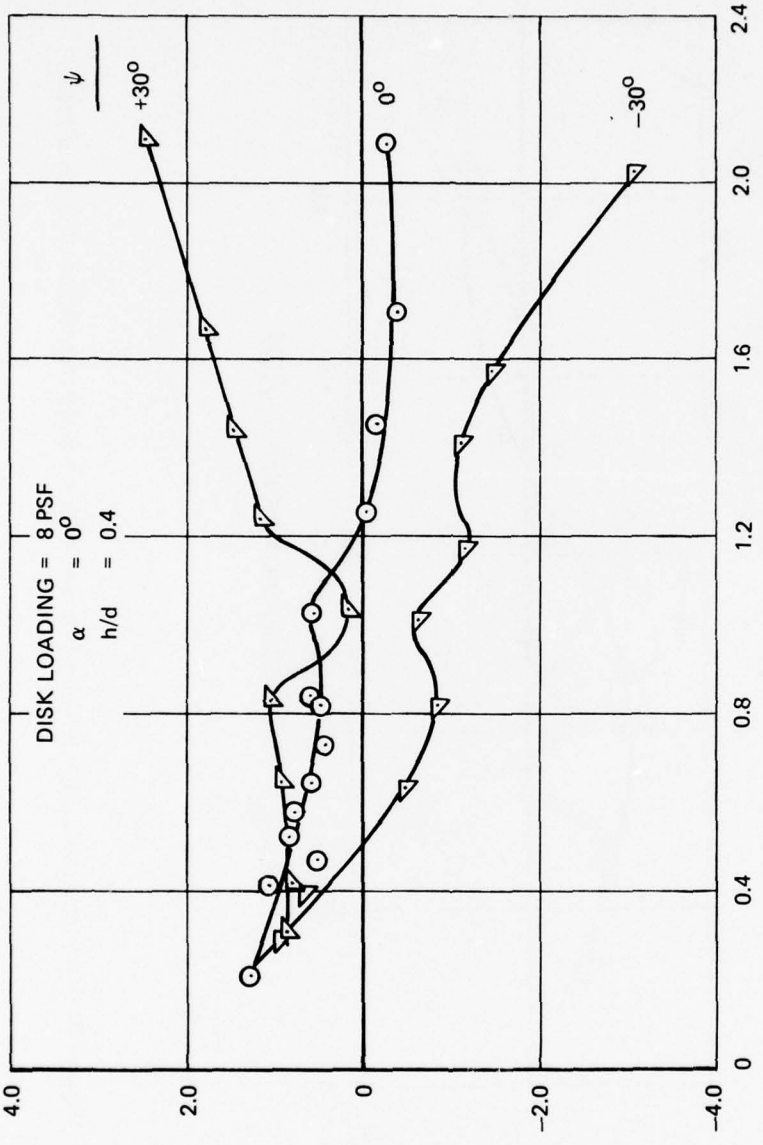

Figure 50. Variation of Fuselage Rolling Moment With Airspeed for Right and Left Wind Azimuth.

ROTOR/EMPENNAGE INTERACTIONS

INTRODUCTION

The interaction of interest in this phase of the study was the dynamic effect of the rotor/hub wake on the empennage. Lateral upsets were observed to occur intermittently in flights of the YUH-61A at all speeds between 60 knots and maximum speed with the most severe occurrences observed at high rates of descent at 80 knots. These were measured to be lightly undamped bursts with a predominant frequency near 5 Hz. It was concluded from subsequent analysis that the phenomenon was probably excitation of a negatively damped mode involving the tailboom, the natural frequency of which was near 5 Hz. An unfavorable modal coupling with the tail rotor drive system was also suspected. It was decided to attack the problem both by damping improvement and by reducing the wake disturbances in the low end of the spectrum. The latter effort was undertaken in the wind tunnel and consumed over 50 percent of the effort compared to the other work discussed in this report.

The means of measuring the wake dynamically was an anemometer system using purchased hot film sensors and Boeing-developed calibration and data processing systems. The sensors were mounted on a rake that was remotely positioned vertically and longitudinally. Two split film sensors were mounted centrally at 90 degrees to one another and provided lateral and vertical flow angles (α and β) plus associated velocity components in their respective planes. Data from these probes provided the parameters for measuring success in modifying the wake. β was normally used on-line since the wake problem was a dynamic side force matter and since it was observed that usually α and the velocities were significantly improved at the same time as was β. In addition to the split film probes, six single film probes were arranged along the rake bar, three on the left and three on the right of the split film pair. These provided velocity only and were not primary data in the evaluations.

Analog outputs were transmitted to an on-line spectral analyzer and to tape for off-line processing. Additional details are provided in Appendix B.

WAKE DATA FORMAT

The runs undertaken to study the wake problem are listed in Tables 9 and 10. Standard spectrographs from each of these are presented in Volumes VII and VIII for split films and single films, respectively. A second kind of frequency plot, the 1/3-octave band format, is also shown for each case in Volumes IV and VI.

The frequency analysis computer programs did not output the mean values. Rather than take time to modify these, a conventional harmonic analysis program was used for certain cases where mean values were of interest. These output data are presented in Volume V.

Finally, the data are organized in their most useful format for comparative analysis by cross plots of flow angles and velocities versus waterline. These are assembled in Volume III where a plot is shown for each test configuration and its baseline. The basis for the cross plot is the 1/3-octave band split film data of Volume IV.

TABLE 9. TEST RUNS FOR BASIC INVESTIGATION OF THE HUB WAKE

Run No.	Configuration	V_{TUN} (kn)	MR/TR Speed (rpm)	Disk Ldg (psf)	Model Angles		MR Ht (h/d)	Tail Rotor
					α (deg)	ψ (deg)		
111	K_{11}/15-in. Long. wake traverse at TR centerline	80	1,433/0	8	6.0	-2.0	∞	Off
112	K_{11}/9-in. Vert wake traverse above TR centerline	80	1,433/0	8	6.0	-2.0	∞	Off
113	K_{11}/9-in. Vert traverse through MR vortex	80	1,433/0	8	6.0	-2.0	∞	Off
114	K_{11}/8-in. Vert traverse below TR centerline	80	1,433/0	8	6.0	-2.0	∞	Off
115	K_{11}/13-in. Vert traverse behind stabilizer	80	1,433/0	8	6.0	-2.0	∞	Off
116	K_{11}/Lateral traverse - left stabilizer	80	1,433/0	8	6.0	-2.0	∞	Off
117	K_{11}/116 continued	80	1,433/0	8	6.0	-2.0	∞	Off
118	K_{11}/116 continued	80	1,433/0	8	6.0	-2.0	∞	Off
119	K_{11}/Lateral traverse - right stabilizer	80	1,433/0	8	6.0	-2.0	∞	Off
121	$K_{11}+T_2$/Effect of tail rotor flow on wake	80	1,433/ 4,500	8	6.0	-2.0	∞	On
135	K_{11}/Wake in 900 fpm climb	80	1,433/0	8	-6.0	-4.5	∞	Off
136	K_{11}/Wake in 800 fpm descent	80	1,433/0	8	6.0	-2.0	∞	Off

TABLE 10. TEST RUNS FOR THE EVALUATION OF WAKE-ALTERING DEVICES

Run No.	Configuration	V_{TUN} (kn)	MR/TR Speed (rpm)	Disk Ldg (psf)	Model Angles		MR Ht	Tail Rotor
					α (deg)	ψ (deg)	(h/d)	
137	K_{11}-$H_{1.0}$+$H_{1.2}$/ Effect of 7.6-inch-diam solid hubcap	80	1,433/0	8	6	- 3.8	∞	Off
138	K_{11}/Repeat of base run	80	1,433/0	8	6	- 3.8	∞	Off
139	K_{11}+$VG_{2.1}$/Effect of vortex generators on aft crown	80	1,433/0	8	6	- 3.8	∞	Off
140	K_{11}+D_1/Flat-topped "doghouse" fairing on aft crown	80	1,433/0	8	6	- 3.8	∞	Off
141	K_{11}+D_2/Rounded-top fairing	80	1,433/0	8	6	- 3.8	∞	Off
142	K_{11}+FV_1/Deflection vane on crown between nacelles	80	1,433/0	8	6	- 3.8	∞	Off
143	K_{11}+X_1/Variable porosity spoiler	80	1,433/0	8	6	- 3.8	∞	Off
149	K_{13}+H_1-N_1/Effect of nacelles off also add stiff pitch arms (K_{13})	60	1,075/0	4.5	6	- 3.8	∞	Off
150	K_{13}+H_1/ 60-knot baseline	60	1,075/0	4.5	6	- 3.8	∞	Off
151	K_{13}+$H_{1.3}$/16 inch diam helmet fairing	60	1,075/0	4.5	6	- 3.8	∞	Off
152	K_{13}+$H_{1.0}$/Pylon and intake fairing	80	1,433/0	8	6	- 3.8	∞	Off
153	K_{13}+$H_{1.2}$/Repeat 137 with K_{13} pitch arms	80	1,433/0	8	6	- 3.8	∞	Off
154	K_{13}+$H_{1.5.2}$/ 10-in. open hubcap, 7-in. underbody, 1.25-in. gap	80	1,433/0	8	6	- 3.8	∞	Off
156	K_{13}+$H_{1.0}$/Baseline with K_{13}, i.e., stiff pitch arms	80	1,433/0	8	6	- 3.8	∞	Off
158	K_{13}-M+$H_{1.0}$/Wake studies with blades off, hub not rotating	80	0/0	8	6	- 3.8	∞	Off
159	K_{13}-M-$H_{1.0}$/Wake studies with hub off	80	0/0	8	6	- 3.8	∞	Off
160	K_{13}-M+$H_{1.0}$/Same as 158 except hub is rotating	80	1,433/0	8	6	- 3.8	∞	Off
161	K_{13}-M+$H_{1.5.2}$/Repeat of 154 without blades	80	0/0	8	6	- 3.8	∞	Off
162	K_{13}-M+$H_{1.5.3}$/Same as 161 except 4-in. gap	80	0/0	8	6	- 3.8	∞	Off
163	K_{13}-M+$H_{1.5.4}$/Same as 161 except 2-in. gap	80	0/0	8	6	- 3.8	∞	Off
164	K_{13}-M+$H_{1.5.1}$/Same as 161 except 0.5-in. gap	80	0/0	8	6	- 3.8	∞	Off
165	K_{13}-M+$H_{1.0.1}$/10-in. open hubcap no underbody, same cap vert position as Run 154	80	0/0	8	6	- 3.8	∞	Off
166	K_{13}-M+$H_{1.0.2}$/Same as 165 with cap lowered by 0.5 in.	80	0/0	8	6	- 3.8	∞	Off

TABLE 10 - Continued

Run No.	Configuration	V_{TUN} (kn)	MR/TR Speed (rpm)	Disk Ldg (psf)	Model Angles α (deg)	Model Angles ψ (deg)	MR Ht (h/d)	Tail Rotor
167	K_{13}-M+$H_{1.7.1}$/16-in. open cap, no underbody, 2 in. gap	80	0/0	8	6	- 3.8	∞	Off
168	K_{13}+$H_{1.7.1}$/Blades on, same cap config. as 167	80	1,433/0	8	6	- 3.8	∞	Off
169	K_{13}+$H_{1.7.2}$/16-in. open cap, no underbody, 4-in. gap	80	1,433/0	8	6	- 3.8	∞	Off
170	K_{13}+$H_{1.0}$+$D_{4.0}$/Extended flat top fairing on aft crown	80	1,433/0	8	6	- 3.8	∞	Off
171	K_{13}+$H_{1.7.2}$+$D_{4.0}$/Same fairing as 170 same cap as 169	80	1,433/0	8	6	- 3.8	∞	Off
172	K_{13}+$H_{1.0}$+$E_{1.0}$(0 psi)/Basic air ejector zero blowing baseline	80	1,433/0	8	6	- 3.8	∞	Off
173	K_{13}+$H_{1.0}$+$E_{1.0}$(40 psi)/Same as 172 with 40 psi supply	80	1,433/0	8	6	- 3.8	∞	Off
174	K_{13}+$H_{1.0}$+$E_{1.0}$(150 psi)/Same as 172 with 150 psi supply	80	1,433/0	8	6	- 3.8	∞	Off
175	K_{13}+$H_{1.0}$+$E_{2.5.1}$(40 psi)/Ejector with wide chord shroud at 40 psi	80	1,433/0	8	6	- 3.8	∞	Off
176	K_{13}+$H_{1.0}$+$E_{2.5.1}$(150 psi)/Same as 174 with 150 psi supply	80	1,433/0	8	6	- 3.8	∞	Off
177	K_{13}+$H_{1.5.4}$+$E_{2.5.1}$(150 psi)/Same as 176 with 10-in. cap like 163	80	1,433/0	8	6	- 3.8	∞	Off
178	K_{13}+$H_{1.0}$+$W_{1.0}$+$E_{1.1}$(0 psi)/Nacelle mounted wing	80	1,433/0	8	6	- 3.8	∞	Off
179	K_{13}+$H_{1.0}$+$W_{2.0}$+$E_{1.0}$(0 psi)/Double-slotted flapped wing	80	1,433/0	8	6	- 3.8	∞	Off
180	K_{13}+$H_{1.0}$+$W_{3.0}$+$E_{1.0}$(0 psi)/Single slotted flapped wing	80	1,433/0	8	6	- 3.8	∞	Off
181	K_{13}+$H_{1.0}$+$E_{1.2}$(0 psi)/Baseline with ejector tube moved aft	80	1,433/0	8	6	- 3.8	∞	Off
182	K_{13}+$H_{1.9.0}$+$E_{1.2}$(0 psi)/Standard 10-in. frisbee	80	1,433/0	8	6	- 3.8	∞	Off
183	K_{13}+$H_{1.9.1}$+$E_{1.2}$(0 psi)/16-in. fabricated frisbee	80	1,433/0	8	6	- 3.8	∞	Off
184	K_{13}+$H_{1.0}$+$E_{3.5.2}$(40 psi)/Wide chord with lip at 40 psi	80	1,433/0	8	6	- 3.8	∞	Off
185	K_{13}+$H_{1.0}$+$E_{3.5.2}$(150 psi)/Same as 184 with 150 psi air	80	1,433/0	8	6	- 3.8	∞	Off
186	K_{13}+$H_{1.0}$+$W_{4.0}$/Boom-mounted stub wing	80	1,433/0	8	6	- 3.8	∞	Off
187	K_{13}+$H_{1.0}$+$E_{3.5.4}$(150 psi)/Like 185 with modified shroud	80	1,433/0	8	6	- 3.8	∞	Off
188	K_{13}+$H_{1.0}$+I_1+$E_{1.0}$(0 psi)/Baseline with I_1 instr ring	80	1,433/0	8	6	- 3.8	∞	Off
189	K_{13}+$H_{1.8.1}$+$E_{1.0}$(0 psi)/Solid cap, 10-in. diam, 3.25-in. height	80	1,433/0	8	6	- 3.8	∞	Off
190	K_{13}+$H_{1.8.2}$+I_1+$E_{1.0}$(0 psi)/Same as 190 except + 4.12-in. height	80	1,433/0	8	6	- 3.8	∞	Off

TABLE 10 - Continued

Run No.	Configuration	V_{TUN} (kn)	MR/TR Speed (rpm)	Disk Ldg (psf)	Model Angles α (deg)	Model Angles ψ (deg)	MR Ht (h/d)	Tail Rotor
191	$K_{13}+H_{1.0.2}+I_1+E_{1.0}$ (0 psi)/10-in. cap, no underbody, 1.87-in. gap	80	1,433/0	8	6	- 3.8	∞	Off
193	$K_{13}+H_{1.0.2}+I_1+E_{1.0}$ (0 psi)/10-in. cap, no underbody, 1.25-in. gap	80	1,433/0	8	6	- 3.8	∞	Off
194	$K_{13}+H_{1.11.1}+I_2+E_{1.0}$ (0 psi)/7.6-in. cap, underbody, 1.25-in. gap	80	1,433/0	8	6	- 3.8	∞	Off
195	$K_{13}+H_{1.11.1}+I_2+E_{1.0}$ (20 psi)/Same as 194 with 20 psi air	80	1,433/0	8	6	- 3.8	∞	Off
196	$K_{13}+H_{1.11.1}+I_2+E_{1.0}$ (40 psi)/Same as 194 with 40 psi air	80	1,433/0	8	6	- 3.8	∞	Off
197	$K_{13}+H_{1.11.1}+I_2+E_{1.0}$ (150 psi)/Same as 194 with 150 psi air	80	1,433/0	8	6	- 3.8	∞	Off
198	$K_{13}+H_{1.11.1}+I_2+E_{4.0}$ (0 psi)/Same as 194 except blowing tube 2 in. aft	80	1,433/0	8	6	- 3.8	∞	Off
199	$K_{13}+H_{1.11.1}+I_2+E_{4.0}$ (40 psi)/Same as 198 with 40 psi air	80	1,433/0	8	6	- 3.8	∞	Off
200	$K_{13}+H_{1.11.1}+I_2+E_{4.0}$ (150 psi)/Same as 198 with 150 psi air	80	1,433/0	8	6	- 3.8	∞	Off
201	$K_{13}+H_{1.11.2}+_2+E_{4.0}$ (150 psi)/Same as 200 except center support cap	80	1,433/0	8	6	- 3.8	∞	Off
202	$K_{13}+H_{1.11.2}+I_2$/Baseline with I_2 and no blowing tube	80	1,433/0	8	6	- 3.8	∞	Off
203	$K_{13}+H_{1.0}+E_{5.0}$ (0 psi)Bifurcated air duct baseline	80	1,433/0	8	6	- 3.8	∞	Off
204	$K_{13}+H_{1.0}+E_{5.0}$ (150 psi)/Bifurcated duct with 150 psi air	80	1,433/0	8	6	- 3.8	∞	Off
205	$K_{13}+H_{1.0}+E_{5.0}$ (40 psi)/Same as 204 with 40 psi air	80	1,433/0	8	6	- 3.8	∞	Off
207	$K_{13}+H_{1.2.1}+I_1+E_{1.0}$ (0 psi)/7.6-in. solid cap, no gap	80	1,433/0	8	6	- 3.8	∞	Off
208	$K_{13}+H_{1.2.2}+I_1+E_{1.0}$ (0 psi)/ Same as 207 except 0.55-in. gap	80	1,433/0	8	6	- 3.8	∞	Off
210	$K_{13}+H_{1.15}+I_1+E_{1.0}$ (0 psi)/Repeat of 189	80	1,433/0	8	6	- 3.8	∞	Off
211	$K_{13}+H_{1.14.1}+I_1+E_{1.0}$ (0 psi)/Like 189 and 210 except cap is open	80	1,433/0	8	6	- 3.8	∞	Off

The 1/3-octave band method was developed for acoustics analysis and divides the frequency range of interest into prescribed intervals of octaves and 1/3 octaves and computes the root mean square value of the time-variant parameter over the intervals. When this is plotted as a bar chart, as in Volumes IV and VI, it facilitates comparison between configurations, which is difficult to do with the typically jagged and irregular spectrographs as are shown in Volumes VII and VIII.

The frequency range of interest extends from approximately 1Ω to 2Ω which happens to encompass four of the bars (1/3-octave bands). To obtain data for the cross plots of Volume III, these four (7, 8, 9, and 10) are averaged.

DESCRIPTION OF CONFIGURATIONS

In the sections that follow, summary graphs derived from the data plotted in Volume III are presented and discussed to provide insight into basic wake behavior and to evaluate the changes wrought by the various flow-altering devices. The order of discussion follows the same order as Volumes II through VIII and is essentially as follows:

Baseline characteristics

Effect of hubcaps and covers

Effects of air ejector systems

Effects of combined caps/ejectors

Effects of wings and miscellaneous devices

The configurations involved here are too numerous to describe in this section but are shown in detail in Appendix B. Basically, they represent attempts either to smooth the wake by introducing fresh, relatively steady air, by bringing the air around the hub more efficiently to depress the most turbulent portion below the fin and tail rotor, or by a combination of both.

BUILDUP TO BASELINE

Figures 51 and 52 show α_t and β_t respectively for the buildup from the blades off and hub off conditions to the complete rotor turning. The base case exhibits very low levels, less than 1/2 degree, for both parameters. The level becomes quite high for hub stationary or rotating. For β_t, the rotating case is somewhat worse, no doubt due to a swirl imparted by the blade shanks and retention hardware. For α_t, the reverse is true. With blades on, there is a significant improvement for both parameters – doubtless because the hub wake is displaced downward and entrained in the rotor flow. At the higher waterlines, the low-frequency turbulence approaches the rotor off level. At lower waterlines, it is approaching the blades off level. The objective of the wake attenuation program is to get as close as possible to the 1/2-degree level, the inherent bare body turbulence.

Figures 53 and 54 show the effect of engine nacelle removal on the wake parameters. An improvement in α_t is noted by nacelle off over an 8-inch distance; however, the curve crosses over at waterline 41. For β_t, a similar variation is noted.

Figures 55 and 56 compare the wake profiles behind and in front of the empennage. It is considerably worse behind it, receiving the turbulence generated by the tail rotor hub. This test

was run to determine if the tests could be run with the rake behind the tail, which would avoid physical interference with the horizontal stabilizer.

A lateral sweep was made just in front of the horizontal stabilizer, the results of which are shown in Figures 57 and 58. Figure 57 shows the lateral profiles of α_t and β_t with peak values for both occurring 8 inches to the left of the centerline, apparently the lateral center of the hub wake. Vertically these are measured at WL 37, not far from the vertical wake center, which is indicated in subsequent figures to occur at WL 39-40. This orientation of the wake is consistent with flow studies where smoke was released at the hub and its passage aft observed.

The smoke work indicated that for 80 knots and for very high descent rates such as 2,000 fpm, the wake center is aligned closely with the fin due to the negligible trim sideslip angle. Vertically it is close to the center of the tail rotor. As the descent rate is decreased, the wake center moves to the left as the trim sideslip becomes more positive and to the downside as the aerodynamic angle of attack becomes less. When the climb regime is attained, the wake is far to the left and below the stabilizer. In this position, it is no threat to the aircraft and indeed, the lateral kicks were not felt in this mode.

At speeds higher than 80 knots, the wake also moves away from the fin and tail rotor as the aircraft trim angle of attack becomes more negative and the trim sideslip becomes more positive. Thus, the problem becomes less with speed, although this trend is somewhat restrained by increasing dynamic pressure on the fin.

The sizable peaks shown on the right of Figure 57 seem anomalous in view of the smoke visualization results, as do those of the curves in Figure 58. Here, the mean values of α_t and β_t, i.e., the local values of downwash and sidewash angle, show depressions on the right side much more severe than the left. The mean velocity also shows a significant hole on the right. These remain unexplained and can only be inferred as peculiar to this particular location very close to the stabilizer. At any rate, working only with the left wake in gaging success produced successful solutions in this test and then a year later in testing for the wake problems of raised rotor.

The wake work was performed always with the tail rotor removed in order to be able to get the rake holding the hot film transducers properly positioned in the wake so as to verify that its absence would not significantly alter the wake. The effect of the tail rotor on the α_t and β_t profiles is shown in Figures 59 and 60. It is apparent that the tail rotor added turbulence to the α_t and β_t components as would be expected. However, the curve shapes are very similar, and it was concluded that it would be acceptable to continue wake work without the tail rotor.

CLIMB VERSUS DESCENT

As stated earlier, it was known from flight experience that climb was free from lateral disturbances. This trim condition is compared to the descent in Figures 61, 62, 63, and 64. Figures 61 and 62 show α_t and β_t comparison, Figure 63 shows V_{β_t} (velocity from the β probe), and Figure 64 shows the steady velocity.

It is unfortunate that additional α_t and β_t points could not be obtained for run 135, the climb case. The flat trend is believed to continue to the lower waterlines, however, as indicated by the shape of V_β in Figure 63 and the profile on steady velocity in Figure 64. The additional data

available for velocity indicates significantly lower velocity turbulence level for the climb in the comparison of Figure 63.

In Figure 64, the mean velocity profile for descent indicates the center of the wake to be about WL 40 with a large depression extending from 46 down as far as the test data went. On the other hand, the velocity for the climb case holds at values near freestream down to the bottom of the fin.

These climb/descent comparisons add more convincing evidence that the lateral upset problem is associated with wake proximity. Therefore, the solutions must either move the wake away or reduce its turbulence level.

COMPARISON OF BASELINE

On each of the subsequent graphs, which portray the effects of the various solutions, a baseline curve is shown to demonstrate the magnitude of the changes in the low-frequency turbulence levels. These baselines will vary as the simulations become more precise in the continuing effort. Figures 65 and 66 show the effect on α_t and β_t of changing the trim yaw angle from -2.0 to -3.8 degrees in recognition of this parameter's role in establishing the lateral position of the wake relative to the fin. For the majority of the runs, the wake measurements were made on the fin centerline; i.e., BL zero.

These same figures also show the effects of using better replicas of the full-scale pitch arms. The so-called stiff pitch arms had a favorable effect on β_t, cutting the turbulence by 50 percent in the lower waterlines.

Another comparison of baselines is portrayed in Figures 67 and 68 where an air ejector tube on the aft crown is shown to have little effect on α_t except at the very lowest point. On β_t it has negligible effect anywhere.

The addition of a small instrumentation ring to simulate better the flight test aircraft produced large changes in both profiles, particularly at the high waterlines, probably due to the ring's high position on the hub. The magnitude of the change is surprisingly large in view of the ring size, only 5 inches in diameter and 1/2 inch high, fitting around the existing 4-inch-diameter instrumentation canister. This highlights another aspect in the formation of the helicopter wake.

Reference 9 provides a formula for the Kaman vortex frequencies in the wake of bodies as follows:

$$f = s\frac{V}{h} \tag{1}$$

where s is the Strouhal number given as

$$s = \frac{0.21}{C_D{}^{1/2}} \tag{2}$$

9. Hoerner, Sighard F., FLUID DYNAMIC DRAG, Midland Park, New Jersey, published by the author, 1958.

Substitution yields

$$f = \frac{0.21}{C_D{}^{1/2}} \quad \frac{V}{h} \quad \text{- - - - - - - - - - - - in Hz.} \tag{3}$$

Dividing by rotor speed with both f and Ω in Hz results in

$$\frac{f}{\Omega} = \frac{0.21}{C_D{}^{1/2}} \quad \frac{V}{h} \quad \frac{2\pi R}{\Omega R} = \frac{0.66}{C_D{}^{1/2}} \quad \frac{\mu}{h/R} \tag{4}$$

for the model and test condition

$\mu = 0.2$

$h/R = 0.3$ . . . . . using fuselage width for h.

$$\text{Therefore,} \quad \frac{f}{\Omega} = \frac{0.44}{C_D{}^{1/2}} \tag{5}$$

For excrescent bodies there can be a large variation in the effective C_D from perhaps 0.2 to 1.5. This would provide a range in possible frequencies from 0.36 to 0.8 times Ω. For an h/R of 0.15, this frequency range becomes 0.72 to 1.6, and for 0.075 the range is 1.44 to 3.2 times rotor speed.

The purpose of this arithmetic is simply to show how the inherent sizing of helicopter fuselages and of the attached bodies, components, and excrescences lends itself to the generation of wake frequencies in the low rotor multiples. Only with very detailed investigation is it possible to pinpoint the source of specific frequencies in the wake. It is probable that some of the wake content is due to interactions between rotor wake and body wakes, which makes the analysis even more challenging.

EFFECT OF SOLID HUBCAPS

Figures 69 and 70 show the effect of solid hubcaps on α_t and β_t. The solid caps tested had the concavity filled so that the underside was flat. Results are shown for caps with zero and 0.55-inch air gap between the bottom surface and the instrumentation canister. The zero gap configuration shows excellent results for α_t but it is worse than the baseline for β_t. The opposite is true with the 0.55-inch gap configuration.

EFFECT OF OPEN HUBCAPS WITHOUT UNDERBODY

The notion of using a hollow cap to form a flow vane function was considered, and a number of configurations were tested. Figures 71 and 72 show the results for a 10-inch-diameter open cap for three values of gap. The largest gap seems best for α_t in the region between WL 45 and 49. The curves cross over, and below WL 45 the smallest gap is superior. The same thing happens for β_t, although the 1.87 curve may prove to be the least at locations below WL 43.

The 16-inch-diameter caps were also tried out for 2- and 4-inch gaps as shown in Figures 73 and 74. The 4-inch gap proved best for both α_t and β_t. The α_t variation here is significantly

improved over the best provided by the 10-inch cap of Figure 71. The β_t profile is a little better here than with the 10-inch cap, but this trend toward the low waterline is uncertain with a point missing at WL 43.

EFFECT OF OPEN HUBCAPS WITH UNDERBODY

It was suggested that a smoother passage of air would be facilitated by a fairing directly on top of the hub, covering the instrumentation canister. A number of configurations of the open cap with the lower cap or underbody were therefore tested.

The first of these was a 7.6-inch-diameter cap with a 1.25-inch gap, as shown in Figures 75 and 76. The β_t profile is not as good as that of the solid cap of Figure 69, the only 7.6-inch configuration previously tested. β_t of Figure 76 exhibits a concave downward slope at the low end of the curve approaching the wake center compared to the steep upward trend of Figure 70 for the solid cap.

Those runs were followed by a series to investigate use of the underbody with a 10-inch-diameter open cap. Figures 77 and 78 show results for a 10-inch-diameter open cap with underbody for a 1.25-inch gap and a special case where aft crown strakes were installed. This arrangement comprised three parallel longitudinal strakes 1 foot in length, which were 1 inch high at the front and 2.25 inches high at the back. This installation was an attempt to inhibit separation of the flow and to act as a straightener.

Figure 77 shows the best curve for α_t thus far for any diameter cap, bending in a way so as to peak at the wake center slightly over 2 degrees. The strakes have a small adverse effect here. Figure 78 similarly shows β_t as superior to its counterpart. The strakes here have a small but favorable effect on the low end.

Blades-off tests were conducted using the same configuration of cap to determine if its favorable effect was apparent on the hub flow with or without the rotor flow. If so, testing could proceed with the simplified technique of using no blades. Figures 79 or 80 confirm the notion of the hub flow cleanup for both α_t and β_t. However, the blades themselves cause as great a cleanup (compare with Figures 77 and 78) for all locations, except at WL 43 in the case of α_t and without exception for β_t. The rotor wake also causes the hub wake center to move down from the vicinity of WL 46 to the area of WL 40. The conclusion here was that, although the effects of devices were apparent in a similar sense with or without the blades, the rotor has an effect by itself equal to or greater than the devices. Since the interactions between rotor and devices are not completely understood, it was felt prudent to continue with the rotor on for all work. It will be noted that a 1.25- or 2.0-inch gap appears best with or without the rotor.

EFFECT OF AIR EJECTOR SYSTEM

A considerable volume of pressurized air was dumped overboard on the YUH-61A aft crown. This primarily represented the exhaust of the transmission cooling system. A scheme of wake improvement was proposed that would apply this air to an ejector to entrain the turbulent flow behind the hub, mixing it with fresh, relatively steady air and then deflecting it downward. This was tested with various shroud geometries and air pressures. The principal results are shown

in Figures 81 and 82 for the baseline and various shrouds with 150 psi, the maximum used. The associated mass flow provided an order of magnitude scaled equivalently to the full-scale potential for this use.

An examination of Figures 81 and 82 reveals the wide-chord shroud as probably the best overall variant. It produces a concave downward trend at the lower waterlines for both α_t and β_t and was clearly superior for α_t. The bifurcated duct is better for β_t for a short interval, but it trends steeply upward at the low end.

EFFECTS OF COMBINED CAP AND EJECTOR

It was expected that the separate favorable effects might be additive if the cap and the ejector were installed on the same configuration. This approach was attempted using a 7.6-inch-diameter open cap like the one of Figures 75 and 76, and the air ejector. Figure 83 indicates a favorable effect on α_t with 20 psi air. Unfortunately the α probe was inoperative for the 150 psi run. However, a negligible effect is apparent on Figure 84 for β_t with 20 psi or 150 psi air. The test was repeated with the air tube moved 2 inches aft, which produced a measurable effect for α_t and β_t at WL 43 as shown in Figures 85 and 86.

A combined configuration using a 10-inch-diameter cap was also evaluated, but with only minimal improvement. The combination approach was then abandoned, since the hoped-for dramatic change making worthwhile the configuration complexity never materialized.

CRITIQUE OF WAKE INVESTIGATION

This was the first time at Boeing Vertol and probably anywhere in the helicopter industry that a systematic attempt to modify the wake dynamics had been attempted using a full powered model and precision flow measurements. There is next to nothing published in this technical area, either on the real structure of the dynamic wake or on related testing methodologies. Consequently, new ground was being broken all the way and the test team had to do a lot of guessing. There were some mistakes, misdirections, and inefficiencies, but a great deal was learned and much was accomplished.

The initial recommendation for flight evaluation was the scaled-up 10-inch-diameter open cap with underbody as the prime configuration (Figures 77 and 78), and an air ejector system with a bifurcated shroud (Figures 81 and 82). It was decided to start with a 7.6-inch (37 inches full scale) open cap without underbody with the objective of the lowest possible weight penalty. Fortunately this worked quite well and reduced the 5-Hz intermittent pilot lateral seat accelerations to the 0.02-g level all the way down to a 2,000-foot-per-minute rate of descent. With pilot comments of "not noticeable" in level flight and merely "light" at the high rates of descent, the problem was pronounced solved.

This was especially gratifying to the wind tunnel team members, because the apparent improvement in the model results with the best configurations was not large and the objective of the 1/2- to 1-degree level was not attained. It was very difficult, using devices, to depress the wake significantly or to attenuate its low-frequency elements. It is probably necessary to work with the basic fuselage sizes and contours, the hub size, the distances between rotor and fuselage

and between other elements, and perhaps the parameters of the rotor itself to make the changes needed to attain the 1/2-degree level.

The question remains as to why the modest improvement from the wind tunnel in its flight test implementation produced a completely effective solution to the lateral upset problem. The answer may lie in the nonlinear nature of the force changes. At any waterline on the fin, the force change will be proportional to the difference in the product of the flow angle times the local velocity squared:

$$\Delta F_{fin} \sim (\beta + \Delta\beta)\ (V + \Delta V)^2 - \beta V^2. \tag{6}$$

The change as a fraction of the initial force

$$\frac{\Delta F_{fin}}{\beta V^2} = \frac{(\beta + \Delta\beta)\ (V + \Delta V)^2}{V2} - 1 \tag{7}$$

which expands to

$$\frac{\Delta F_{fin}}{\beta V^2} = \frac{\Delta\beta}{\beta} + \frac{2\Delta V}{V} + \frac{(\Delta V)^2}{V} + \left(\frac{2\Delta V}{V}\right)\left(\frac{\Delta\beta}{\beta}\right) + \left(\frac{\Delta V^2}{V}\right)\left(\frac{\Delta\beta}{\beta}\right) \tag{8}$$

Each of the elements is time-dependent and can be expressed as a trigonometric series in Ωt, or in ζt where ζ is arbitrary. The evaluation of the fin force change is, therefore, not straightforward, and it is evident that the consideration of only $\Delta\beta$ in abbreviated harmonic representation (β_t) as was done for these tests will not be adequate to evaluate the force change. It suggests that the proper way to conduct a test of this type is to measure dynamically the force change either on the fin or on the tail rotor. Strain gage equipment is adequate for this purpose. The area of concern will be the dynamics of the model fin structure, its mounting and connections, and of the balance itself. Normally, in working prototype or production aircraft problems one must accept existing models and their balances.

In the reported test it was determined that several structural frequency modes of the empennage balance lay near 1Ω. While this would provide a system very receptive to disturbances, similar to the real empennage, its unknown amplifications made it unacceptable in gaging the reduction of the forcing function. Due to lack of development time, this approach was not adopted for this test. The approach taken of monitoring the wake angles did result in successful hardware on the full-scale aircraft. However, a simpler solution may have resulted from an approach working directly with fin or tail rotor force.

Future powered models should be modularized to permit easy insertion of special hardware for dynamic/aerodynamic load testing of the empennage.

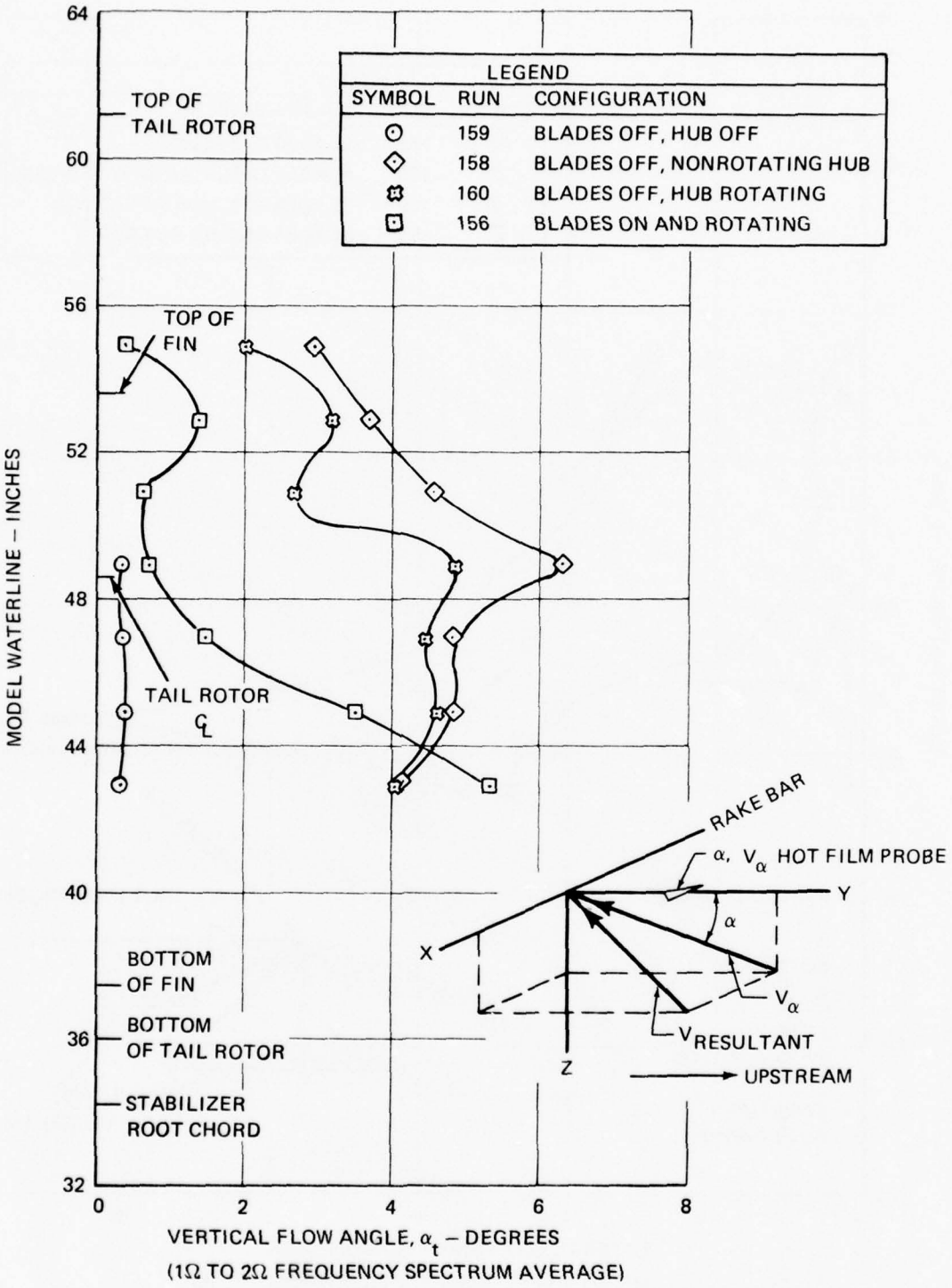

Figure 51. Buildup to Baseline for Vertical Flow Angles.

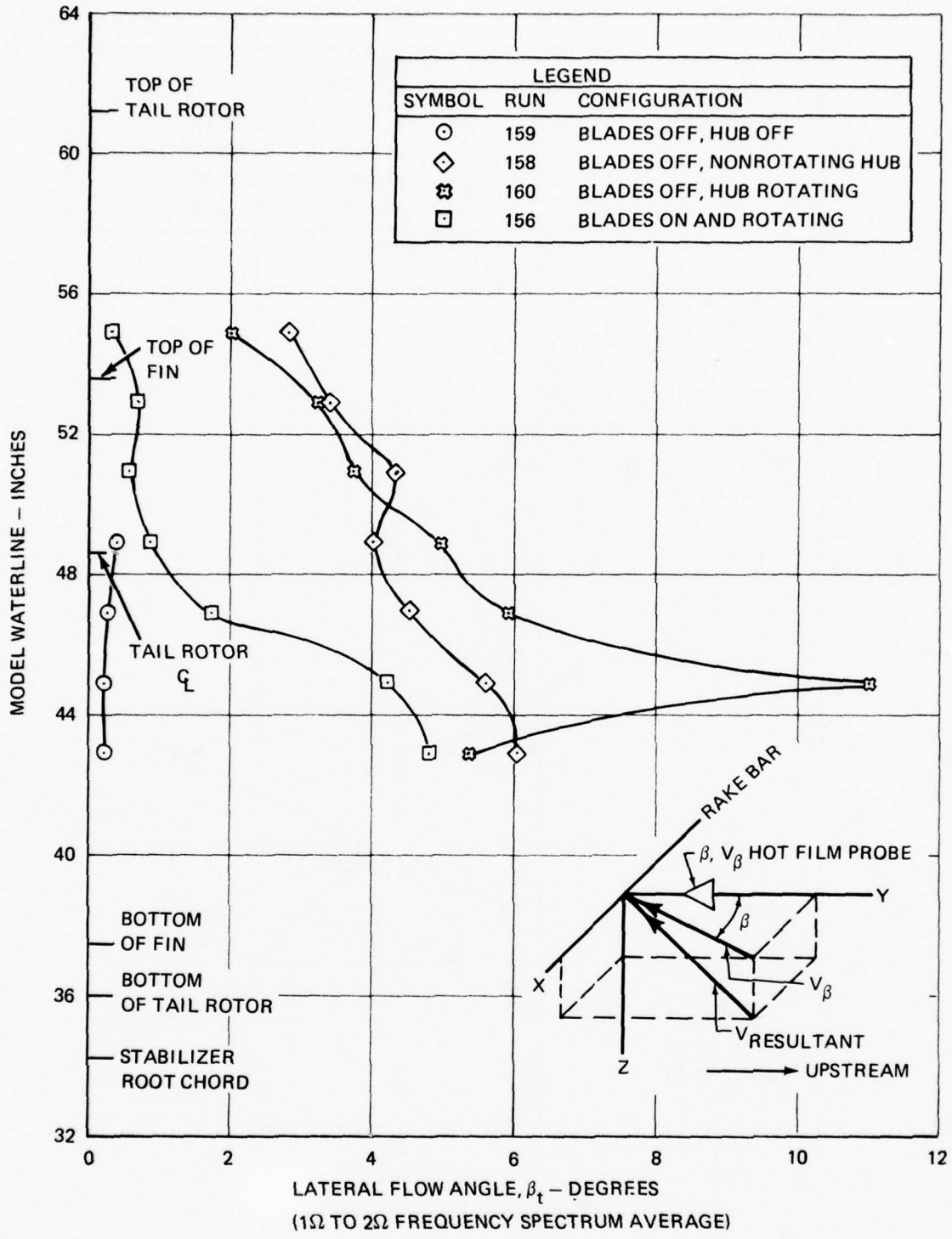

Figure 52. Buildup to Baseline for Lateral Flow Angles.

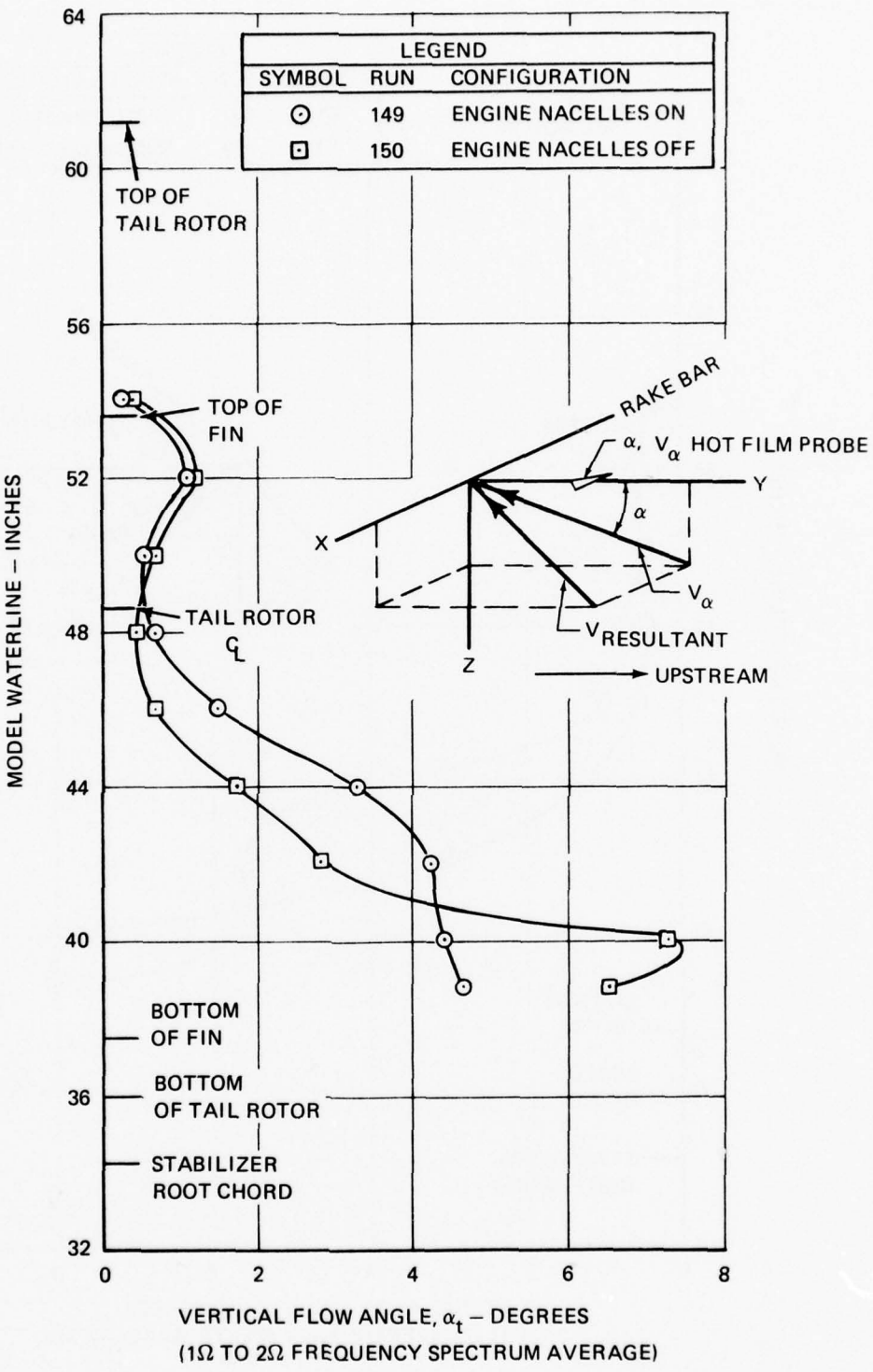

Figure 53. Effect of Engine Nacelle Removal on Vertical Flow Angles.

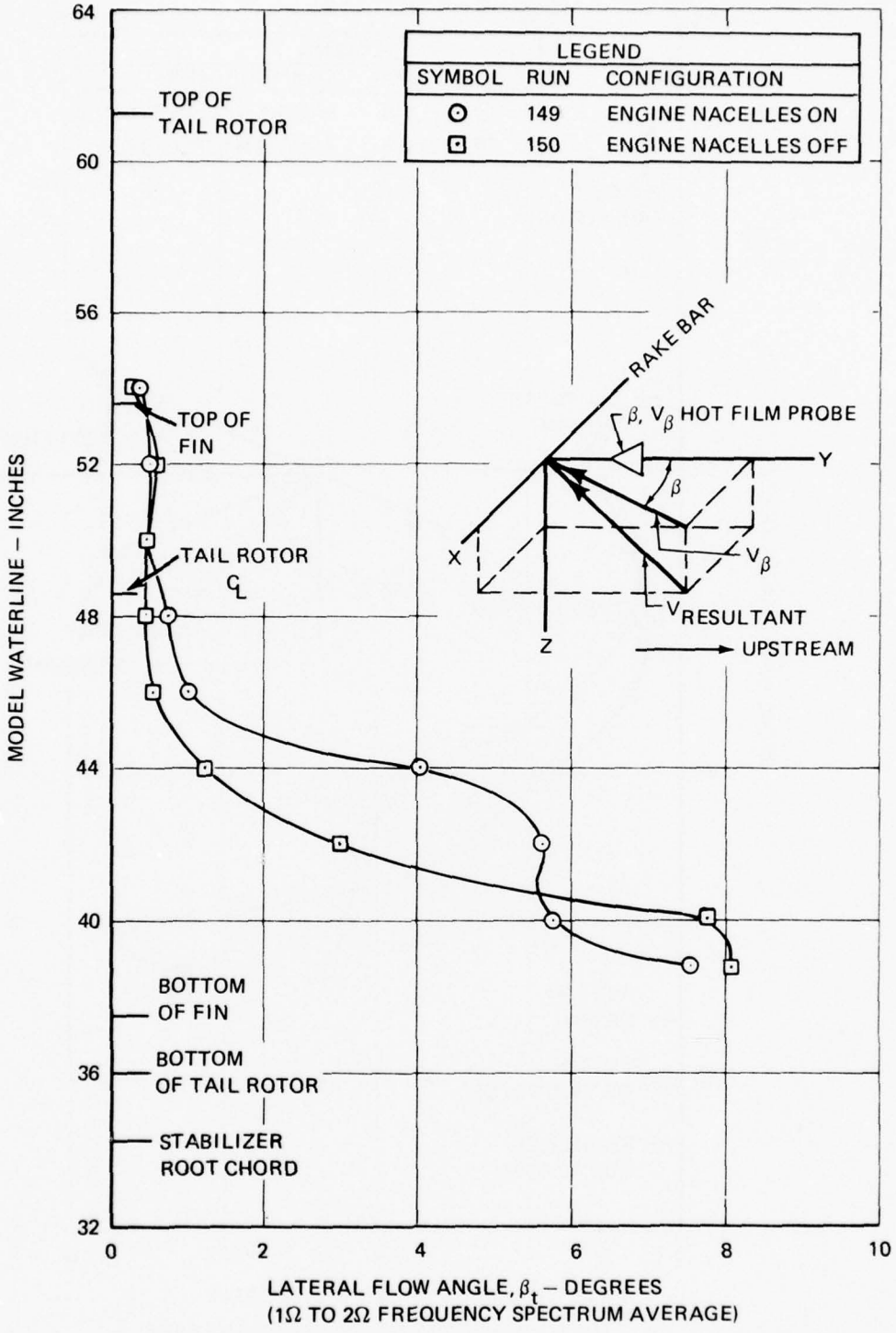

Figure 54. Effect of Engine Nacelle Removal on Lateral Flow Angles.

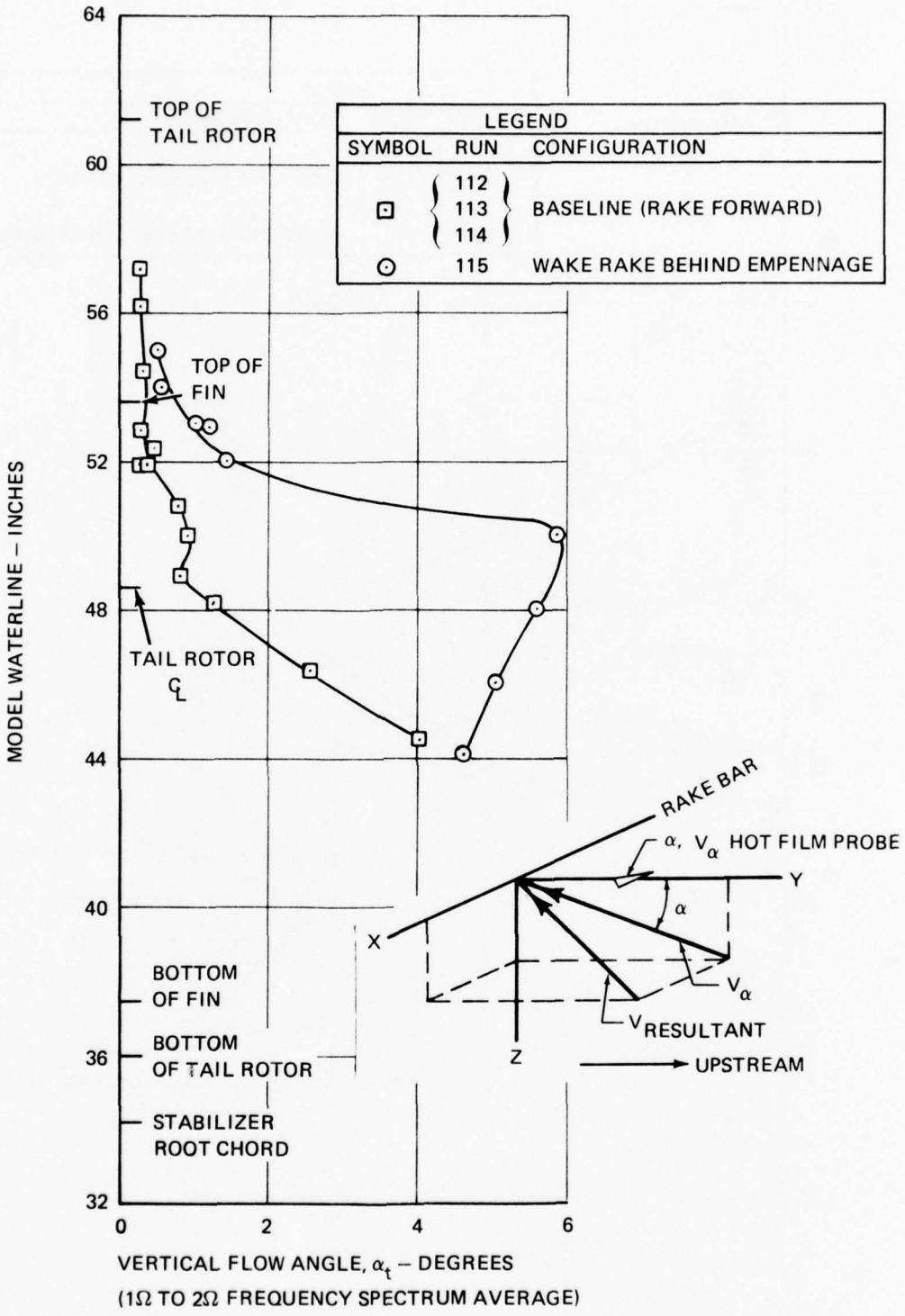

Figure 55. Wake Behind and in Front of Empennage – Vertical Flow Angles.

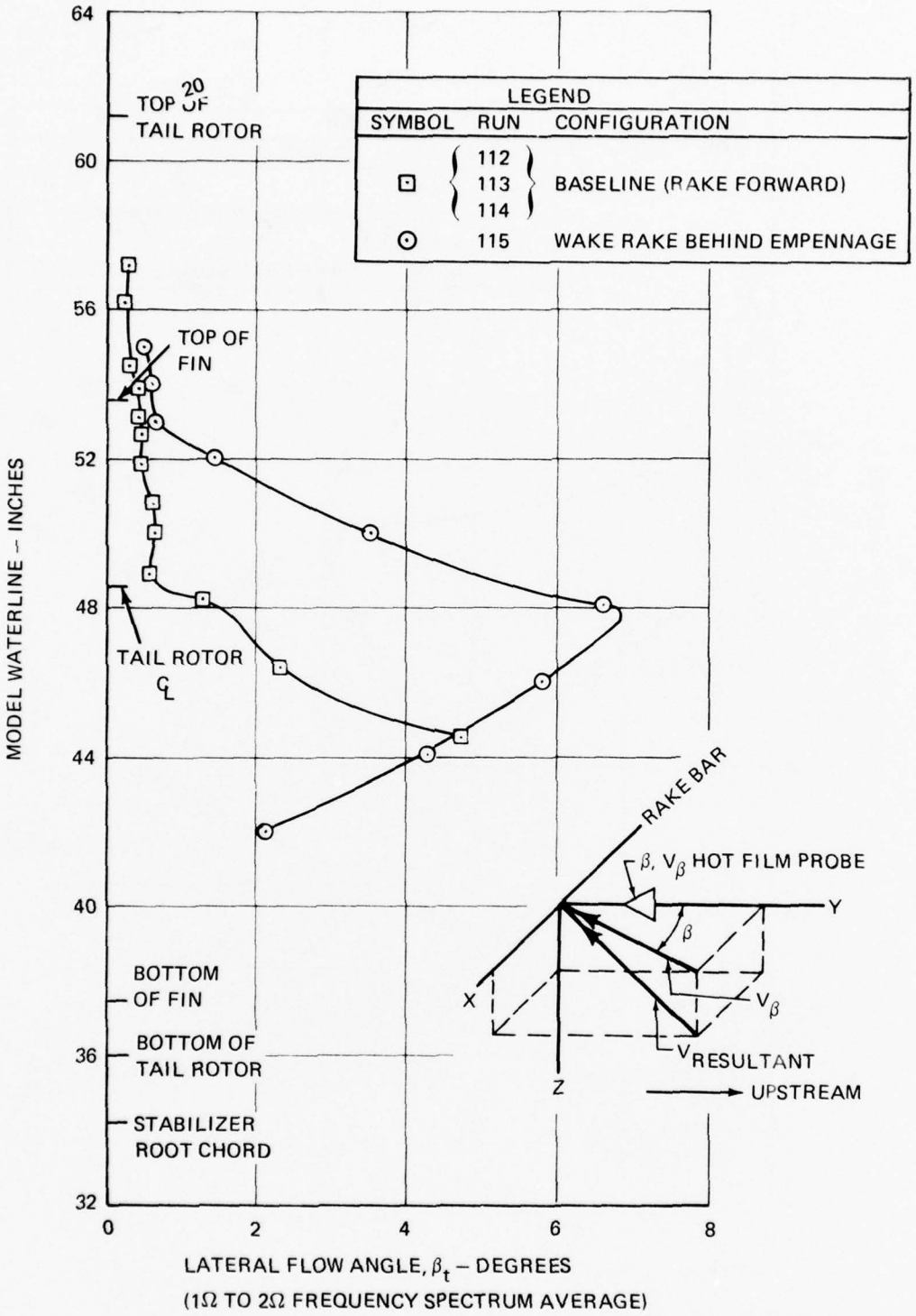

Figure 56. Wake Behind and in Front of Empennage – Lateral Flow Angles.

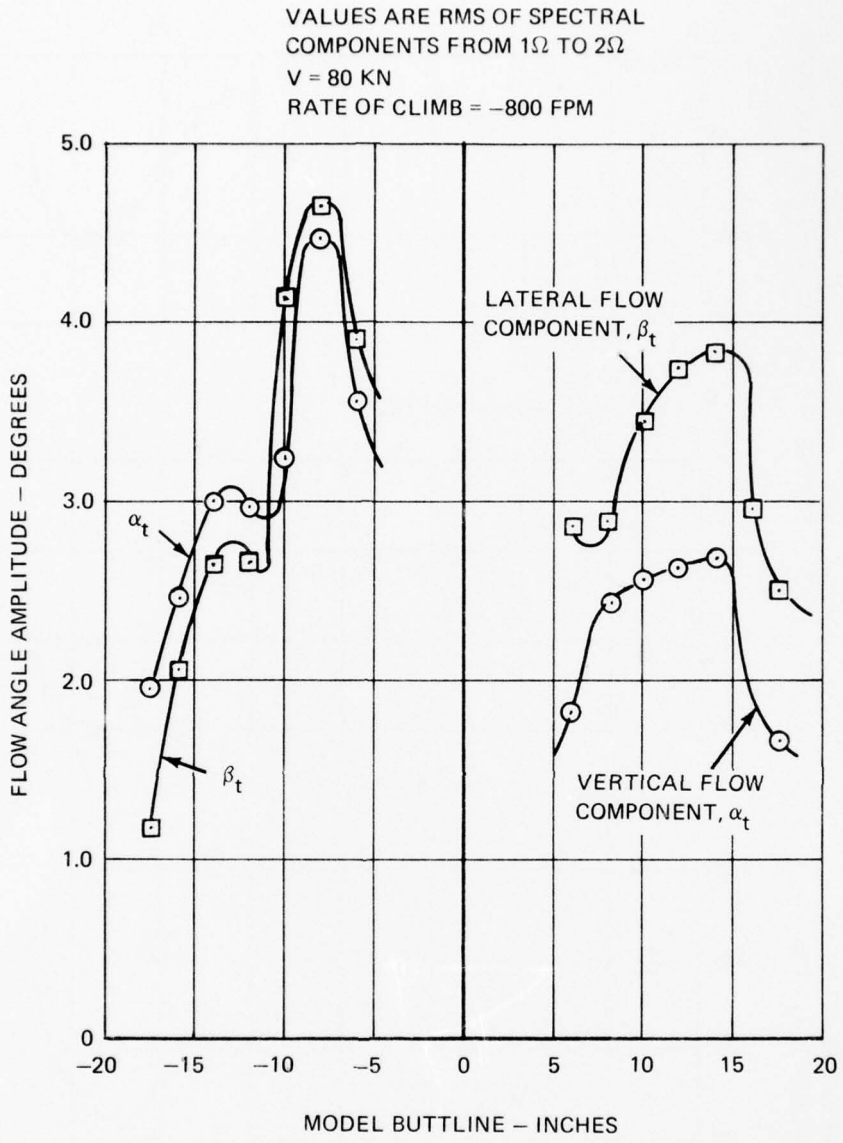

Figure 57. Lateral Variation of Low-Frequency Turbulence in Front of Stabilizer.

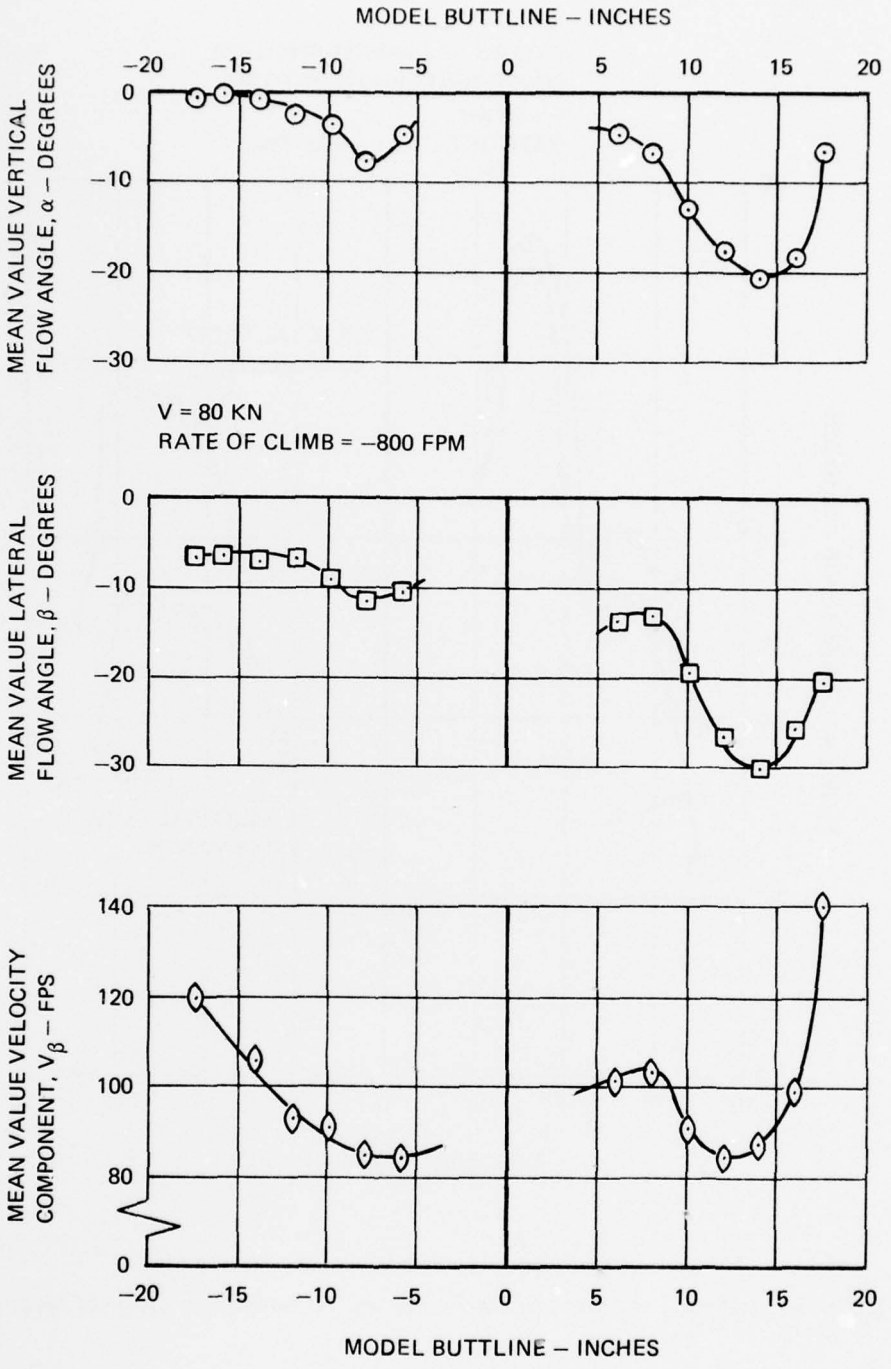

Figure 58. Lateral Variation of Wake Steady Values in Front of Stabilizer.

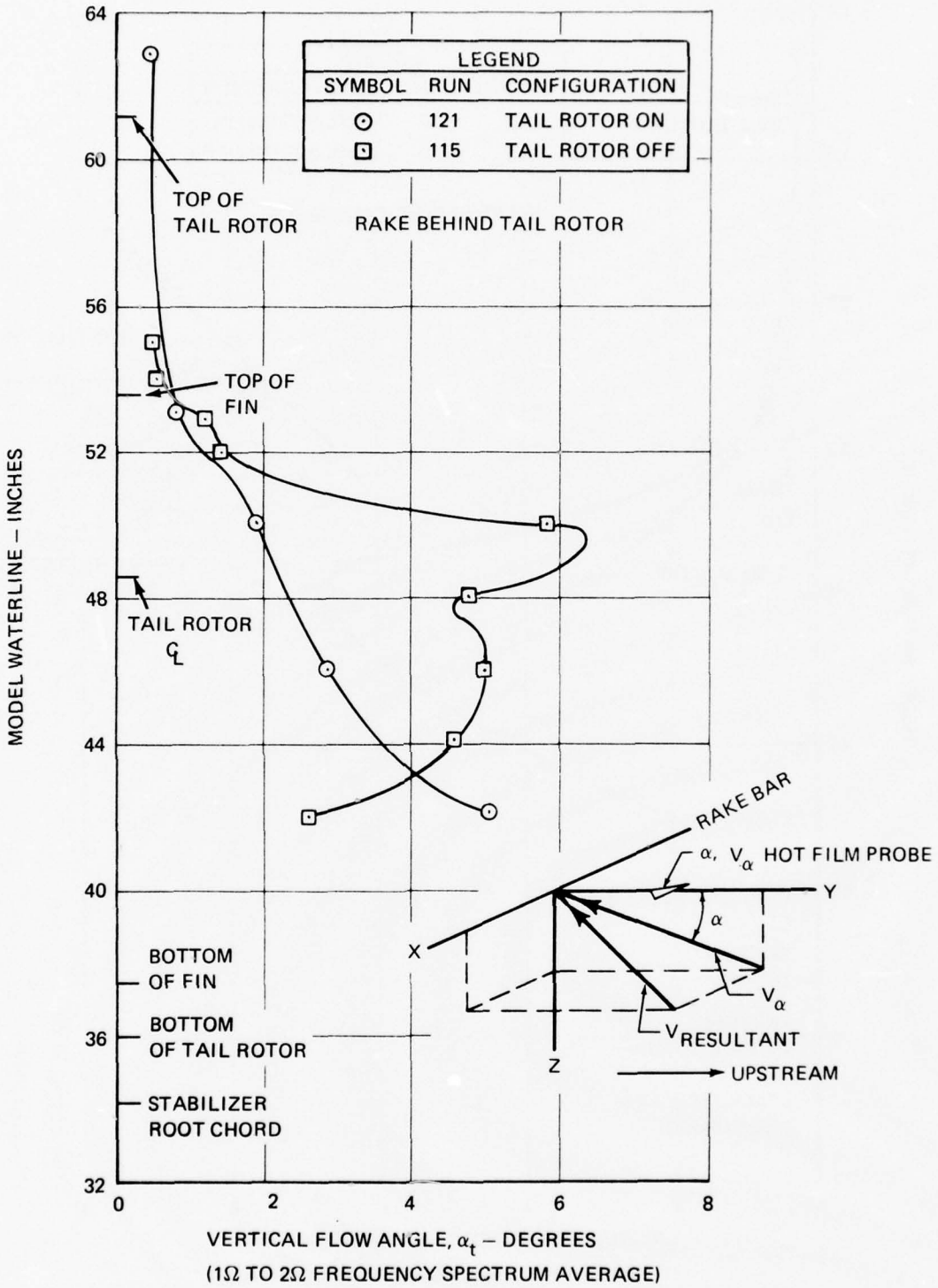

Figure 59. Effect of Tail Rotor Presence on Vertical Flow Angles.

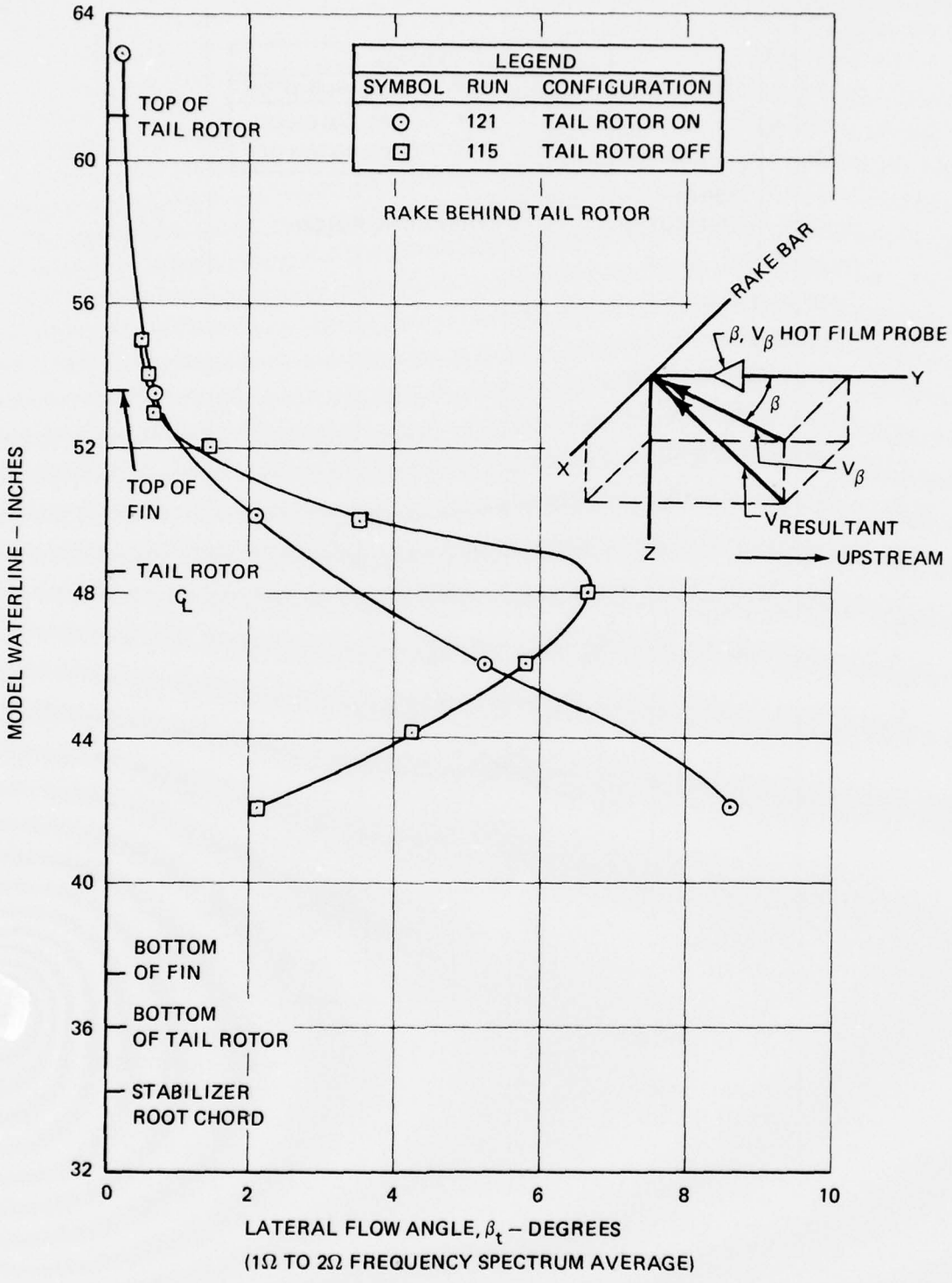

Figure 60. Effect of Tail Rotor Presence on Lateral Flow Angles.

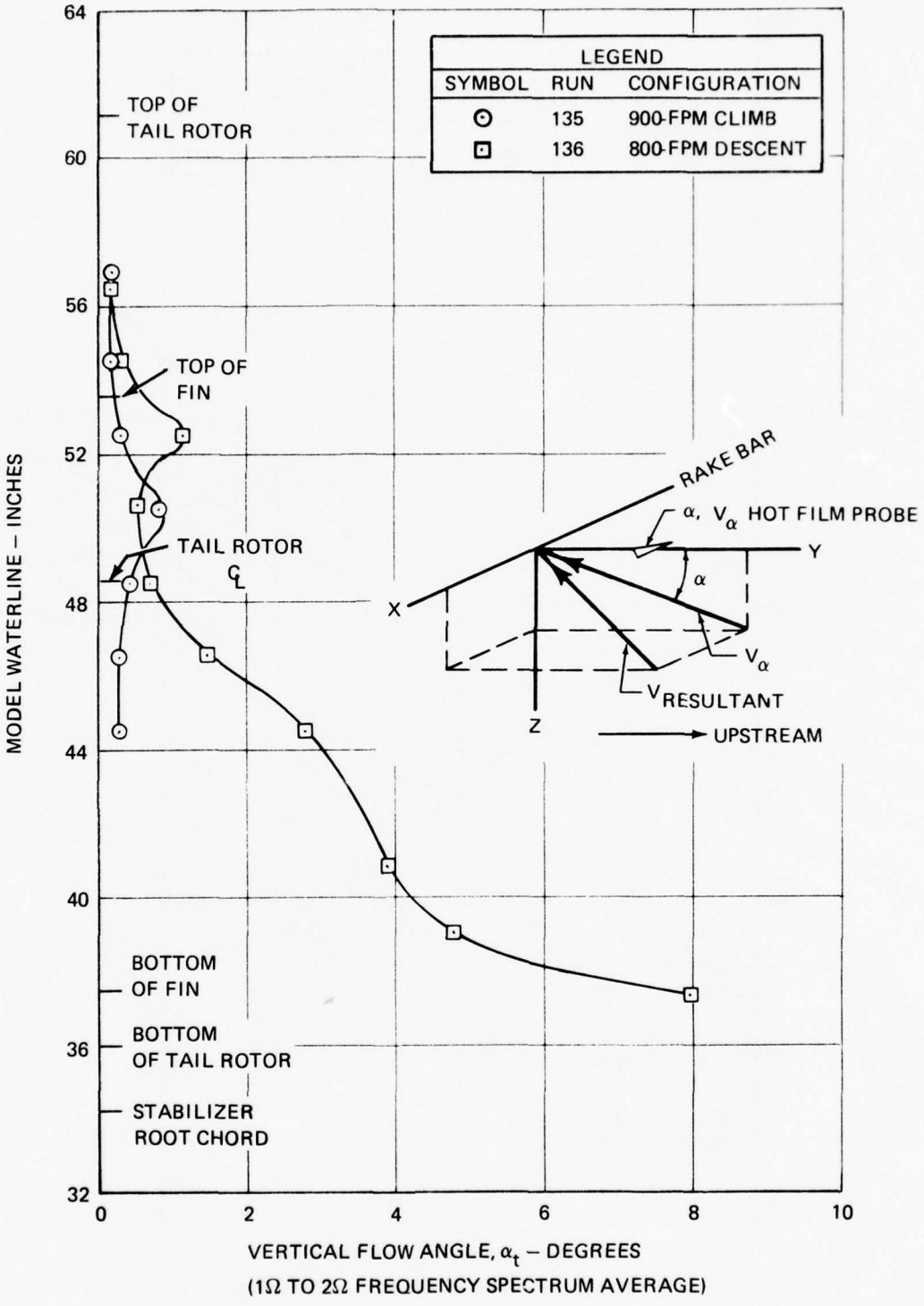

Figure 61. The Wake in Climb and Descent – Vertical Flow Angles.

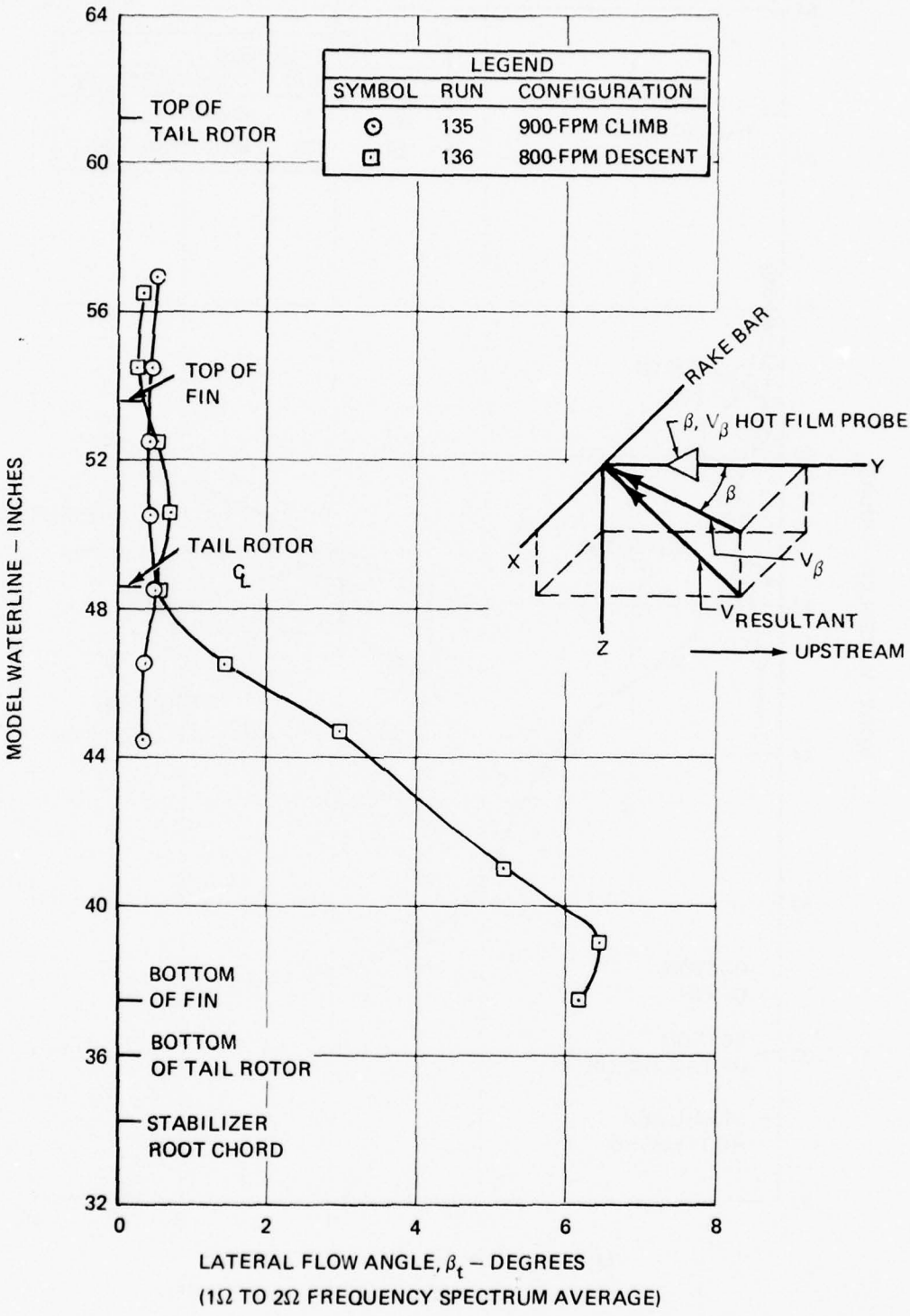

Figure 62. The Wake in Climb and Descent – Lateral Flow Angles.

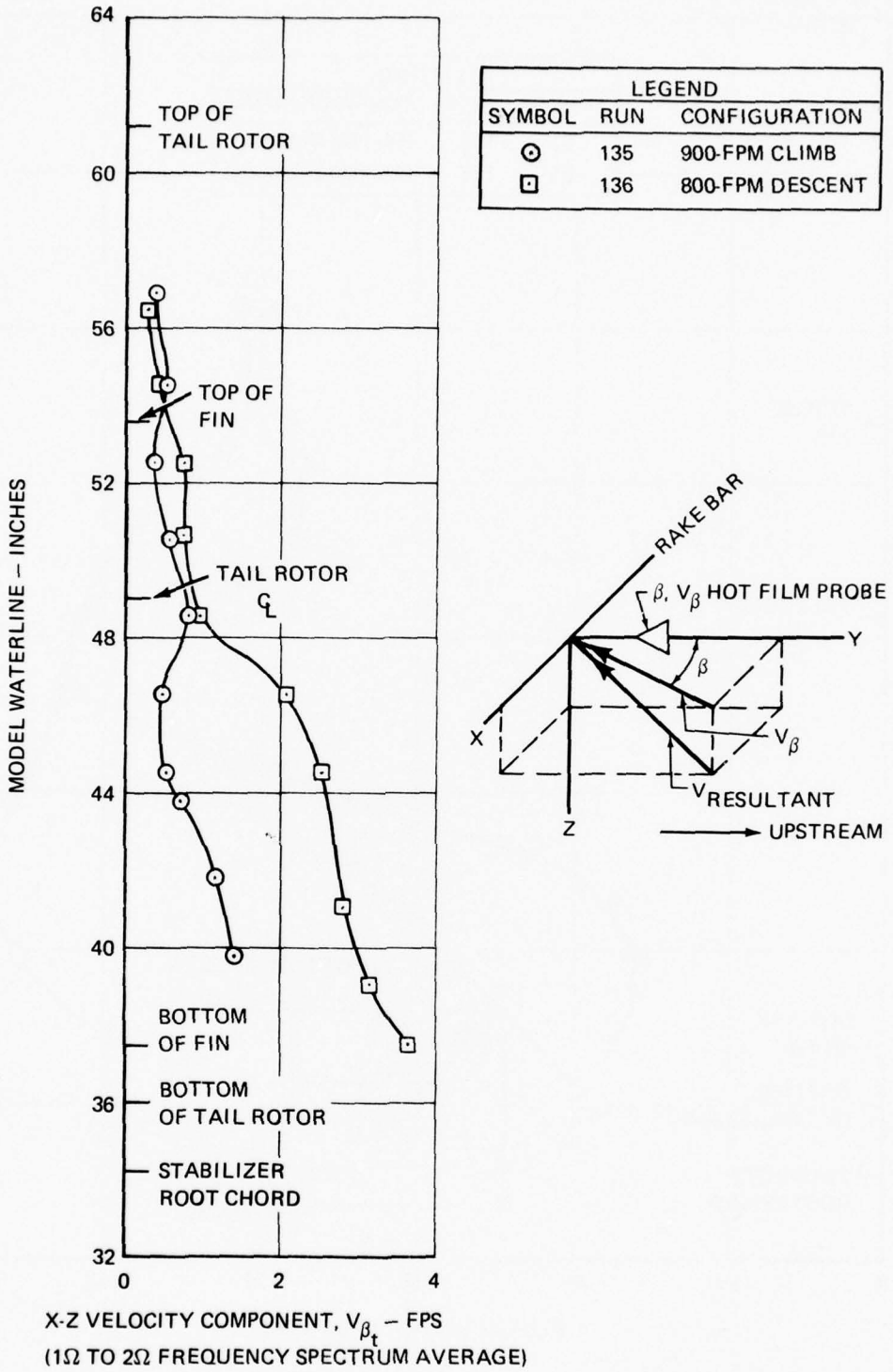

Figure 63. The Wake in Climb and Descent – Unsteady Velocity Components.

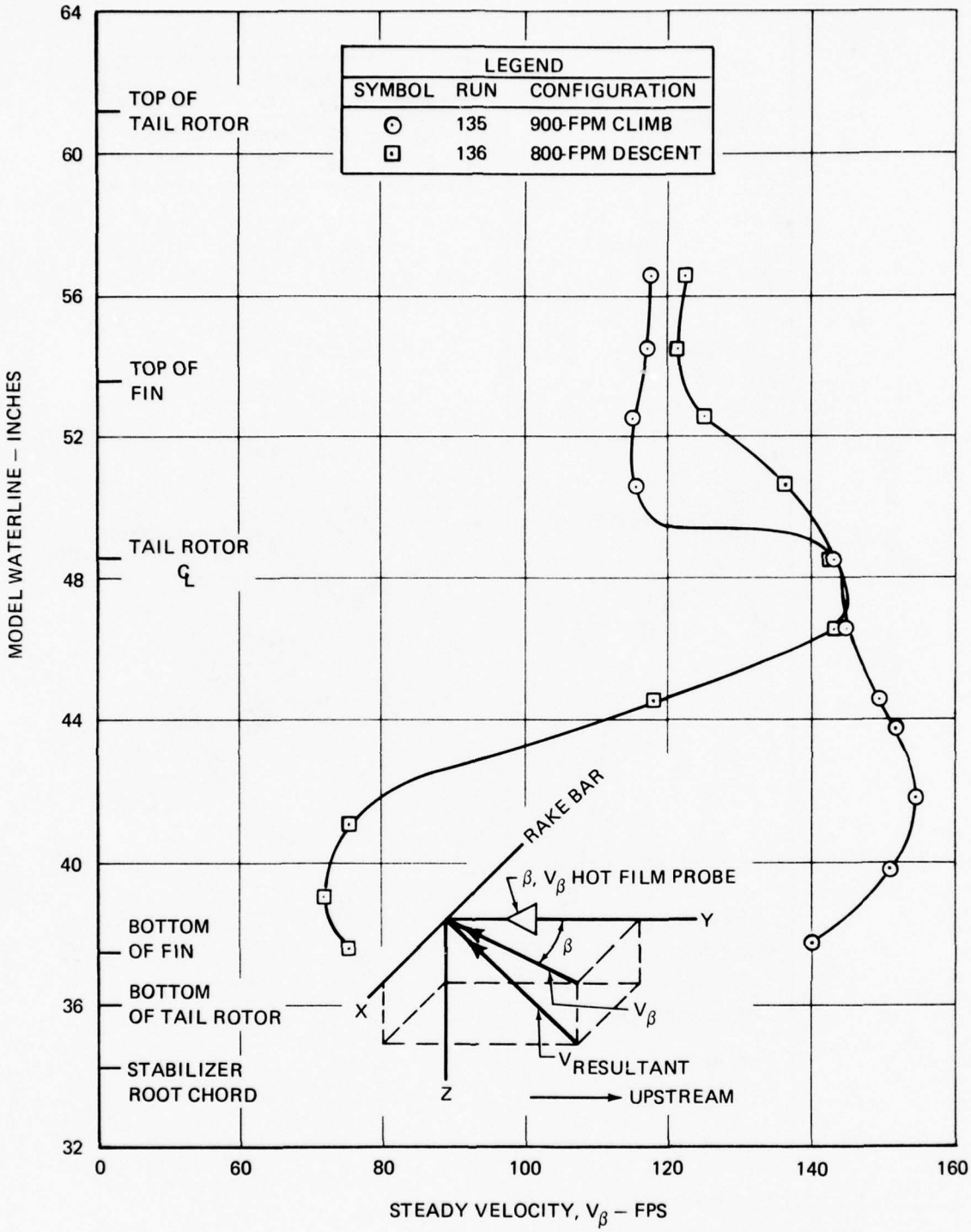

Figure 64. The Wake in Climb and Descent – Steady Wake Velocities.

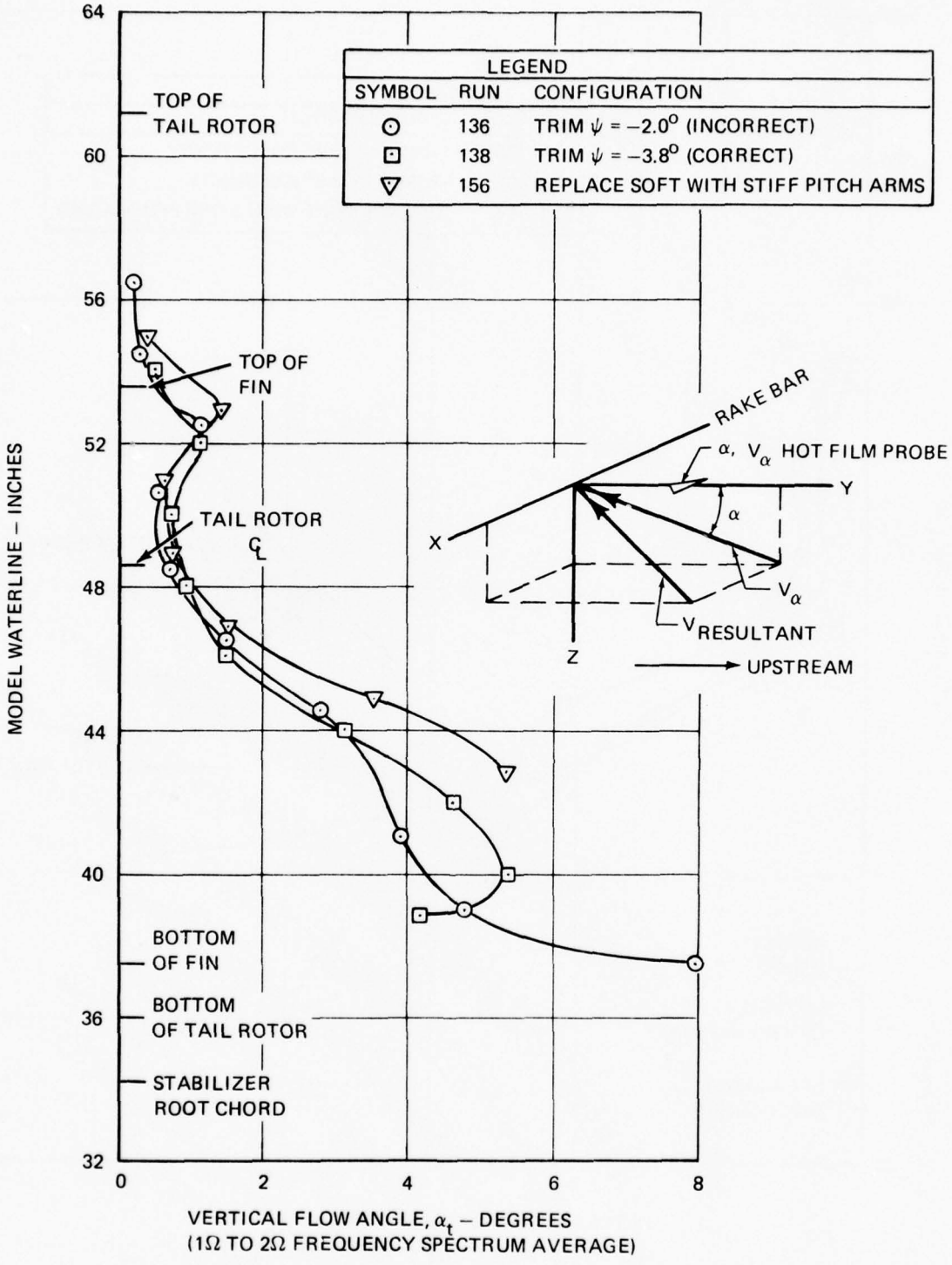

Figure 65. Comparison of Baselines – Vertical Flow Angles.

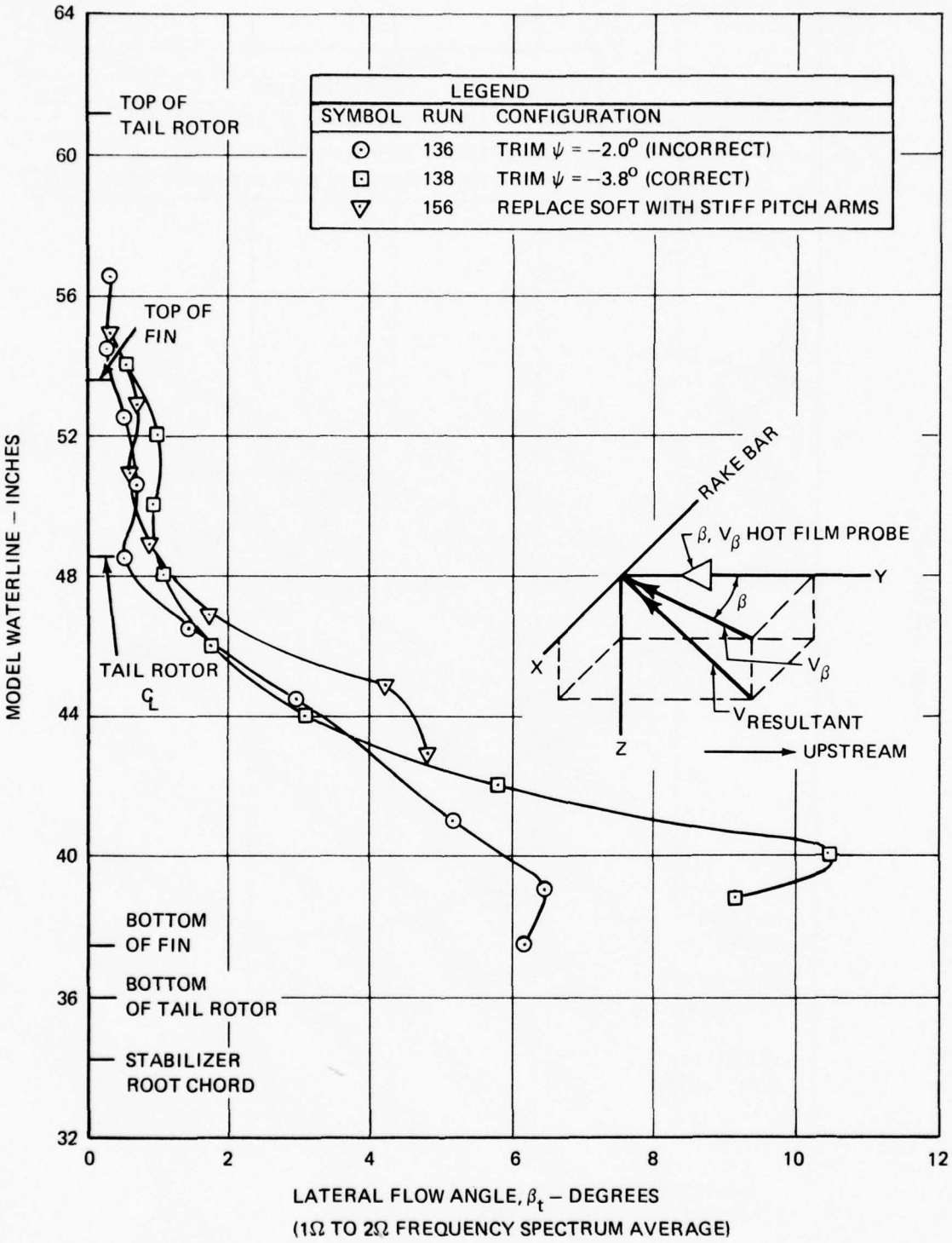

Figure 66. Comparison of Baselines – Lateral Flow Angles.

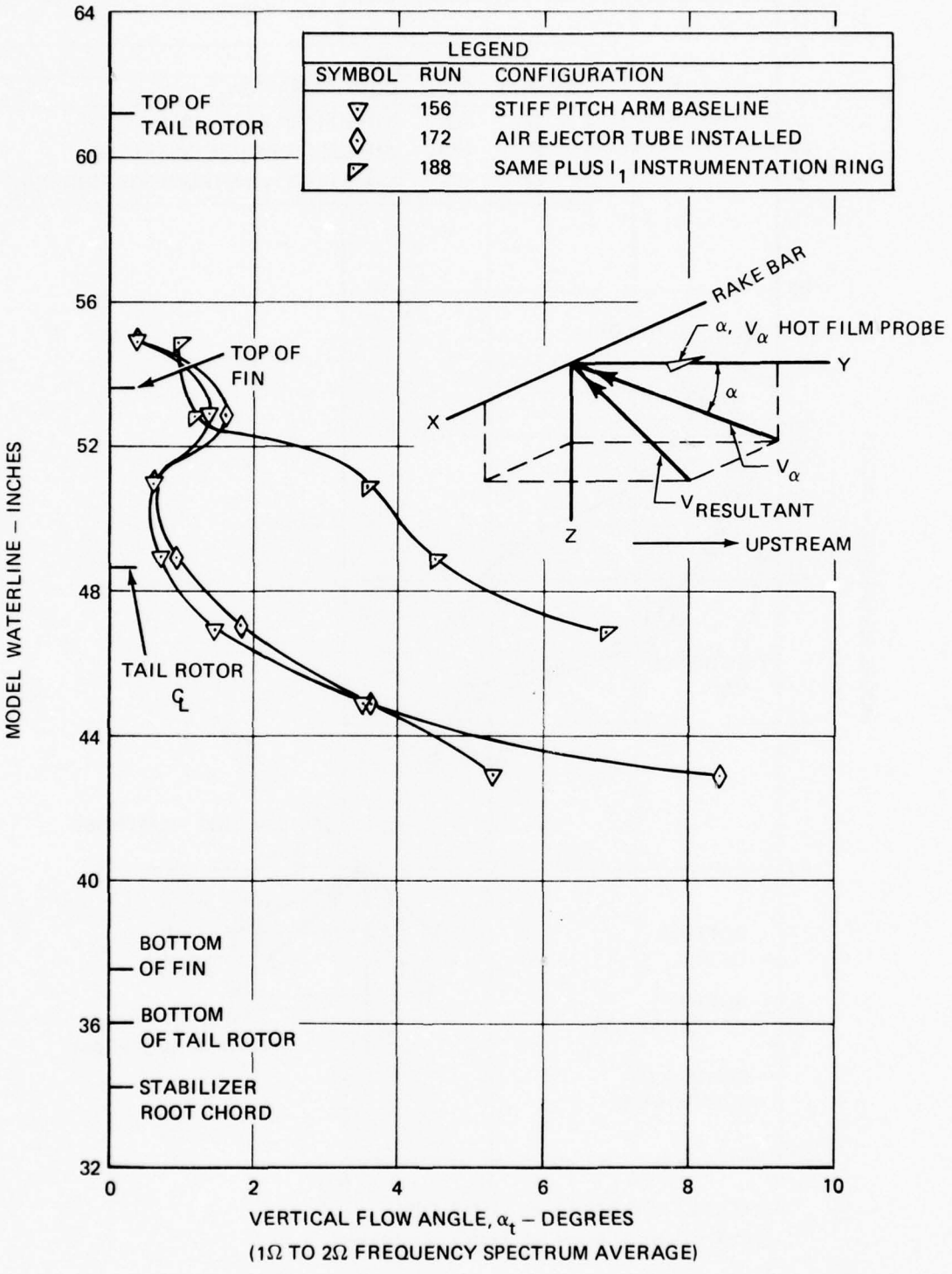

Figure 67. Comparison of Baselines – Vertical Flow Angles.

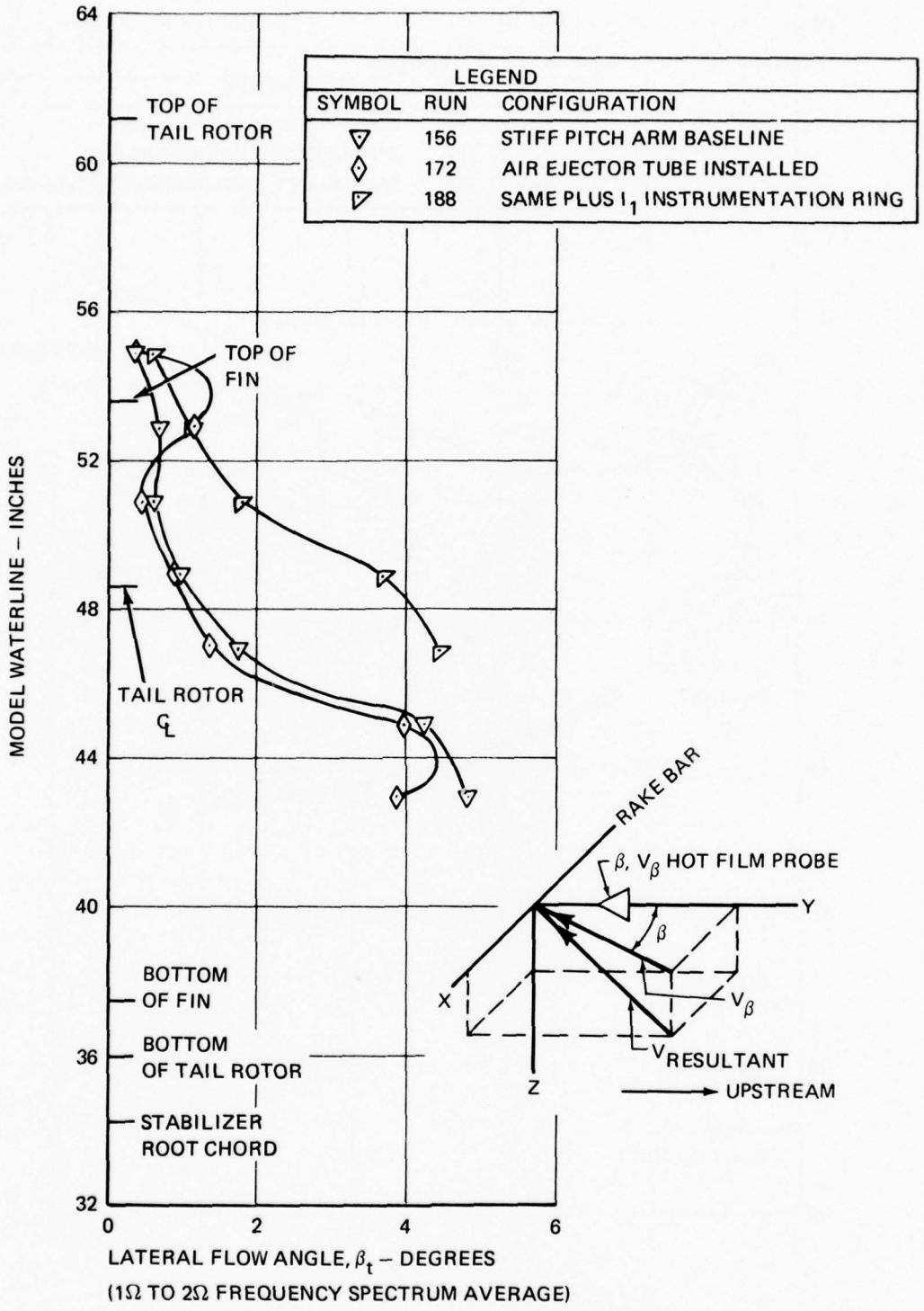

Figure 68. Comparison of Baselines – Lateral Flow Angles.

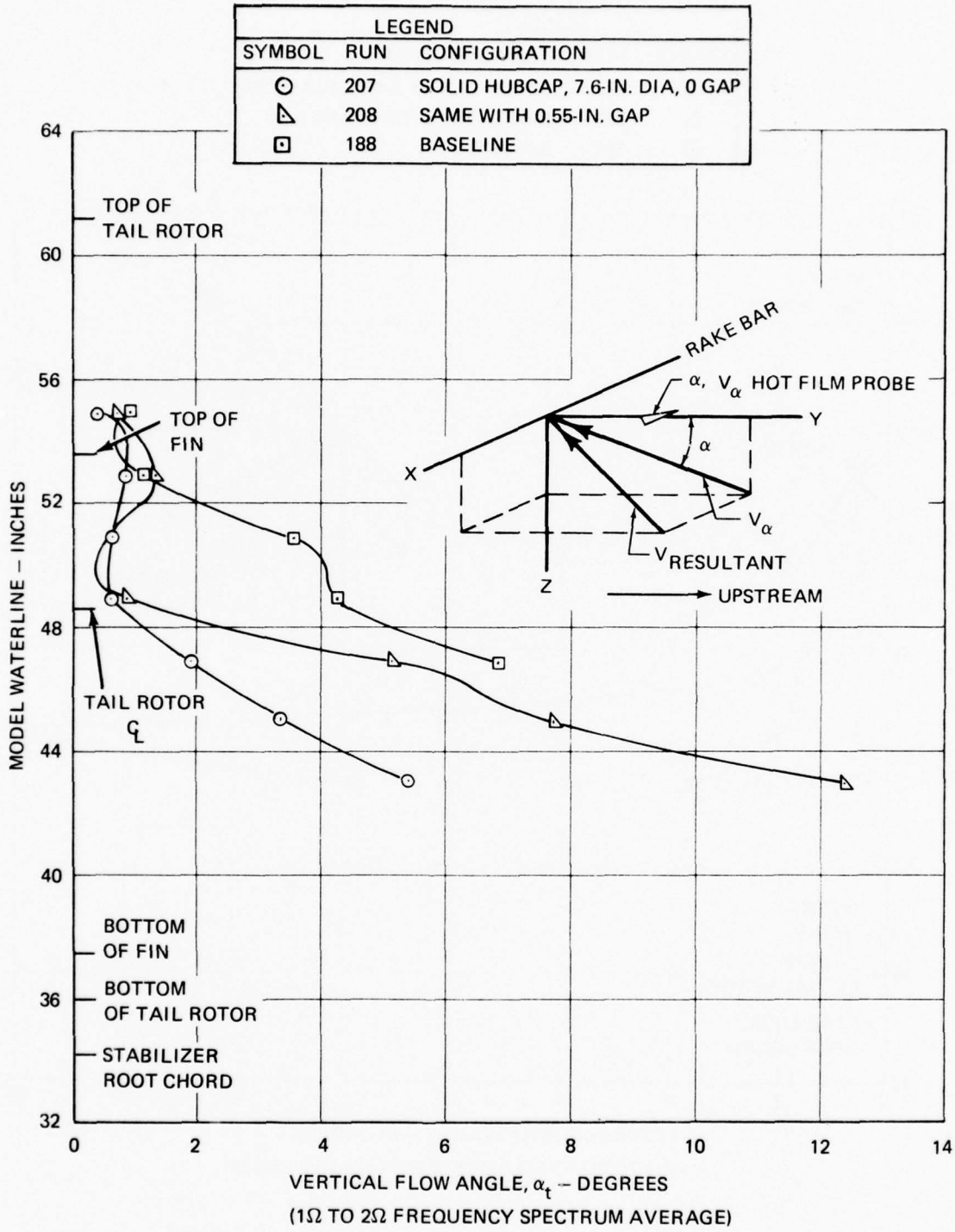

Figure 69. Effect of Solid Hubcaps on Vertical Flow Angles.

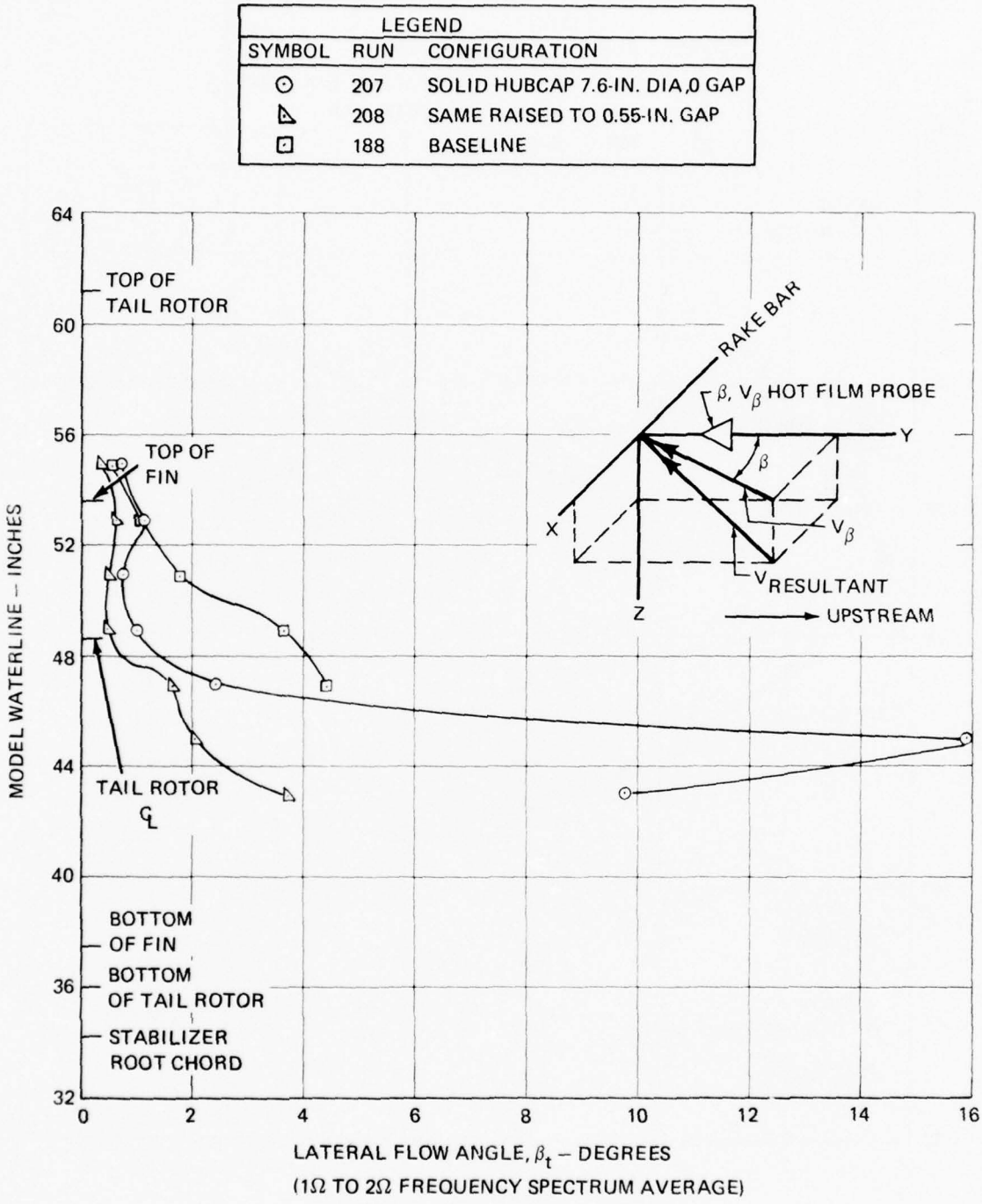

Figure 70. Effect of Solid Hubcaps on Lateral Flow Angles.

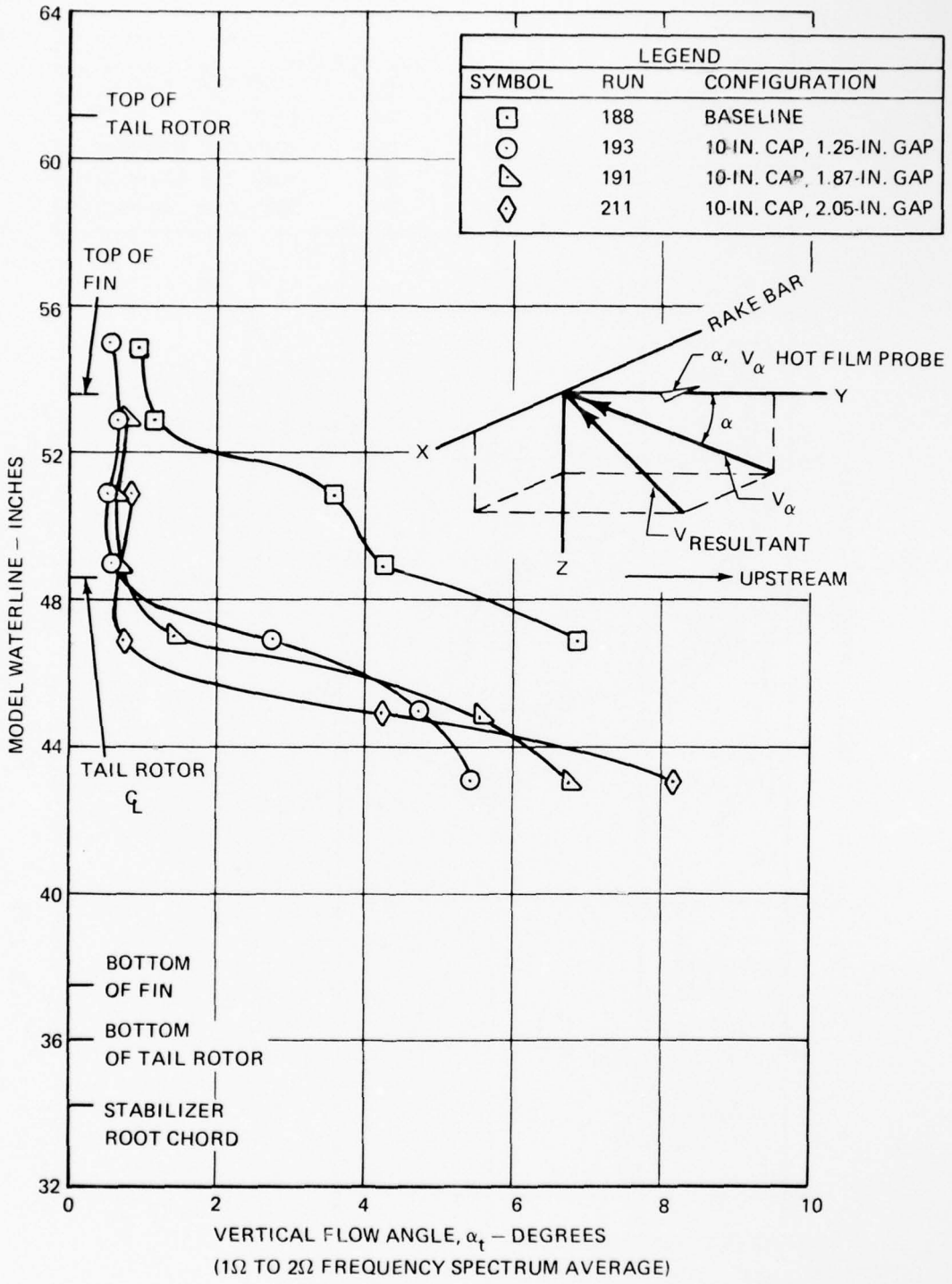

Figure 71. Effect of Open Hubcaps Without Underbody on Vertical Flow Angles.

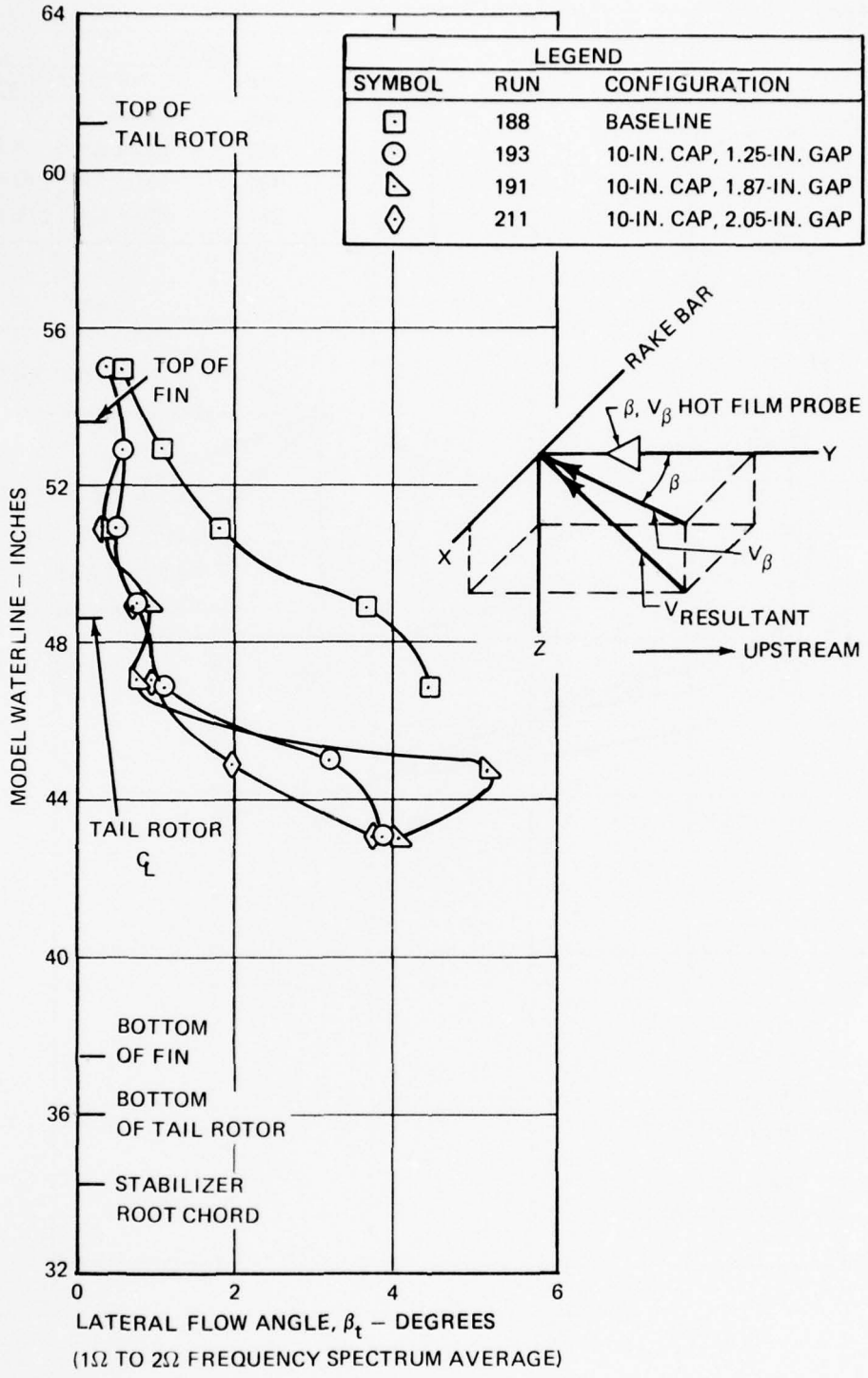

Figure 72. Effect of Open Hubcaps Without Underbody on Lateral Flow Angles.

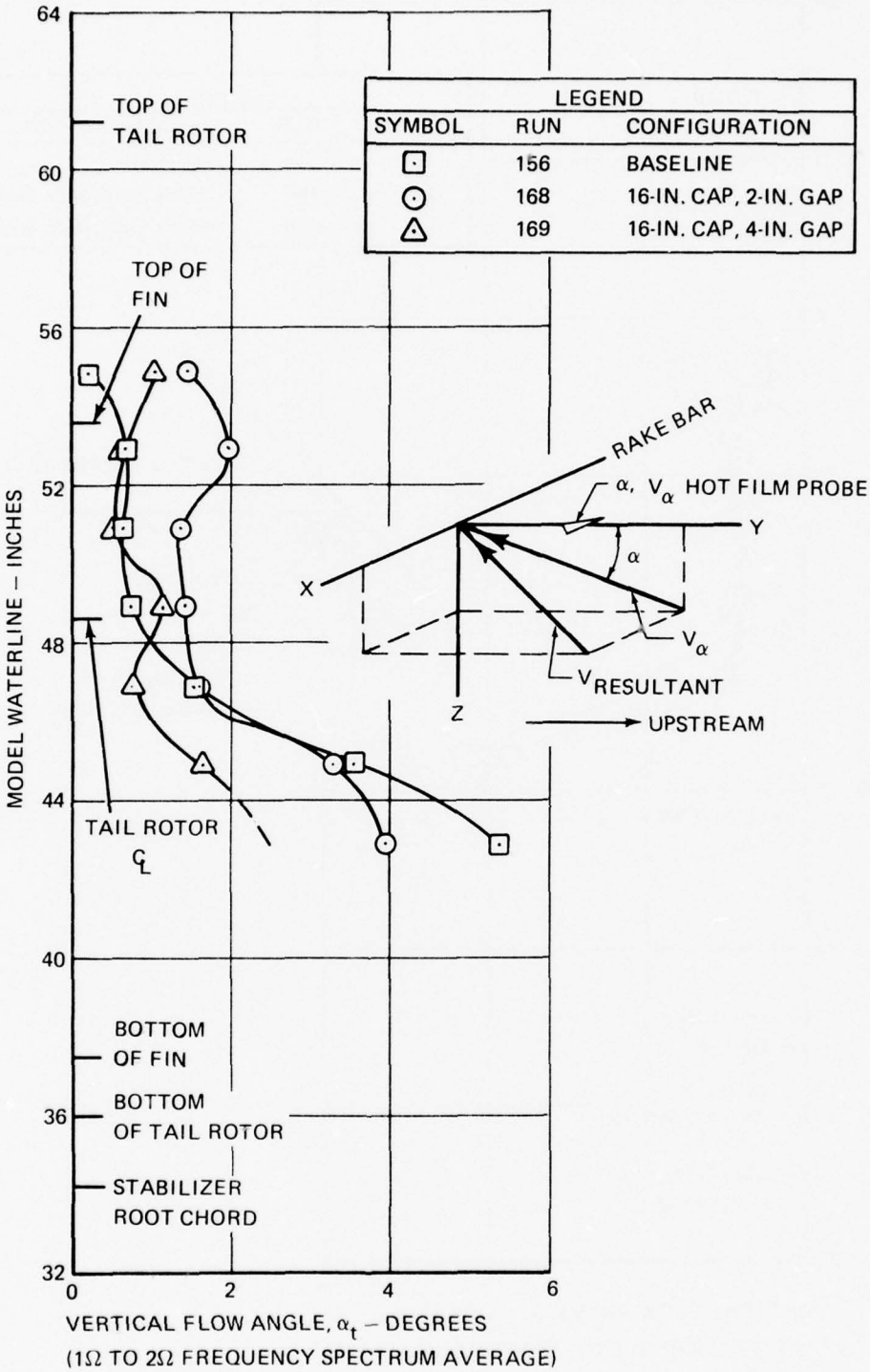

Figure 73. Effect of Large-Diameter Open Caps Without Underbody on Vertical Flow Angles.

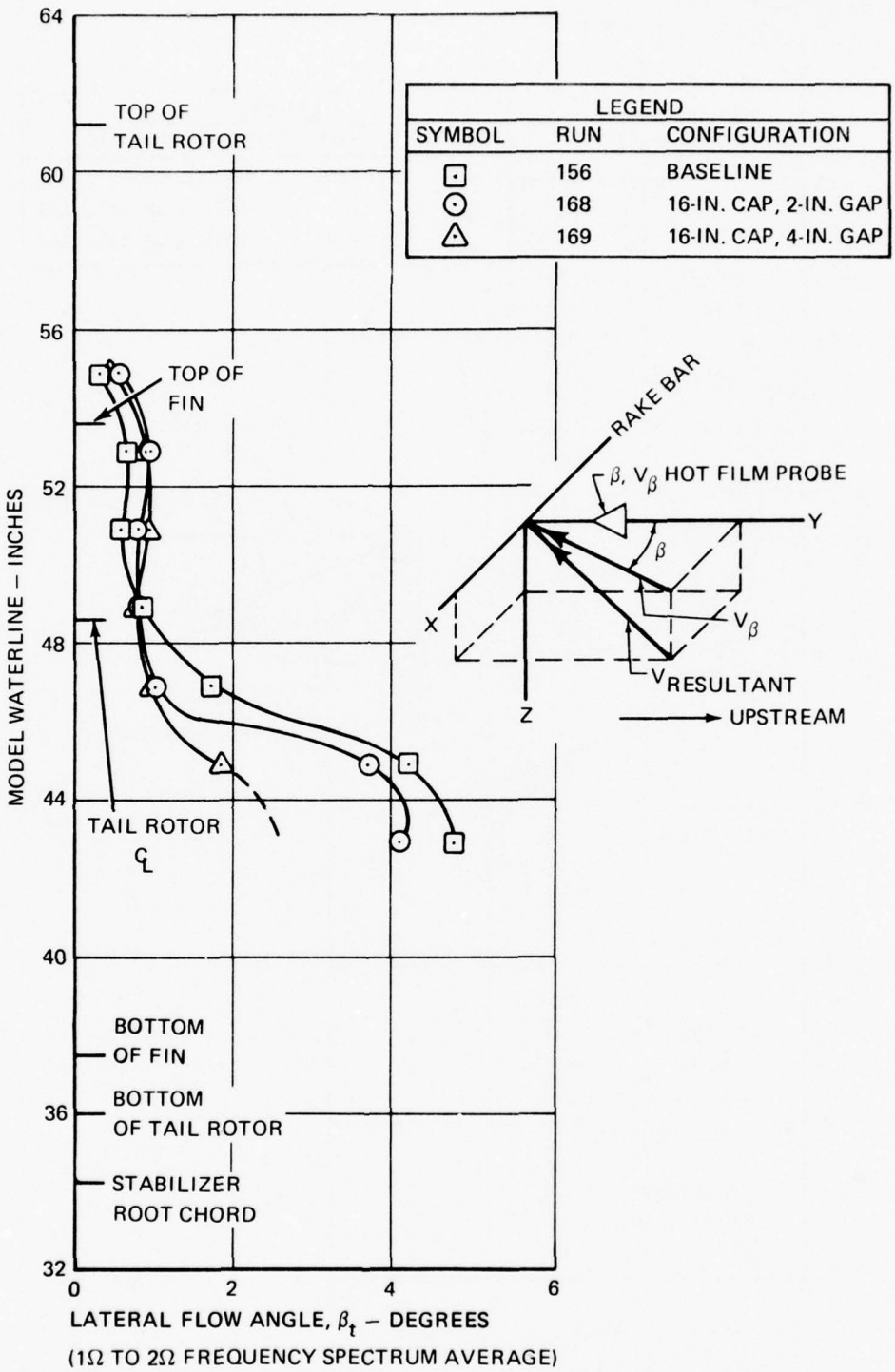

Figure 74. Effect of Large-Diameter Open Caps Without Underbody on Lateral Flow Angles.

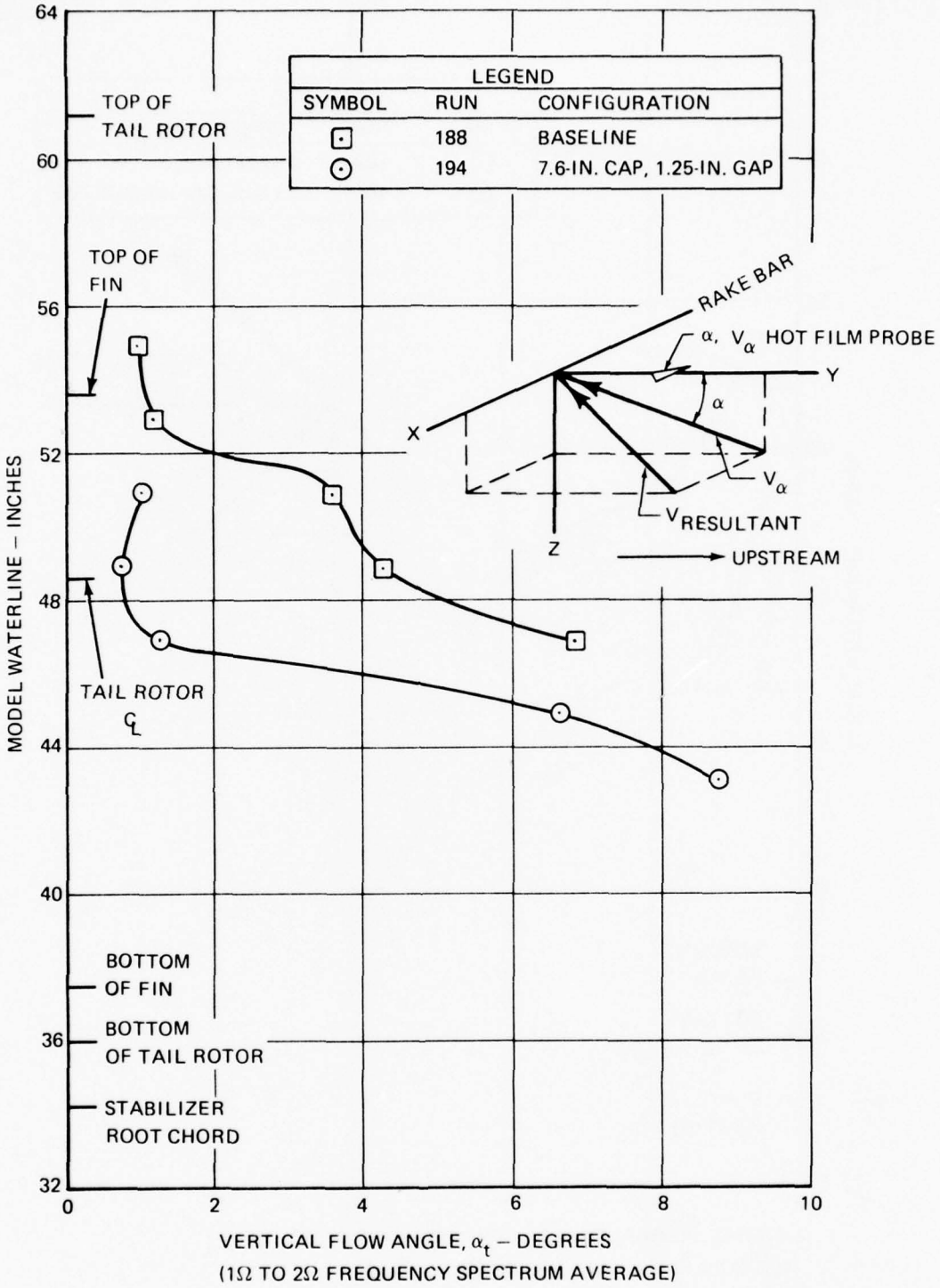

Figure 75. Effect of Small-Diameter Open Hubcap With Underbody on Vertical Flow Angles.

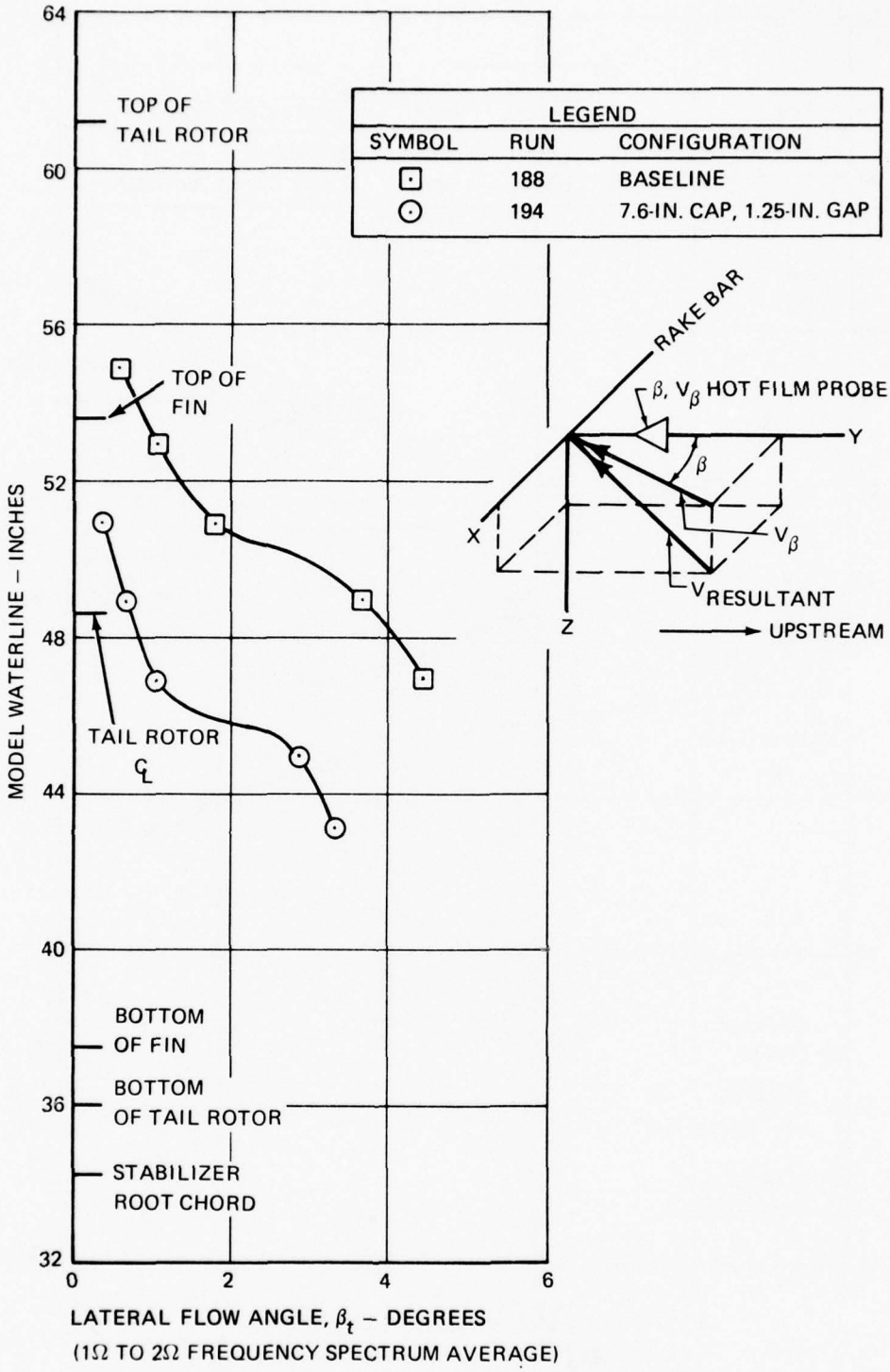

Figure 76. Effect of Small-Diameter Open Hubcap With Underbody on Lateral Flow Angles.

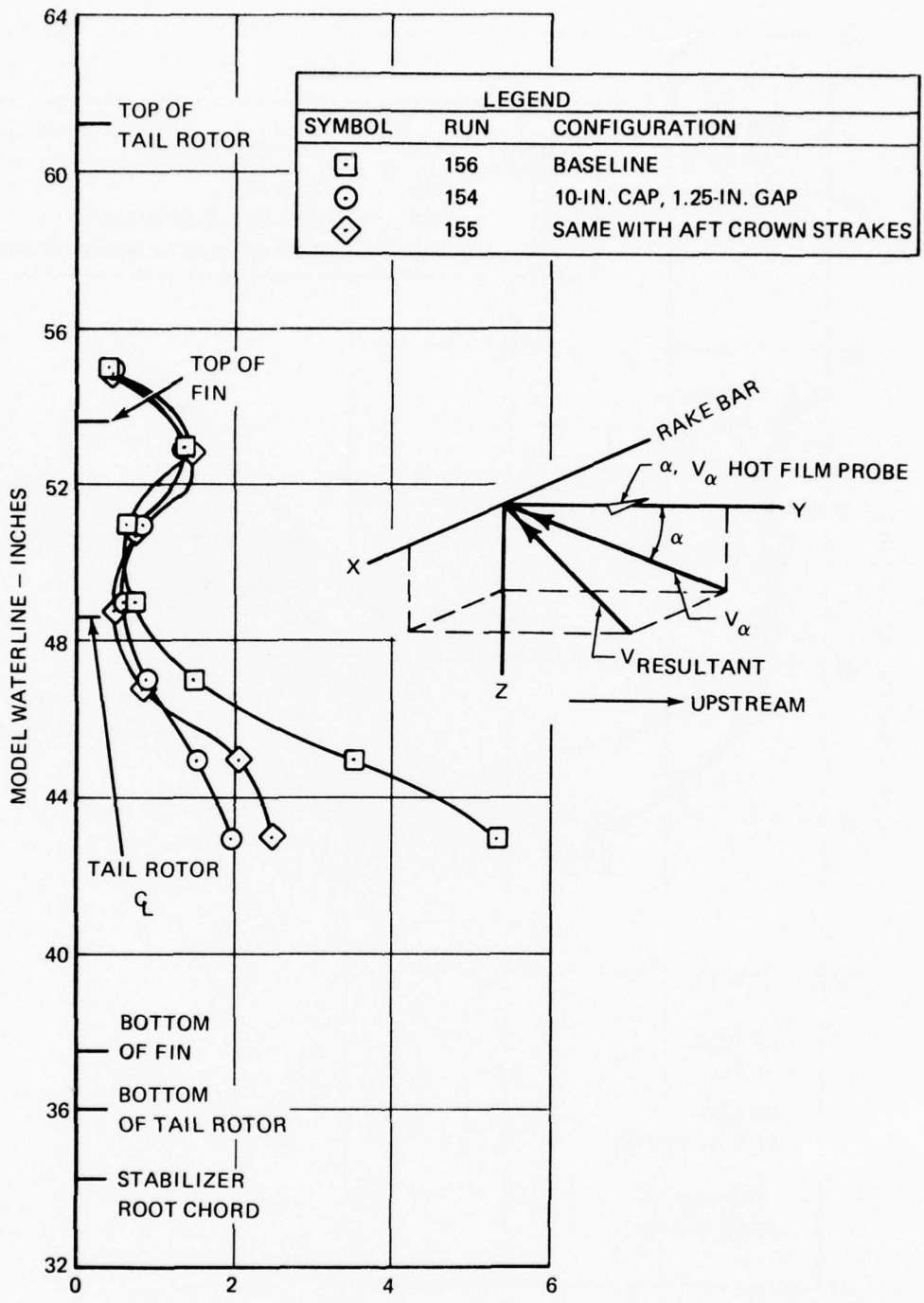

Figure 77. Effect of Medium-Diameter Open Cap With Underbody on Vertical Flow Angles With Blades On.

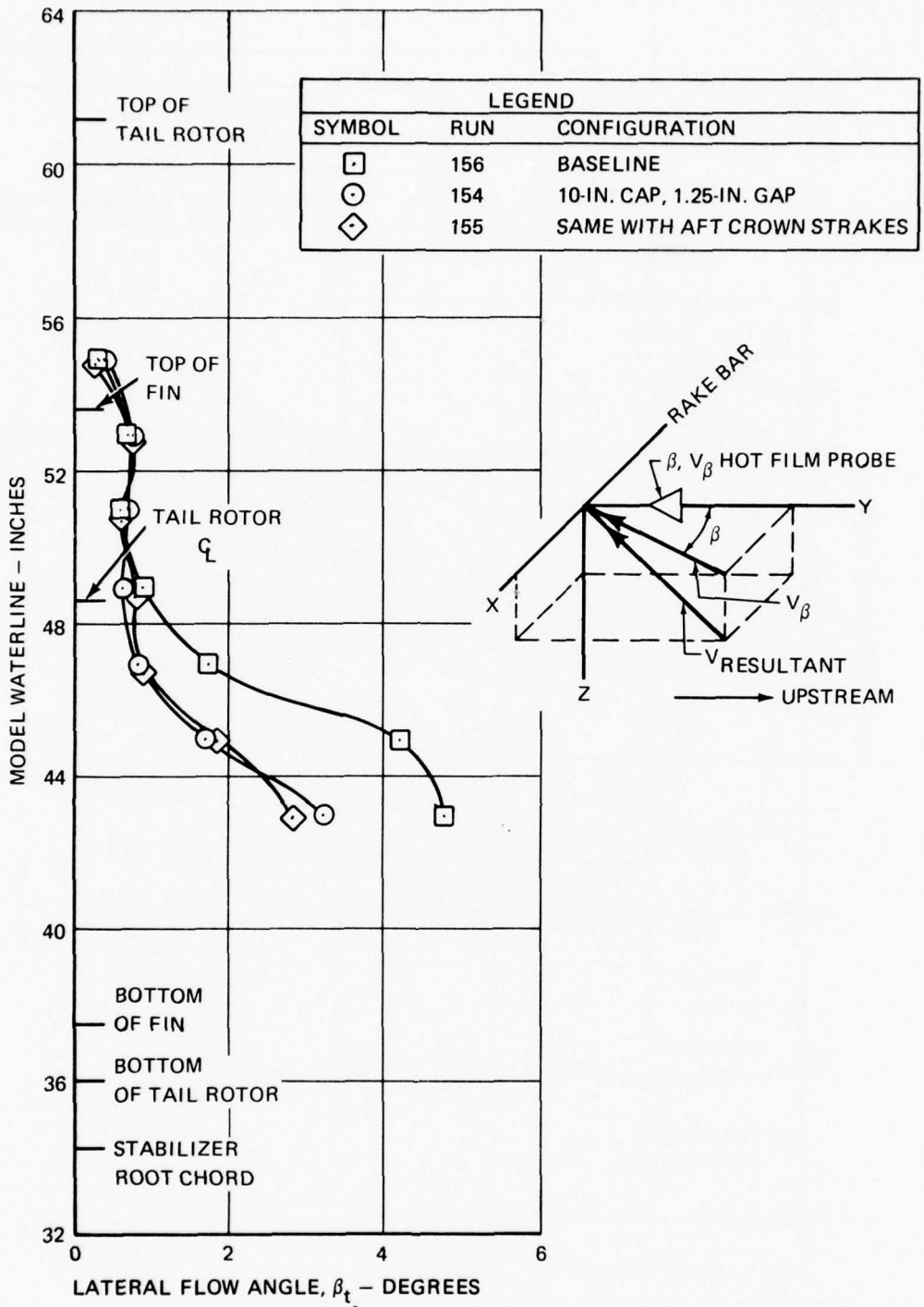

Figure 78. Effect of Medium-Diameter Open Cap With Underbody on Lateral Flow Angles With Blades On.

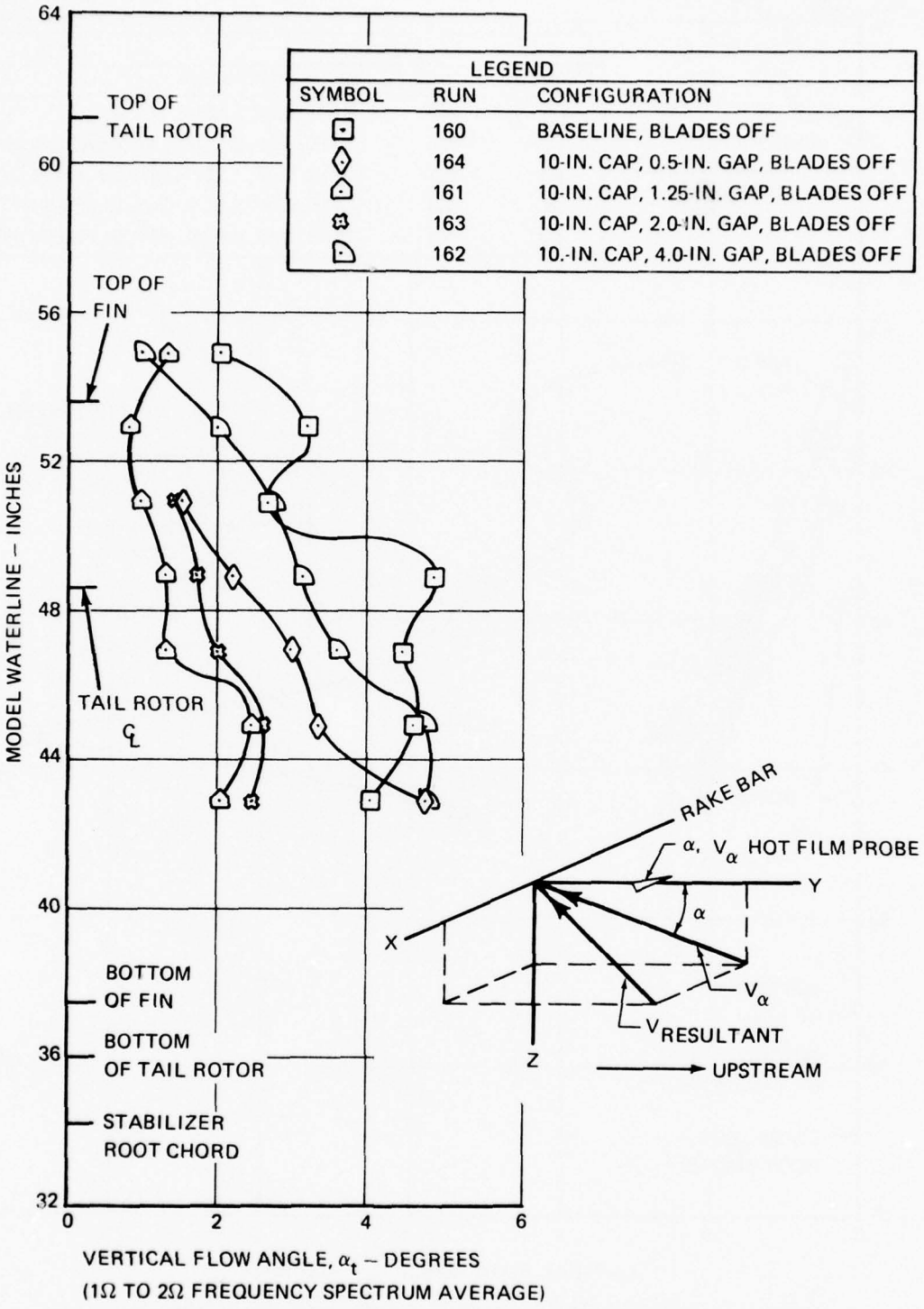

Figure 79. Effect of Medium-Diameter Open Cap With Underbody on Vertical Flow Angles for Several Gap Values With Blades Off.

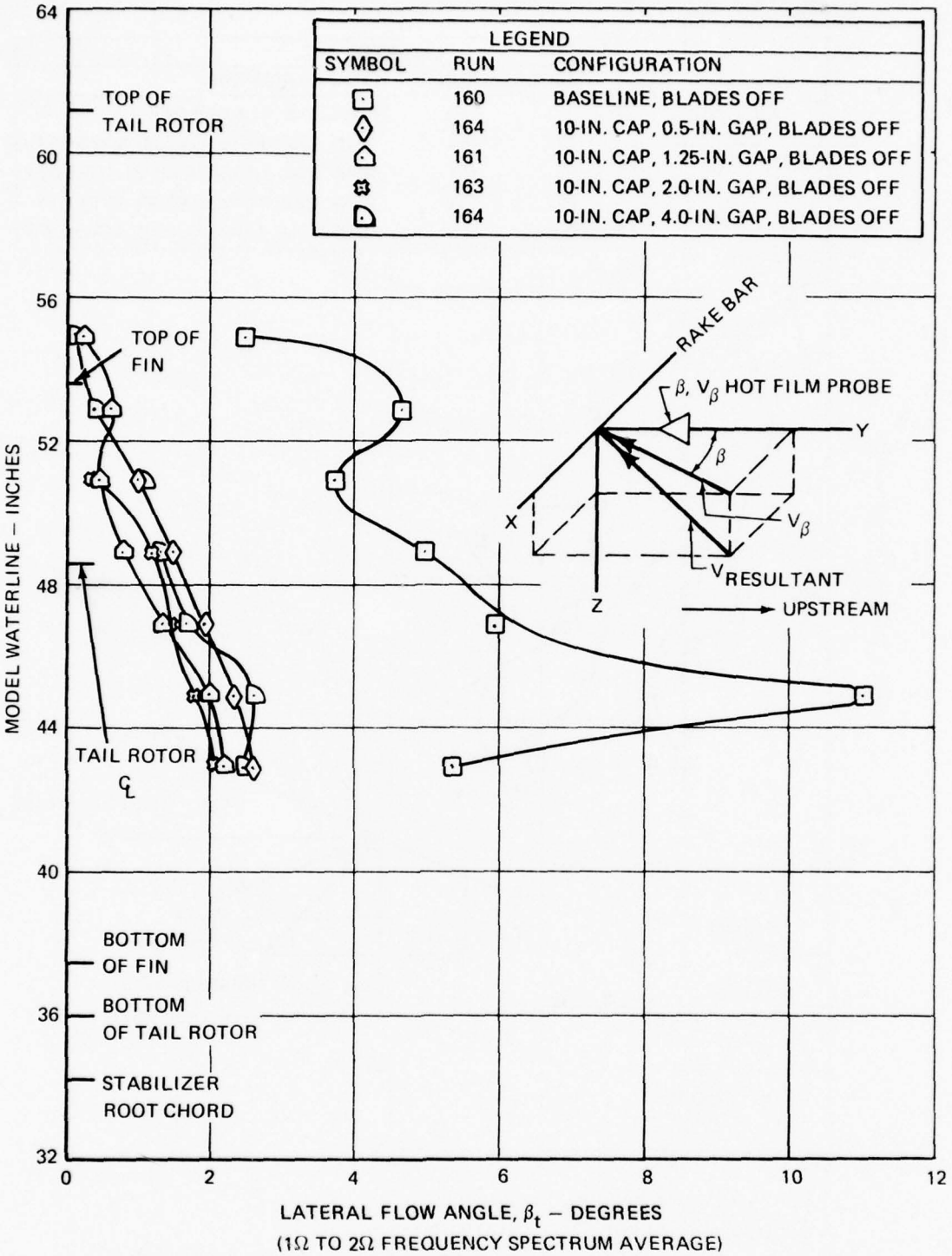

Figure 80. Effect of Medium-Diameter Open Cap With Underbody on Lateral Flow Angles for Several Gap Values With Blades Off.

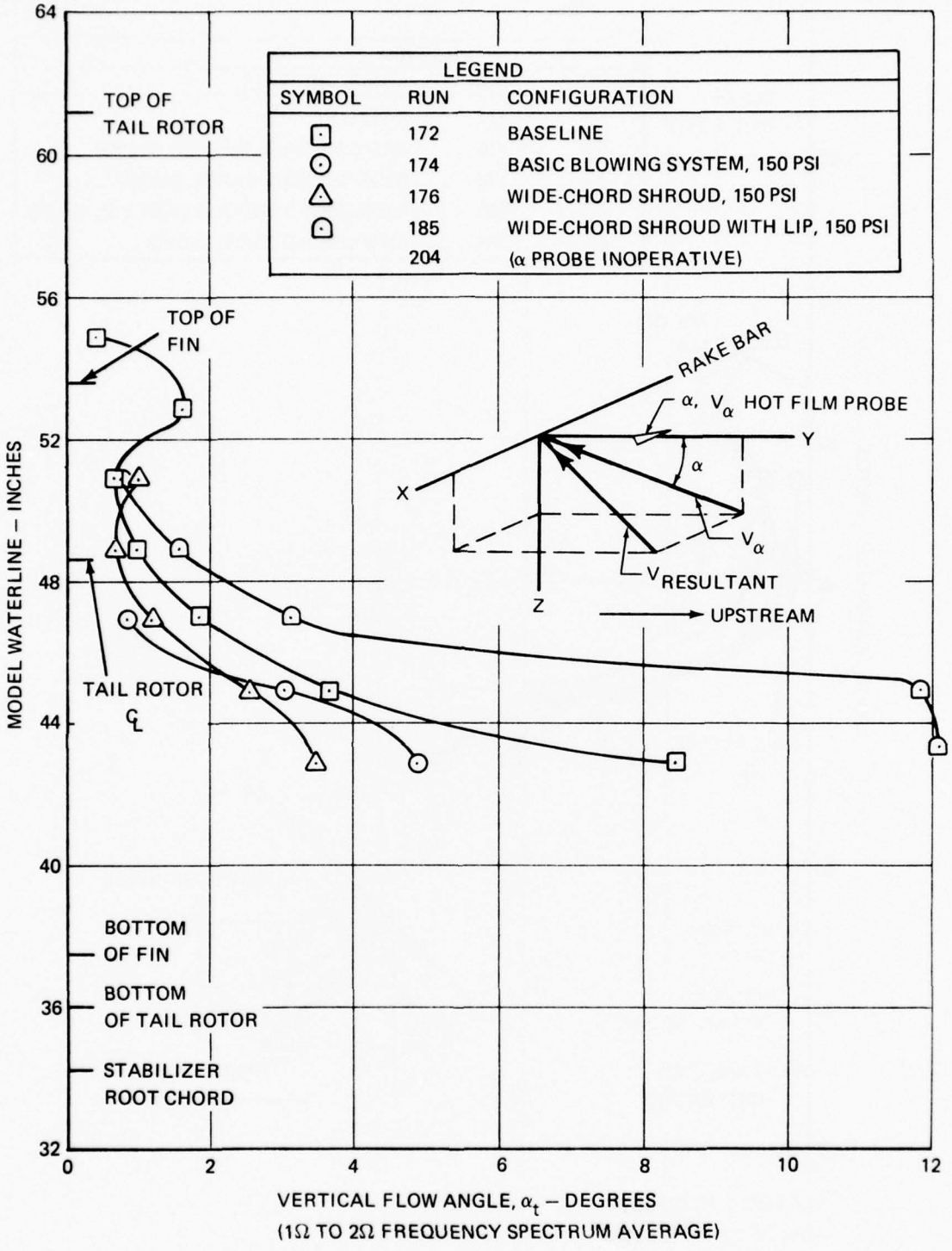

Figure 81. Effect of Ejector System Variations on Vertical Flow Angles.

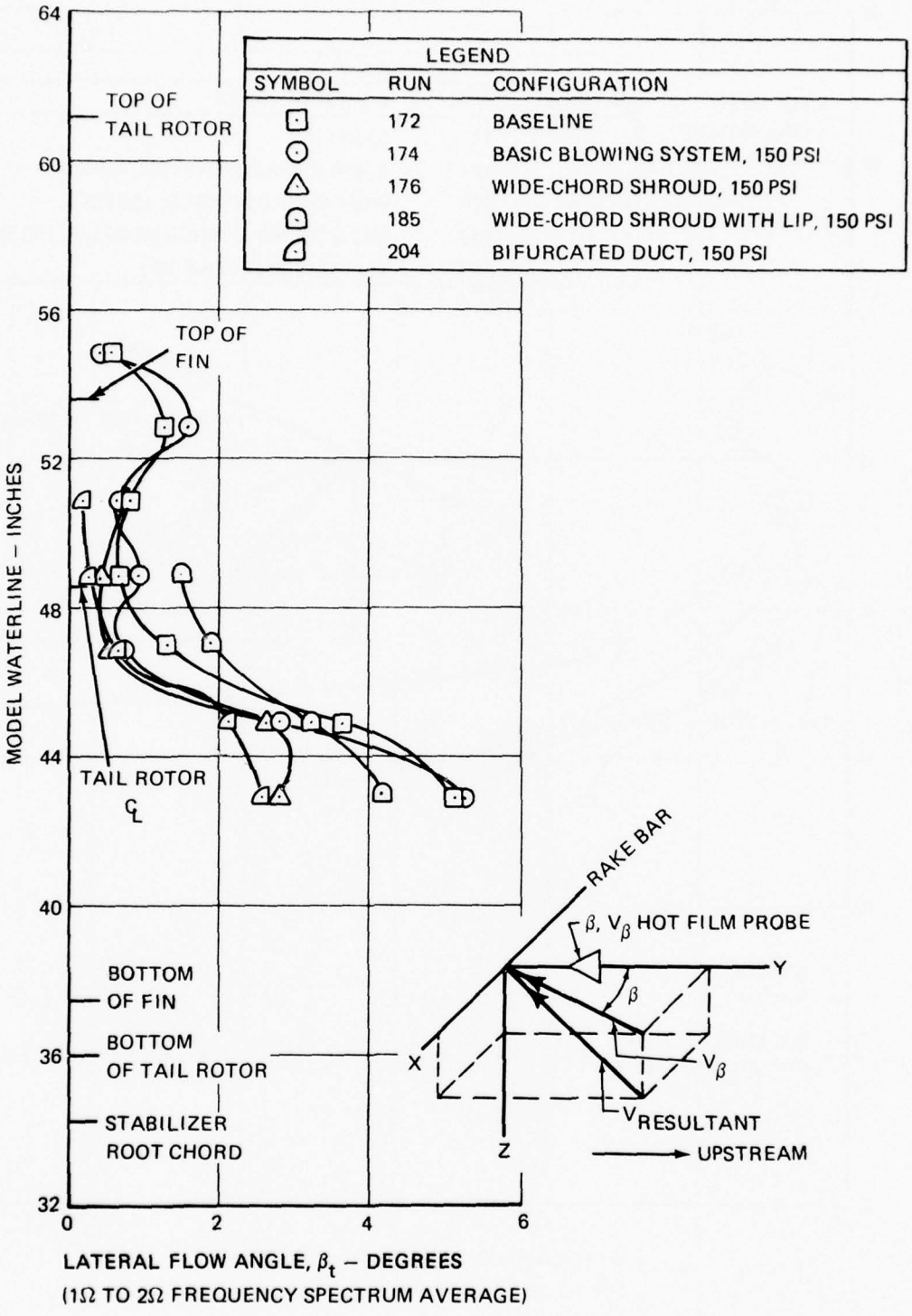

Figure 82. Effect of Ejector System Variations on Lateral Flow Angles.

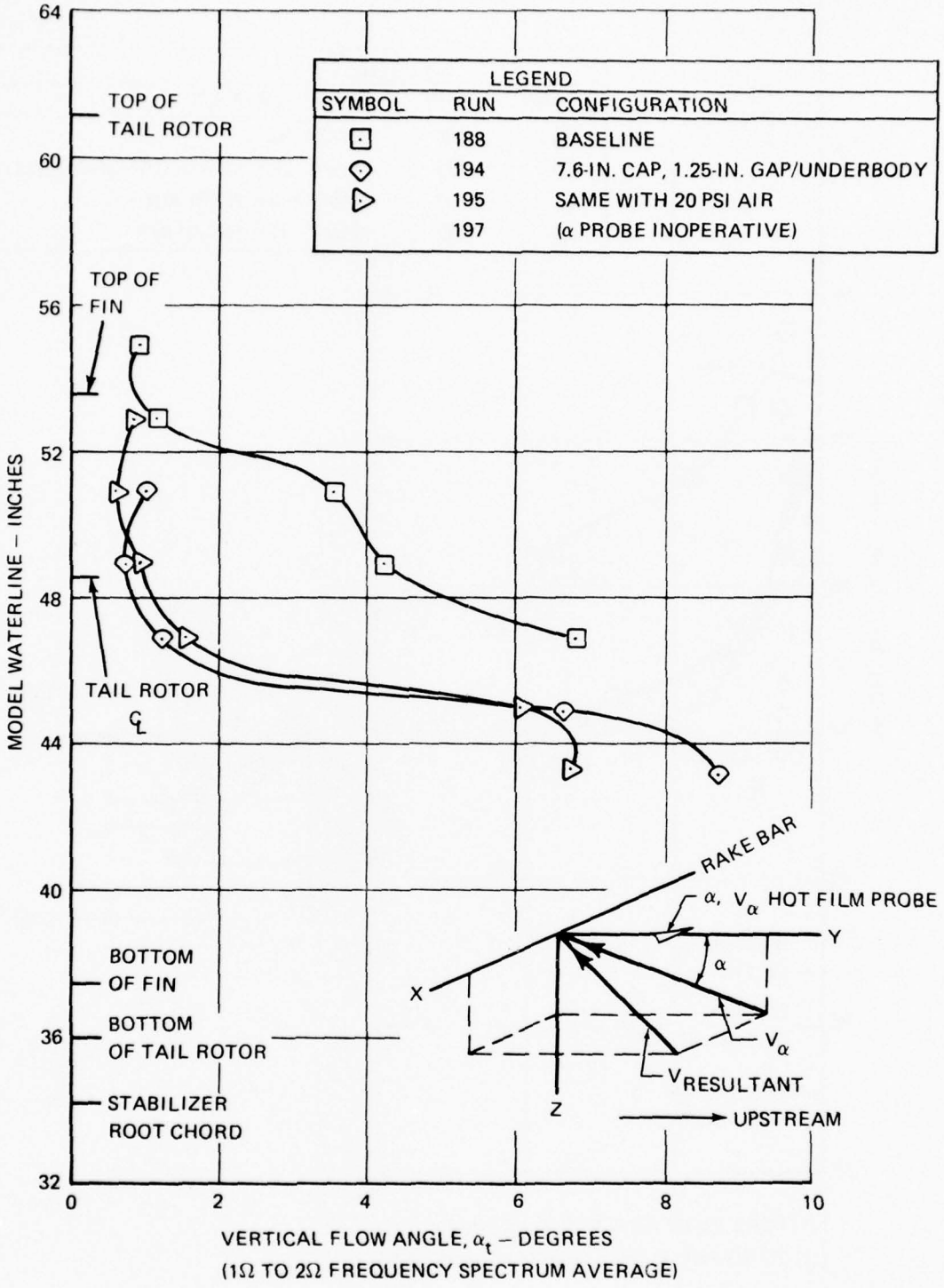

Figure 83. Combined Effect of Hubcap and Air Ejector System on Vertical Flow Angles.

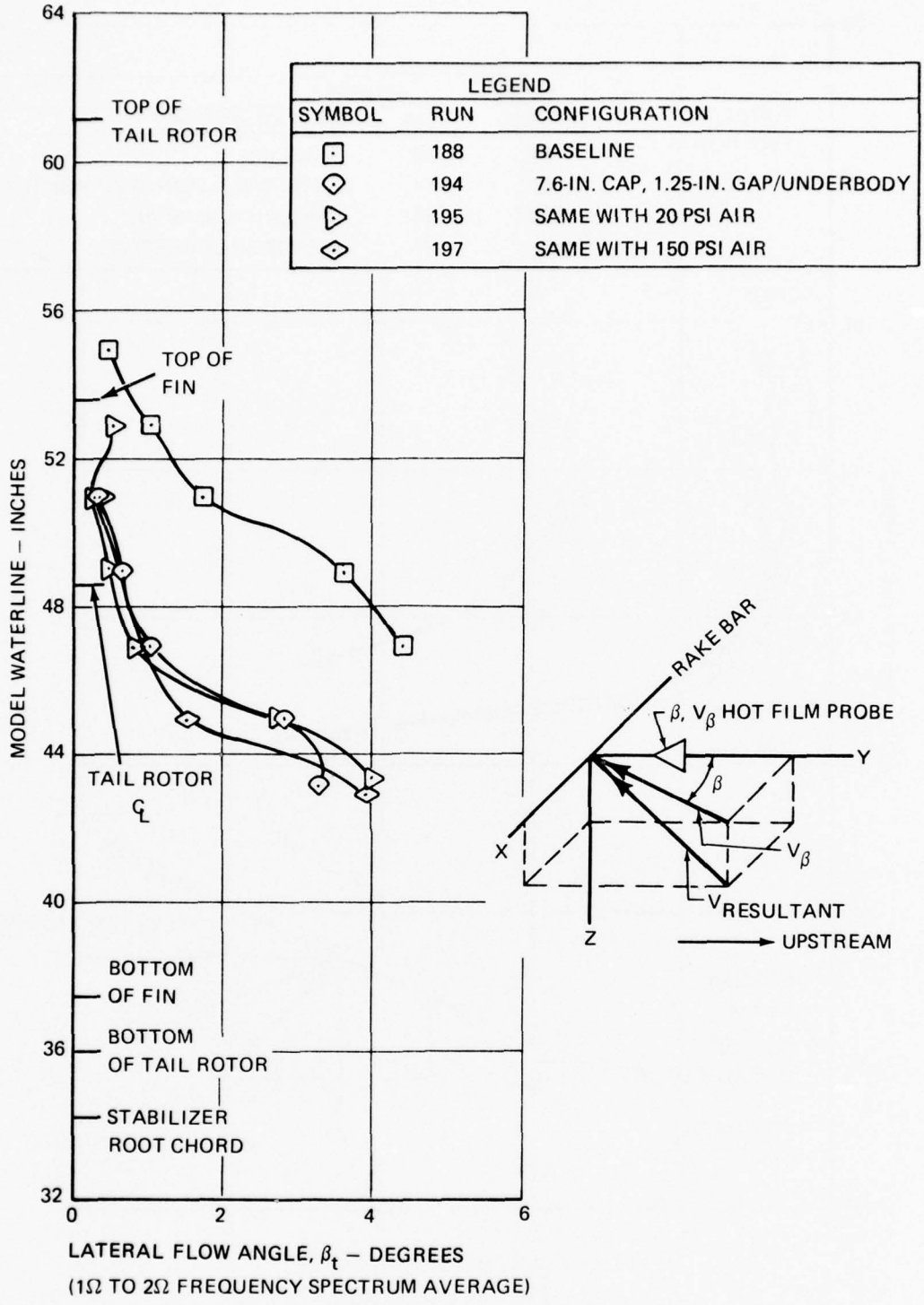

Figure 84. Combined Effect of Hubcap and Air Ejector System on Lateral Flow Angles.

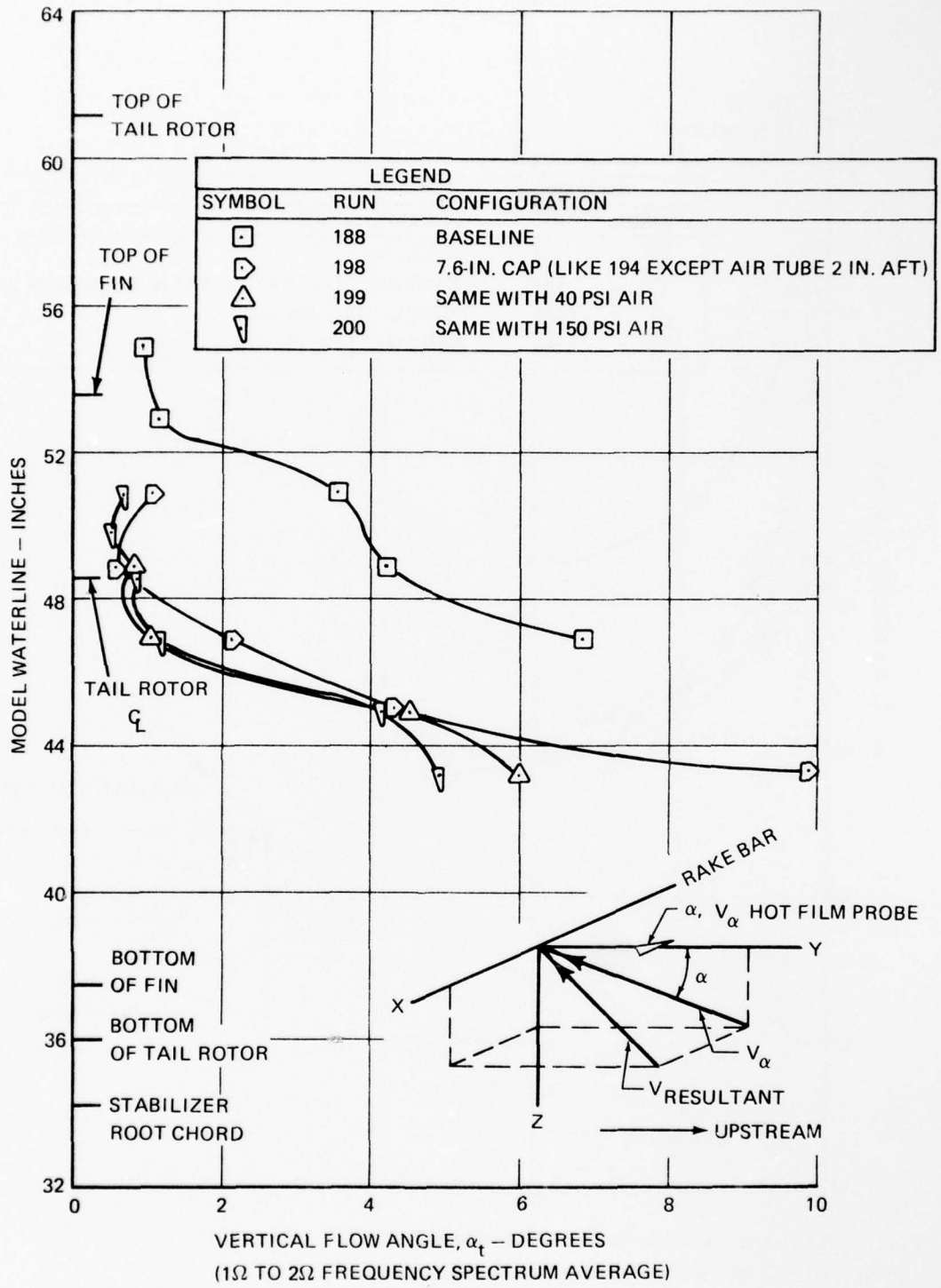

Figure 85. Combined Effect of Hubcap and More Aft Ejector on Vertical Flow Angles.

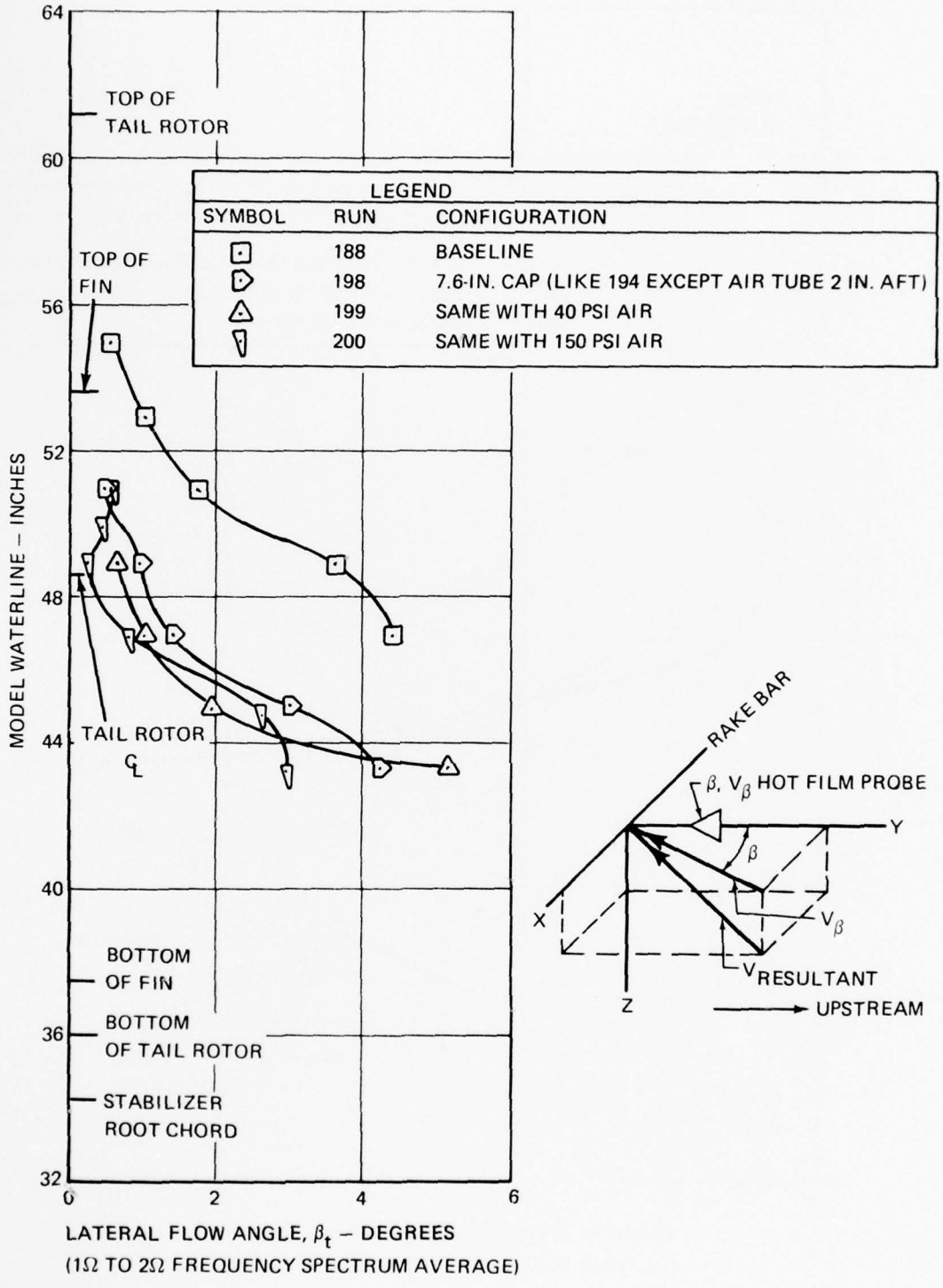

Figure 86. Combined Effect of Hubcap and More Aft Ejector on Lateral Flow Angles.

ROTOR/EMPENNAGE/GROUND INTERACTIONS

The wind tunnel test had no specific objectives relating to interactions of the empennage with the ground, the tail rotor with main rotor, or the tail rotor with the vertical fin. However, because of the study of ground effect at low speed reported in earlier sections, an opportunity presented itself to gather additional empennage interaction data for subsequent study.

The rotor/empennage/ground interaction area is important in tail rotor sizing and in designing the geometrical arrangement of the empennage configuration. These matters have received considerable attention in other programs, particularly the work earlier cited in References 3 and 4. The novel aspect of this program is the relatively high ratio of swept fin area to tail rotor disk area of 35 percent compared to 23 percent for the Reference 3 effort and 20 percent for the Reference 4 study. Indeed, the tail rotor design guidelines of Reference 10 are based entirely upon data from tests using the lower ratios.

Other programs discussed in the references emphasized wide variations in wind azimuth in order to study control problems in rear quartering winds. The current tests addressed no problems of this type and the model yaw variations were limited to plus or minus 30 degrees. The test runs are listed in Table 11 and are identical to those considered in previous sections on rotor/ground and rotor/fuselage/ground interactions. The section initially addresses the effects of tail rotor proximity on main rotor power and loads, and fuselage lift and moments. The remainder is devoted to the study of the fin loads due to the presence of tail rotor.

IGE TRIM

During these runs the requirement for tail thrust was the scaled value for the corresponding flight trim condition. This sets the tail rotor disk loading identical to full scale and assures flow similarity with regard to the tail rotor contribution. Required values varied typically from 60 pounds in maximum power conditions to 42-50 pounds in hover and 33-39 pounds at 30 knots, depending on the gross weight and density. A strength problem limited the thrust to approximately 25 pounds, however, so that we find it varying from 22 to 27 on the tail rotor balance. The test data are not used to derive the trim requirements, i.e., pedal position, since the critical conditions for this were not covered.

TAIL ROTOR/MAIN ROTOR INTERACTIONS

For ψ = 0 degrees there are no expected differences between tail rotor on and off and generally the balance data confirm this. Figure 87 shows the effect on power required with a slight decrease evident with tail rotor on. Similar inconsequential effects are noted in Figures 88 and 89 in the hub rolling and pitching moments. The same small changes are noted for the fuselage lift of Figure 90 and for the fuselage pitching moment of Figure 91. The yawing moment of Figure 92 shows significant differences over the speed range, probably due to flow changes over the tailboom under the influence of the tail rotor flow environment or the absence of it. These parameters would show large values and large sensitivities to tail rotor presence for yaw angles

10. Wiesner, W., and Kohler, Gary, TAIL ROTOR DESIGN GUIDE, Boeing Vertol Company; USAAMRDL Technical Report 73-99, Eustis Directorate, U.S. Army Air Mobility Research and Development Laboratory, Fort Eustis, Virginia, January 1974, AD775391.

TABLE 11. TEST RUNS FOR THE EFFECTS OF GROUND PROXIMITY

Run No.	Configuration	V_{TUN} (kn)	MR/TR Speed (rpm)	Disk Ldg (psf)	Model Angles		MR Ht (h/d)	Tail Rotor
					α (deg)	ψ (deg)		
83	K_g/Baseline for D.L. variation	◇11	1,433/ 4,500	8	0	0	0.4	On
84	K_g/Added detail to 83	10↔20 /2's	1,433/ 4,500	8	0	0	0.4	On
85	K_g/Increased D.L.	◇11	1,433/ 4,500	10	0	0	0.4	On
86	K_g/Added detail to 85	20↔26 /2's	1,433/ 4,500	10	0	0	0.4	On
87	K_g/Reduced D.L.	◇11	1,433/ 4,500	6	0	0	0.4	On
88	K_g/Added detail to 87	12↔18 /2's	1,433 4,500	6	0	0	0.4	On
89	K_g/Reduced D.L.	◇11	1,433/ 4,500	4	0	0	0.4	On
90	K_g/Effect of pos yaw	◇11	1,433/ 4,500	8	0	+30	0.4	On
91	K_g/Effect of neg yaw	◇11	1,433/ 4,500	8	0	-30	0.4	On
92	K_g/Effect of neg angle of attack	◇11	1,433/ 4,500	8	-6.6	0	0.4	On
93	K_g/Effect of pos angle of attack	◇11	1,433/ 4,500	8	+10	0	0.4	On
94	K_g/Reset α to mean value over transition	◇11	1,433/ 4,500	8	5	0	0.4	On
95	K_g/Added detail to 94	12↔20 /2's	1,433/ 4,500	8	5	0	0.4	On
96	K_g/Added detail to 94	10↔30 /2's	1,433/ 4,500	8	5	0	0.4	On
97	K_g/Added detail to 94	10↔30 /2's	1,433/ 4,500	8	5	0	0.4	On
98	K_g/Reduced D.L.	10↔30 /2's	1,433/ 4,500	6	5	0	0.4	On
99	K_g/Increased rotor height	10↔30 /2's	1,433/ 4,500	8	5	0	0.475	On
100	K_g/Increased rotor height	◇11	1,433/ 4,500	8	5	0	0.475	On
101	K_g/Effect of tail rotor stopped	◇11	1,433/0	8	5	0	0.4	Stopped
102	K_g/Increased rotor to ground height	◇11	1,433/ 4,500	8	5	0	0.6	On
103	K_g/Increased rotor to ground height	◇11	1,433/ 4,500	8	5	0	0.7	On
104	K_g/Increased rotor to ground height	◇11	1,433/ 4,500	8	5	0	0.8	On
105	K_g/Increased rotor to ground height	◇11	1,433/ 4,500	8	5	0	1.0	On

NOTE: ◇11 for V_{TUN} = 0, 10 to 40 knots by 5's, then 50 kn

approaching the rearward flight condition. The data here for ψ equal to zero is a good basis for a future program covering the full azimuth range.

TAIL ROTOR/VERTICAL FIN INTERACTION

The aerodynamic interaction between the tail rotor and vertical fin is characterized chiefly by a large fin force that is opposite in sign to the tail rotor thrust for either a pusher or tractor tail rotor. The tractor rotor downwash impinges on the fin in the manner of the main rotor wash on the fuselage, causing download. The pusher tail rotor, apparently by drawing air over the adjacent left side fin surfaces, causes negative pressurization resulting in an integrated force to the left. It is aggravated by closeness to the fin in the case of the pusher; in fact, there is a value for fin/rotor gap below which more adverse fin force will be produced than by the tractor configuration. The ratio of gap to tail rotor radius in this test is approximately 0.33.

Figure 93 shows the ratio of fin load to tail rotor thrust as a function of nondimensional airspeed, i.e., forward speed divided by the ideal hover-induced velocity of the tail rotor. The ratio is shown for four disk loadings for which little variation is apparent. Peak values vary between 33 and 36 percent. In Reference 10, Figure 8-1 would predict a value of 25 percent. Allowing for the higher swept fin area, a linear correction factor would give 38 percent. However, the graph of Figure 8-1 is intended as the maximum possible value, which usually occurs around $\psi = -45$ degrees. With this fin and tail rotor, the ratio would be considerably higher than 38 percent, with ψ of -30 degrees and -75 degrees.

Figure 94 shows the fin force ratio for tail rotor on and off. The main rotor is operating in both cases. The conclusion must be that its flow does not produce any significant fin force by itself. It remains for a future test program to test with the main rotor not running, i.e., to extend the disk loading range of Figure 93 to zero to get the main rotor contribution when the tail rotor is running. A few points from an earlier test with tail rotor alone indicate that a substantial augmentation from the main rotor must prevail.

Figure 95 shows the effect of model pitch attitude on the fin force variation with speed. Significant differences occur at the higher speeds with the maximum effect occurring for level fuselage ($\alpha = 0$ degrees) and level rotor ($\alpha = 5$ degrees). Peak values are still in the 33-36-percent area and it is concluded that attitude is not a very significant parameter. Also, since the attitude variation is moving the tail rotor essentially vertically in relation to the ground, that boundary itself is not a significant element in determining the fin/tail rotor force ratio.

As expected, a large change with wind direction is evident in Figure 96, which shows fin side force ratio versus airspeed for plus and minus 30 degrees of yaw compared to zero degrees. In fact, at a nondimensional speed of 2.15 (approximately 50 knots), the fin side force ratio is almost 1; i.e., the fin force is equal and opposite to the tail rotor. This high an interference force was not expected, based upon an earlier test where yaw sweeps were made. Figure 97 shows the results of the earlier test with tail rotor thrust, fin force, and their ratio plotted versus azimuth for a constant speed of 25 knots. On the same graph are plotted the points from the subject test. The symbol ψ used on this graph to denote wind azimuth is opposite in sense to ψ used elsewhere in this report for model azimuth.

The tail rotor thrust of that test (BVWT 169) is substantially less (50-60 percent) than that experienced during the earlier test, BVWT 131. Yet the fin force is essentially the same for both zero and 30 degrees. This causes the fin force to tail rotor thrust ratio to be substantially higher for the subject test with its lower tail rotor thrust. The nonlinearity evidenced here in the fin force/thrust relationship strongly suggests that the higher thrust may be drawing the flow off the adjacent side of the fin, in effect, stalling it.

Fin stall in this context has not been comprehensively investigated with this model on any test. However, by collecting points from various runs of BVWT 131 and 169, it is possible to see the pattern of the fin force variation with tail rotor thrust at one airspeed. Figure 98 shows this function at 25 knots airspeed for model azimuth values of zero, −30, and −75 degrees. Note that these would show a plus sign to express wind azimuth.

Rays from the origin locate constant values of fin force to tail rotor thrust ratio from −0.2 to −0.8. An essentially nonlinear character is apparent in the three curves. For ψ = 0 degrees, the curve shows a small positive value for fin force at zero thrust, indicating the effect of rotor swirl. It is straight to about 22 pounds thrust, crossing the rays from the positive side to about minus 0.34. Subsequently, the curve bends around in a manner characteristic of stall with a decrease in fin force ratio clearly evident. Thus at ψ = 0 degrees, the tail rotor starts as quite efficient with regard to fin loss with the help of main rotor side wash (swirl), then becomes more inefficient as the fin loads up in the negative direction and finally becomes more efficient as the fin stalls and loses adverse lift.

The curve for ψ = −30 degrees has a similar shape but it is offset substantially by a fairly predictable amount. Calculation of fin side force at freestream dynamic pressure with the fin 30 degrees to the wind yields approximately 7 pounds compared to 8.6 pounds measured at zero tail thrust. At low thrust values the fin loss expressed as fin force to thrust ratio will be higher than −1, starting at minus infinity and becoming less negative as thrust increases. This trend is accelerated as the fin begins to stall at about 25 pounds thrust (C_T/σ = 0.07). Of course, it is not possible to pinpoint the inception of stall or to describe precisely the curve behavior in stall because of the small number of points. The curve for ψ = −75 degrees is slightly more positive than that for −30 degrees in the linear region. Obviously, it must totally stall because of the high oblique angle of flow for all thrusts.

The slope is similar for all three curves and the most well defined, that for ψ = −75 degrees, shows a slope value of −0.33 pounds of fin force per pound of thrust. This is approximately the force that would be produced by the fully developed tail rotor downwash impacting upon the fin. The formula for the slope is as follows:

$$\frac{\Delta Y_{Fin}}{\Delta T_{TR}} = C_D \frac{A_{Fin}}{A_{TR}} \qquad (9)$$

where A_{Fin} is that part of the fin area swept by the tail rotor. For this model it is 0.35 and, for a C_D equal to one, the slope would be very close to the actual value of 0.33.

This is a puzzling result since the mechanism is not anything like that suggested above. It would describe very well a tractor tail rotor whose downwash impacts directly on the fin. For a

pusher, however, the fin is on the low-velocity side of the tail rotor. Until additional testing can shed some light on this problem, the slope similarity must be labeled an interesting coincidence.

Another way of considering these data is to plot the empennage side force, that is, the thrust plus the fin force, versus thrust. This is sometimes called the net thrust available for antitorque or maneuvering. Figure 99 shows this parameter for ψ = 0, −30, and −75 degrees. The line at 45 degrees indicates the ideal relationship of zero fin load to provide a measure of the fin load effect. The inefficiency of this configuration is clearly apparent comparing the actual to the ideal.

Clearly more questions are posed than are answered in the presentations of Figures 97, 98, and 99. The data matrices need to be completed in terms of thrust, azimuth, speed, and main rotor disk loading. It is further suggested that the format of Figures 97, 98, and 99 and the previous plots versus azimuth and speed are all necessary to understand the nonlinear nature of the fin/tail rotor/main rotor interactions.

FIN SPANWISE LIFT DISTRIBUTION

Although pressure transducers were not used on the fin during the ground effect tests, the fin rolling moment was measured and may be used in conjunction with the side force to obtain the spanwise (vertical) center of lift location. Figure 100 illustrates the geometry involved in the derivation. The fin rolling moment is the difference of two measurements, the empennage rolling moment and the rolling moment due to tail rotor thrust when both are referred to the same moment center, namely, the empennage balance longitudinal axis. By definition, this moment has to be equal to the fin force times the distance from the reference line to the center of lift so that

$$z = \frac{RM}{Y} \tag{10}$$

As a fraction of the reference span h,

$$\frac{z}{h} = \frac{RM}{Yh} \tag{11}$$

This parameter has been calculated for the various test conditions of Runs 83 to 105 and, for much of the transition speed range, has a value close to 0.5 with the single exception of ψ = +30 degrees. This is slightly above the area centroid, which is at 0.44.

The center of lift location is plotted in Figure 101 for ψ = 0, −30, and +30 degrees. The curve for ψ = −30 degrees is virtually flat for the entire range of transition speeds and that for ψ = zero is initially flat and then drops down into the negative region.

The function for ψ = +30 degrees is seen to start out at z/h equal to 0.5 like the others but then becomes asymptotic to a nondimensional speed of 1.25. This can be more easily understood with reference to Figure 102, which displays the fin force and moment separately. The occurrence of the asymptote is obviously due to the fin force passing through zero. The moment

moves toward the positive side and then passes through zero at 1.6, which is reflected in the center of lift change in Figure 101.

Vertical lift distribution may be inferred from these variations. At 1.25 with the force equal to zero, a negative couple must exist with a lift distribution as shown. Below 1.25 a preponderance of negative lift (to left) must exist on the upper fin to be consistent with the negative force. Above the 1.25 point, the positive lift on the bottom will become more influential, finally producing at 1.6 a moment about the balance center just offsetting the negative moment produced by the upper fin pressures. The lower fin positive lift becomes completely dominant beyond 1.6 in the normal forward flight pattern.

The curve for ψ = 0 degrees becomes asymptotic at a nondimensional speed of about 2.2 much farther out than the similar speed for ψ = 30 degrees. At this point the fin moment, which must be a pure couple, is positive in sign with the lift on the upper fin acting to the right and the lift on the lower part acting to the left. This is opposite in sign to the couple in the ψ = 30-degree case because side force has become positive.

At low speed the force and moment for ψ = 0 degrees and ψ = 30 degrees are similar in sign and magnitude; in fact, they are almost identical in both respects at a nondimensional speed of 0.73. Presumably the lift distributions at this speed are also the same. The manner in which the lift distribution varies between speeds of 0.73 and 2.2 is not apparent and must await some future test with pressure transducers. The lift distributions are important mainly in conjunction with flow visualization work to understand mechanisms of adverse fin force generation.

EFFECTS OF ROTOR-TO-GROUND HEIGHT

The height variations were done only for ψ = 0 degrees. The trends with speed are similar in shape; they show a rise in the value of the fin force ratio to a peak negative value of about −0.35 to −0.4. This is followed by a trend toward the positive side, crossing zero past a nondimensional speed of 2.0. Other investigators have also pondered the significance of the ground proximity in the adverse fin load generation. Figure 102 shows the fin force to tail rotor thrust ratio of this test compared to that obtained in Reference 10. The large difference reflects the difference in area ratios, the dissimilarities in models, and the larger amounts of fin stall in the Reference 10 data because of the high thrusts that were used.

Despite these dissimilarities, the shape of the curves is almost the same.

The effect of ground proximity is basically favorable; however, at an h/d of 0.6 a sharp break in both curves reverses the favorable trend. This has been attributed to the unfavorable inflows associated with the main rotor vortices as the wake is displaced upward by the approaching ground boundary. The adverse fin force then reverts almost to the out-of-ground-effect level before it resumes the initial trend.

The unfavorable fin/tail rotor interaction is large everywhere. It is not a ground-oriented problem for net thrust and power considerations. However, the large perturbation in the two curves of Figure 103 indicates that for this speed 0.6 h/d is very likely the threshold of high turbulence and great unsteadiness on the directional axis as the main rotor vortex flow becomes more confined by the ground and more localized to the empennage airspace. It is probable that

the roughness boundary height increases for higher speed and conversely for lower speeds. At the higher transition speeds the turbulence will be less due to the generally lower induced velocities, but the band may extend to an h/d of 1.0.

CRITIQUE OF FIN/TAIL ROTOR INTERACTIONS

This was the first reported wind tunnel test of a high fin-to-tail-rotor area configuration that can result from the requirement for directional trim with the tail rotor inoperative. The adverse fin forces have been found to dwarf in magnitude any other known interaction effect. The values here are orders of magnitude higher than those reported in other tests.

This is the first study to define the role of fin stall due to tail rotor flow, i.e., it is a favorable effect occurring at the highest tail rotor thrusts. The unstalled fin at lower thrusts more typical of trim will show a greater negative fin force resulting in a less efficient fin/tail rotor configuration. Guidelines based upon assumptions of linearity, i.e., constant ratio of net thrust to gross thrust (net empennage force to tail rotor thrust) as tail rotor varies, need to be reexamined as the current study indicates the contrary is true.

Reassessment of the results of earlier preliminary design trade studies of antitorque configurations is highly recommended. Such studies rarely put the tail rotor in its worst operating conditions nor used more than nominal adverse fin loads. More realistic fin losses such as those discovered in this study will tip the balance more in favor of unconventional arrangements of fin and tail rotor or entirely different devices.

More important than more trade studies, however, is the need for a more comprehensive tail rotor data basis. In order of importance some of the data requirements are as follows:

1. Fin force versus tail rotor thrust through fin stall and beyond to tail rotor stall itself for many nondimensional speeds and azimuths.
2. The effect of tail rotor to fin gap for high fin area configurations.
3. The effect of tail rotor vertical position relative to the fin and the determination of the extent of the pressurized fin area. It is not necessarily limited to the swept or shadow area.
4. The effect of the main rotor flow on the adverse fin load. The few points available suggest that this interaction is most significant. At $\psi = 0$ degrees as much as one-half the fin load may result from main rotor presence.
5. Quantitative definition of the turbulence levels accompanying aerodynamic interactions of main rotor, tail rotor, and the ground. State-of-the-art dynamic flow testing technology will permit this to be done on powered wind tunnel models.

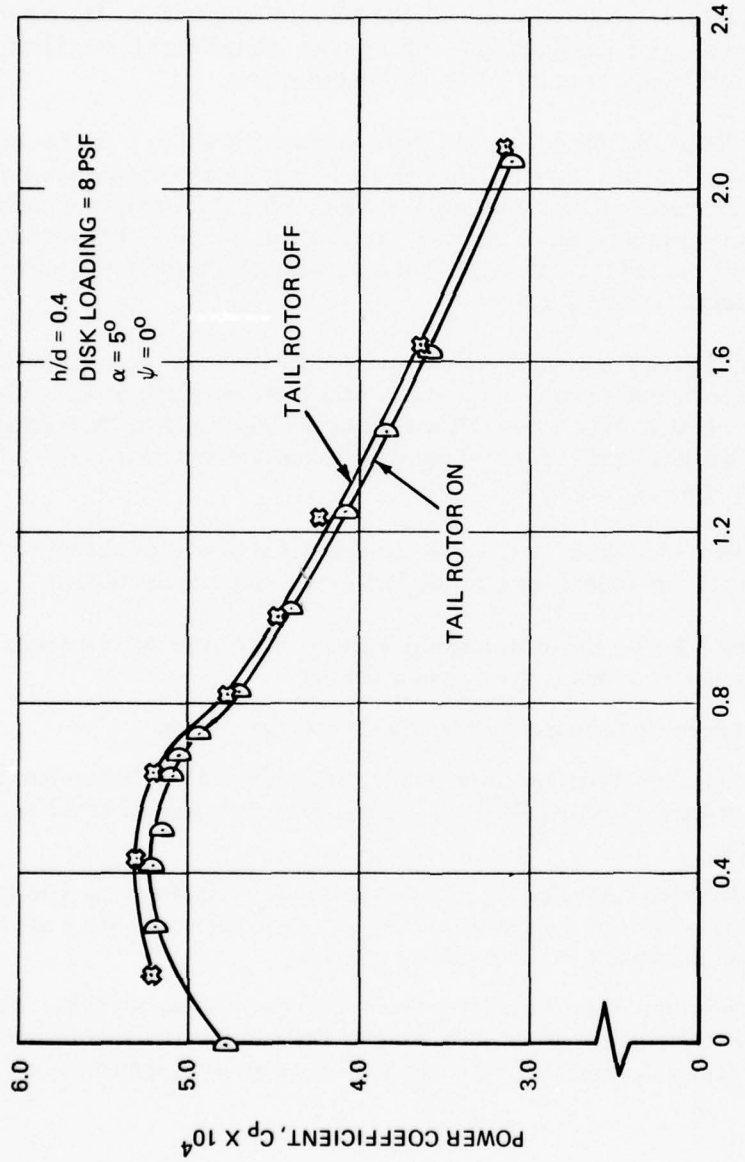

Figure 87. Variation of Power With Airspeed In Ground Effect Showing Effect of Tail Rotor Presence.

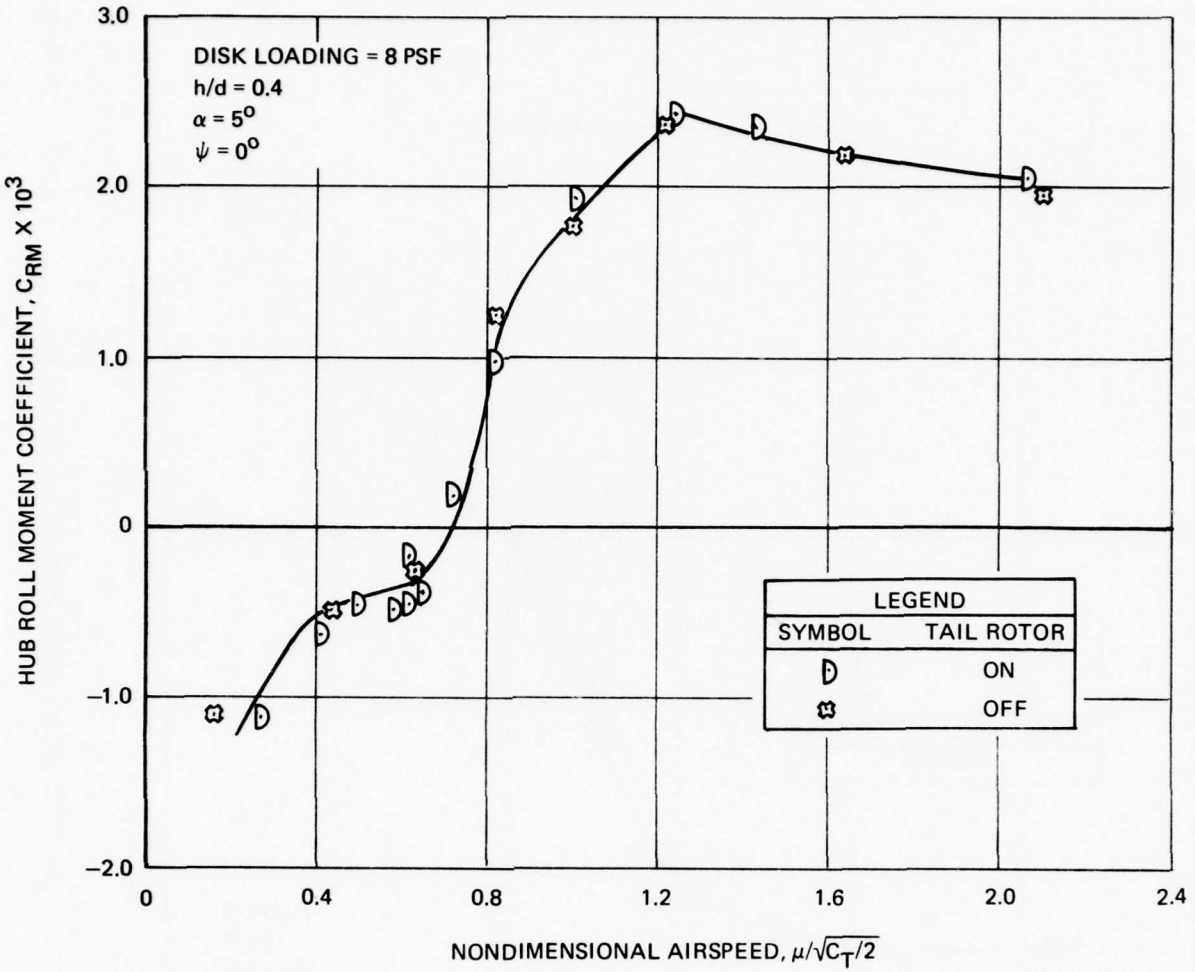

Figure 88. Variation of Hub Roll Moment With Airspeed Showing Effect of Tail Rotor Presence.

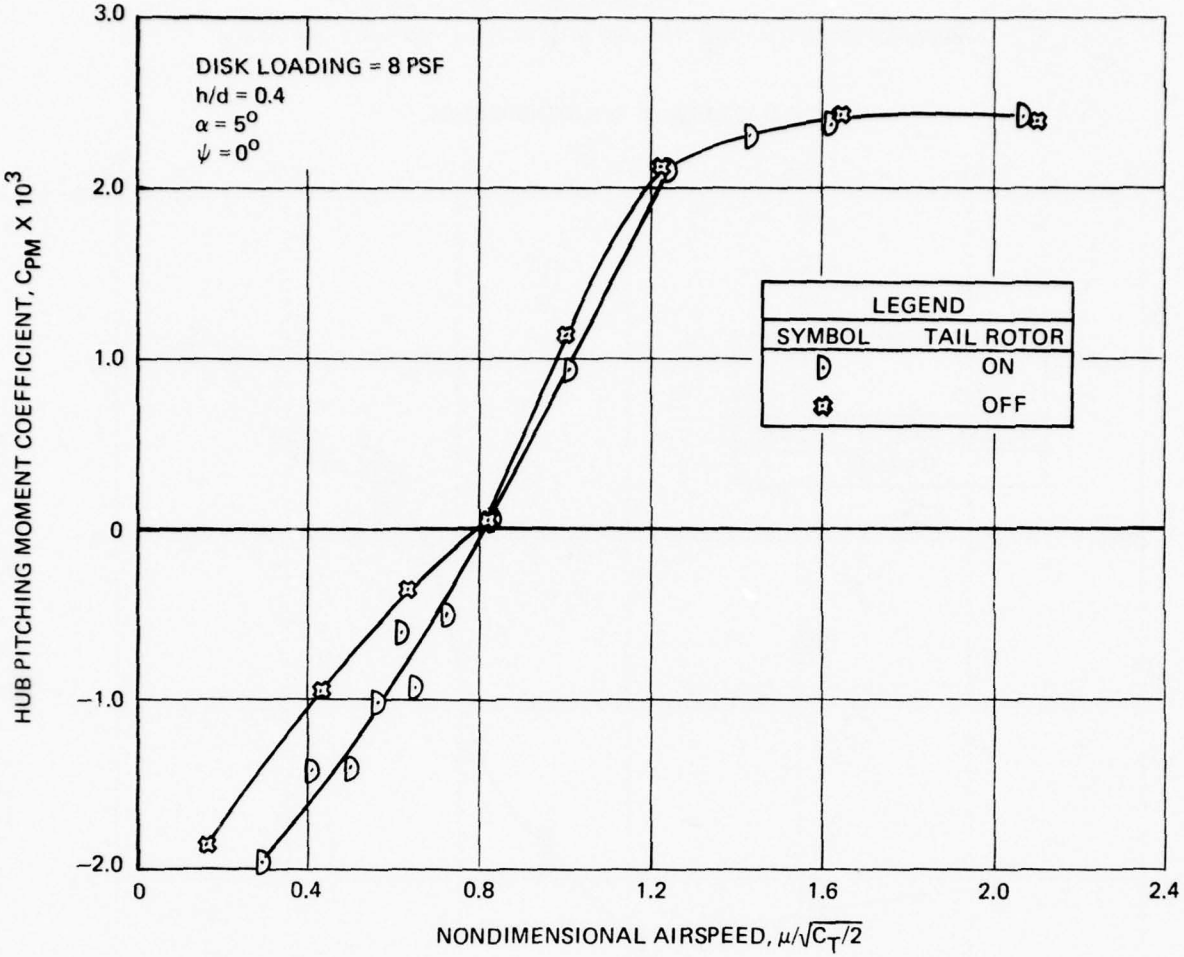

Figure 89. Variation of Hub Pitching Moment With Airspeed Showing Effect of Tail Rotor Presence.

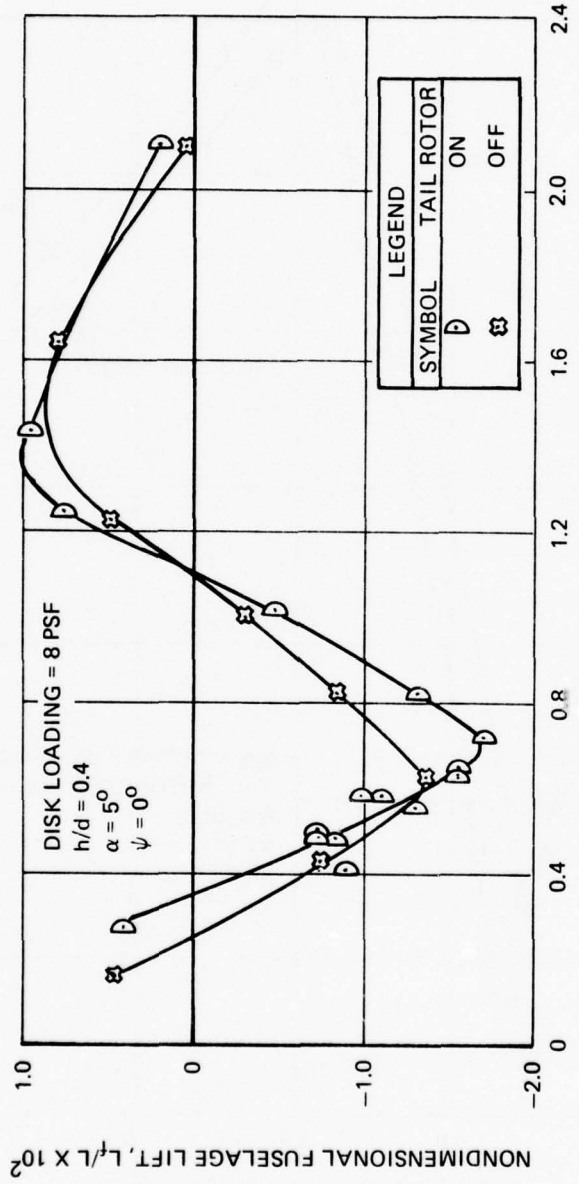

Figure 90. Fuselage Lift as a Function of Airspeed Showing Effect of Tail Rotor Presence.

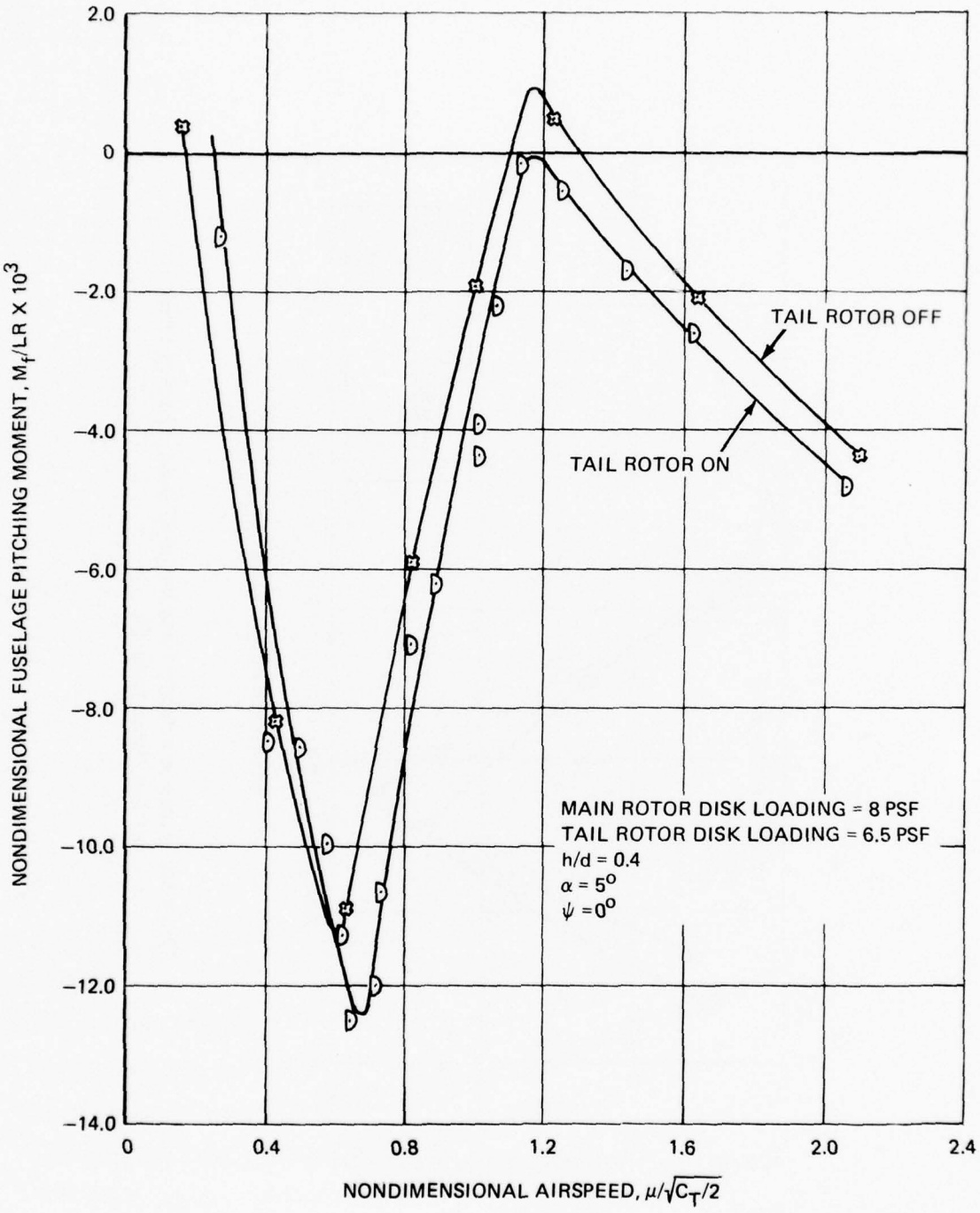

Figure 91. Variation of Fuselage Pitching Moment With Airspeed Showing Effect of Tail Rotor Presence.

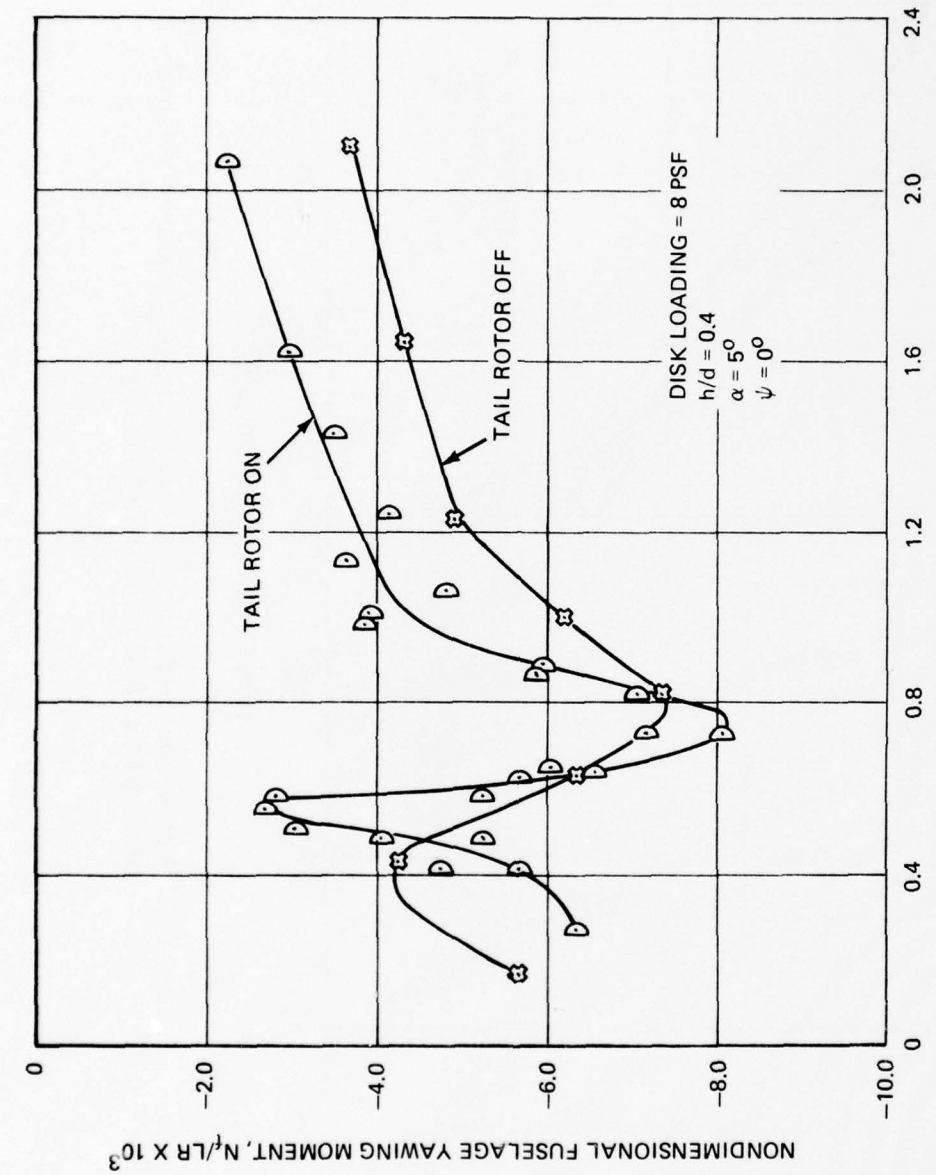

Figure 92. Variation of Fuselage Yawing Moment With Airspeed Showing Effect of Tail Rotor Presence.

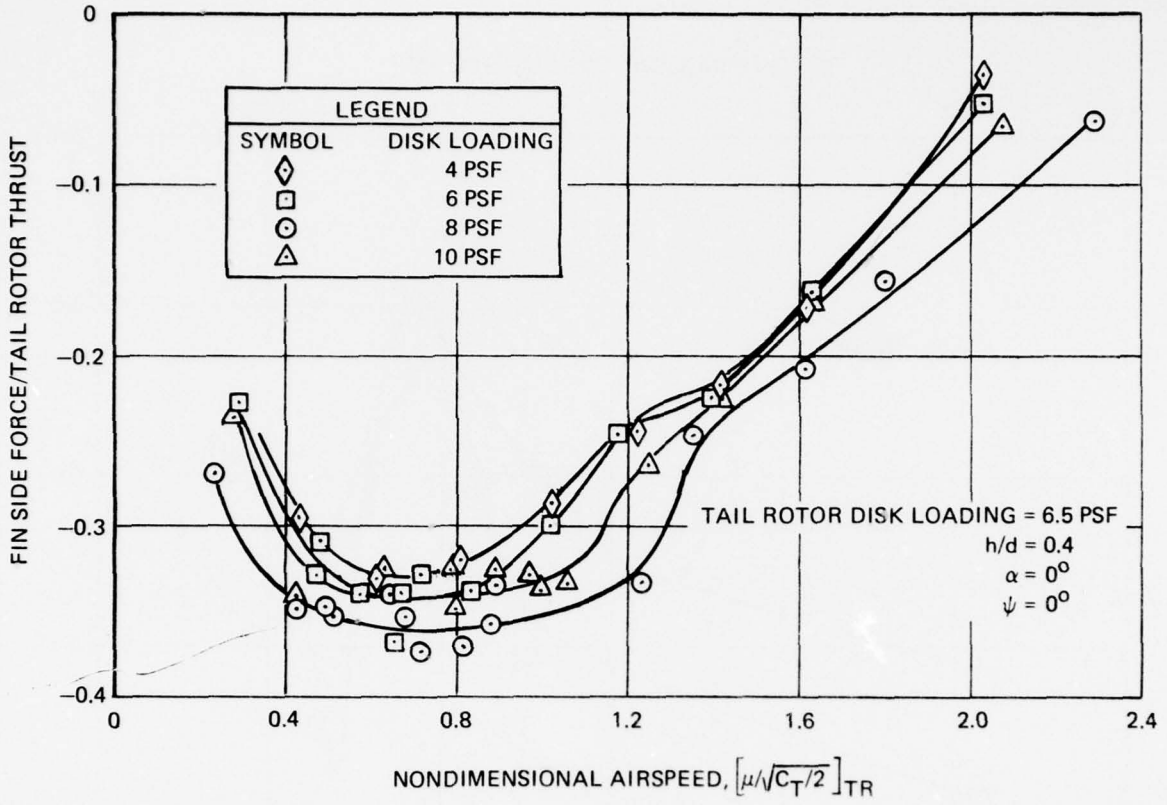

Figure 93. Ratio of Fin Side Force to Tail Rotor Thrust as a Function of Airspeed Showing Effect of Main Rotor Disk Loading.

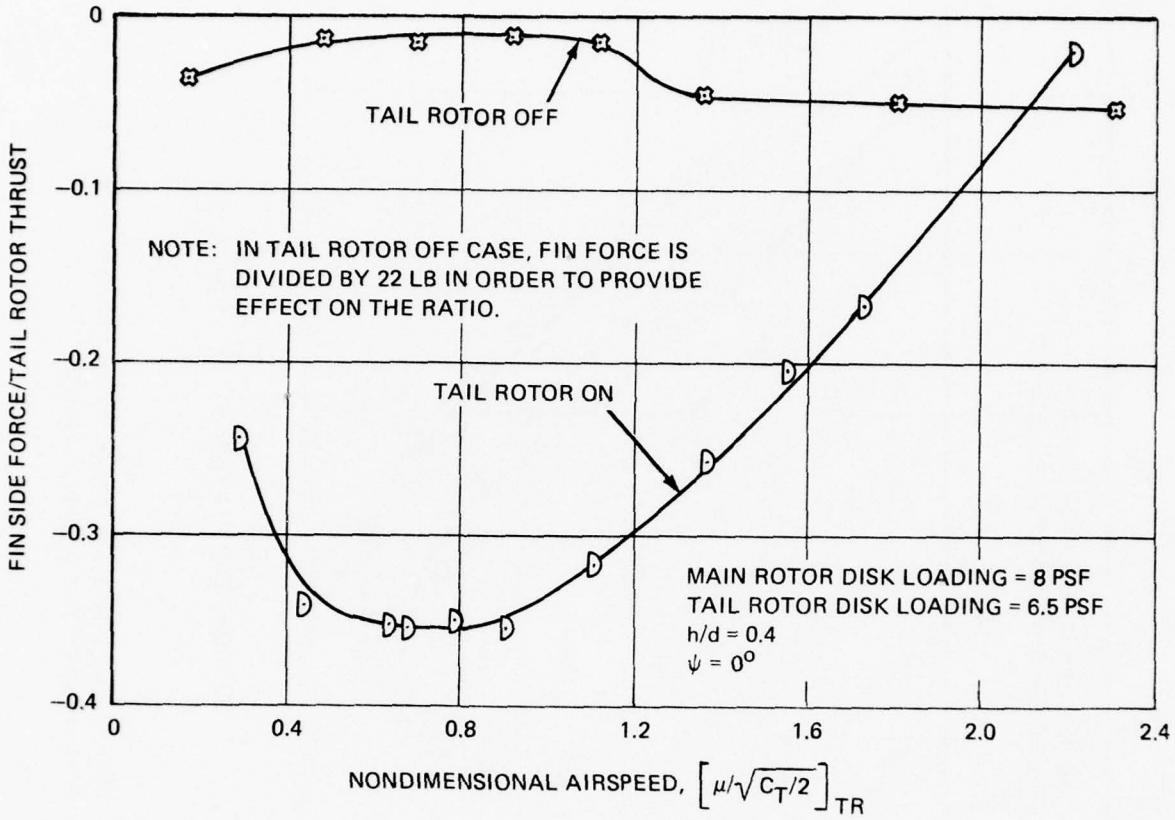

Figure 94. Ratio of Fin Side Force to Tail Rotor Thrust as a Function of Airspeed Showing Effect of Tail Rotor Presence.

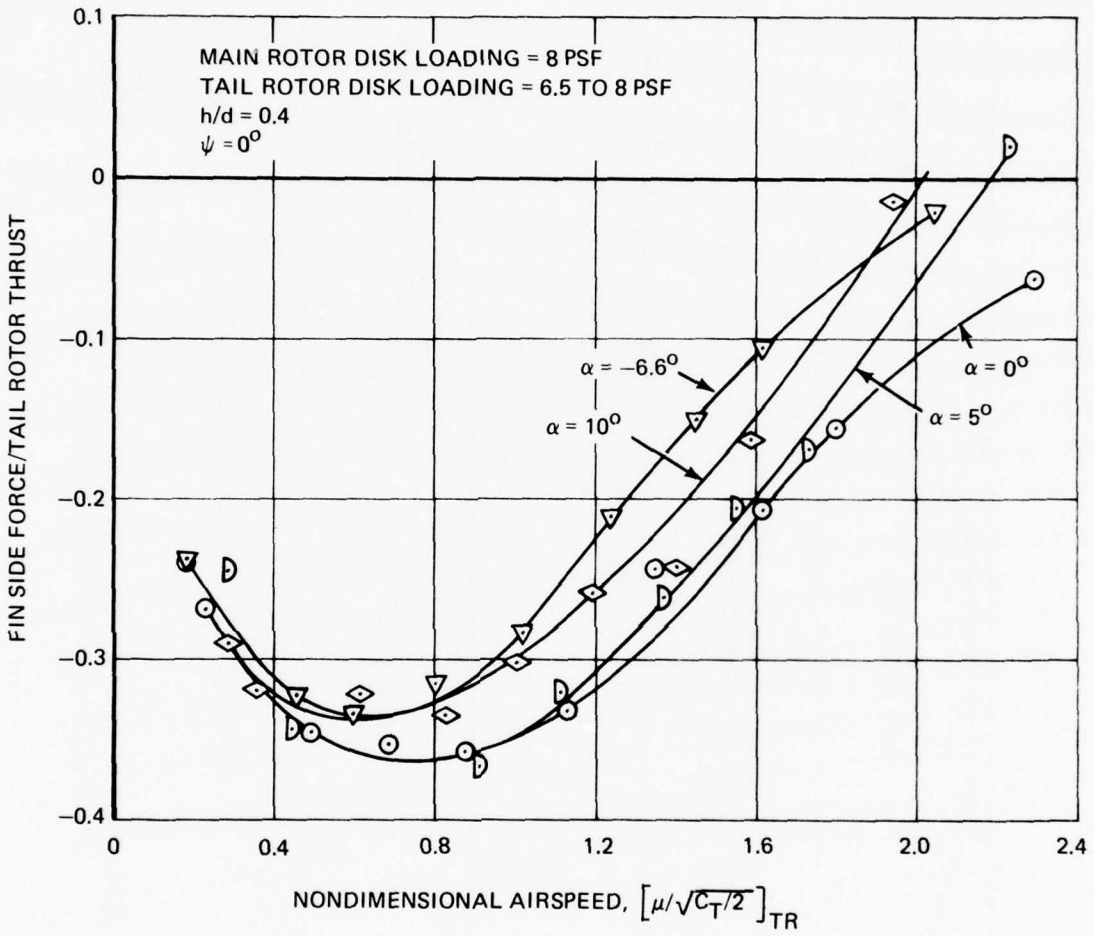

Figure 95. Ratio of Fin Side Force to Tail Rotor Thrust as a Function of Airspeed Showing the Effect of Model Attitude.

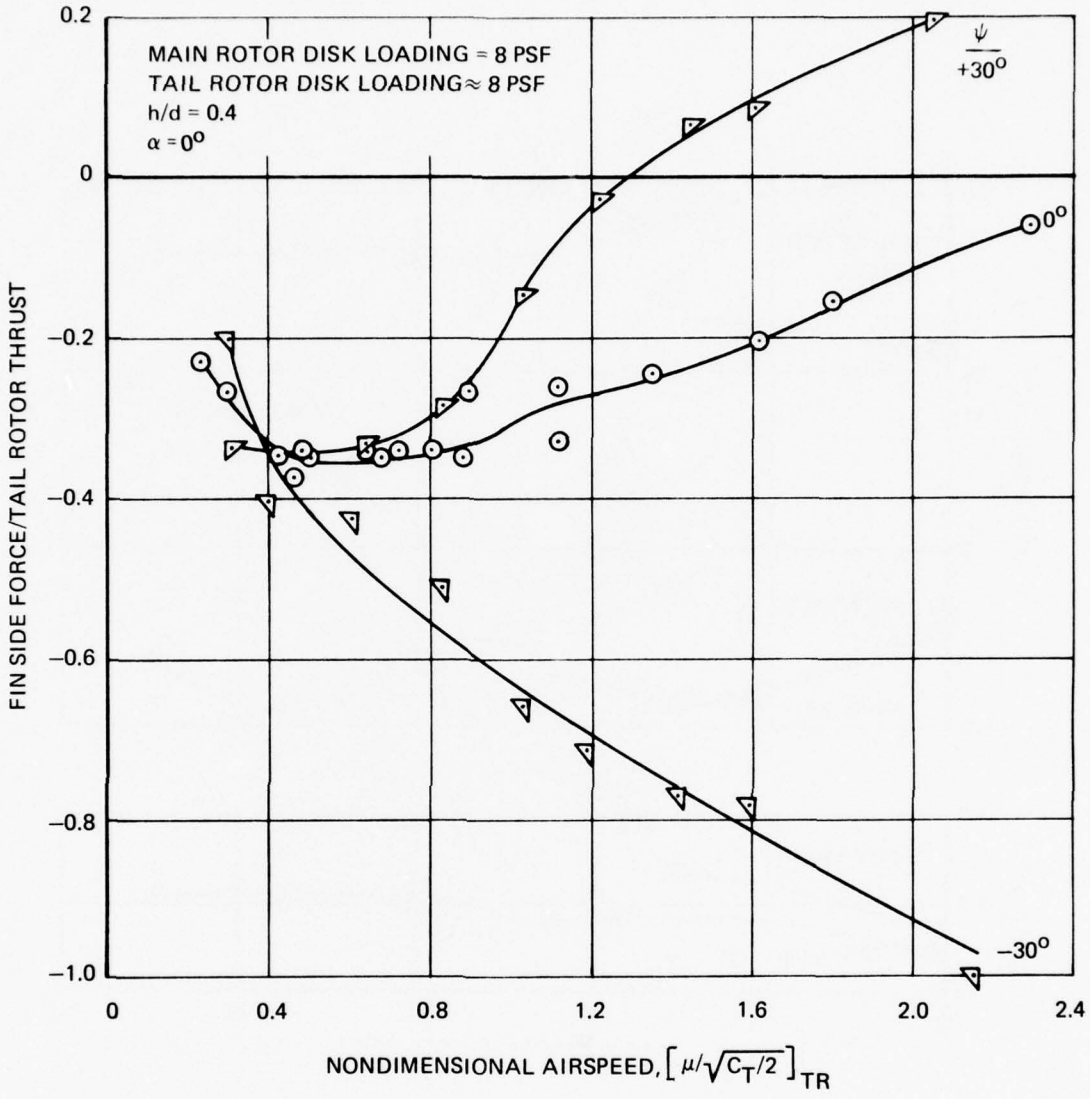

Figure 96. Ratio of Fin Side Force to Tail Rotor Thrust as a Function of Airspeed for Right and Left Wind Azimuth.

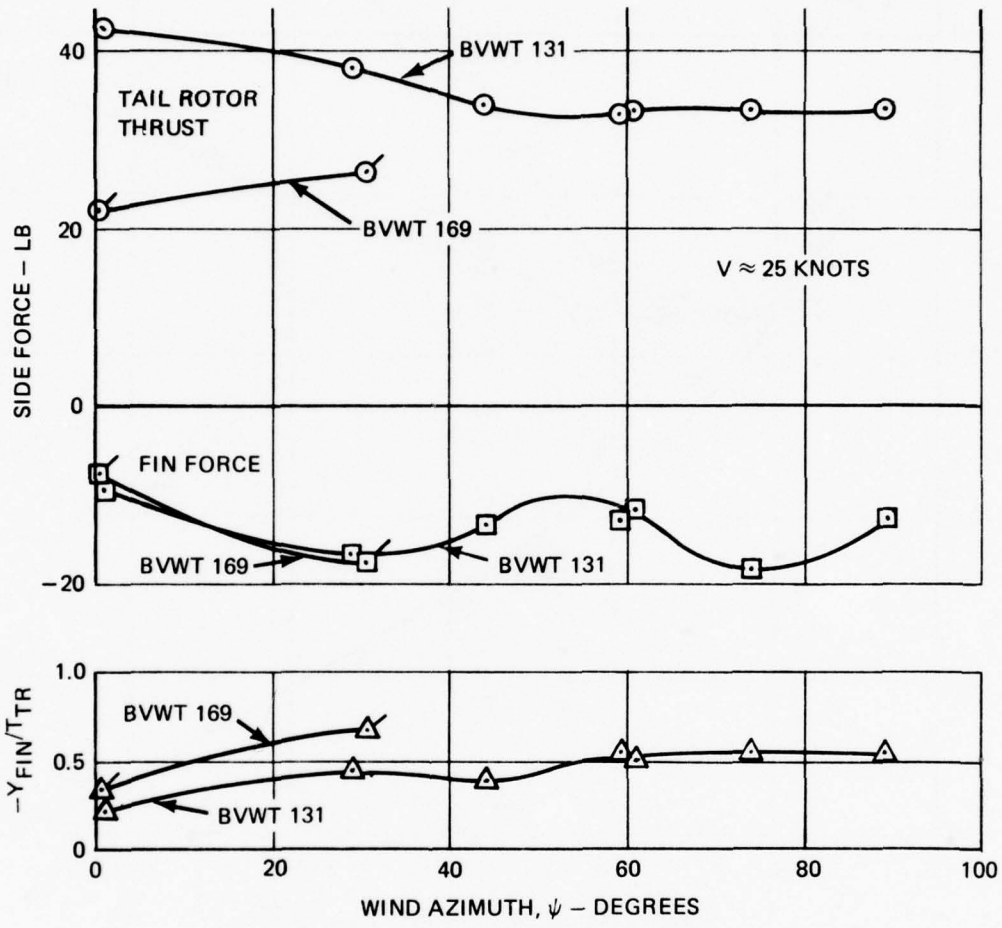

Figure 97. Variation of Side Forces With Wind Azimuth for Two Levels of Tail Rotor Thrust.

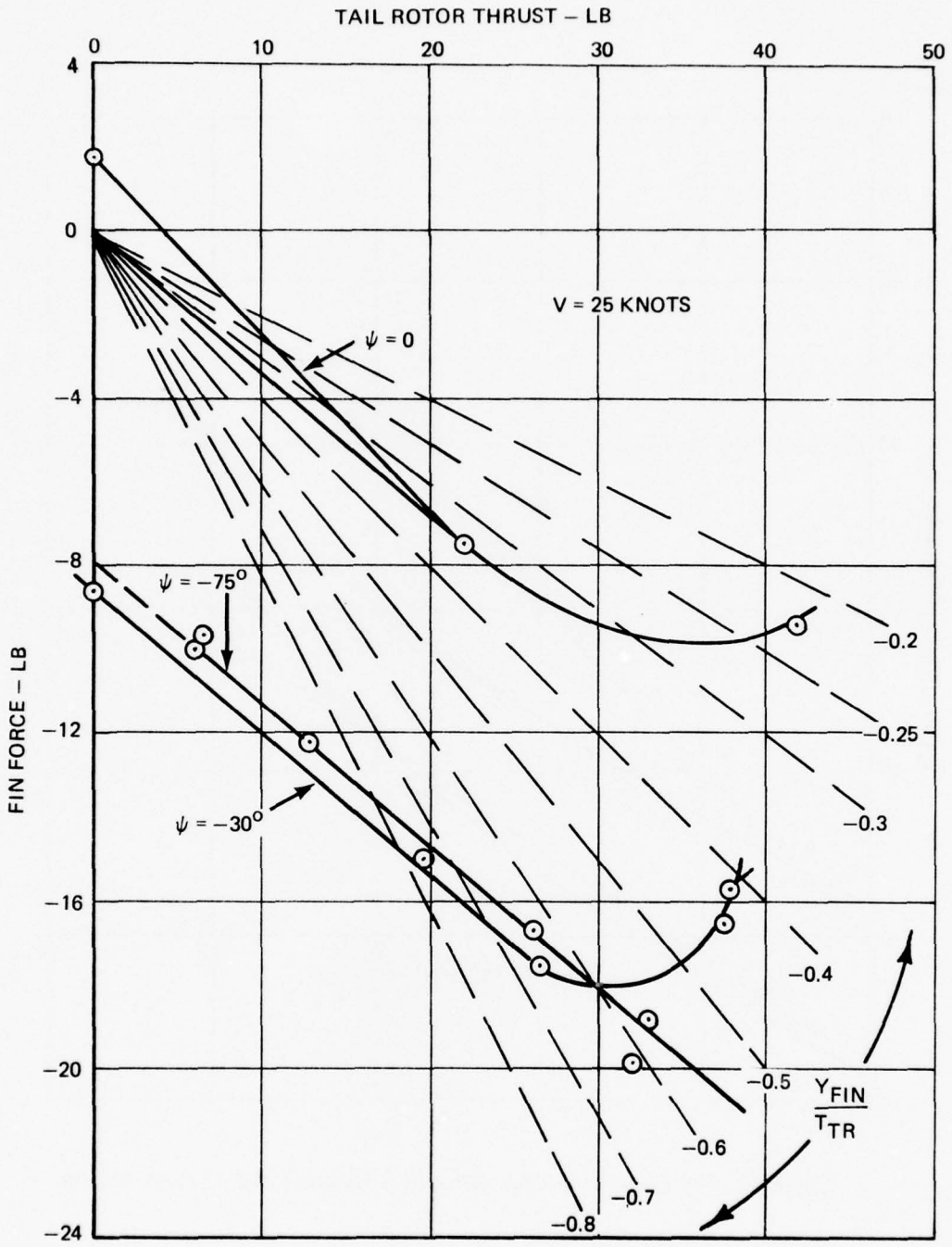

Figure 98. Fin Force as a Function of Tail Rotor Thrust.

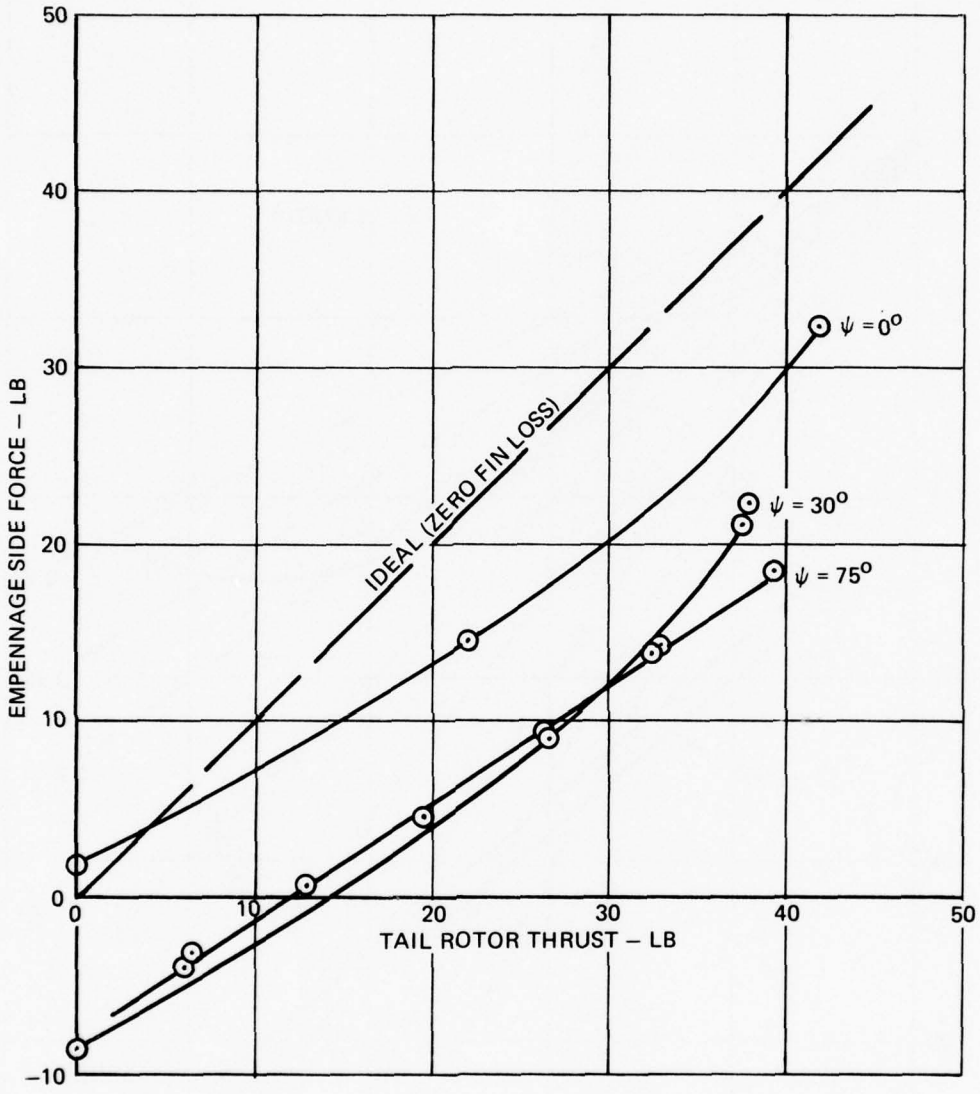

Figure 99. Net Empennage Side Force as a Function of Tail Rotor Thrust.

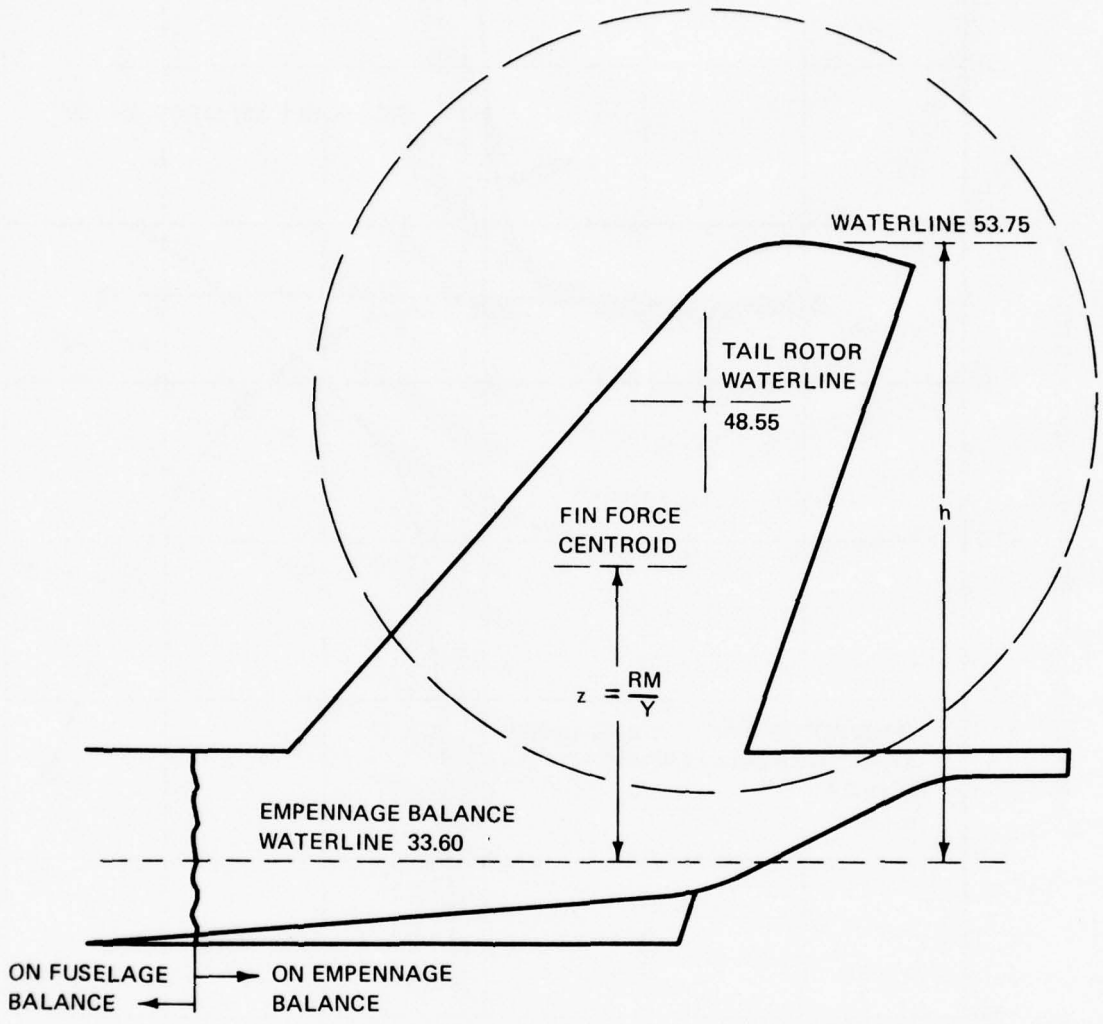

Figure 100. Fin Geometry Relating to Center-of-Pressure Derivation.

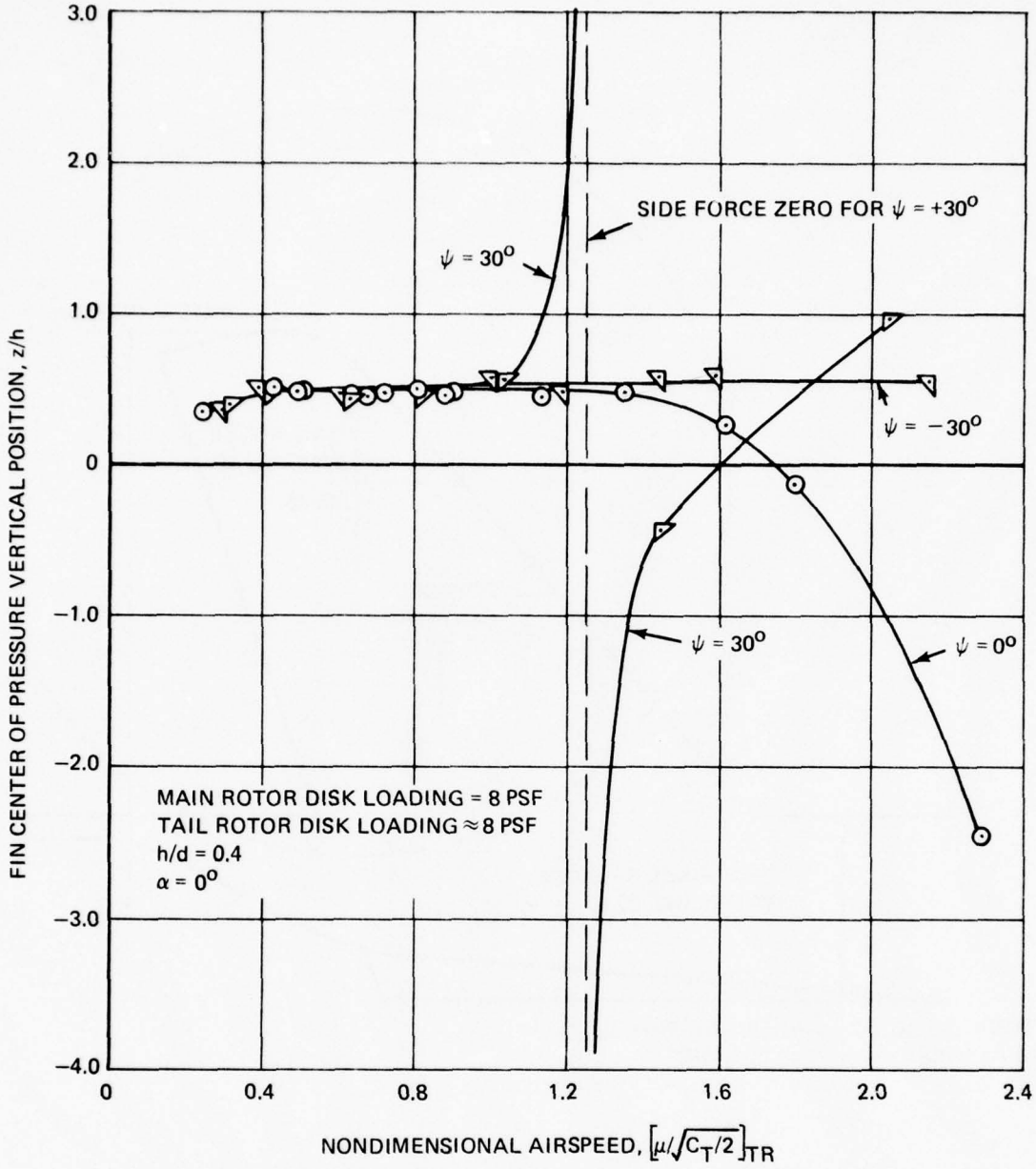

Figure 101. Variation of Fin Center of Pressure With Airspeed for Right and Left Wind Azimuth.

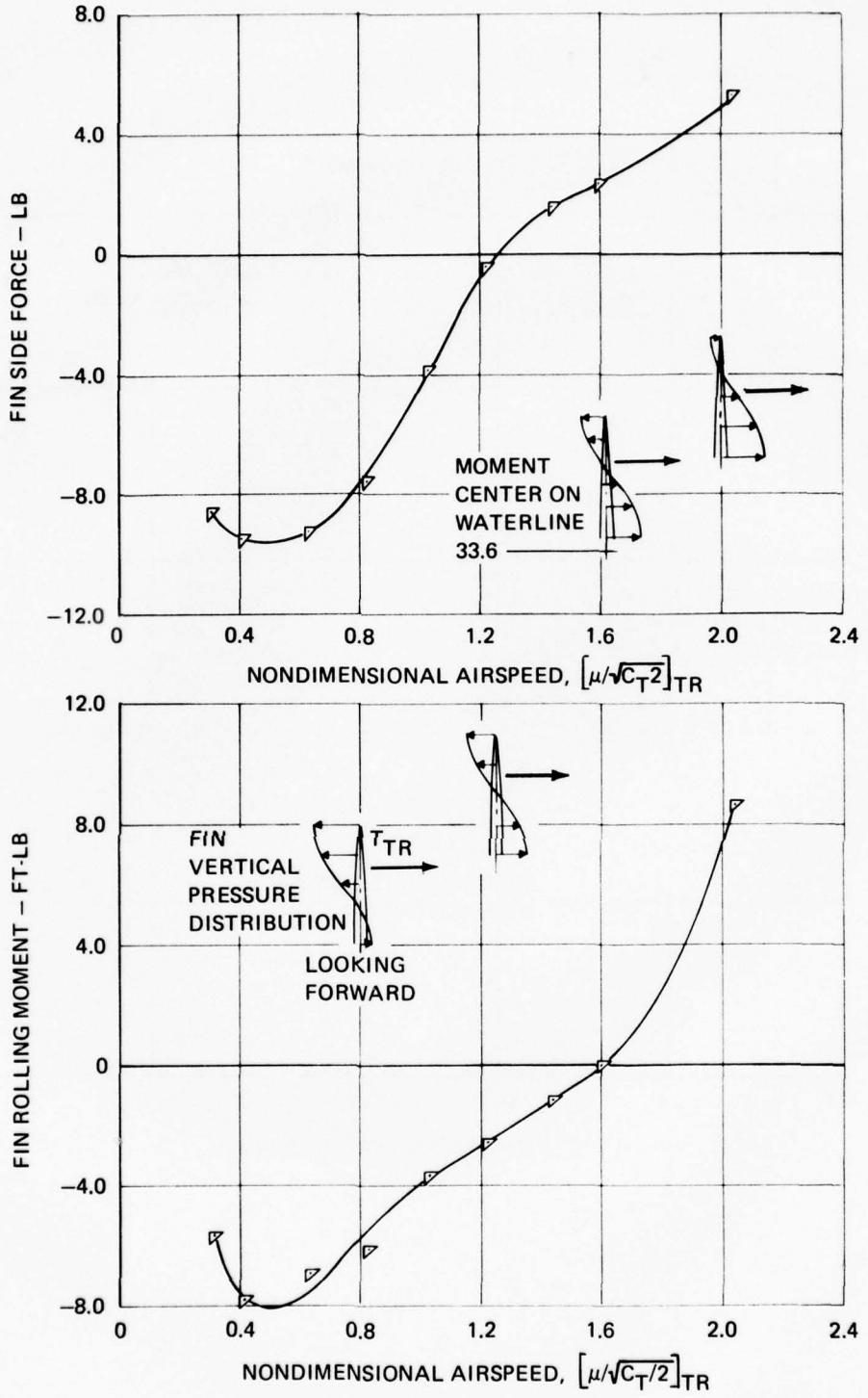

Figure 102. Variation of Fin Side Force and Rolling Moment With Airspeed Showing Implied Lift Distribution Changes for $\psi = 30^{o}$.

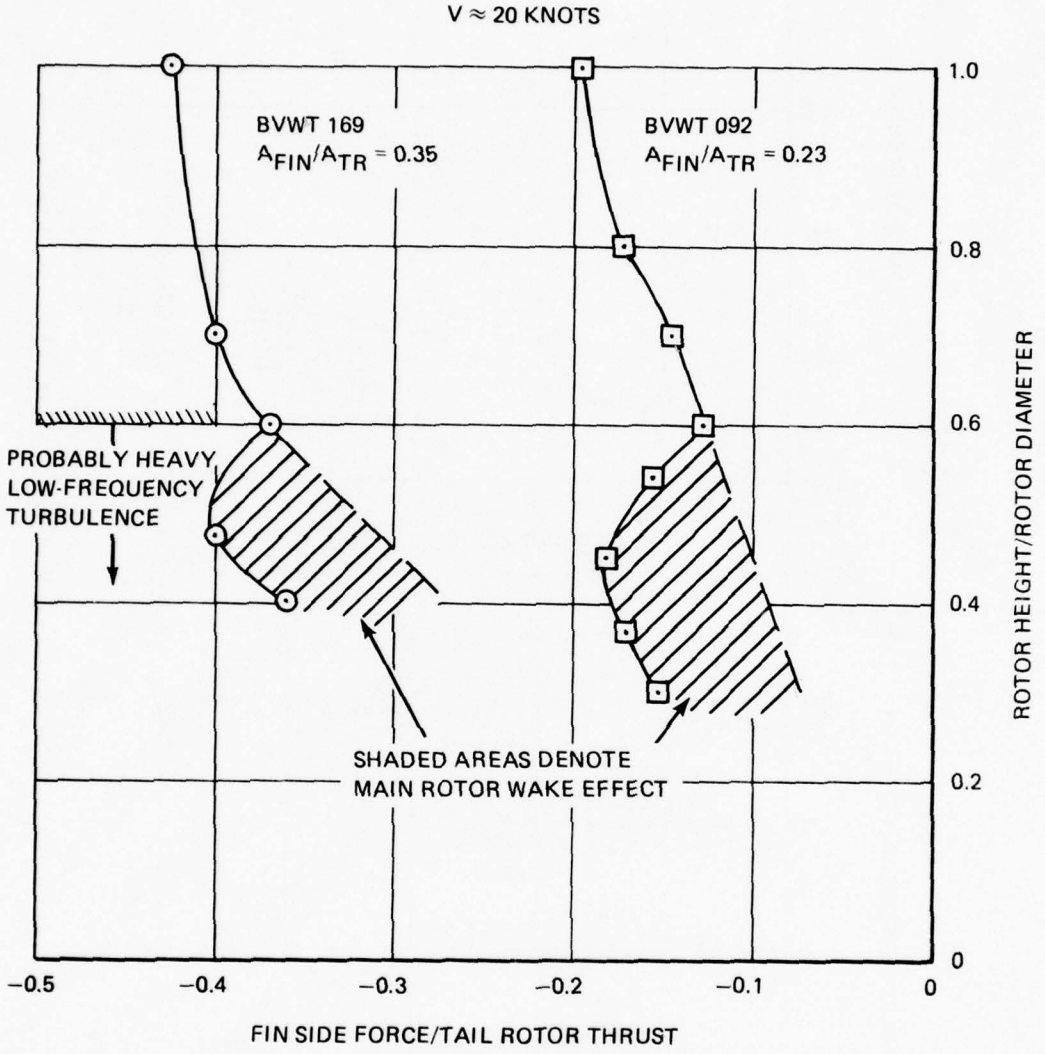

Figure 103. Fin Side Force/Tail Rotor Thrust Ratio as a Function of Rotor Height/Diameter Ratio.

TECHNICAL GUIDELINES

GENERAL

The data from the wind tunnel tests have been shown in tables and graphs and the results analyzed and discussed in the previous sections. General guidelines based upon that study have been formulated for the instruction both of helicopter design staffs and of operations planning groups. Although there are a few exceptions, the guidelines will be generally applicable to all single-rotor helicopters regardless of rotor configuration. The difference due to rotor articulation, blade parameters, and airfoil are not expected to influence the major conclusions of the study from which the guidelines were derived.

Within the test matrix, available data on configurations and conditions of the reported program were used. Additional data requirements have been identified at various places in the analysis sections and in the conclusions. Accomplishment of such test programs or analysis of other existing data will make it possible to expand understanding of the aerodynamic flow complexities and to write more comprehensive guidelines. After these programs and analyses have been completed, it would be possible to take a "cookbook" approach similar to that of the Tail Rotor Design Guidelines of Reference 10.

The scope of the guidelines is presented in Table 12, which is arranged (similar to Tab'e 2) with the first column showing the interaction and the second column listing the associated problems or interactional phenomena causing problems. Following these are two more columns showing the guideline topics categorized as design or operational. Because of the relationships between the guidelines and the underlying analysis, it has been found logical to arrange the discussion below in three basic categories: guidelines related to the ground vortex, to the main rotor wake effects, and to the fin/tail rotor area.

GUIDELINES FOR THE GROUND VORTEX FLIGHT REGIME

The only way the ground vortex effects can be avoided is to fly over them. Effects on the aircraft will be minimal at an h/d of 0.6 or 0.7 and largely gone at an h/d of 1.0 for a disk loading of 8 psf. However, the ground vortex is still present at h/d of 1.0 and must be reckoned with for its effects at or near the ground. Overflight may be completely feasible for many situations even in the war theater NOE. For a 50-foot-diameter rotor, 0.6 h/d would provide a wheel height of approximately 20 feet, which is still quite close to the ground. Takeoffs and landings can be made safely at such height. Therefore, operations can probably be adjusted to avoid the worst of the ground vortex effects. However, the essence of the NOE doctrine is the avoidance of detection by operating below the tree line and the top priority theater is Europe, where the average tree height will be moderate. This means that the real situations will compel the new high-disk-loading helicopter to operate down in the 0.4 h/d area where the ground vortex is in full fury. Operational planning, therefore, should take account of the special requirements here. New aircraft planning must develop new criteria for components and equipment and for performance and handling qualities that will best meet the needs of the environment. Not everything is known about the ground vortex and the larger flow pattern in the helicopter airspace. Enough is known, however, to establish guidelines for the operation of current aircraft, design of new aircraft, the development of new criteria, and the acquisition of an expanded data base from wind tunnel and flight measurements.

TABLE 12. AERODYNAMIC INTERACTIONS AND RELATED GUIDELINES

Interactions	Phenomenon/Problem	Design Guideline	Operational Guidelines
Rotor/Ground	Formation of ground vortex IGE main rotor power IGE hub forces and moments	Assurance of adequate control for IGE trim changes	Assurance of adequate power margins Selection of optimum takeoff corridor Minimization of dust cloud intensity and debris entrainment Effect of ground vortex wake on the selection of parked aircraft locations and the possibility of significant vortex persistence Effect of ground vortex wake on other aircraft in formation flying
Rotor/Fuselage	Vibratory pressures Fuselage loads Rotor power	Avoidance of high vibratory surface pressures Design conditions for adverse pressures Avoidance of adverse rotor system loadings	
Rotor/Fuselage/ Ground	IGE fuselage download IGE fuselage moments	Selection of design parameters to minimize download and increase IGE upload Implications of ground vortex flow for (a) Cooling air inlet location (b) Low airspeed instrumentation (c) Weapon launch (d) Engine air induction	Use of ground effect to avoid download
Rotor/Empennage (Tail Rotor, Pylon, and Stabilizer)	Wake structure Wake-induced loads Pressures on stabilizer and pylon	Selection of flow-altering devices to minimize wake problems	
Rotor/Empennage/ Ground	Tail rotor/main rotor mutually interactive loads Adverse fin load	Effect of fin stall	

Control of the Aircraft

There appears to be ample cyclic pitch present in the system to accommodate the trim changes on the lateral axis due to the ground vortex passing under the rotor. The problem is the rate of pitch change with speed, which is about 1/2 degree per knot change. There is no way to program this easily because it would take an impossibly long boom with sensor to pick up the vortex approach before it came abreast of the rotor. A heavy dose of rate feedback in the SCAS for the narrow range of speed involved was found effective in the YUH-61A, where double the normal gain was used. It was also found that repeated exposure to flight through the vortex developed an anticipatory technique in the pilots such that the upset was much less. However, the workload would be intolerable without substantial assists to the pilot, especially when hovering in gusty winds near the vortex passage speed.

Power Margin

Although the power rises substantially moving out of hover, it is extremely doubtful that it will exceed the hover-out-of-ground-effect value even for the lowest h/d and highest disk loading values contemplated. Thus, it will never be critical for power and the OGE design power margin will prevail.

However, when operating near the OGE hover ceiling, the power margin offered to the pilot by ground effect would be largely taken away by a small amount of wind. The result would be a high workload in maintaining altitude at the same time moment equilibrium is demanding an unusual pilot effort.

Takeoff Path Selection

As mentioned before, the easiest way to avoid the ground vortex effect is to fly over it where this option exists. The best takeoff path would be a steep climb to 20-to-30-foot wheel height, then an acceleration to climb speed. The reverse procedure would be used for the approach to landing. There is some evidence that negative attitude and hence high acceleration lessens the rolling moment distortion, but there is insufficient data to describe the trend at the high altitudes of deceleratory flight.

Another way of minimizing the ground vortex effect is to place the aircraft in a sideslip so that the major upset appears on the pitch axis instead of on the roll axis. Because of the much higher pitching moment of inertia, the aircraft response will be appreciably less. The model was found to have a very flat variation of rolling moment with speed for a ψ of -30 degrees. The optimum value will vary according to the phase angle between feathering and flapping. This was approximately 70 degrees for the hingeless rotor of the model. More work is required to gain the required understanding.

Suffice it to say that for hovering in ground effect in a 15-to-20-knot wind there will be two values for easiest station maintenance, depending on the rotor articulation.

Special Design Considerations

The expected NOE operation of the helicopter for sustained periods in the ground vortex flow has some profound implications for the design of certain components and equipment. Chief among these will be engine air induction, cooling air induction, low airspeed instrumentation, and weapons launch systems.

During the UTTAS program the ground vortex flow was observed to transport exhaust gas forward and up to the inlet with consequent severe temperature transients in the inlet. These transients caused engine surge on a number of occasions. The exhaust ingestion severity will be a function of speed, pitch attitude, height, disk loading, and exhaust velocity. Inlet duct and exhaust pipe locations and geometry seem to have little influence except for the nozzle areas that determine exhaust velocity. Exact boundaries for zero ingestion are not yet determined in terms of the above parameters.

The other side of the problem is the susceptibility of the engine to surge from flow distortion of this type. Design criteria that recognize the flow irregularities of the ground vortex and the possibilities of ingestion are needed so that engine design will properly allow for this possibility. Before this can be done the problem needs to be better understood for both current and new aircraft and the aerodynamic data base needs to be expanded.

Fresh ambient air is always required for the cooling of the engine compartment, the transmission, and various heat-generating equipment. The circulation of exhaust, both the ground-reflected hover type and the ground vortex flow at 20 to 30 knots, poses a serious threat to adequate cooling in the NOE environment unless taken into account in the design phase. This cannot be done, however, until a data base is established regarding temperature distribution prevalent for various conditions.

It is very possible that NOE will ultimately require low air data instrumentation to provide displays of airspeed and rate of climb from hover through transition. The highly irregular ground flow poses a challenging problem for location of the devices that must sense the remote relative wind magnitude and direction.

Weapons launch within the NOE would encounter severe and fluctuating wind gradients from the ground vortex flow. At one location for a disk loading of 8 psf and an h/d of 0.33, mean velocities of about 100 feet per second were measured with fluctuations of ± 100 percent, and this was not in the vortex itself.

Special Operational Considerations

Apart from the operational aspects of power control and maneuver already discussed, there are other special considerations that may be important in NOE planning. These include the dust cloud, the noise signature, debris entrainment, and the ground vortex effect on nearby helicopters either in formation or parked on the ground.

As pointed out earlier, the ground vortex maintains a well-defined identity and considerable strength even with the rotor one diameter overhead. The rate of change of vortex strength with rotor height has not been established. Certainly for substantial heights, the ground vortex will

generate a large, dense dust cloud proportional in its severity to disk loading. Although the European theater is not an arid region, dust signatures of the magnitudes expected may preclude certain tactics and the phenomenon therefore needs quantitative definition.

An associated phenomenon that surfaced during Army testing of the YUH-61A is entrainment of rocks and other surface debris by the high-velocity winds associated with the ground vortex flow. The case in point involved high-altitude, hot-day running takeoffs with marginal power above a broken surface runway. The testing had to be terminated because of the barrage of high-velocity paving fragments that pelted the airframe. This is perhaps an extreme example but rock-strewn areas are common in nature and debris is always found in battle zones.

Noise has been the subject of much research for avoidance of both internal annoyance and external detection. Negligible effort has addressed the noise increase with the passage of the ground vortex. This has been observed in the powered wind tunnel model tests but measured data have not been analyzed. It is not clear whether the increase is rotor noise or separate aerodynamic noise from the vortex. It intensifies as the vortex passes under the rotor leading edge and peak values (as heard) are associated with positive angles of attack and low h/d, providing maximum containment. The relevance of ground vortex related noise to detection should be determined.

During the Indo-China war, landings and takeoffs of the UH-class helicopter in formation were common, with many aircraft close together on the ground and in the air at the same time. Whether the scenario for the potential European conflict envisions such operations is not clear. If such is the case, the use of the new higher disk loading helicopters with higher, more concentrated rotor wake energy poses questions of serious aerodynamic interference between adjacent helicopters due to the ground vortex. The vortex forms the classical bow wave in front of the helicopter at a distance depending on speed. The strength of the vortex at remote lateral distances has not been determined but flow visualization using smoke indicates significant energy transfer along the axis of the vortex. The potential upsets to helicopters flying into the ground vortices of the aircraft ahead may be large. Visibility limitations and debris entrainment with respect to parked aircraft are other potential hazards.

Need for Research on Ground Vortex

The questions raised above outweigh the firm design and operational guidance provided. That is the state of the art. Much research is required to obtain the needed data base.

GUIDELINES FOR WAKE EFFECTS ON THE AIRFRAME

Modern design trends toward high disk loadings and configuration compactness lead to greater severity in wake-induced loadings on the airframe. Compactness will often mean closeness of the rotor to the fuselage with the possibility of adverse blade-to-surface interactions. This can result in high vibratory aerodynamic pressures on the airframe surfaces, particularly the forward crown. Also, the impulsive airloads impacted to the blade will excite its bending modes. This can have two effects; first, possible aggravation of the blade fatigue loadings and second, an increase in the hub vibratory loads.

Another effect to be concerned about in selecting the rotor-to-fuselage gap is the interaction of the hub flow with adjacent fuselage flows over the aft crown. Apparently the large separated area immediately aft of the hub presents a fall of pressure to the oncoming flow above the fuselage. If the hub is quite low, any unfavorable pressure gradient already existing on the aft crown will be intensified and the flow will experience an early separation. Usually the part of the surface flow just aft of the shaft and pitch links is separated to begin with and the presence of the nearby hub flow will expand this separation to the entire aft crown surface area.

If the hub is higher, a marginal situation can prevail where separation occurs in an intermittent fashion. Here flow restoration occurs as lateral inflow brings in fresh air to the separated areas. Above this height the flow becomes stable. The threshold will depend upon surface gradients, i.e., the contour, probably hub frontal area, and possibly blade root cutout.

In the case of strong intermittent separation, a considerable mixing of the flows takes place resulting in a rotor/hub wake with large low-frequency flow angle and velocity oscillations that generate upsetting loads on the fin, stabilizer, and tail rotor.

Vibratory Surface Air Loads

When the rotor is about one chord length above the forward crown, local pressures up to 0.1 pound per square inch will occur for disk loadings around 8-10 pounds per square foot. This will flex the skin, producing high-frequency noise of annoying magnitude. Noticeable but less bothersome is a drumming of the surface at low (rotor) frequencies. Damping treatments will alleviate the high-frequency problems. Raising the rotor to two chord lengths apparently reduces the low-frequency noise to a "not noticeable" pilot rating, as the rotor frequency vibratory pressures are reduced by 50 percent.

Structural Loads

The change in mechanically transmitted vibratory loads through the blades and hub is not clear from the results obtained in the test. Certainly this will depend upon a blade's structural dynamic properties; therefore, hingeless and articulated systems will differ significantly in the susceptibility to fuselage proximity with regard to blade bending and transmitted loads to the airframe.

Another effect to be concerned about in the blade excitations is the transmission of torque oscillations to the drive system dynamics.

The most adverse flight condition for vibratory surface pressures and related blade loadings is maximum forward speed in a descent at maximum gross weight. The configuration should therefore be validated for this condition using wind tunnel test data and appropriate structural analysis.

Wake Effects

There are two ways to smooth out the wake to avoid adverse intermittent loadings on the empennage. One is to introduce relatively fresh air behind the hub with a hubcap. This tends to damp out the fluctuations in the hub wake due to interaction with the fuselage flow. The

second approach is to contour the aft crown in such a way as to insure positive pressure gradients directly under the root cutout where the negative pressures behind the hub are large. The first approach will work best for a rotor in a very low position, such as one chord length high at the cutout. The second approach has worked well for a rotor two chord lengths high and may work also for a lower position. It is the preferred solution since it offers lower drag as well. It is emphasized that both approaches must be developed in the wind tunnel with the rotor on and turning.

Another approach is simply to raise the rotor until the hub flow is so remote as to avoid interaction with the fuselage flow. This probably is a higher drag solution, however, because of the longer shaft and/or pylon.

The hub wake center passes to the left of the empennage for all trimmed flight conditions. It is closest to the tail rotor and fin for positive aircraft angles of attack typical of descent conditions. Putting the tail rotor on the right side of the fin probably would substantially reduce the wake effects on the lateral axis. However, this benefit is offset by the tractor installation with regard to fin loss.

GUIDELINES FOR THE FIN/TAIL ROTOR

General

In 1974, a compendium of tail rotor design guidelines illustrated by many generalized design charts was issued by the U.S. Army Air Mobility Research and Development Laboratories. This is the "Tail Rotor Design Guide" (Reference 10). That document summarized all the pertinent data available at the time and generalized it for broad application to preliminary design. In addition to an extremely comprehensive treatment, it is noteworthy in casting the tail rotor design problem in the context of the complex interactive flow pattern in the empennage environment. Important interaction-related aspects are addressed, including tail rotor placement versus main rotor and fin, direction of rotation, critical IGE hover height, main rotor/tail rotor power interactions, and critical azimuth for thrust and power. This is also the reference and context for the discussion and contributions of this report relative to the fin/tail rotor aerodynamics.

Where the Reference 10 guidelines emphasize tail rotor design, however, the contribution of this study to design guidance extends to design of the whole empennage. It makes no sense to design the tail rotor with great care and attention to detail and then have to increase its size by 50 percent merely because of the presence of the fin and its adverse load. The empennage – tail rotor, fin, and stabilizer – must be designed as a subsystem in itself for good aerodynamic efficiency and freedom from adverse interactional effects. This is mandatory with the large fins resulting from modern requirements for directional trim in the event of tail rotor failures.

Fin Designed for Tail Rotor Loss

Figure 104 illustrates the typical lateral-directional trim that could be provided by various sized fins in the event of complete tail rotor loss. The graph shows bank angle as a function of fin side area, and rate of climb; the associated sideslip angles are noted by the dashed lines. The ratio of fin area to tail rotor disk area is noted parenthetically for each fin area.

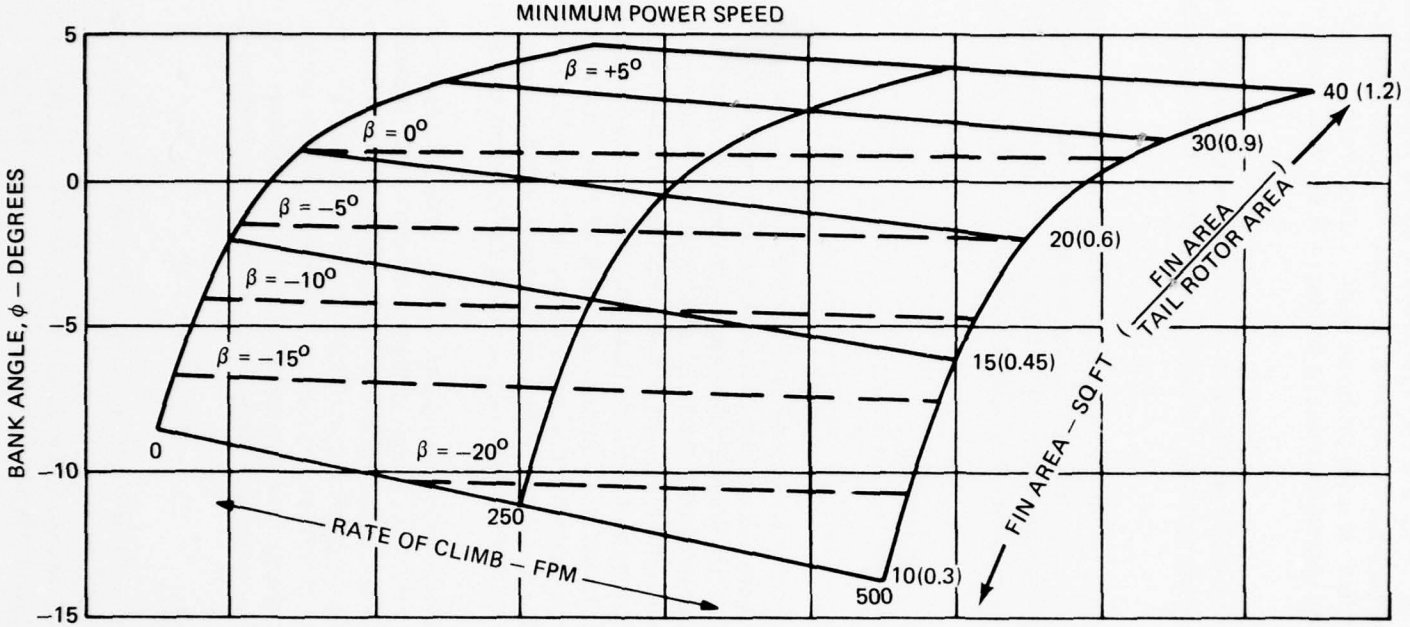

Figure 104. Trim Bank Angle and Associated Sideslip Resulting From Complete Loss of Tail Rotor as a Function of Fin Area for Various Rates of Climb.

The cited area ratio has been less than 0.3 prior to the military requirement for safe flight without the tail rotor. The graph indicates that very large bank and sideslip angles will result from low ratios. Pilots are accustomed to trimming bank angle to zero by horizon reference in visual flight, leaving sideslip as the dependent variable in normal situations with the tail rotor operational. Reversion to ball-and-needle flight reference at such extreme aircraft attitudes is of questionable acceptability, especially with collective manipulation needed simultaneously to maintain altitude or to descend into the emergency landing area.

A need clearly exists to determine by flight investigations the limitations on trim change and the final trim itself for this emergency mode of flight. Whatever is found, however, a trend to large fixed fins is still expected for future helicopter design. This means larger adverse fin interaction with the tail rotor and larger frontal area presented to winds from the side. Hence, there will be a more serious conflict in design philosophy imposed by the large fin needed for acceptable flight without the tail rotor on the one hand, and by the need for minimal adverse fin load due to the tail rotor's presence on the other. Design studies are needed to examine alternatives to the fixed fin, such as fin with rudder, all-movable fins, and even more sophisticated schemes like circulation control. Success here would be measured by the smaller fins and, by extension, smaller tail rotors permitted by lower fin interference.

Adverse Fin Load

The adverse fin load in sideward flight is due to two mechanisms. The first is the flat plate drag load due to the fin side area presented to the relative wind. The second is the generation of pressure on the fin surface adjacent to the tail rotor as the surface is washed by the induced flow of the tail rotor. This pressure will be positive for a tractor tail rotor and negative when the tail rotor is installed on the opposite side of the fin in a pusher configuration; it will oppose the tail rotor thrust in either case. The latter effect is significant even in the nonsidewind cases of $\psi = 0$ and 180 degrees azimuth.

The probability of larger fins will demand more attention to empennage design to minimize sideload from wind pressure and to minimize the adverse sideload due to the tail rotor flow. Fundamental studies of the empennage layout are required to determine configurations showing more acceptable adverse loads like 5 percent of tail rotor thrust, instead of the anticipated 50 percent or more with the larger fins in conventional installations. Consideration should be given to radical departures from the traditional empennage configuration involving wide separation of the elements, movable geometry, and nontraditional locations. All-movable fins seem at first glance to be a step toward greater complexity, but if the tail rotor size is reduced 50 percent, the additional fin weight may be worth it.

The data previously shown in Figure 98 give some indication of the penalty of a large fin area presented to the sidewind. It is seen that a 9-pound adverse fin load exists at $\psi = -30$ degrees for zero tail rotor thrust. At 35 knots and a higher yaw angle, the fin load would approach 20 pounds. This is quite a penalty for the tail rotor to overcome when the requirement is 30 pounds in the opposite direction. The tail rotor would have to provide 50 pounds instead of 30, for a penalty of 66 percent. This makes the notion of a movable fin feathering into the wind much more attractive.

Before such studies can be undertaken, more base data are required. The fin force/thrust relationships must be obtained up to 35 knots and through the full azimuth range at all speeds for the high fin-area-to-tail-rotor-area ratios that are contemplated.

Fin Stall

The loss of lift (fin force) in Figure 98 is not classical wing stall, but apparently a disattachment of the flow on the tail rotor side of the fin under the influence of the pressure drop across the rotor. This will increase with disk loading until essentially all the flow coming around the fin will go directly to the rotor disk and not follow the fin surface. Design programs should include wind tunnel tests to understand this process for any empennage configuration.

Although the stalling reduces the adverse fin load, it appears to be quite unsteady in the flow visualization and is therefore to be avoided in the design lest it result in intermittent upsets on the directional axis. The flow separation would be completely avoided by an empennage configuration with widely separated fin and tail rotor. The critical separation distance needs to be examined as a function of tail rotor thrust and other relevant parameters.

Dynamic Environment

These wind tunnel tests and others of the same type indicate by dynamic flow measurements and by flow visualization that the flow environment of the empennage, especially at low speed, is highly unsteady and generally unfavorable to ride quality and aircraft steadiness. Nap-of-the-earth operational requirements will make this aspect a primary concern of the designer. The unsteadiness will be a function of disk loading, height above the ground, and wind direction and velocity as they affect the main rotor wake orientation with respect to the empennage. The flow of the ground vortex, which is dependent on main rotor wake energy, will also cause much unsteadiness.

The general directions below are presented for empennage design for avoiding roughness and insuring smooth, steady flight in the lateral-directional mode:

1. Helicopters that fly close to the ground (NOE) should have as low a gross weight as possible. The disturbance level is probably a function of the total energy in the downwash. The smaller helicopter will also fly at a higher h/d for the same wheel height.

2. Disk loading should be low to reduce the velocities in the rotor vortex system and in the ground vortex as well.

3. The vertical position of the tail rotor should be selected for steadiness as well as maximum thrust. In Reference 10 this is not considered. Probably the highest position will be best for steadiness.

4. The widest separation between fin and tail rotor should be maintained to eliminate the intermittent flow separation.

5. Dynamic isolation of the tail rotor or of the entire empennage to minimize transmission of jolts due to turbulence is a subject worthy of study.

Forward Flight Considerations

The interaction of concern in forward flight is the main rotor wake impingement on the fin and tail rotor. Smoothing of the wake disturbances has been discussed previously in terms of proper design in the hub/pylon/fuselage area. However, there will always be the probability of upsets in turbulent atmospheric conditons, and the susceptibility of the empennage should be minimized as much as possible. The following design approaches should be considered in this regard:

1. Installation of the fin and tail rotor as far as possible to the right, away from the center of the hub wake.

2. Isolation of the tail rotor so as to filter out the sharp, pulse-like loads arising from turbulent inflow.

CONCLUSIONS AND RECOMMENDATIONS

GENERAL

Problems of aerodynamic interference have been addressed within a generalized philosophical structure of flow interaction phenomena. Under this approach, the analyses of this report have covered five interactions observed and measured during Boeing Vertol Wind Tunnel Test 169. This test, however, was not undertaken with such general aerodynamic objectives but was designed to solve three specific problems of the prototype aircraft. The data are therefore somewhat constrained to those purposes. The need for more data, i.e., for expansion of the test matrix and/or its extension to other significant variables, is evident.

As with other generalistic investigations, the principal results are a sorting out of the interplay of variables, improved understanding of the physical mechanisms, more comprehensive definition of what is not known, and, finally and most importantly, what more needs to be known so that adequate design and operational guidelines may be formulated and so that a generally applicable analytical methodology may be developed.

In support of the latter, the requirement is a complete flow description of the interaction of interest, which will include flow visualization in association with data measurements. It is emphasized that the dynamic aspects must be carefully considered. If there is one lesson from this work, it is that all the helicopter aerodynamic interactions are extremely unsteady, showing time-variant components that rival the mean in magnitude. Typically, the steady and unsteady flow pattern will change rapidly with changes in the aircraft trim airspeed and often in a highly nonlinear manner.

Formerly, complex interactional problems were addressed in the most simplistic manner emphasizing the steady state aspects. This was due entirely to a lack of adequate experimental tools and techniques necessary to observe and measure three-dimensional dynamic flow. A classic example is hub drag, which for years has been extensively studied in an empirical manner as a steady state problem with the unknowns categorized as interferences. It is known now that the hub area involves one of the most complex interaction flows on the helicopter, which can be influential in many other problem areas. As an example, a design acceptable for hub drag does not necessarily guarantee a trouble-free wake nor is the reverse true. The latter was clearly demonstrated by the use of the hubcap, which made the wake much smoother, thereby curing a lateral upset problem. However, it still showed a performance debit because of higher overall drag.

The conclusion is also very evident that helicopter airframe aerodynamics is fully as complex and problem-fraught as the aerodynamics of the rotor, which has received almost exclusive attention and relatively lavish funding for many years. One of the principal lessons derived from recent aircraft development programs is that the airframe and its family of interactions merit an increase in emphasis and priority and a more deserved share of the R&D funds available.

Specific conclusions and recommendations within each interaction category are offered in the following paragraphs in regard to data basis, theoretical aspects, design criteria, operational implications, and future programs.

ROTOR/GROUND INTERACTIONS

The wind tunnel data have confirmed the observed effects of the ground proximity during transition. The chief aerodynamic feature of the flow is the ground vortex. It has been identified and tracked by flow visualization using smoke and its occurrence correlated with loads arising on the rotor and airframe. These results agree well with flight observations made during the UTTAS program.

This will remain a regime of flight fraught with many potential problems until the ground vortex and its interactions with the rotor and airframe are understood sufficiently to permit mathematical models of the flow to be made.

The design of all subsystems that use external air must account for the actual qualities of the surrounding air, i.e., velocity, temperature, direction, and periodicity. Standards must be developed for the operation of air-using systems in this essentially unfavorable environment. Also, tactical planning and doctrine should realistically account for the aerodynamic environment insofar as it contributes to noise, dust, debris, and interference with other aircraft. NOE operations cannot attain their full potential until there is a full accountability for all these aspects.

The data base is very sketchy at present. Detailed measurements are needed for the ground vortex and its flows induced at the rotor and on the airframe. The constituents of the unsteady part need to be determined and related to the problem parameters. Initially, the data should be obtained for the rotor alone, and then the effect of the fuselage presence should be determined.

In addition to the generalized flow investigation, the following specific items of work are needed:

1. Better definition of the data trends already established, i.e., more closely spaced data points.

2. Extension of the work to the complete range of wind azimuth and velocity.

3. A more accurate trend with rotor height for all the parameters of interest, including the unsteady components.

4. Determination of the best data sampling and averaging techniques.

5. Detailed study of the formation of the rotary-wing tip vortices and their interaction with the ground vortex and the tail rotor flow.

6. The persistence of the ground vortex disturbance after the helicopter leaves the airspace and the vortex generation ceases.

7. Measurement of the flow paths in the vortex flow associated with exhaust ingestion. Identification of influential design parameters.

8. The magnitude of debris entrainment as high ground vortex velocities sweep the ground.

9. Evaluation of the dust cloud buildup under various conditions of the ground vortex occurrence.

ROTOR/FUSELAGE INTERACTIONS

The narrow fuselage-to-rotor vertical gap resulting from the UTTAS program requirement for transportability without rotor disassembly proved to be impossible to sustain in the configuration. Some of the adverse interactions were discussed in this report. Although some trends have been established, there is still a general lack of design guidance in placing the rotor with respect to the fuselage. The following aspects of the problem should be investigated:

1. The change in blade airloading and the associated change in fuselage surface loading as the blade passes over the crown.

2. The effect on these changes as crown cross section and curvature are varied for different rotor heights.

3. The hub loads that result from these interactions and the consequent vibratory loads. These will vary with blade parameters such as hinge offset and number of blades.

4. The increase in blade bending stresses. These will vary with blade construction so several types should be considered, i.e., flapping rotor blade, hingeless rotor blade, teetering rotor blade, etc.

5. The changes in the patterns and stability of the flow above the aft crown and in the hub wake as geometrical changes are made to the crown contour and height.

These experimental investigations are needed to complete the technical basis for mathematical models to permit prediction of the effects for generalized application to design. The attainment of reliable standard analytical and testing methodologies is a goal to be sought both by the contractor and the customer.

ROTOR/FUSELAGE/GROUND INTERACTIONS

The ground vortex produces measurable effects on the fuselage lift and moments. A sharp loss in lift was measured for the YUH-61A fuselage in transition at constant wheel height. It is a possibility that this would occur intermittently under high and variable wind conditions and significantly contribute to the pilot workload and fatigue. If so, avoidance of flat-bottomed fuselages may be necessary for helicopters designed for prolonged NOE flight. The following research is necessary:

1. Evaluation of forces and moments on various fuselage shapes in the NOE environment, both wind tunnel models and actual aircraft.

2. Measurement of surface pressures at various transition speeds in ground effect.

3. Measurement of flow velocity and direction adjacent to the fuselage as the ground vortex passes.

These measurements should provide steady and unsteady data. The generalized information from these programs would provide guidance for locating air intakes and air data sensors, as well as fuselage loads and pressures.

ROTOR/EMPENNAGE INTERACTIONS

The aerodynamic interactions that have a significant influence on the wake have been discussed previously under the category of Rotor/Fuselage Interactions. The effect of the wake on the empennage was dealt with separately in terms of modifying the wake characteristics in the vicinity of the fin and tail rotor. It was concluded that the low-frequency part of the wake can be reduced significantly by smoothing methods like the induction of fresh air into the wake or (from a subsequent test) by tailoring the aft crown to achieve a favorable pressure gradient.

Further work on wake effects needs to be done in the following aspects:

1. More comprehensive surveys of the wake cross section as it varies with flight condition and disk loading. This would allow a more logical placement of empennage components for minimal interaction.

2. Understanding of the relationships between empennage loads and the wake fluctuations in order to define the relative susceptibility to upsets.

3. Development of standards for wake quality so that rational design loads will be available for empennage design.

4. Development of standard methodologies for both analytical and wind tunnel measurements.

Another area needing more insight is the impingement of the rotary-wing tip vortex on the empennage. The following research should be conducted:

1. Definition of the conditions for occurrence and the associated speed, height from ground, disk loading, wind azimuth, and aircraft angle of attack so that occurrence boundaries may be established.

2. Understanding the nature of the loadings on the fin, tail rotor, and/or horizontal stabilizer due to this occurrence.

ROTOR/EMPENNAGE/GROUND INTERACTIONS

It has been shown that the larger fins of modern helicopters will experience unacceptably large adverse loads due to sidewind and due to interaction with the tail rotor (blockage). The larger fins are necessary to provide directional trim in the event of a tail rotor loss. It is not clear, however, how large the fins must be because maximum permissible sideslip and bank angles have not been determined. A fin that would provide zero bank angle and a small negative sideslip angle for flight at minimum power speed would be very large indeed.

Near-term research needs to address both ends of the empennage design problem occasioned by the opposing requirements of safe flight with lost tail rotor versus high adverse interactional forces. The following programs are required:

1. Flight evaluation of the tail rotor loss conditions by actual or realistically simulated disengagement of the tail rotor drive using a helicopter especially modified to permit

reversion to directional trim with fin alone. This will permit determination of the degree of lateral-directional trim pilots need to fly safely following tail rotor failure. Design criteria will thereby be provided for fin design and methodology will be available for feasible flight demonstrations that the criteria have been met.

2. At the same time, more understanding of the adverse fin load (blockage) is required in order to achieve low-loss empennage designs. Specific research should include:

   a. Variation of fin force and tail rotor thrust past the fin stall and into rotor stall, using both tractor and pusher tail rotor arrangements with large fins.

   b. The effect of tail-rotor-to-fin gap for high fin areas.

   c. The effect of tail rotor vertical position relative to the fin and the determination of the extent of the pressurized fin area. It is not necessarily limited to the swept or shadowed area.

   d. The effect of the main rotor flow on the adverse fin load.

   e. Evaluation of the unsteady fin and tail rotor loads resulting from these conditions.

   f. Effect of horizontal stabilizer size and position.

Another aspect of the rotor/empennage/ground interactions that needs further study is the effect of the tail rotor on the main rotor, especially on power required. Research is needed to expand the range of earlier tests to cover higher disk loadings, height above ground, main rotor attitudes, tail rotor position with respect to the main rotor, and wind speeds and azimuths.

The greatly enlarged body of knowledge to be provided by these recommended research programs will justify a reappraisal of previous design trade studies which compared various schemes for directional control.

REFERENCES

1. Sheridan, Philip F., and Wiesner, Wayne, AERODYNAMICS OF HELICOPTER FLIGHT NEAR THE GROUND, American Helicopter Society 33rd Annual National Forum, Preprint No. 77.33-04, Washington, D.C., May 1977.

2. Huston, Robert J., and Morris, Charles E. K., Jr., A WIND TUNNEL INVESTIGATION OF HELICOPTER DIRECTIONAL CONTROL IN REARWARD FLIGHT IN GROUND EFFECT, NASA Technical Note D-6118, National Aeronautics and Space Administration, Langley Research Center, Hampton, Virginia, March 1971.

3. Wiesner, W., and Kohler, G., TAIL ROTOR PERFORMANCE IN PRESENCE OF MAIN ROTOR, GROUND AND WINDS, Journal of the American Helicopter Society, Vol. 19, No. 3, Washington, D.C., July 1974.

4. Yeager, William T., Jr., Young, Warren H., Jr., and Mantay, Wayne R., A WIND TUNNEL INVESTIGATION OF PARAMETERS AFFECTING HELICOPTER DIRECTIONAL CONTROL AT LOW SPEEDS IN GROUND EFFECT, NASA Technical Note D-7694, Langley Directorate, U.S. Army Air Mobility Research and Development Laboratory, Langley Research Center, Hampton, Virginia, November 1974.

5. Empey, R.W., and Ormiston, R.A., TAIL ROTOR THRUST ON A 5.5 FOOT HELICOPTER MODEL IN GROUND EFFECT, Technical Paper, Ames Directorate, U.S. Army Air Mobility Research and Development Laboratory, Moffett Field, California, 1975.

6. Jenkins, Julian L., Jr., TRIM REQUIREMENTS AND STATIC STABILITY DERIVATIVES FROM A WIND TUNNEL INVESTIGATION OF LIFTING ROTORS IN TRANSITION, NASA Technical Note D-2655, National Aeronautics and Space Administration, Langley Research Center, Hampton, Virginia, February 1965.

7. Conner, William J., THE HUEY COBRA IN VIETNAM, Technical Review, Vol. 9, No. 2, Society of Experimental Test Pilots, 1968.

8. Lewis II, Richard B., ARMY HELICOPTER PERFORMANCE TRENDS, Journal of the American Helicopter Society, Vol. 17, No. 2, Washington, D. C., April 1972.

9. Hoerner, Sighard F., FLUID DYNAMIC DRAG, Midland Park, New Jersey, published by the author, 1958.

10. Wiesner, W., and Kohler, Gary, TAIL ROTOR DESIGN GUIDE, Boeing Vertol Company; USAAMRDL Technical Report 73-99, Eustis Directorate, U.S. Army Air Mobility Research and Development Laboratory, Fort Eustis, Virginia, January 1974, AD775391.

AD-A060 389 BOEING VERTOL CO PHILADELPHIA PA F/G 1/3
INTERACTIONAL AERODYNAMICS OF THE SINGLE-ROTOR HELICOPTER CONFI--ETC(U)
SEP 78 P F SHERIDAN DAAJ02-77-C-0020
UNCLASSIFIED USARTL-TR-78-23A NL

3 OF 4
AD
AD 60389

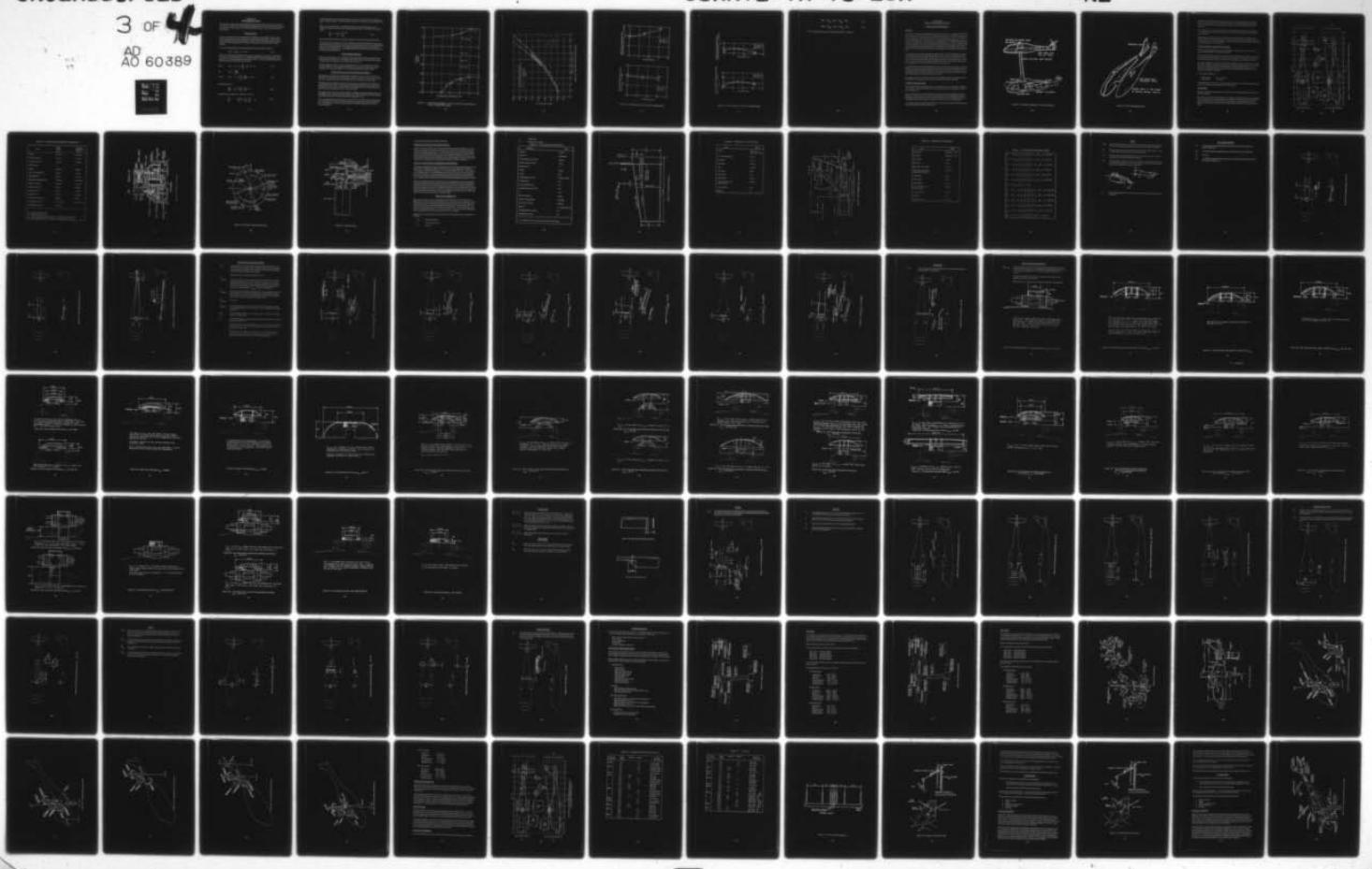

389

APPENDIX A
SUPPLEMENTARY DATA

This appendix contains supplementary material related to some
the main body of this report. These include the fuselage lift in
in ground effect. There is also a section describing the derivati
moment data.

FUSELAGE LIFT

In hover, the downwash is directed downward at 90 degrees to
drag. When hovering very close to the ground a positive pressu
surface, resulting in a negative vertical drag, i.e., positive lift. T
for flat-bottomed fuselages and derives from the same principle
machines.

For the out-of-ground-effect case the incremental lift can be ex

$$dL_f = -c_d \frac{\rho}{2} v_x^2 A_x \, dx$$

where c_d is the profile drag coefficient at A_x, the cross-sectiona
velocity v_x is the value at station x. It is a variable, dependent
the rotor center and vertical distance from the rotor plane. v_x
divided by v_H, the ideal uniform induced velocity.

Thus, $$dL_f = -c_d \frac{\rho}{2} \frac{v_x^2}{v_H^2} v_H^2 A_x \, dx,$$

but $$v_H^2 = \frac{L_R}{2\rho\pi R^2}$$

so that $$dL_f = -c_d \frac{\rho}{2} \frac{v_x^2}{v_H^2} \frac{L_R}{2\pi R^2} A_x \, dx.$$

Dividing by rotor lift,

$$\frac{dL_f}{L_R} = \frac{-c_d}{4} \left(\frac{v_x}{v_H}\right)^2 \frac{A_x}{\pi R^2} \, dx.$$

Integration gives fuselage lift as a fraction of rotor lift:

$$\frac{L_f}{L_R} = -\int_0^x \frac{c_d}{4} \left(\frac{v_x}{v_H}\right) \frac{2 A_x}{\pi R^2} \, dx.$$

For the same geometry, the induced velocity ratio would not be expected to vary significantly as disk loading is changed. The drag coefficient would vary according to effective Reynolds number.

Figure A-1 shows this function, experimentally obtained, versus disk loading for out of ground effect and for h/d of 0.4, plus several points at other h/d's. The OGE curve is approximately

$$\frac{L_f}{L_R} = -0.1 \left[w \frac{\rho}{\rho_o} \right]^{0.5} \qquad \text{(A-6)}$$

Apparently the drag coefficient is varying considerably as velocity changes with disk loading.

The upload ratio for h/d equal to 0.4 varies almost linearly with disk loading in the range tested. It is likely, however, that the trend is to a constant value of the lift ratio at the lower disk loadings as shown by the fairing extension. Thus, high disk loading offers greater hovering efficiency either in or out of ground effect, i.e., proportionately less OGE download and more IGE upload for this particular configuration.

HOVER POWER REQUIRED

Hover power measurements for the YUH-61A model were obtained with the fuselage shell off and are presented in Figure A-2. Corrections for the effect of ground proximity were applied to obtain power for various h/d's in the thrust range of this test.

The data of Figure A-2 may be used for fuselage-on cases by use of the download or upload ratio from Figure A-1. This is applied to the model lift to obtain the required rotor thrust according to the formula in Figure A-2. The power is then read at the correct thrust.

DERIVATION OF CYCLIC PITCH FROM HUB MOMENT

Investigations of the effect of ground proximity and the ground vortex on the control of the helicopter were performed in the wind tunnel at constant cyclic pitch. This is not only a simplification in testing, but also is the most fundamental way of studying the inflow changes.

Experimental data relating hub moments to cyclic pitch may be applied to the constant pitch moment data to find the cyclic pitch required to trim the hub moments to zero or any other prescribed trim value. Figure A-3 presents the hub pitching moment due to longitudinal cyclic pitch and the hub rolling moment due to lateral cyclic pitch.

The hingeless rotor of this test had approximately a 70-degree phase angle between cyclic input and flapping output, resulting in sizable coupling terms. Figure A-4 shows the pitching moment due to lateral cyclic and the rolling moment due to longitudinal cyclic.

A set of simultaneous linear equations is set up to solve for the required changes in longitudinal cyclic pitch ΔA_{1C} for the desired changes in rolling and pitching moment, $\Delta \mathcal{L}$ and ΔM respectively. All increments, of course, are with reference to the particular data point of interest. The relationships are:

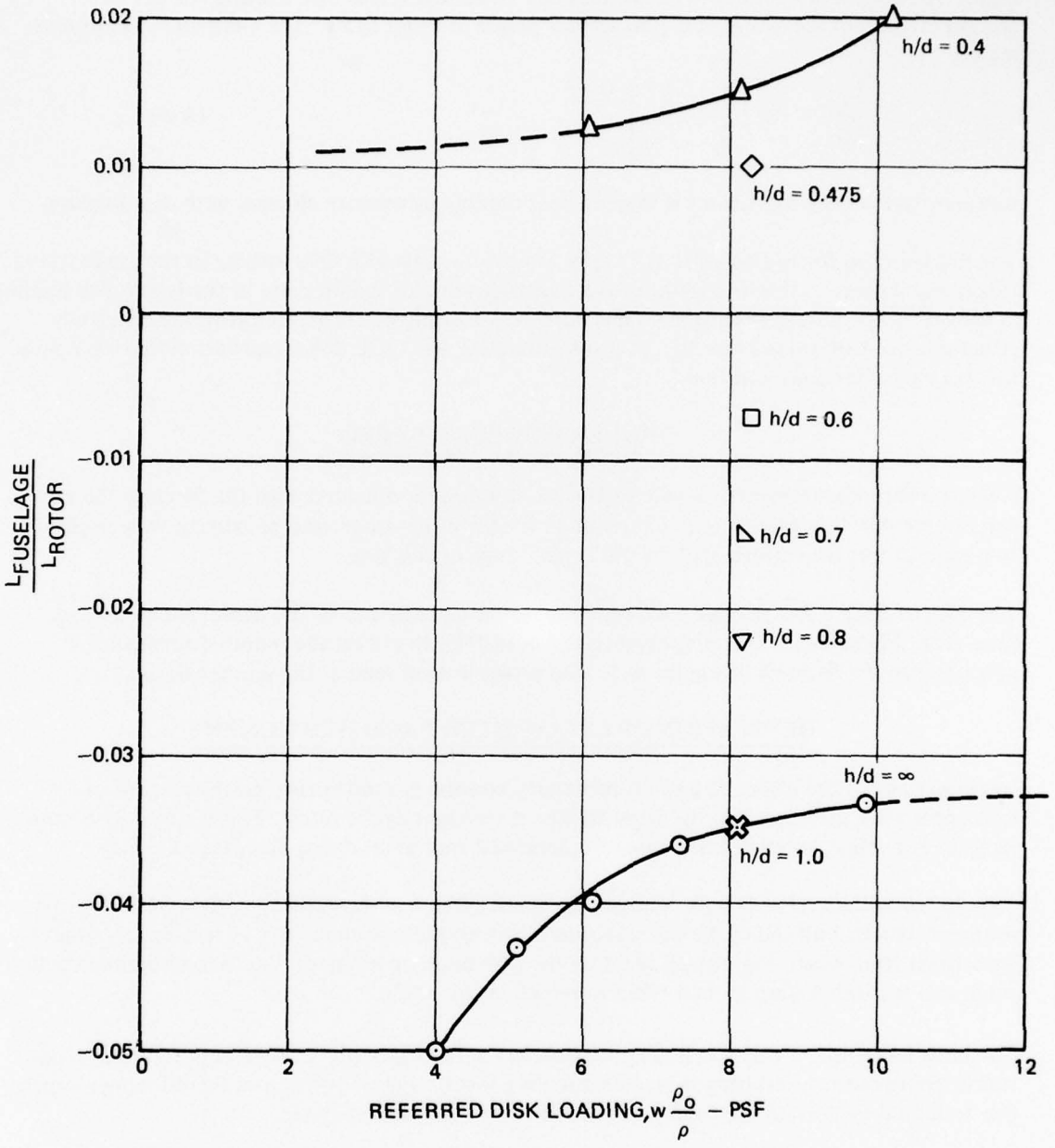

Figure A–1. Nondimensional Fuselage Lift in Hover In and Out of Ground Effect as a Function of Referred Disk Loading.

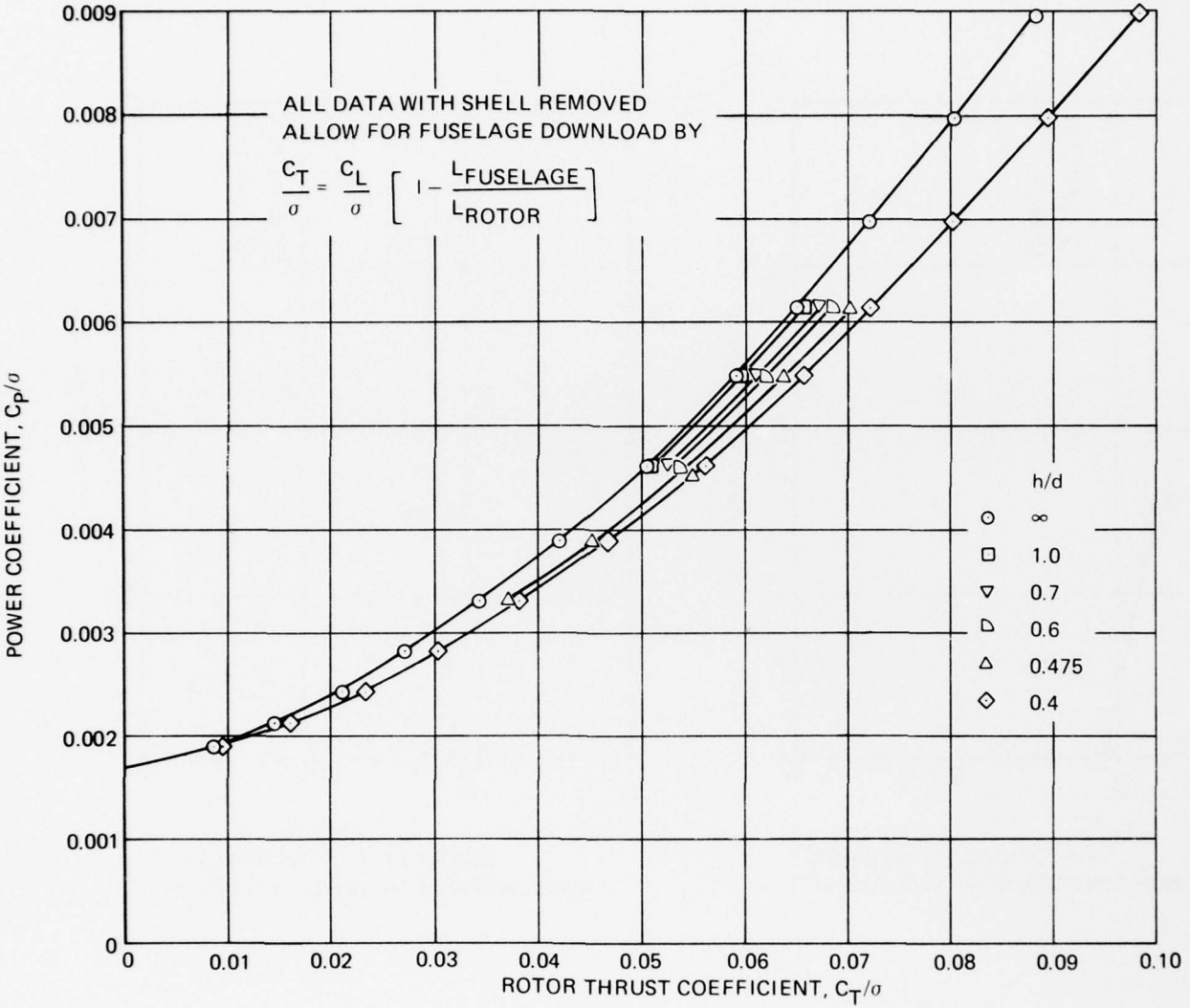

Figure A–2. Hover Power In and Out of Ground Effect.

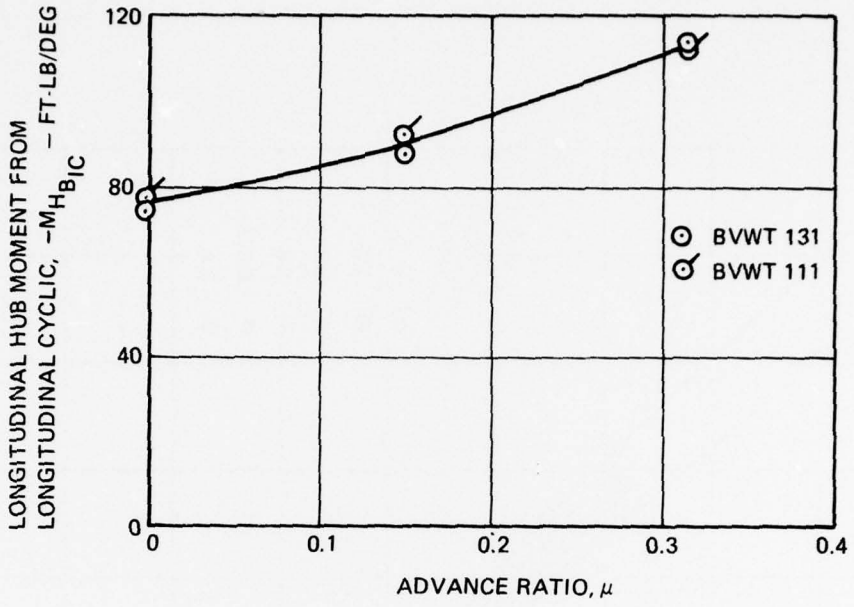

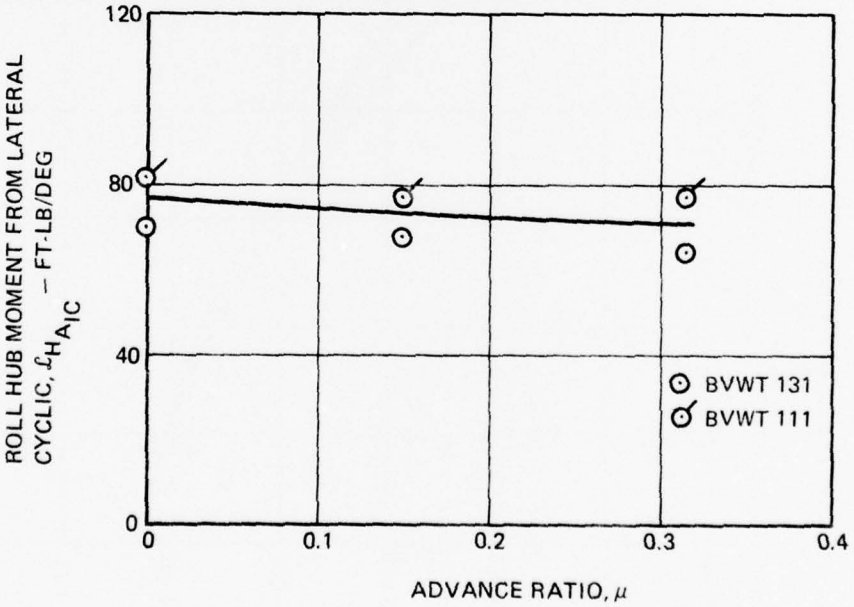

Figure A–3. Control Sensitivities of YUH-61A 1/4.85-Scale Model.

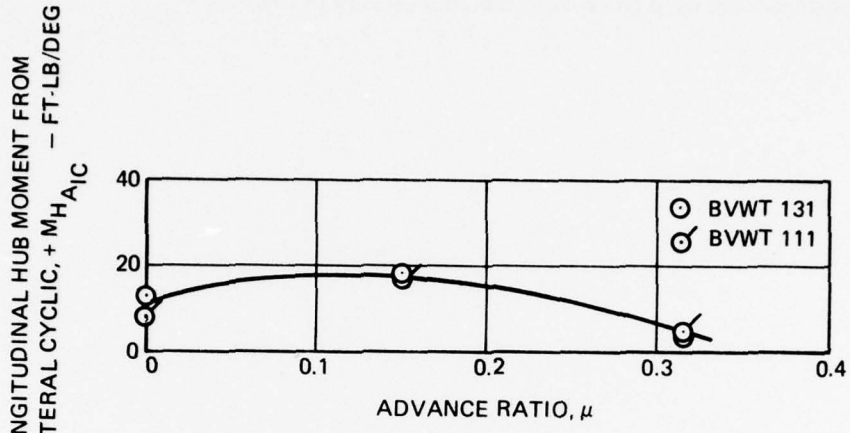

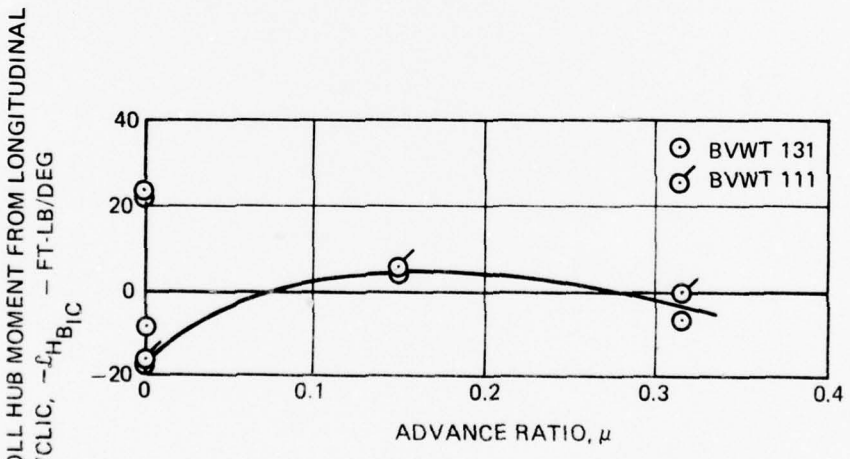

Figure A–4. Control Couplings of YUH-61A 1/4.85-Scale Model.

$$\Delta \mathcal{L}_H = \mathcal{L}_{H_{A_{IC}}} \Delta A_{IC} + \mathcal{L}_{H_{B_{IC}}} \Delta B_{IC} \tag{A-7}$$

$$\Delta M_H = M_{H_{B_{IC}}} \Delta B_{IC} + M_{H_{A_{IC}}} \Delta A_{IC}. \tag{A-8}$$

These relationships were used to develop the data plotted in Figure 24.

APPENDIX B
MODEL AND EQUIPMENT DETAILS

MODEL SYSTEM DESCRIPTION

GENERAL

For this test, the Single-Rotor Helicopter (SRH) model system was configured as the YUH-61A UTTAS helicopter, at a scale of 1/4.85. The model was mounted on a vertical hollow strut (as shown in Figure B-1) extending from the power pod, which contained a three-unit, 400-shp air motor package and 9:1 bevel reduction drive train, giving a maximum output speed, for the main rotor, of 1,600 rpm. The power pod was itself attached to the BVWT pitch/yaw knuckle on the main support sting. The available shaft pitch angle range was −20 to +15 degrees at the knuckle with another ±15 degrees in the main support system. Although the knuckle was used for effecting pitch angle changes, yawing was accomplished through rotation of the vertical support strut by gear-motor and chain drive, the mechanism being contained within the power pod.

Compressed air to power the air motor package was introduced into the power pod by means of a flexible hose contained within the main support sting. Exhaust air was ducted from the motors to the freestream through a 90-degree bent pipe exiting vertically beneath the power pod. For ground effect runs, where the power pod was above the fixed ground plane, exhaust air was ducted from the power pod pipe, through a large-diameter flexible hose, taken under the ground plane, and vented below the tunnel floor to the plenum.

A total loads balance was incorporated into the upper portion of the vertical strut. The drive shaft for the main rotor passed through the center of the balance, which was shielded from the airstream by a knurled detachable cowling. The cowling was attached to the strut below the total loads balance, and being nonmetric, served as a convenient support for the model service lines, instrumentation wire packs, and tail rotor air hose.

The tail rotor, driven by a separate 15-shp air motor, although capable of 7,000 rpm, was run at 4,500 rpm or less because of blade structural limitations prevailing at the time.

FUSELAGE AND NACELLES

Two UTTAS configuration fuselage shells were provided for this test, fabricated of fiberglass 1/4 inch thick. Each shell consisted of two parts, left and right side, which joined together at BL = 0 (Figure B-2).

One set had provision for a pressure transducer in the nose for sensing stagnation pressure at MS 0, and location points for a movable smoke ejection probe with internal gas tubing were established. The smoke probe could be positioned forward or aft of the main rotor hub, at a small distance aft of the left main landing gear,or in the internal duct of the left nacelle.

The nacelles, common to both fuselage shells, were of balsa wood, skinned with fiberglass resin and provided with internal flow-through ducts.

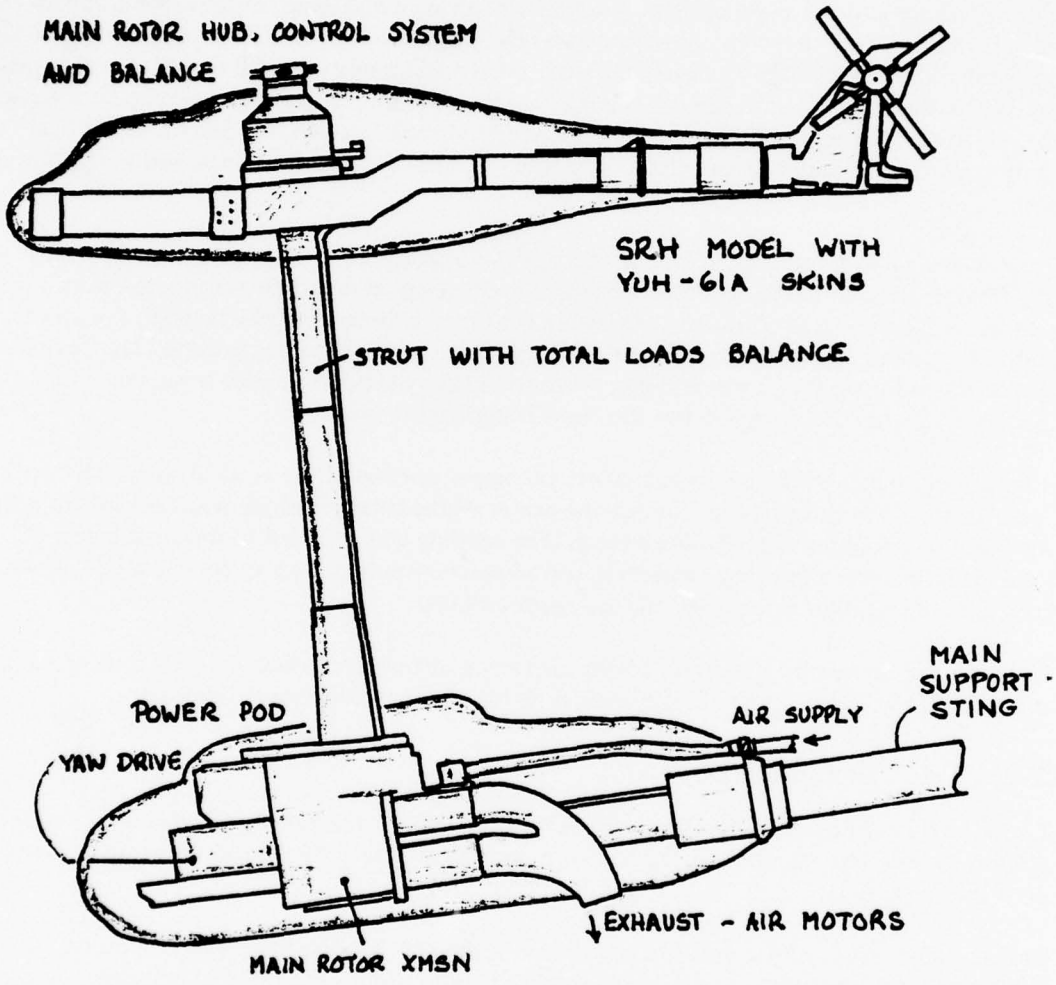

Figure B—1. SRH Model Arrangement in UTTAS Configuration.

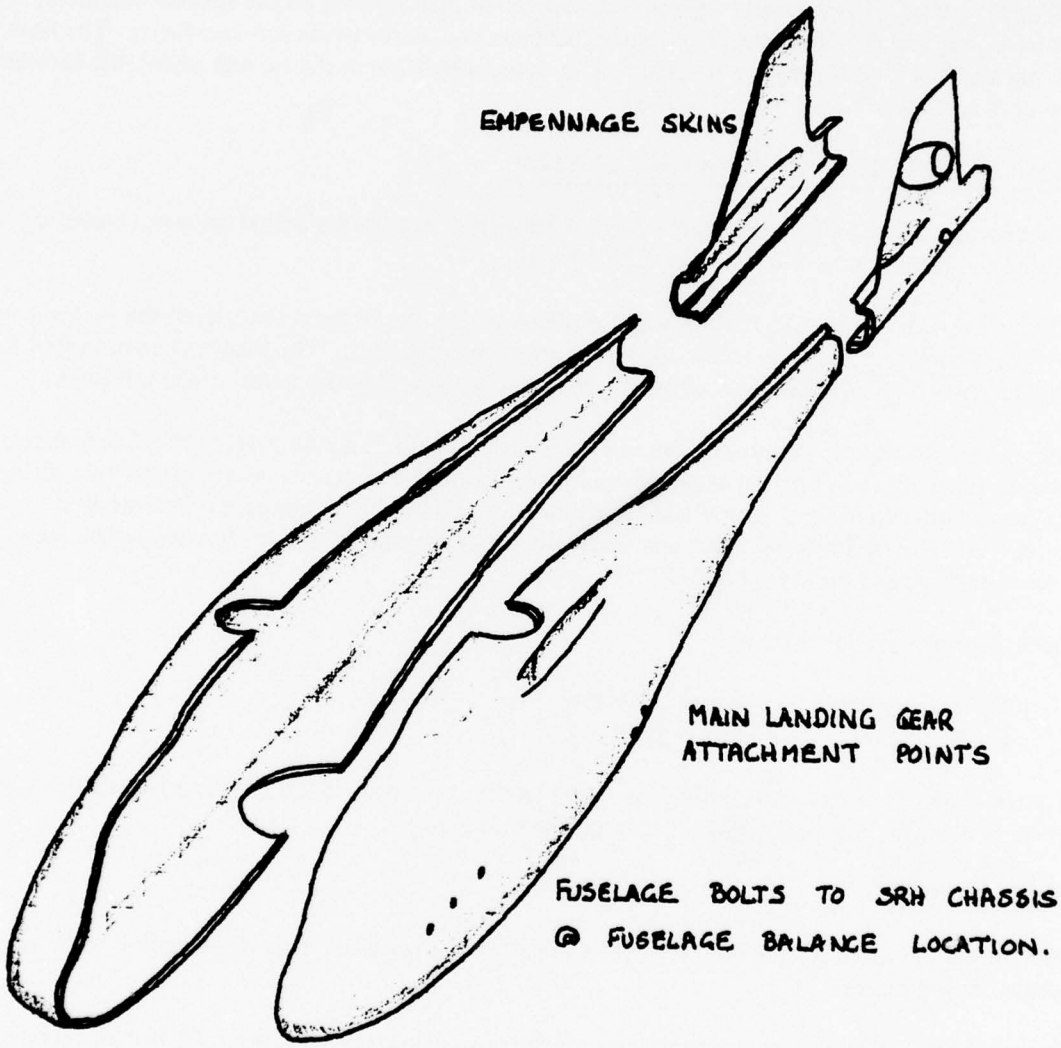

Figure B–2. UTTAS Fuselage Shell Halves.

Another set of fuselage shells was provided for surface pressure measurements. Figure B-3 shows the locations, defined by model coordinates, of 0.1-psi flush-mounted pressure transducers. Transducers were also provided in the nacelles, and in the horizontal and vertical stabilizers.

The fuselage shell, up to the empennage joint, just forward and below the vertical stabilizer root leading edge, was entirely supported by the fuselage balance and not actually attached to the empennage.

Fiberglass skins provided with pressure transducers were also fitted to the vertical stabilizer, which contained the tail rotor drive motor, balance, and instrumentation ancillaries. The horizontal stabilizer, with pressure transducers on upper and lower surfaces, was adjustable through an incidence range of −5 to +53 degrees.

MAIN ROTOR, HUB, AND CONTROL SYSTEM

Main rotor blade parameters are presented in Table B-1, comparing actual values to those required by Mach scaling the full-scale UTTAS blade.

The hub was driven by a shaft that was contained within the support strut from the power pod. It was mounted on bearings in the top of the main rotor balance. The blades were mounted to the hub in elastomeric bearings and connected to the swashplate by adjustable pitch links.

The model swashplate system, shown in Figure B-4, consisted of two parts with a lower sliding ring to give collective pitch change, driven by two hydraulic actuators, surmounted by a tilting spider for introduction of lateral and longitudinal cyclic pitch through separate hydraulic actuators. The positions of these actuators and the appropriate angles pertaining to the control system are shown in Figure B-5.

Control angles available were:

Collective pitch	0 to +21 degrees
Cyclic pitches	±12 degrees

Actual blade angle was measured at one hub position by means of a wiper attached to the blade root, and contacting a resistor film strip on the hub barrel.

TAIL ROTOR

Retention and drive system details of the four-bladed, 2-foot-diameter flexstrap tail rotor are shown in Figure B-6.

Powered by a 15-shp air motor with separate air supply and controls, the tail rotor was mounted on its own balance and is normally operated at 4,500 rpm. Although not fitted with UTTAS-type tapered blades, the rotor was faithful in other respects to the configuration, having a flexstrap blade retention system actuated through leading pitch links by an electrically driven slider.

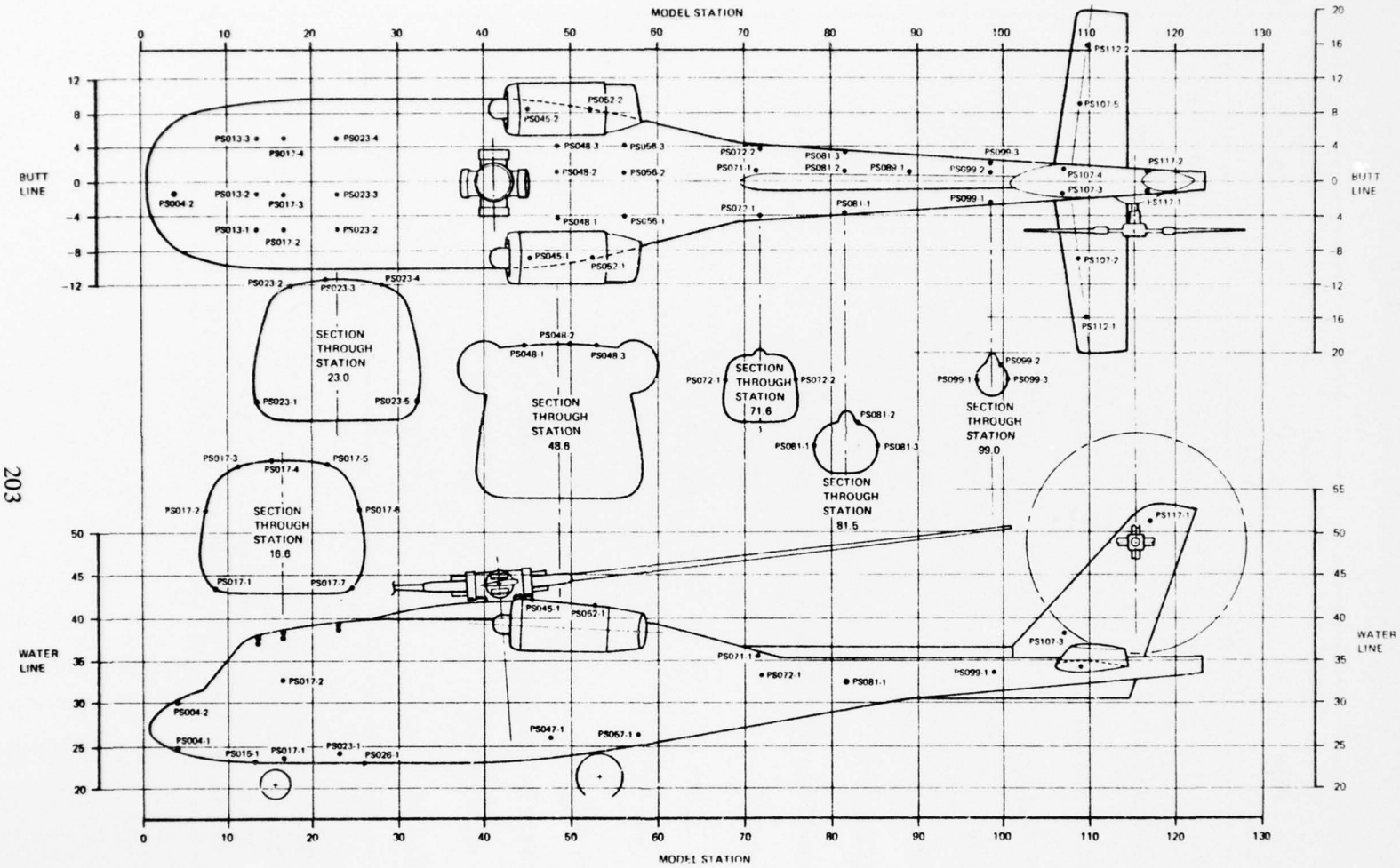

Figure B–3. 1/4.85-Scale Model Geometry and Surface Pressure Transducer Locations.

TABLE B–1. MAIN ROTOR BLADE PHYSICAL PROPERTIES

Item	Model Actual Values	Required Mach-Scaled Values
Radius	60.619 in.	60.619 in.
Chord (reference)	4.742 in.	4.742 in.
Chord (overall tip)	4.790 in.	4.790 in.
Blade Number	4	4
Solidity	0.0996(1)	0.0996
Effective Flap Hinge(2)	0.162R	0.172R
Blade Weight(3)	1.661 lb	1.665 lb
Weight Moment/Blade (flap)	3.208 ft-lb	3.201 ft-lb
Span CG (from C_L)	32.269 in.	32.155 in.
Span CG (from C_L)	0.532R	0.530R
Chordwise CG(1)	1.124 in.	1.110 in.
Chordwise CG	0.2370C	0.2340C
Chordwise CG (dynamics)	0.2340C	0.2317C
Inertia/Blade (flap)(3)	1,311.8 lb-in.^{2}	1,290.7 lb-in.^{2}
Inertia/Blade (pitch)(4)	1.971 lb-in.^{2}	-

(1) Based on reference chord.
(2) Based on analysis (L01).
(3) Item is for blade portion outboard of 0.15 X/R and about 0.15 X/R.
(4) About quarter chord and for blade portion outboard of 0.15 X/R.

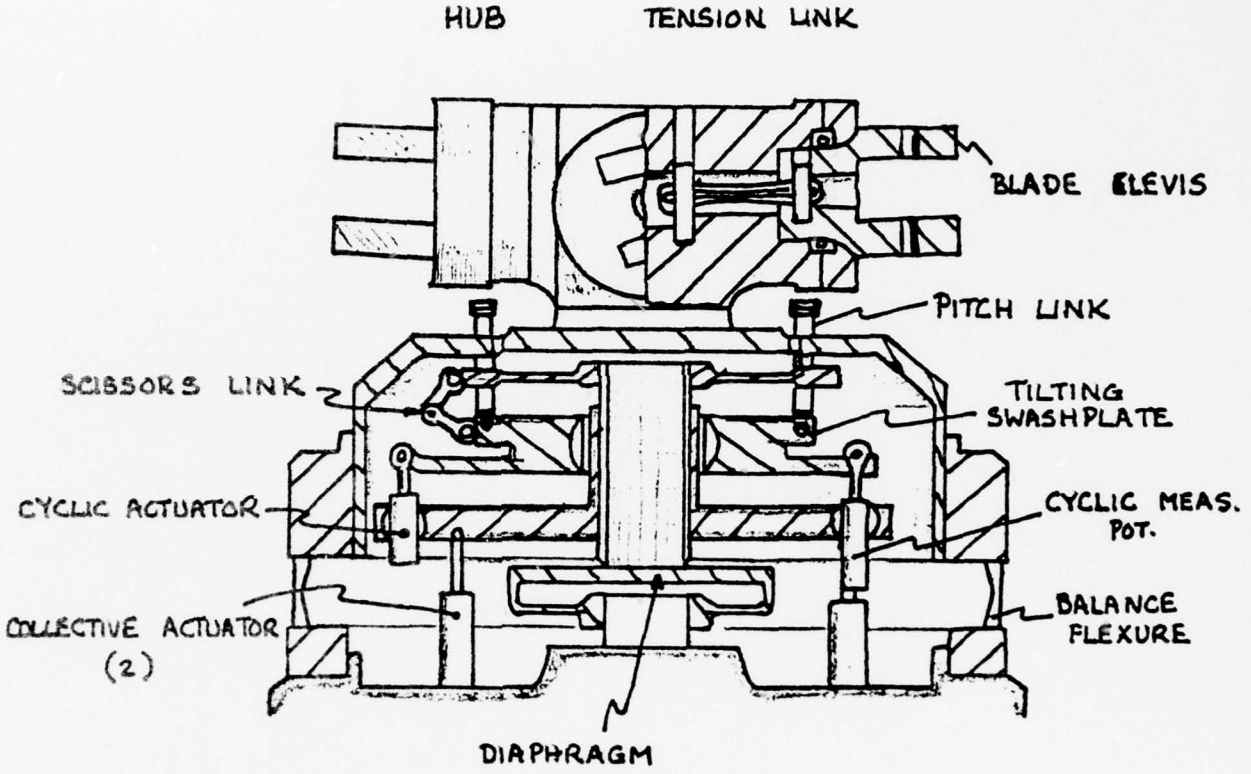

Figure B–4. Main Rotor Control System.

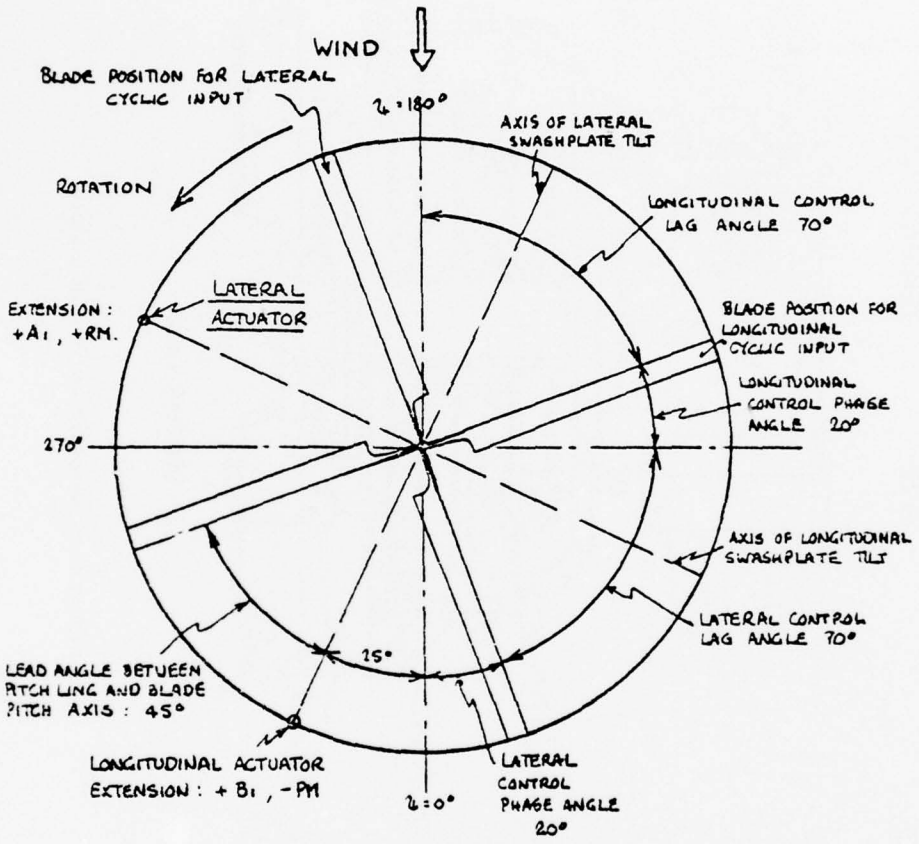

Figure B–5. Main Rotor Control System Phasing.

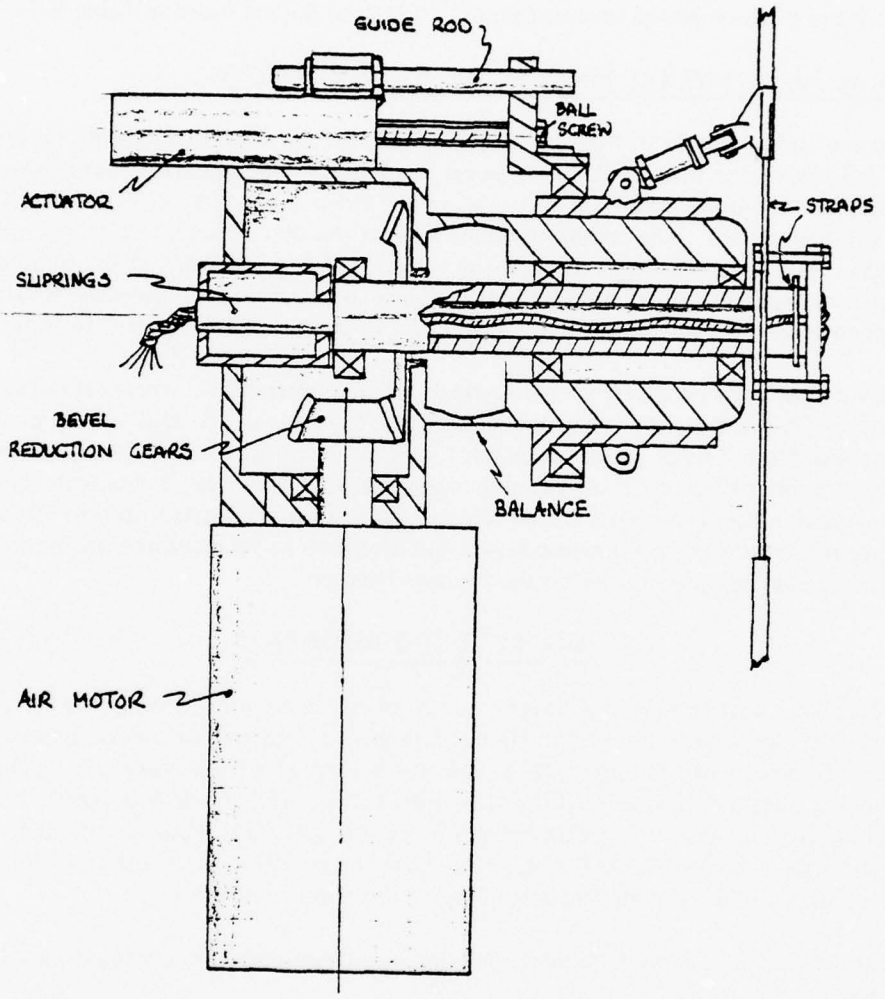

Figure B–6. Tail Rotor Details.

Tail rotor blade parameters are shown in Table B-2.

HORIZONTAL TAIL LOCATION AND GEOMETRY

Figure B-7 shows a planform view of the horizontal tail, the principle dimensions, and its locations on the model. This tail of aspect ratio 5.5 was capable of being remotely positioned through an incidence angle range of −5 to +50 degrees by an actuator and crank mechanism inside the basically flat-sided tailboom. The pivot, which longitudinally coincided with the quarter-chord point of the mean aerodynamic chord (MAC), joined with the structure of the horizontal tail at the sides of the tailboom to form a dihedral angle of 8 degrees. Geometrical characteristics of the essential unswept model horizontal tail are listed in Table B-3.

VERTICAL TAIL/VENTRAL FIN POSITION AND GEOMETRY

The location and geometry of the vertical tail and ventral fin are illustrated in Figure B-8. The vertical tail has a taper ratio of 0.42, an aspect ratio of 1.5, and a quarter-chord sweep of 37.45 degrees. It employs a NACA 63_4 − 421 root airfoil and a NACA 63_4 − 426 tip airfoil per the full-scale article. The airfoil thickness ratio at the tip (25 percent t/c) was increased over that at the root (21 percent t/c) and the vertical tail was truncated at the trailing edge (3.5 inches full scale) to provide sufficient thickness for the necessary full-scale fin structure and to enable the tail rotor gearbox to be enclosed within the right side aerodynamic contours.

Table B-4 presents the geometry of the vertical tail. In addition to the vertical tail geometry and location, Figure B-8 shows the ventral fin, the aft portion of the tailboom as modified to accommodate the tail rotor air motor exhaust, and the pivot location of the horizontal tail. All of these items are mounted off the empennage balance, which is schematically shown along with the relationship of its center to the selected cg position. As noted, station 99 locates the demarcation line for the aerodynamic forces and moments being measured on the empennage balance and those being measured on the fuselage balance.

MODEL TEST COMPONENTS

Many test pieces were used in this program, most of which were involved in the efforts to deflect the hub wake or to alter its frequency content. Variations in test configuration include the Body (B), Aft Crown Fairings (D), Air Ejector System (E), Flow Vane (FV_1), Hubs and Hubcaps (H), Instrumentation Ring (I), Main Rotor Blades (M), Pitch Arms (PA), Pylon (P), Strakes (S), Vortex Generators (VG), Wings (W), and Spoiler (S). These components are described and dimensional sketches for most are shown here. They are arranged in alphanumeric order according to their coding and are referenced to test run number.

Designations for nonvariable elements appearing in the configuration codings in Table B-5 are as follows:

$HT_{1.0}$	Horizontal stabilizer
V	Vertical stabilizer (fin)
T_2^0	Tail rotor

L_1 Landing gear

N_1 Nacelles (flow through)

TABLE B–2. TAIL ROTOR CHARACTERISTICS

Parameter	Value
Diameter	2.062 ft
Planform	Rectangular
Chord (reference at 0.75R)	1.812 in.
Chord (overall at 0.75R)	1.83 in.
Blade Number	4
Solidity	0.1865
Airfoil	VR7
Trailing-Edge Extension	5% (from 0.96C)
Tab Deflection	4.5°
Twist (total geometric)	8.1°
Strap Bias Angle (to 0.75R)	7.4°
δ_3	−65°
Pitch Arm Distance	0.86 in.
Effective Flapping Hinge	0.04292R
Hub Flexure Location	0.0333R
Weight (1)	41.5 gm (0.0915 lb)
Longitudinal Shaft Incidence	0°
Lateral Shaft Incidence	0°

(1) One blade, one half a strap, and one pitch arm with bolts.

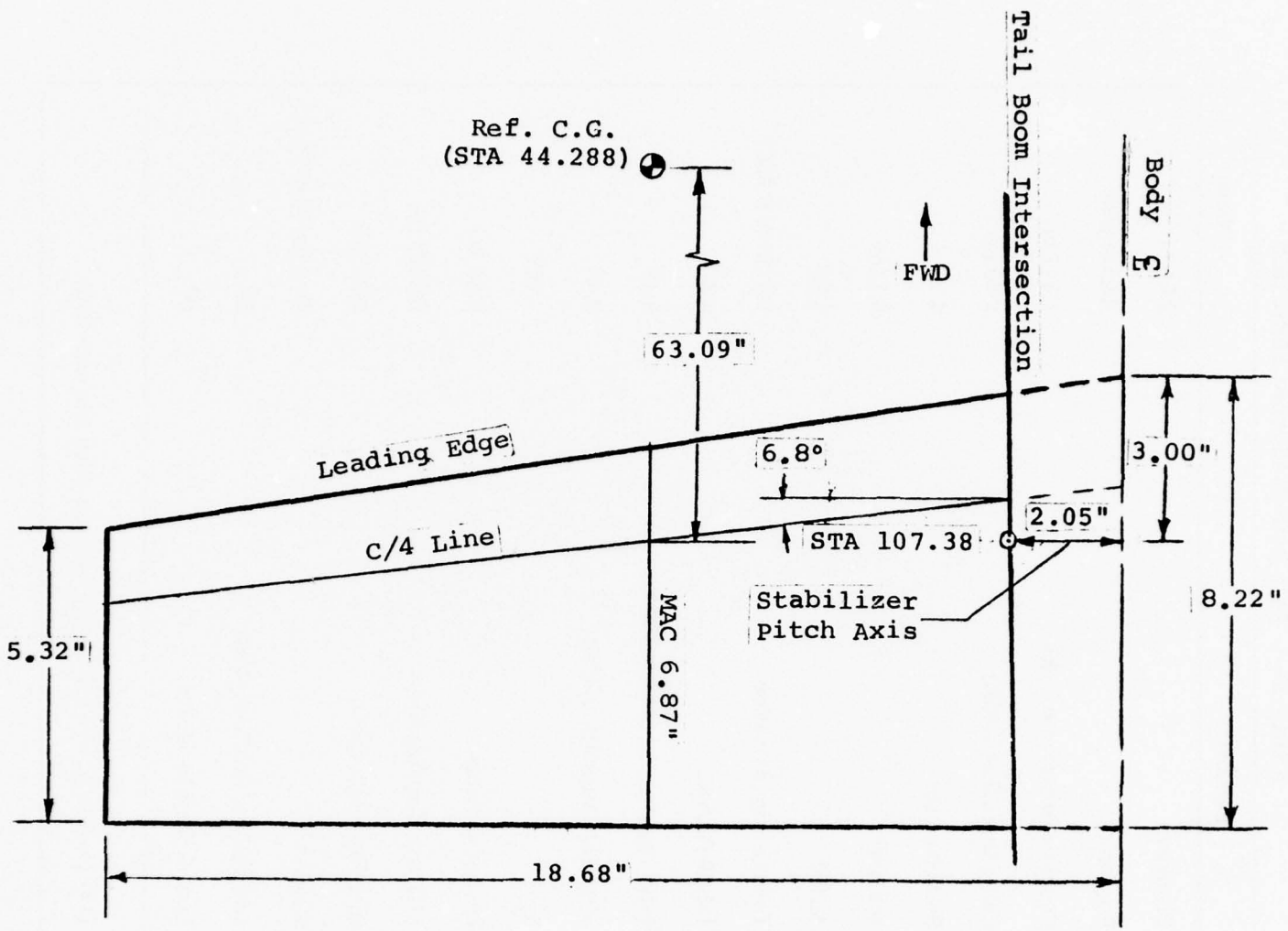

Figure B—7. Horizontal Tail Geometry.

TABLE B–3. HORIZONTAL TAIL GEOMETRY

Item	Model
Airfoil	NACA 0012 (plus a 10% c tab)
Root Chord (body C_L)	8.22 in.
Tip Chord	5.32 in.
Total Span	37.36 in.
Area	1.756 ft^2
Taper Ratio	0.647
Aspect Ratio	5.52
Chord (MAC)	6.87 in.
Tail Arm (MAC C/4 to 12.8 in. aft cg)	63.09 in.
¼ Chord Sweep	6.8^o
Dihedral	8^o

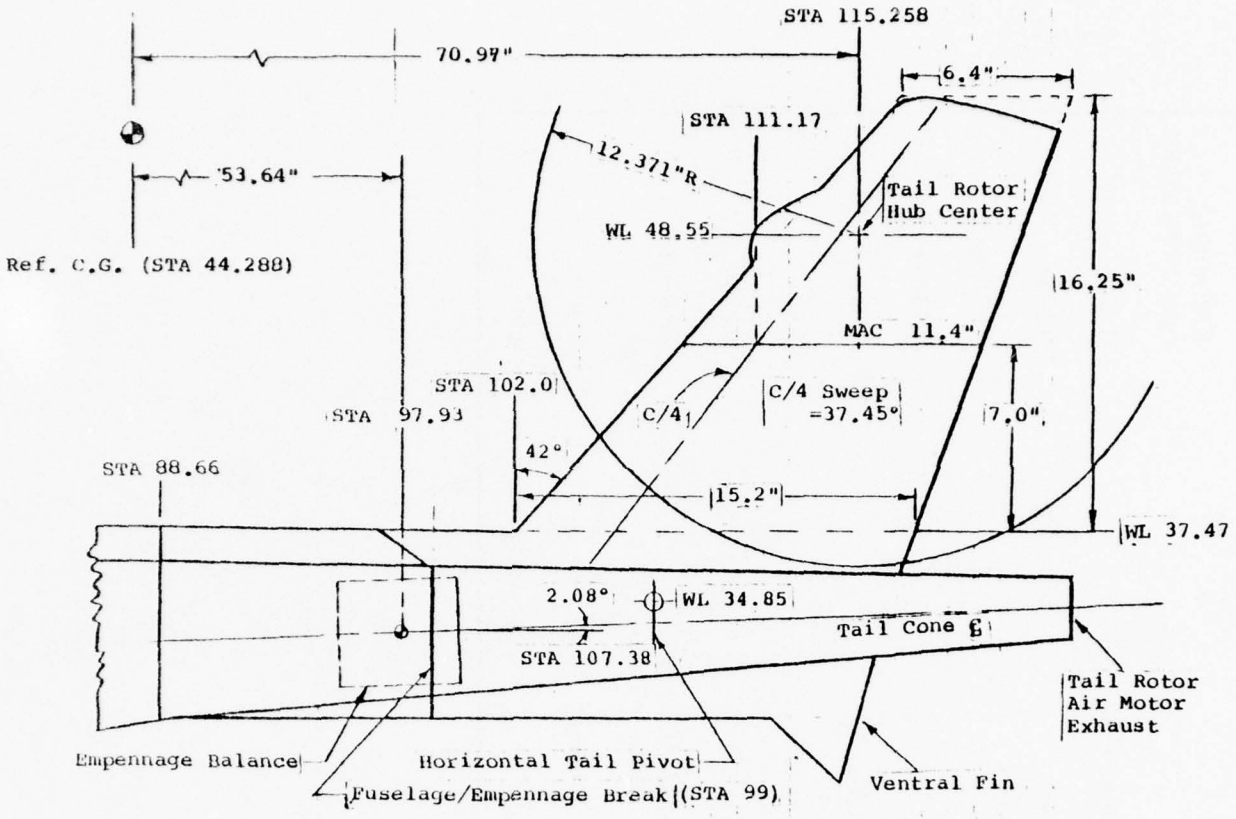

Figure B–8. Model VR096Q Vertical Tail Geometry.

TABLE B–4. VERTICAL TAIL GEOMETRY

Item	Model
Root Airfoil	NACA 63_4 – 421
Tip Airfoil	NACA 63_4 – 425
Root Chord	15.2 in.
Tip Chord	6.4 in.
Span (tip to WL 181.78)	16.25 in.
Area (from top of drive shaft tunnel WL 181.78)	1.219 ft^2
Taper Ratio	0.421
Aspect Ratio	1.50
Chord (MAC)	11.4 in.
Tail Arm (MAC C/4 to 12.8 in. aft cg)	5.574 ft
¼ Chord Sweep	37.45^o
Incidence	0^o
Ventral Fin Area	0.237 ft^2

TABLE B–5. CONFIGURATION SUMMARY CODING

K_1	$= B_2\ M^{0,90,180,270}_{296,297,299,293}\ H_{1.0} HT_{1.0} V\ L_1 T^0_2 N_1 PA_1$
K_2	$= B_2\ M^{0,90,180,270}_{296,297,299,293}\ H_{1.0} HT_{1.0} V\ L_1 N_1 PA_1$
K_3	$= B_2\ M^{0,90,180,270}_{296,297,299,293.2}\ H_{1.0} HT_{1.0} V\ L_1 N_1 PA_1$
K_4	$= B_2\ M^{0,90,180,270}_{296,297,299,293}\ H_{2.0} HT_{1.0} V\ L_1 N_1 PA_1$
K_5	$= B_2\ M^{0,90,180,270}_{296,297,299,293}\ H_{3.0} HT_{1.0} V\ L_1 N_1 PA_1$
K_6	$= B_1\ M^{0,90,180,270}_{296,297,299,293}\ H_{1.0} HT_{1.0} V\ L_1 T^0_2 N_1 PA_1$
K_7	$= B_1\ H_{1.0} HT_{1.0} V\ L_1 T^0_2$
K_8	$= B_{1.2}\ M^{0,90,180,270}_{299,296,390,298}\ H_{1.0} HT_{1.0} V\ L_1 T^0_2 N_1 PA_1$
K_9	$= B_{1.2}\ M^{0,90,180,270}_{299,296,299,298}\ H_{1.0} HT_{1.0} V\ L_1 T^0_2 N_1 PA_1$
K_{10}	$= B_{1.2}\ M^{0,90,180,270}_{299,296,391,298}\ H_{1.0} HT_{1.0} V\ L_1 T^0_2 N_1 PA_1$
K_{11}	$= B_{1.2}\ M^{0,90,180,270}_{299,296,297,298}\ H_{1.0} HT_{1.0} V\ L_1 N_1 PA_1$
K_{12}	$= B_{1.2}\ M^{0,90,180,270}_{299,296,297,391}\ H_{1.0} HT_{1.0} V\ L_1 N_1 PA_1$
K_{13}	$= B_{1.2}\ M^{0,90,180,270}_{299,296,297,298}\ HT_{1.0} V\ L_1 N_1 PA_2$

BODY

$B_{1.0}$ UTTAS fuselage shell halves with two pressure transducers mounted at MS B_2 on the nose. The empennage shell halves were those used in the B_2 configuration.

$B_{1.1}$ The same as $B_{1.0}$ except a pressure transducer was added at MS 5.8, BL 1.6, and a smoke probe was added in front of the hub at MS 35.0.

$B_{1.2}$ The same as $B_{1.1}$ except smoke probe locations were added in front of the left landing gear, in front and behind the left nacelle.

$B_{1.3}$ The same as $B_{1.2}$ except a 1-1/2-by-4-1/2-inch cutout was provided at MS 67.0 to accommodate the support structure for the wings W_2 and W_3. The support structure protruded through the skins as shown below.

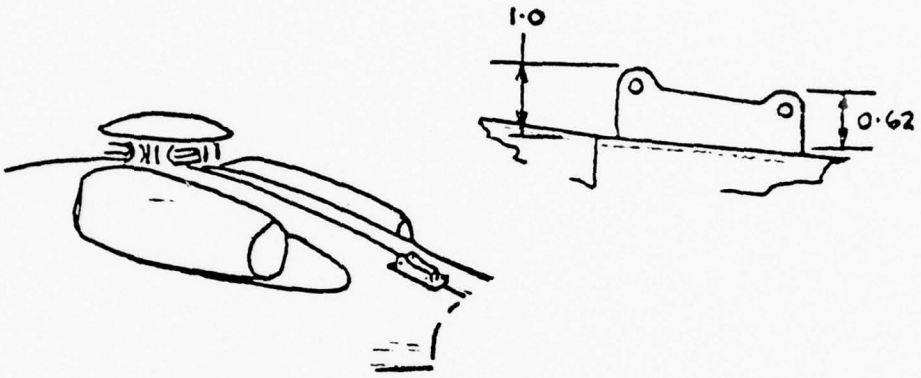

B_2 UTTAS fuselage shell halves with pressure transducers located at locations shown in Figure B-3.

AFT CROWN FAIRINGS

D_1 A flat-topped fairing installed between the nacelles on the model centerline as shown in Figure B-9.

D_2 A round-topped fairing installed between the nacelles as shown in Figure B-10.

D_3 Not used

D_4 A full-length afterbody fairing with flat top extending from the hub to the vertical tail as shown in Figure B-11.

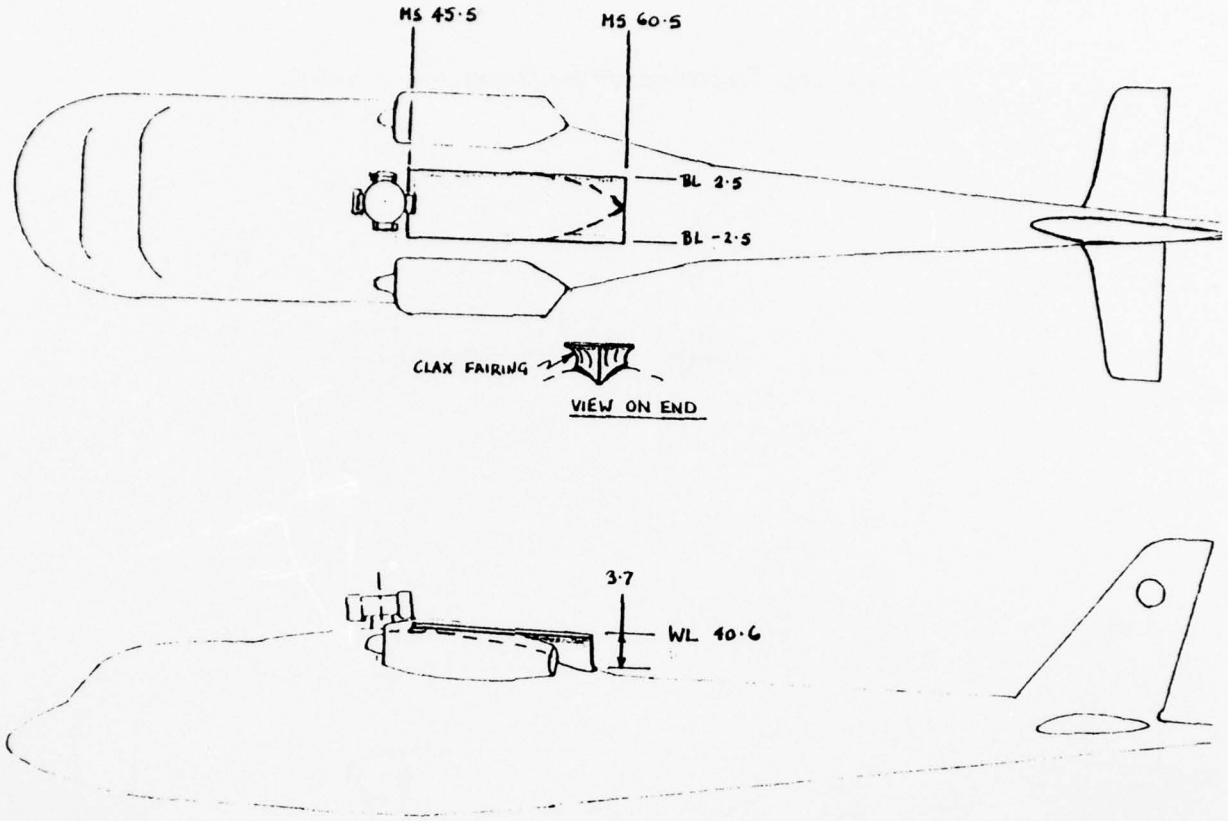

Figure B—9. Flat-Topped Fairing D_1, Run 140.

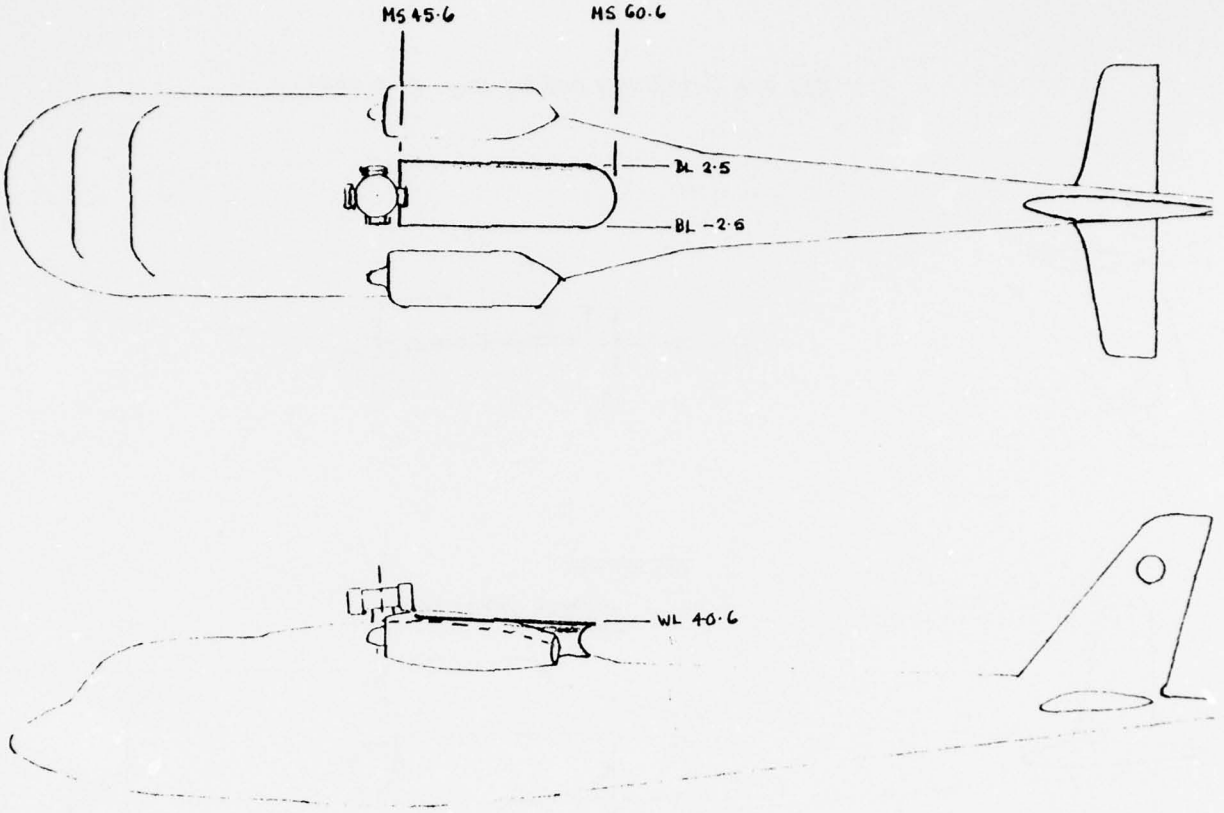

Figure B–10. Round-Topped Fairing D_2, Run 141.

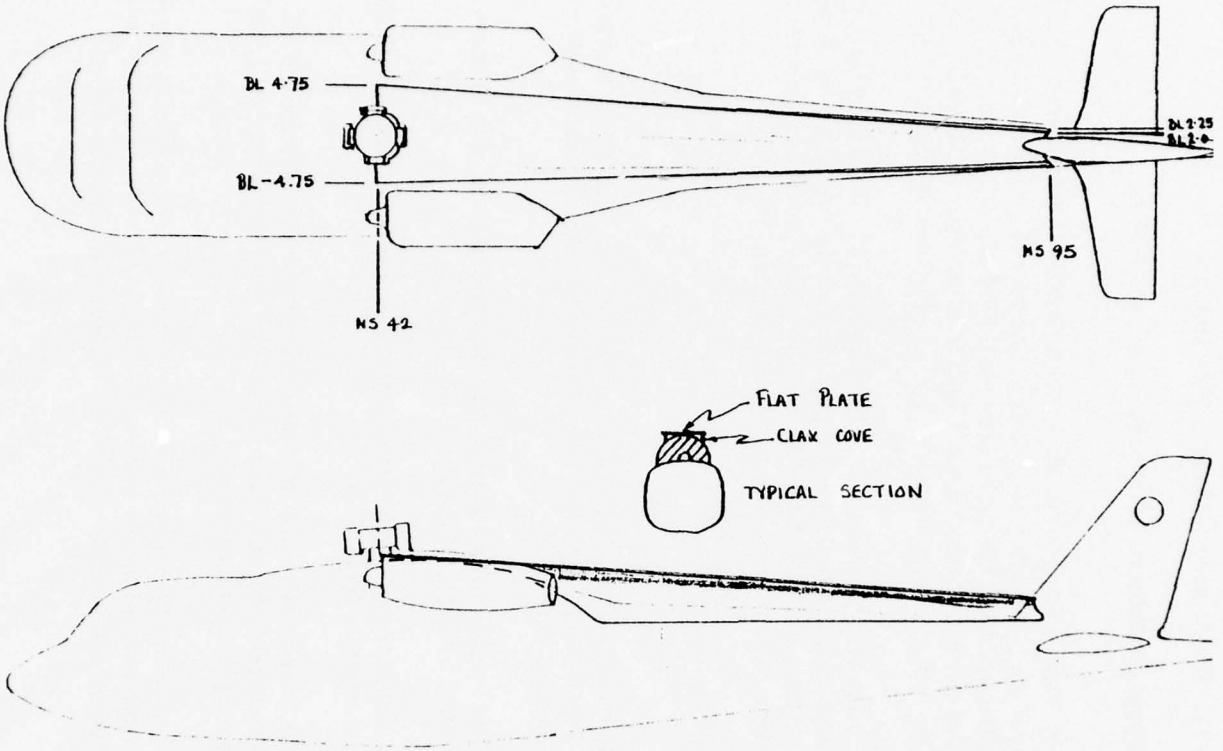

Figure B–11. Extended Flat-Topped Fairing D_4, Runs 170, 171.

AIR EJECTOR SYSTEM VARIATIONS

$E^{Y}_{1.0}$

An air supply device mounted on the fuselage at MS 48.5 (Figure B-12). It consists of an oval steel tube with 25 3/64-inch-diameter holes drilled along the trailing edge. It was faired with a fiberglass eyebrow as shown in Figure B-12. The device is blowing at Y psi supply.

Supply pressures tested were 0, 40, 80, and 150 psi.

$E^{Y}_{2.500.1}$

The same as $E^{Y}_{1.0}$ except the blowing device has been moved 0.5 inch away from the body skin measured at the center hole of the device and a tunnel fairing added to the model between the nacelles at MS 45.15 and extending aft 9 inches. The fairing was 1 inch from the skin at the leading edge and 0.65 inch at the trailing edge. $E^{Y}_{2.500.1}$ is shown in Figure B-13.

$E^{Y}_{3.500.2}$

The blowing tube is at MS 49.15 (Figure B-14). The tunnel fairing of E2 has had a lip added to the leading edge, making the overall length of the fairing 10.625 inches. The lip is 0.75 inch high and contoured to create a smooth intake. Gap from body to fairing is a constant 1.0 inch.

$E^{Y}_{3.500.3}$

Not tested

$E^{Y}_{3.500.4}$

A new tunnel fairing, lifted up on walls of clax built on the nacelles, giving a 2-inch intake depth and 2.6-inch exhaust. It has a chord length of 15 inches (Figure B-15).

$E^{Y}_{4.0}$

The blowing tube installed on the afterbody surface, with eyebrow (as $E^{Y}_{1.0}$) at MS 52.95 (Figure B-16).

E^{Y}_{5}

A shaped fiberglass duct extending from close behind the hub to the afterbody discontinuity (Figure B-17).

The intake had a small leading-edge bead and extended for the full body width between the nacelles. Four inches behind the intake was a 0.1-inch-wide slot venting to the outer surface.

The blowing tube is at MS 52.95. Behind the tube, a balsa fairing is built up on the body surface to maintain a constant duct area. The duct exhausts through a bifurcation around the tail rotor transmission tunnel.

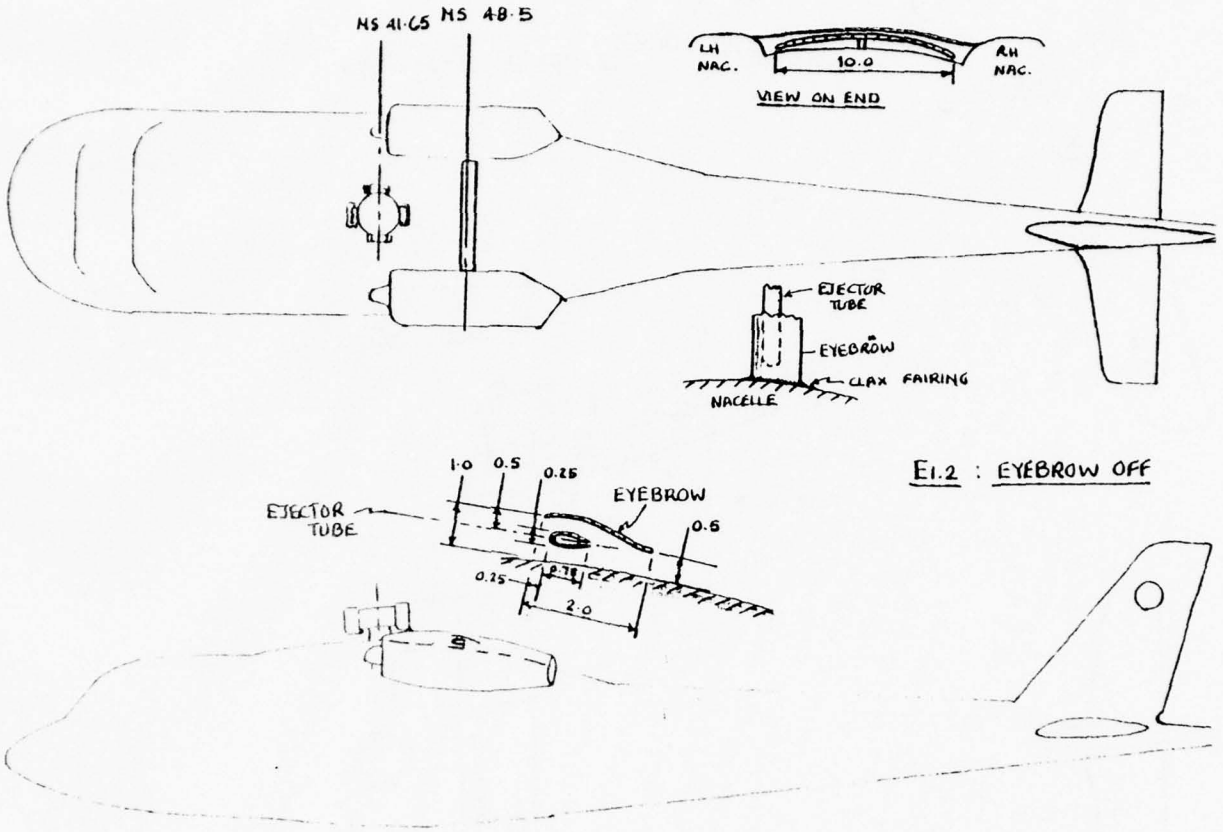

Figure B–12. Ejectors $E^{Y}_{1.0}$ and $E^{Y}_{1.2}$ – Runs 172, 173, 174, 178-180, 188-197, 207-215.

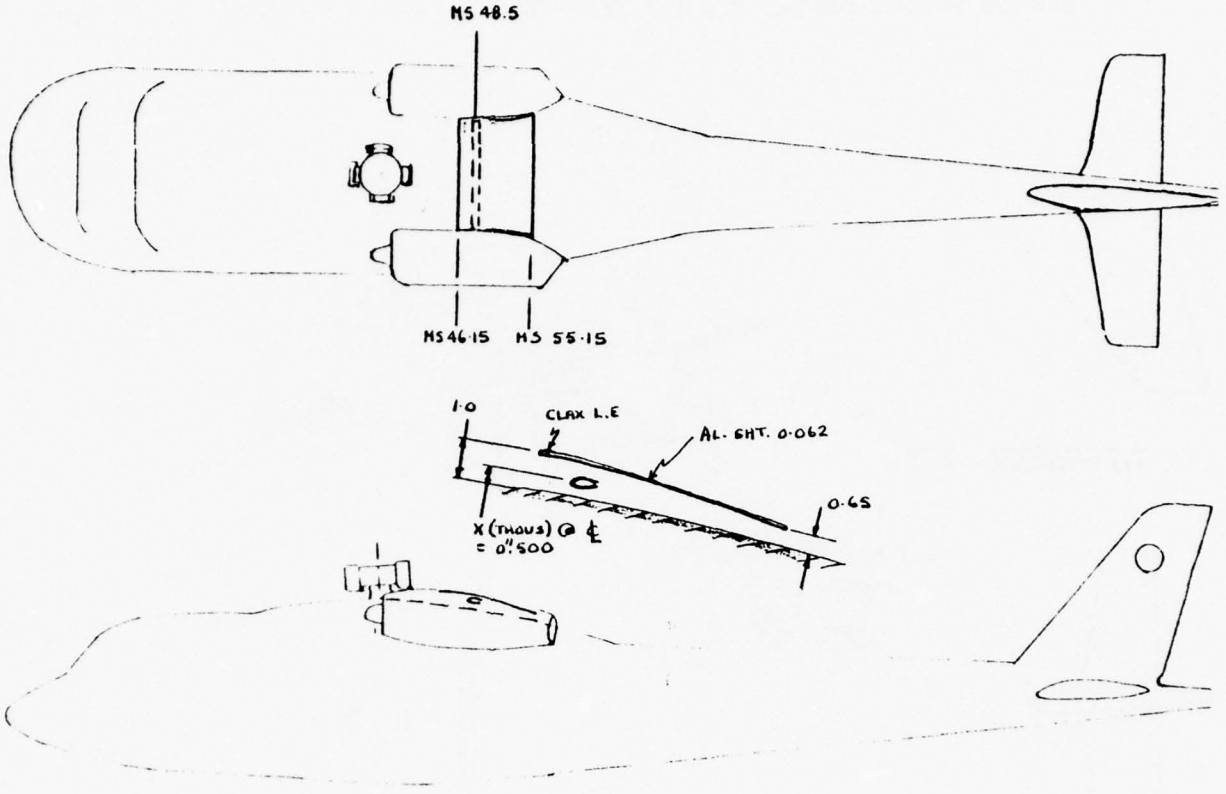

Figure B–13. Ejector $E^{Y}_{2.500.1}$ *– Run 175.*

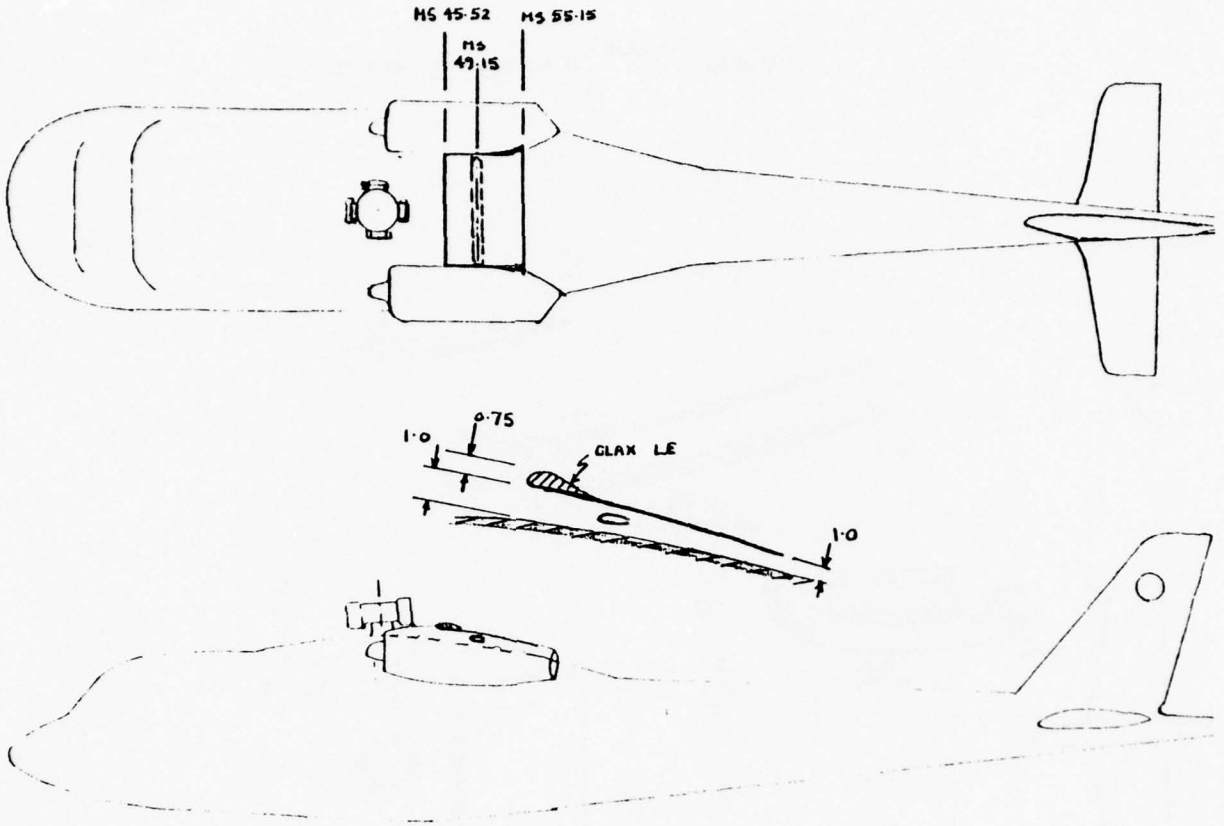

Figure B—14. Ejector $E^{Y}_{3.500.2}$ — Runs 184, 185.

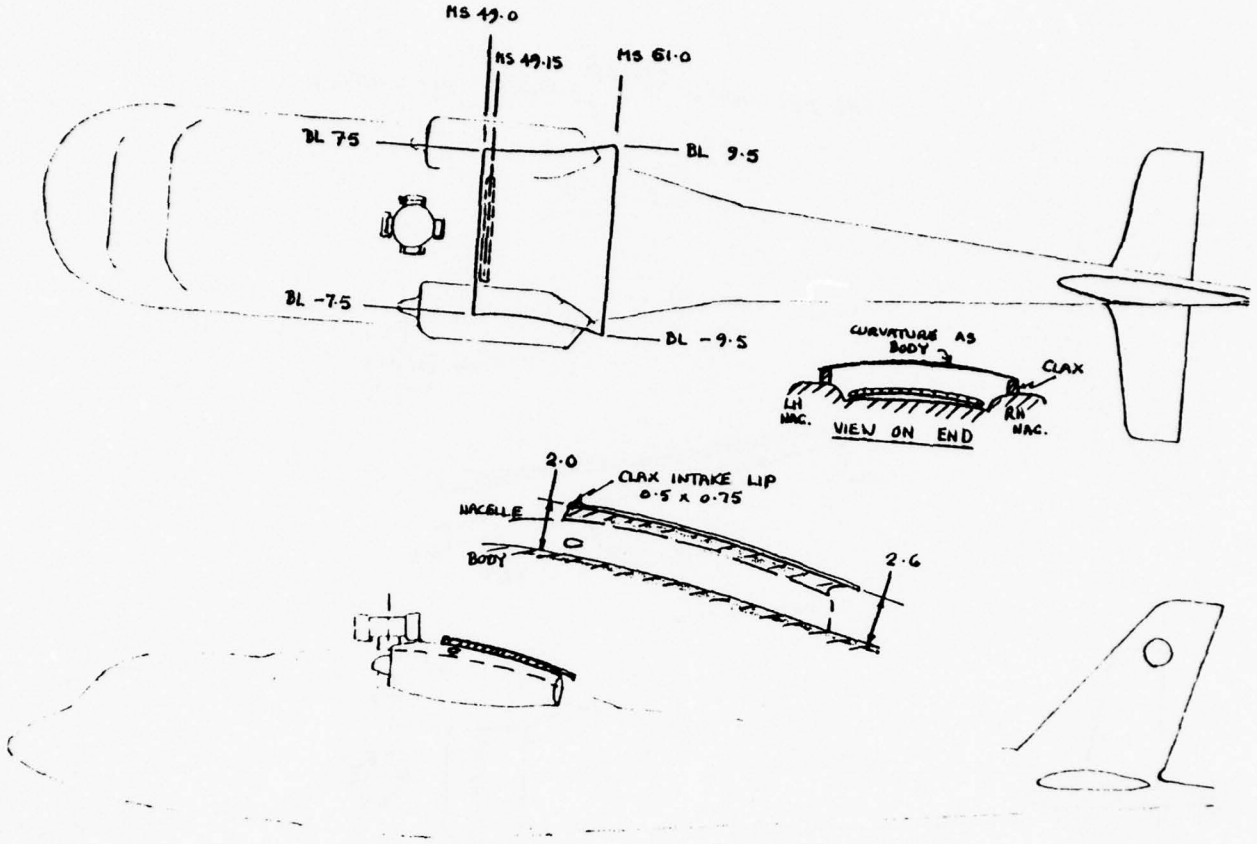

Figure B–15. Ejector $E^{Y}_{3.500.4}$ – Run 187.

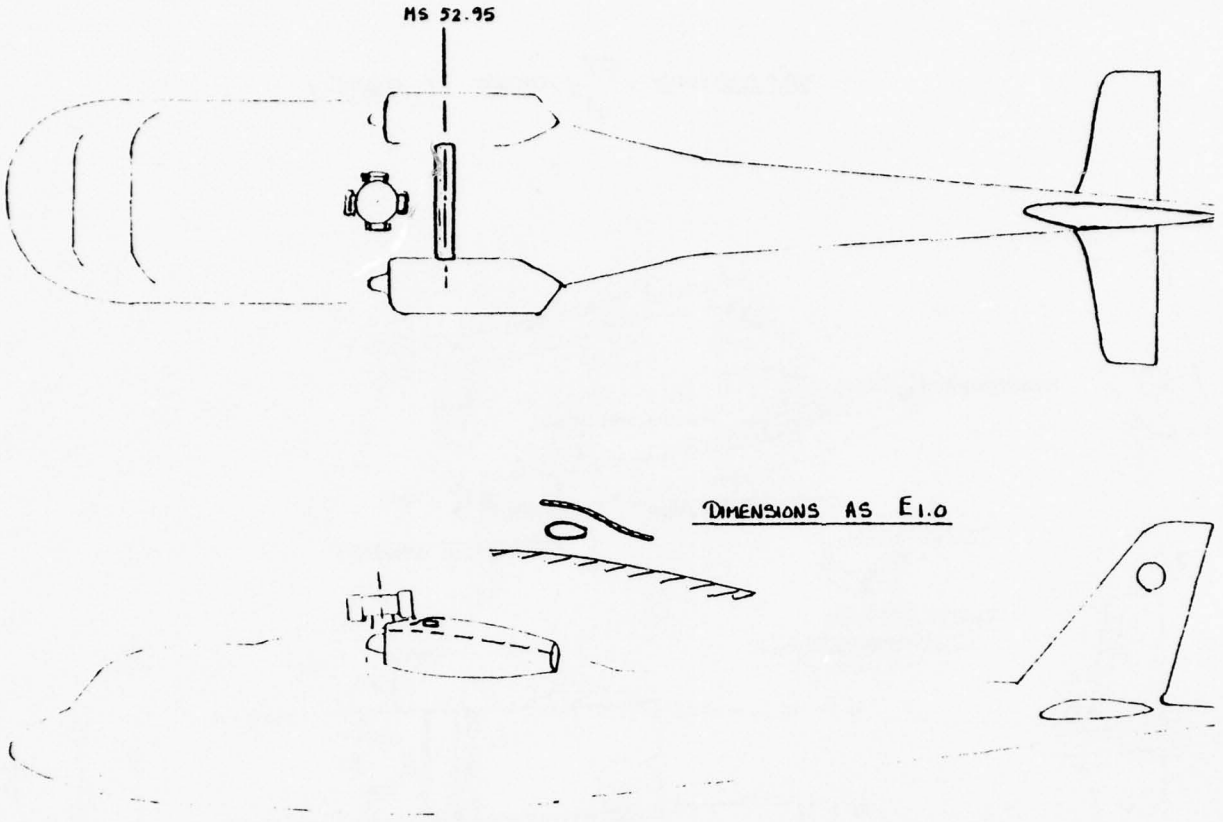

Figure B–16. Ejector $E^{Y}_{4.0}$ – Runs 198-201.

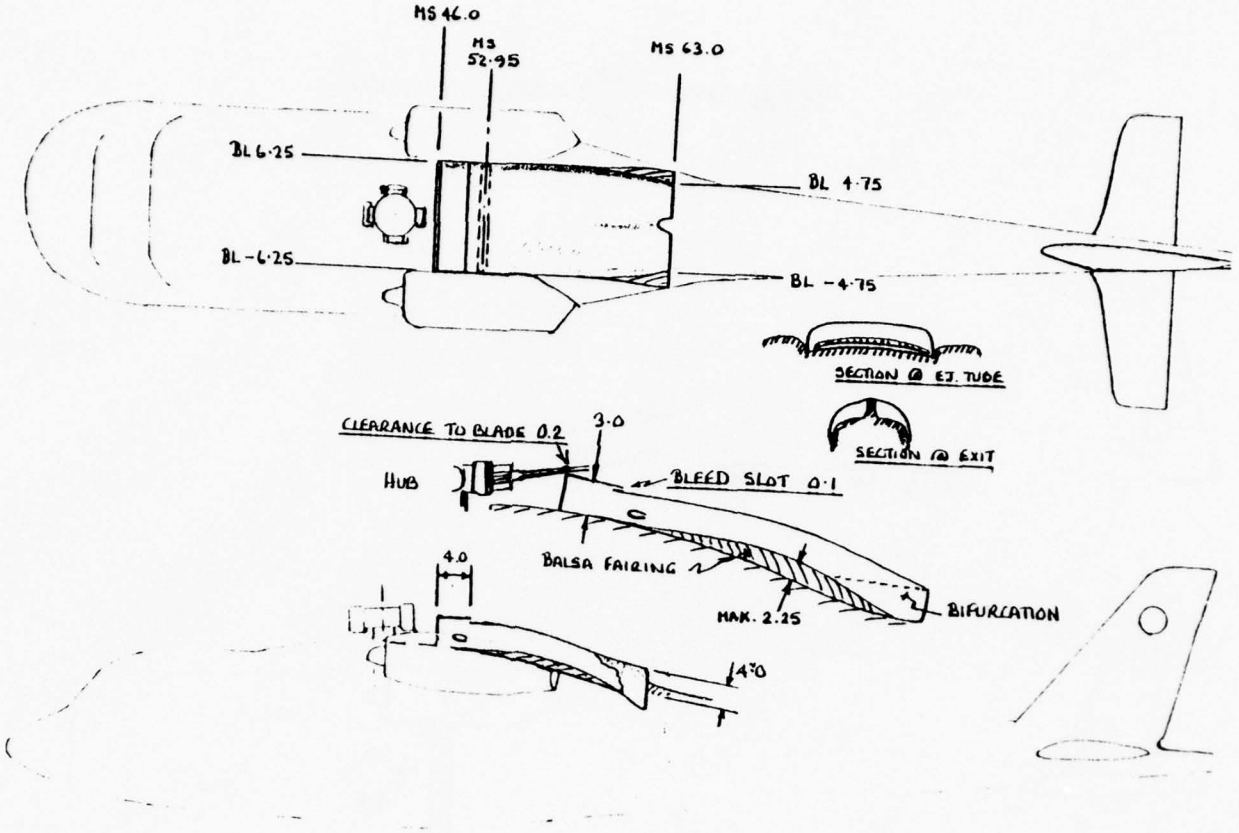

Figure B–17. Ejector $E^{Y}_{5.0}$ – Runs 203-205.

FLOW VANE

FV_1 A 2-1/2-inch-chord, 15-inch-wide flow-turning vane installed between the nacelles at MS 57.7 (Figure B-18).

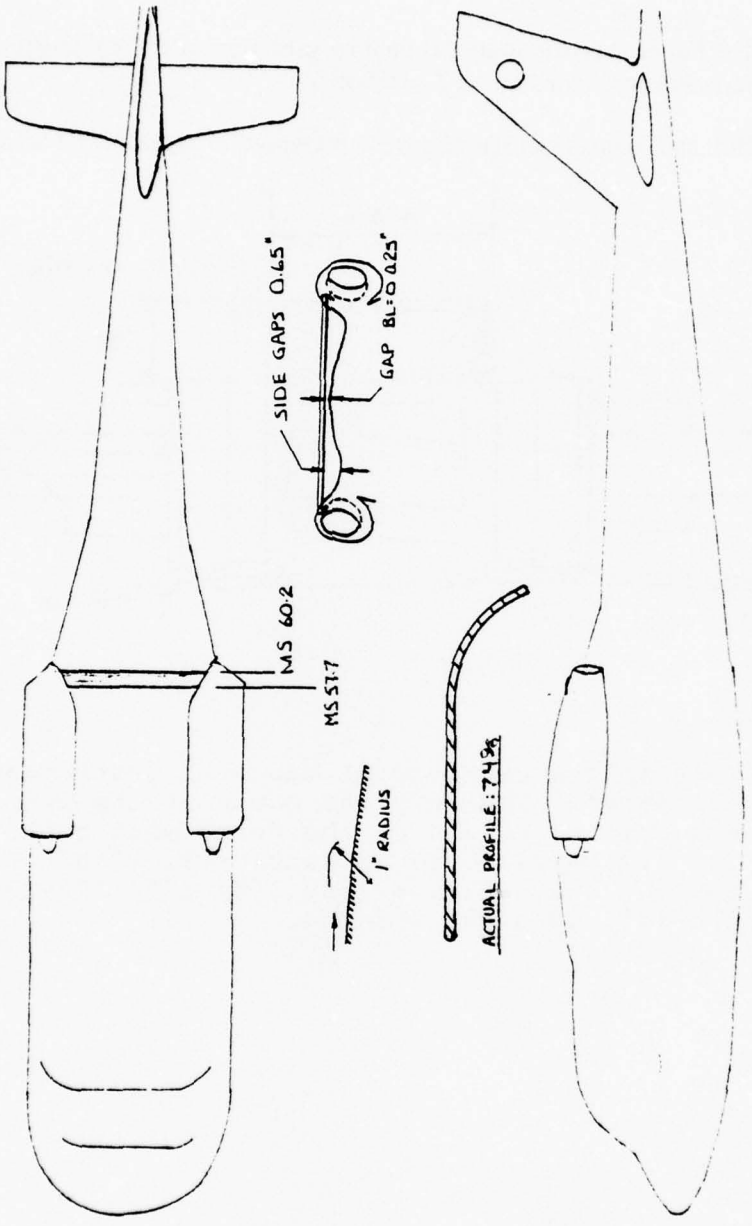

Figure B–18. Flow Vane FV_1 – Run 142.

HUB AND HUBCAP VARIATIONS

$H_{X.YY.Z}$

This is the general symbol for the hub configuration including the basic hub, the hubcap and its supports, and the flight test instrumentation canister. There is one basic hub configuration, X = 1.0, with three minor variations, X = 2, 3, and 4.

The hubcap variations are denoted by subscripts in the YY position. Sub-variations are coded in the Z position.

Hub and hubcap configurations are presented in Figures B-19 through B-48.

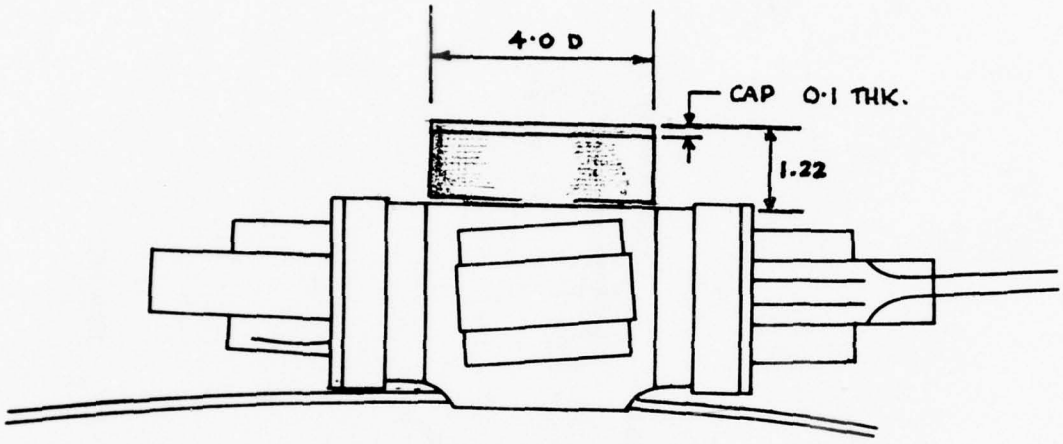

This is the basic model hub with instrumentation cannister. The body and cover of the cannister are drilled to accept the attachment bolts for the hub caps. Used on Runs 0-18, 23-53, 62-64, 80-136, 138-150, 156-158, 160, 170, 172-176, 178-181, 184-188, 203-206.

Figure B–19. Basic Model Hub With Instrumentation Canister, $H_{1.0}$ – for Runs Noted.

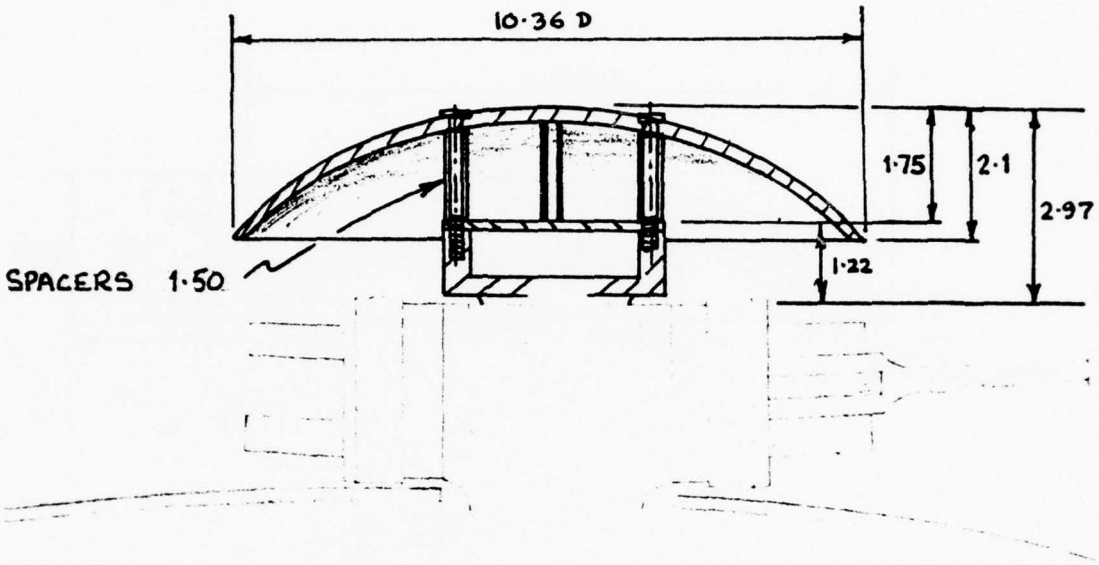

This is the basic hub with instrumentation cannister $H_{1.0}$ with a 10.4 - in. - diam. hub cap installed at a height of 1.75 in. above the cannister cover. This locates the cap at the same height above the top of the hub as it would be if the wooden $H_{1.5}$ cap were fitted, and the cap had a 0.975 - in. gap.

The hub cap is of fiberglass construction, 0.125 in. thick, supported on four threaded studs and held in place by tubular spacers on the studs.

Figure B–20. 10.4-Inch-Diameter Open Hubcap and 1.75-Inch Gap, $H_{1.0.1}$ – Run 165.

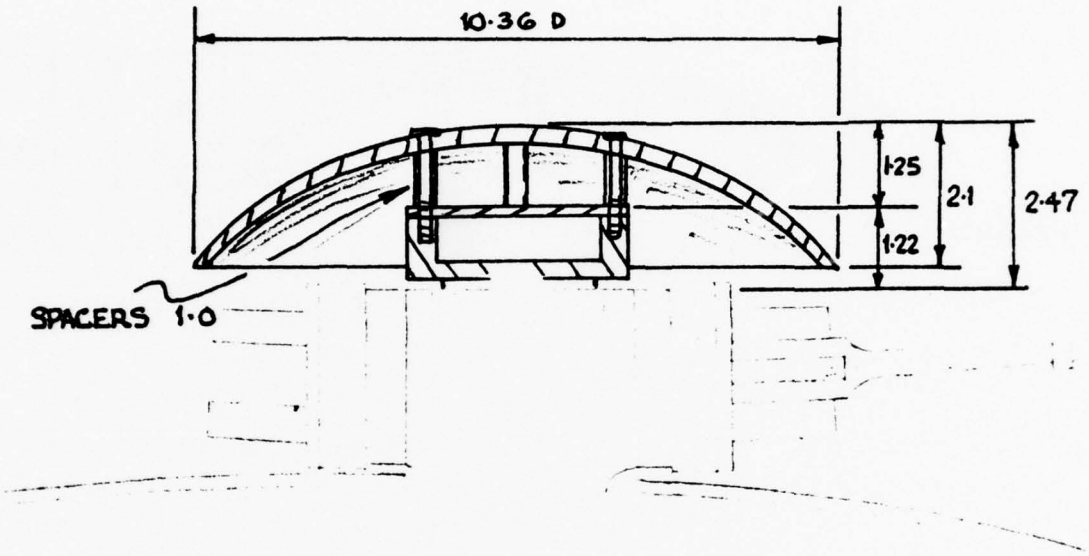

The same as H1.0.1 except the gap from cannister to hub cap is 1.25 in.

Figure B—21. 10.4-Inch-Diameter Open Hubcap at 1.25-Inch Gap, $H_{1.0.2}$

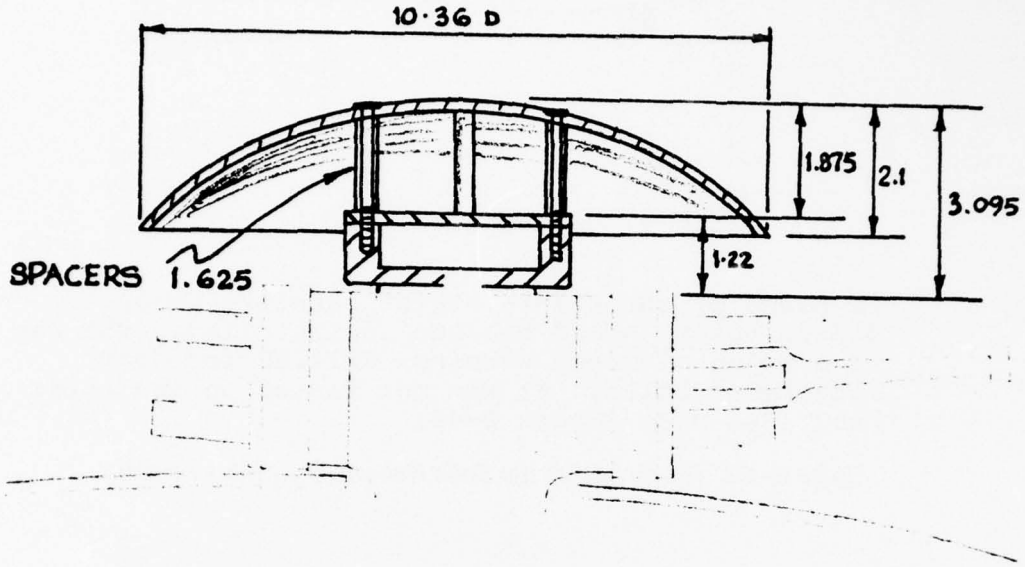

The same as $H_{1.0.1}$ except the gap from cannister cover to parasol is 1.875 in.

Figure B–22. 10.4-Inch-Diameter Open Hubcap at 1.875-Inch Gap, $H_{1.0.3}$ – Runs 191, 192.

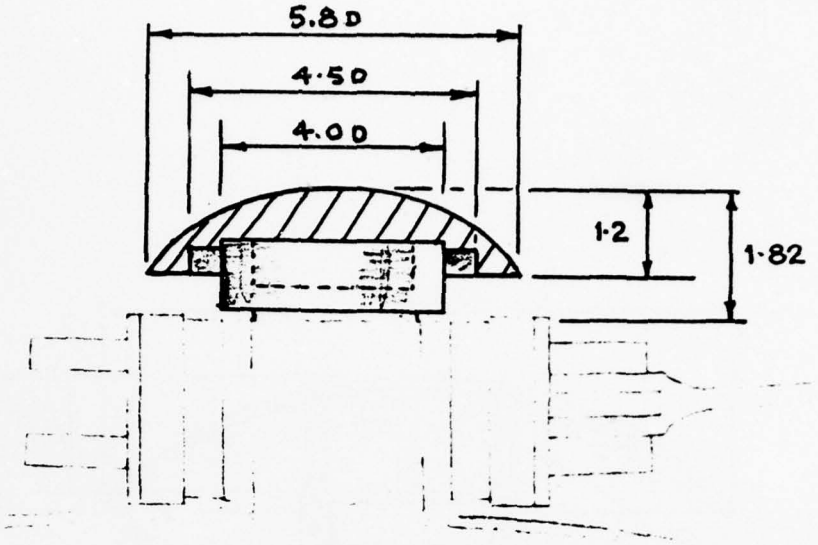

In place of the 0.1-in.-thick cannister cap, a 5.8-in.-diam. solid hub cap is installed. The cap is a solid aluminum turning, drilled for four attachment bolts. It was not tested on the rotating hub. See also Figure B-45.

Figure B—23. 5.8-Inch-Diameter Solid Hubcap, $H_{1.1}$ (Not Tested).

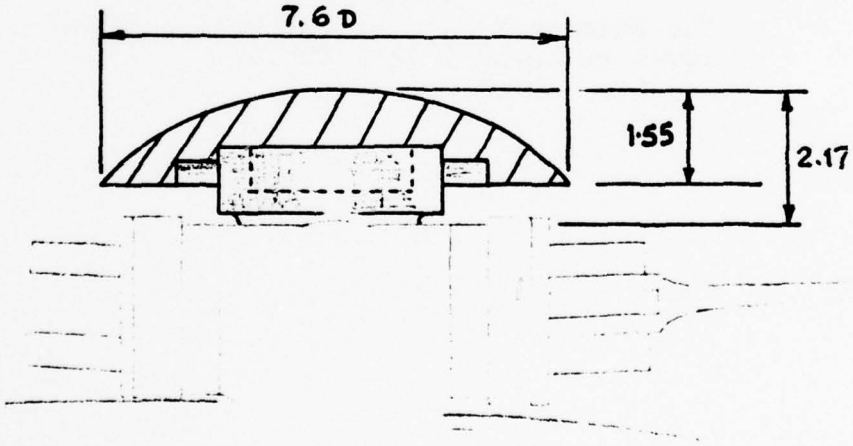

This solid hub cap is similar to $H_{1.1}$ except for its diameter of 7.6 inches.

Figure B—24. 7.6-Inch-Diameter Solid Hubcap, $H_{1.2}$ — Runs 137, 153.

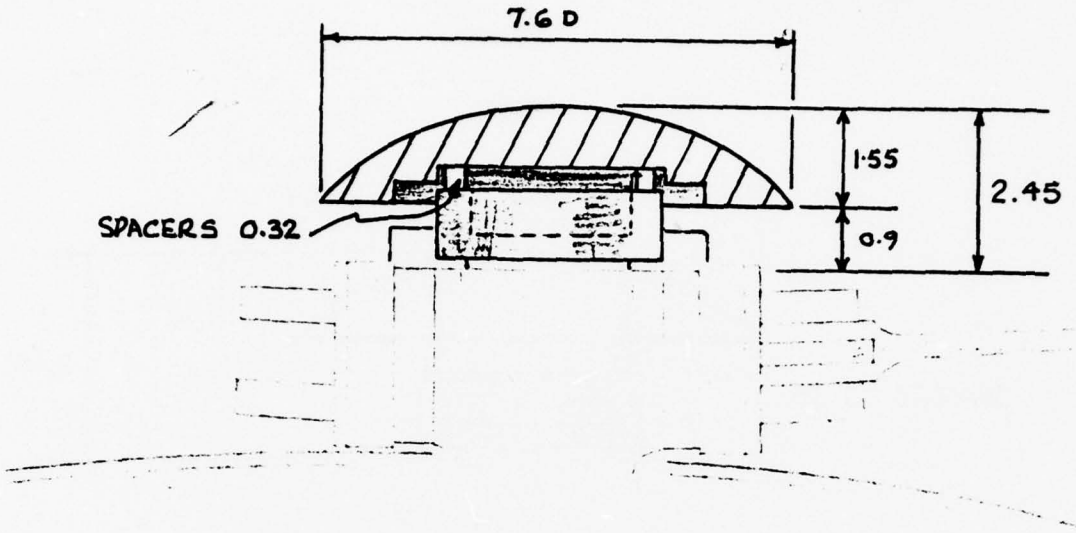

The same as H1.2, but the large (7.6-in.-diam.) solid cap is lifted above the top of the instrumentation cannister by 0.32-in. spacers on the four supporting bolts.

The upper surface of the cap was covered with 0.007-in. grit.

This configuration was only run with the I_1 instrumentation ring fitted around the cannister.

Figure B–25. Raised 7.6-Inch Solid Cap, $H_{1.2.1}$ – Run 207.

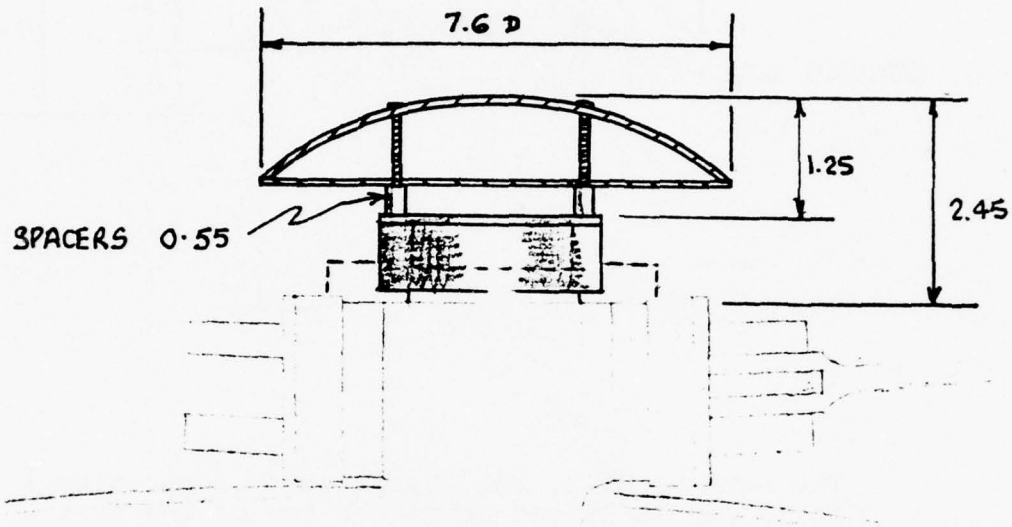

A fiberglass solid(closed)cap, 7.6-in-diam. elevated above the instrumentation cannister (with cover) on 0.55-in. spacers to give an equivalent 1.25-in. height. The undersurface of the beanie is closed by a 0.062-in.-thick aluminum plate.

Figure B–26. Raised 7.6-Inch Solid Cap, $H_{1.2.2}$ – Run 208.

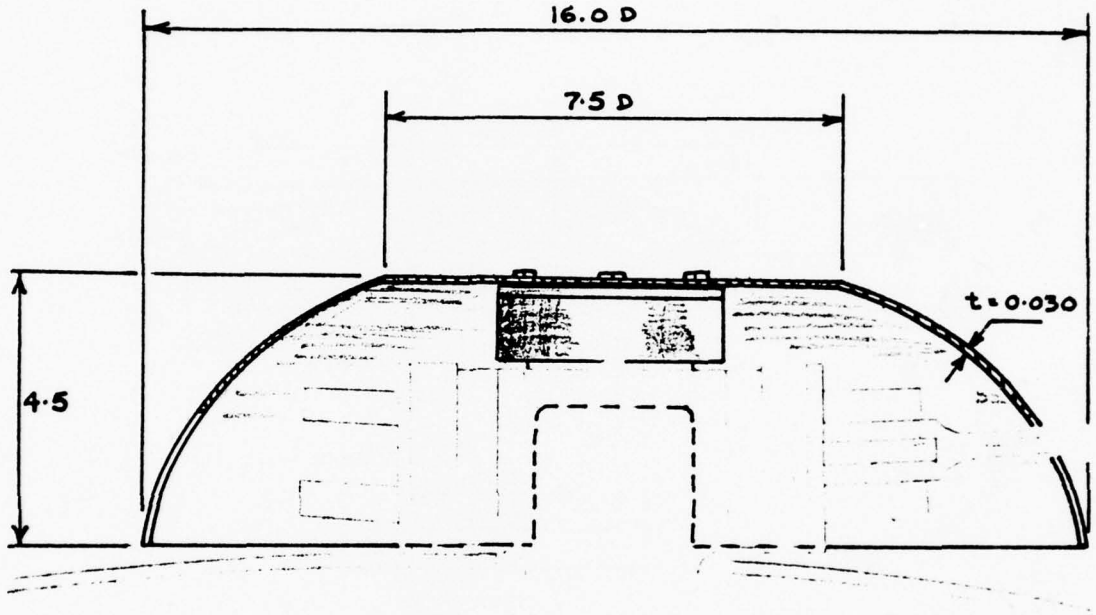

$H_{1.3.0}$ is a helment of thin sheet steel, which completely envelopes the hub. Open cutouts are provided for the blade shanks.

Surface roughness of the helmet was increased by addition of #54 grit (0.012 diam.).

Figure B–27. 16-Inch-Diameter Hub Fairing, $H_{1.3.0}$ – Run 151.

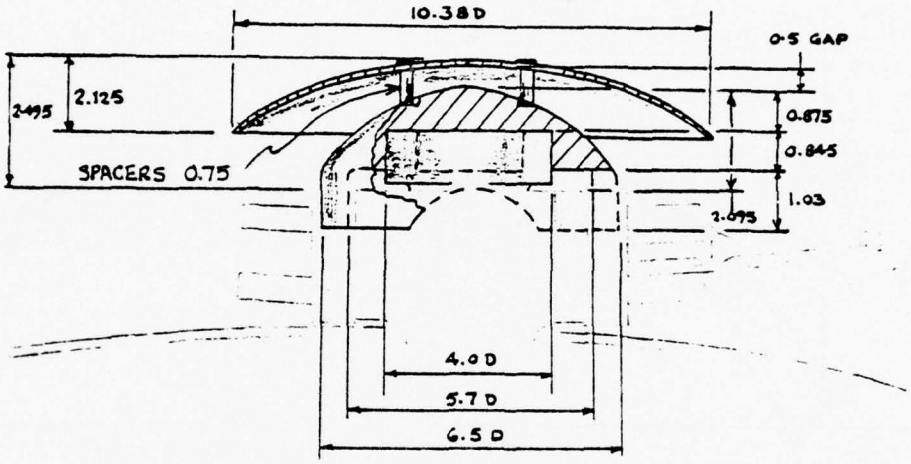

The $H_{1.5}$ configurations consist of two parts - an open 10.4-in.-diam. fiberglass open cap at various heights above a wooden underbody (hub cover) fitted tightly over the hub upper surface and instrumentation cannister.

$H_{1.5.1}$ has a gap of 0.5 in.

Figure B–28. 10.4-Inch-Diameter Open Hubcap With Underbody and 0.5-Inch Gap, $H_{1.5.1}$ – Run 164.

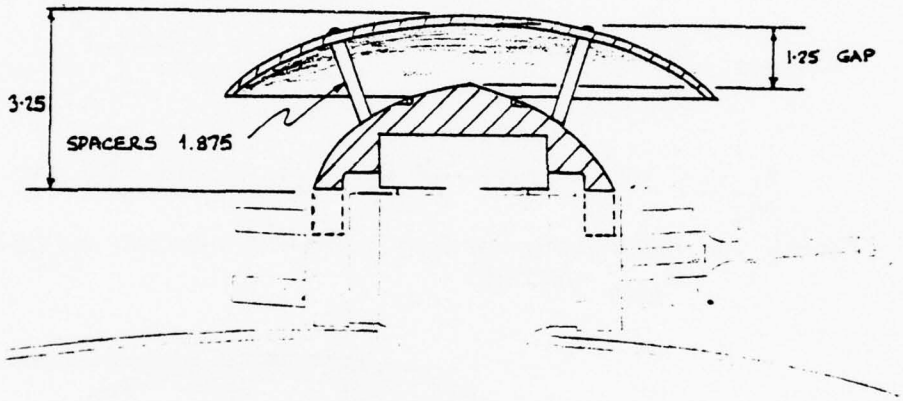

$H_{1.5.2}$ is the same as $H_{1.5.1}$ except that the gap is increased to 1.25 in. and the spacers are canted radially. This configuration was run with and without tape over the bolt holes (for normal spacer arrangement) in the cap.

Figure B–29. 10.4-Inch-Diameter Open Hubcap With Underbody and 1.25-Inch Gap, $H_{1.5.2}$ – Runs 154, 161.

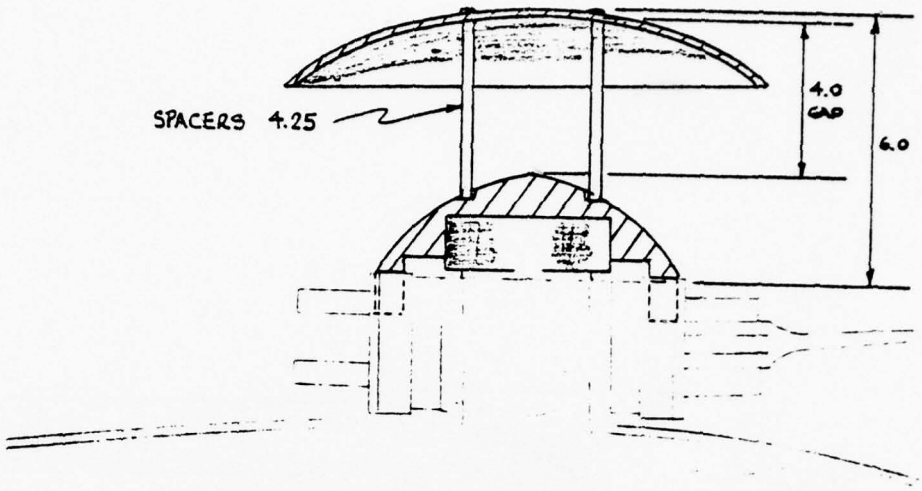

$H_{1.5.3}$ is the same as $H_{1.5.1}$, except the gap is 4.0 in.

Figure B–30. 10.4-Inch-Diameter Open Hubcap With Underbody and 4.0-Inch Gap, $H_{1.5.3}$ – Run 162.

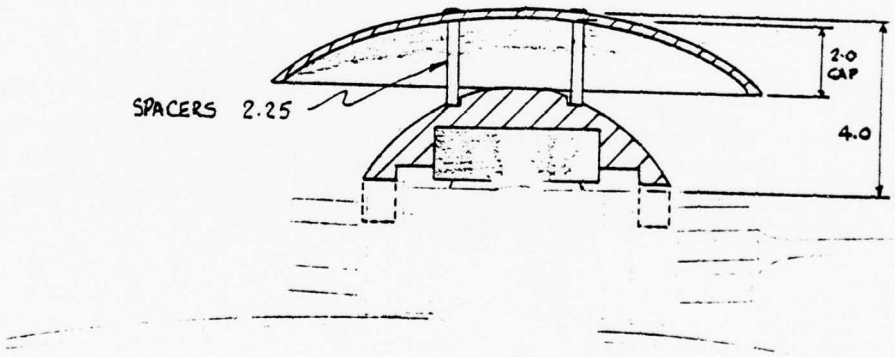

$H_{1.5.4}$ is the same as $H_{1.5.1}$, except the gap is 2.0 in.

Figure B–31. 10.4-Inch-Diameter Open Hubcap With Underbody and 2.0-Inch Gap, $H_{1.5.4}$ – Run 177.

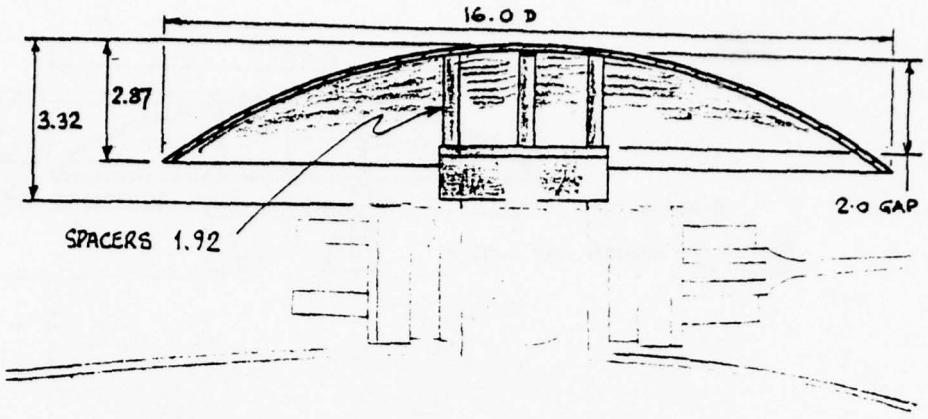

$H_{1.7.1}$ is an open 16-in.-diam. fiberglass hub cap mounted over the instrumentation cannister (with cover) with a 2-in. gap.

Figure B–32. 16-Inch-Diameter Open Hubcap Without Underbody and With 2-Inch Gap, $H_{1.7.1}$ – Runs 167, 168.

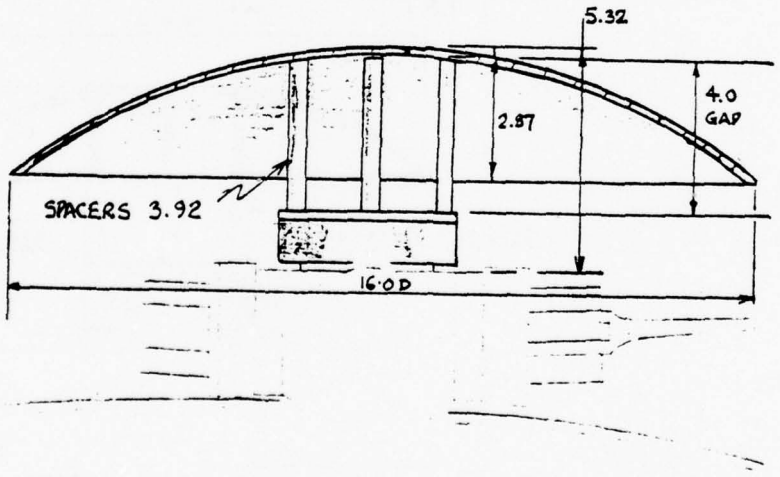

$H_{1.7.2}$ is the same as H1.7.1, except the gap is 4 in.

Figure B–33. 16-Inch-Diameter Open Hubcap Without Underbody and With 4-Inch Gap, $H_{1.7.2}$ – Runs 169, 171.

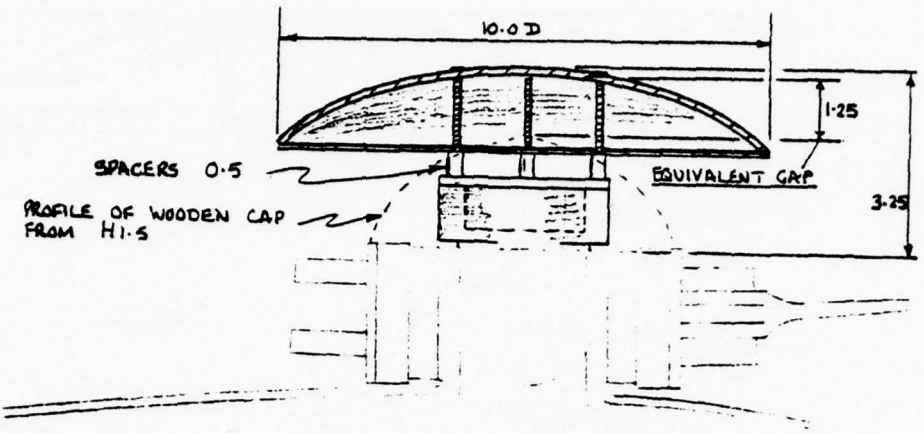

$H_{1.8.1}$ is a 10.0-in.-diam fiberglass solid cap with bottom aluminum closure plate mounted over the closed instrumentation cannister at the same location as $H_{1.5.2}$, an equivalent height of 1.25 in. above the location of the top of the underbody, which is not fitted.

Figure B–34. 10-Inch-Diameter Solid Hubcap With 1.25-Inch Gap, $H_{1.8.1}$ – Run 189.

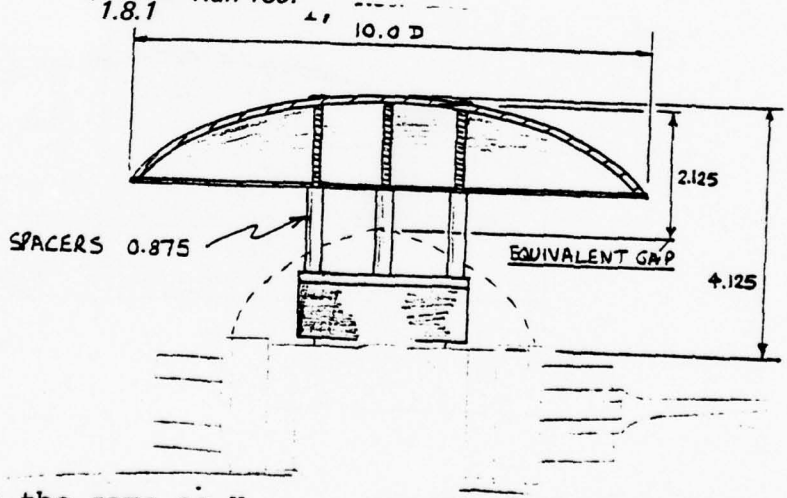

$H_{1.8.2}$ is the same as $H_{1.8.1}$, except that equivalent gap is 2.12 inches.

Figure B–35. 10-Inch-Diameter Solid Hubcap With 2.12-Inch Gap, $H_{1.8.2}$ – Run 190.

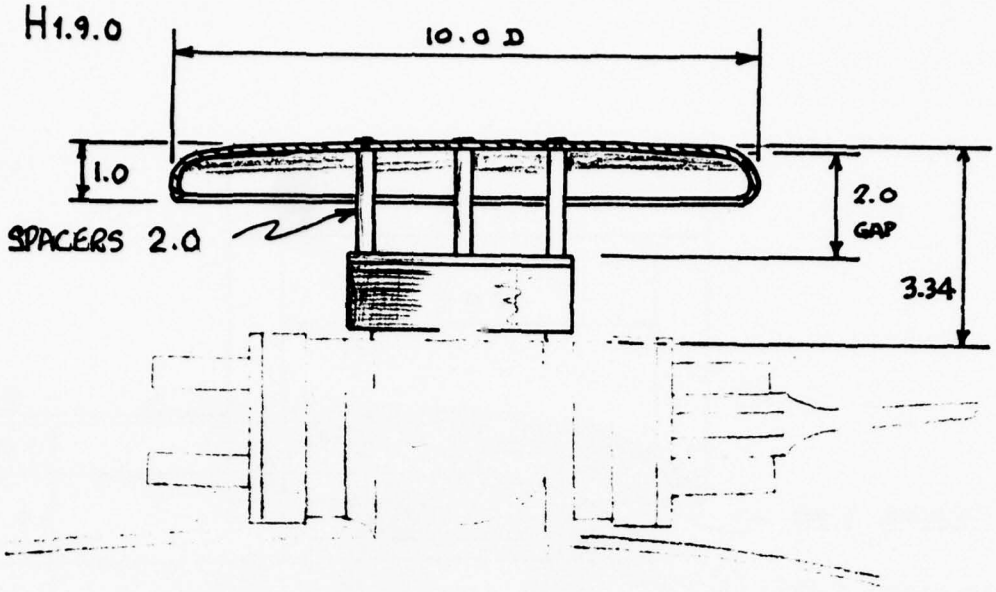

$H_{1.9.0}$ is the basic surmounted by a production 10.0 - in.-diam. Wham-O-Frisbee 2 in. above instrumentation cannister cap. The Frisbee was strengthened by a fiberglass insert.

Figure B—36. 10-Inch-Diameter Wham-O Frisbee, $H_{1.9.0}$ — Run 182.

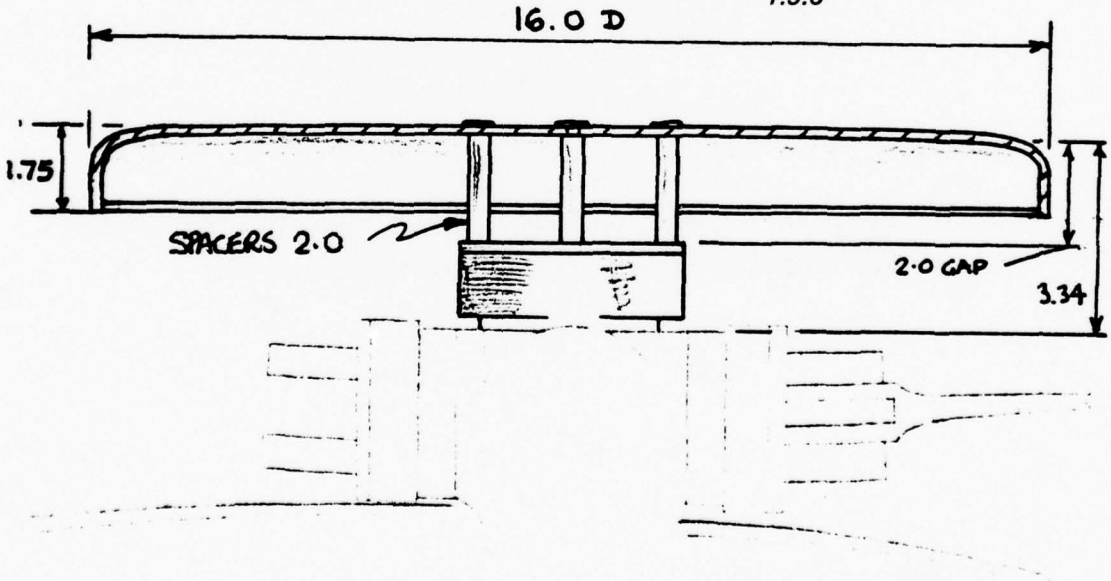

$H_{1.9.1}$ is similar to $H_{1.9.0}$, except with a 16-in.-diam. Frisbee fabricated of fiberglass.

Figure B—37. 16-Inch-Diameter Fabricated Frisbee, $H_{1.9.1}$ — Run 183.

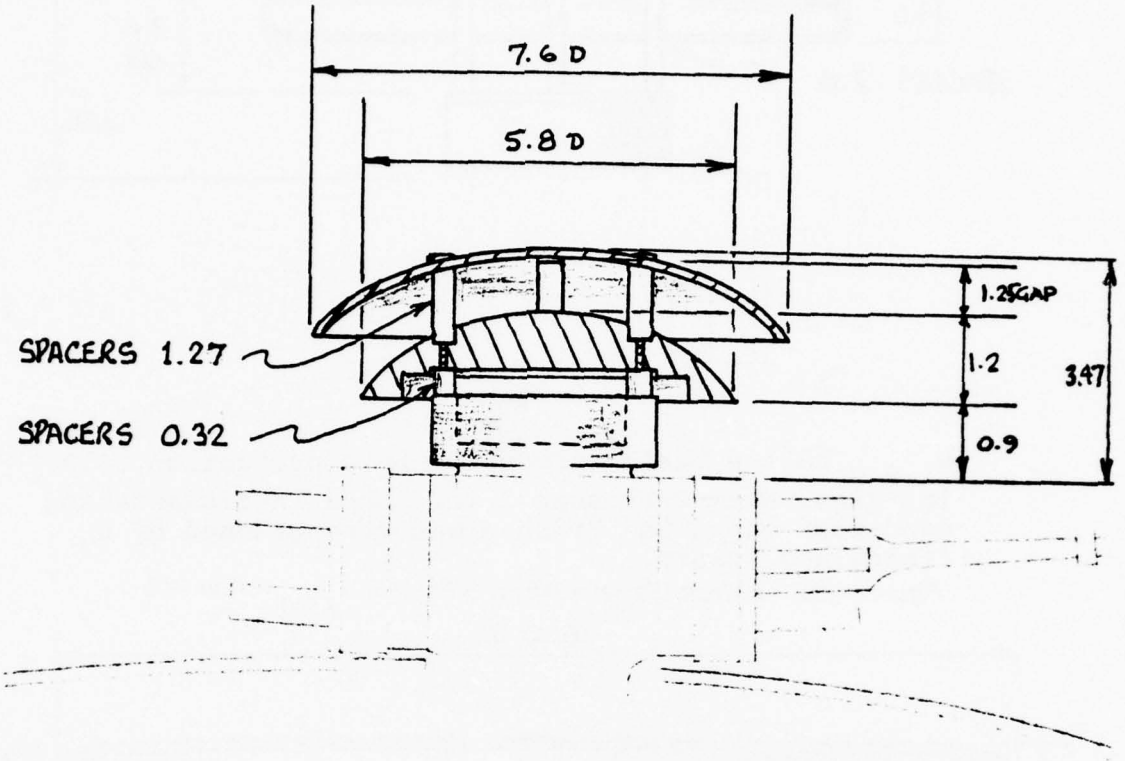

$H_{1.11.1}$ is a 7.6-in.-diam. metal open hub cap with wooden underbody and a 1.2-in. gap.

Figure B—38. 7.6-Inch-Diameter Open Cap With Underbody and 1.2-Inch Gap, $H_{1.11.1}$ — Runs 194-200.

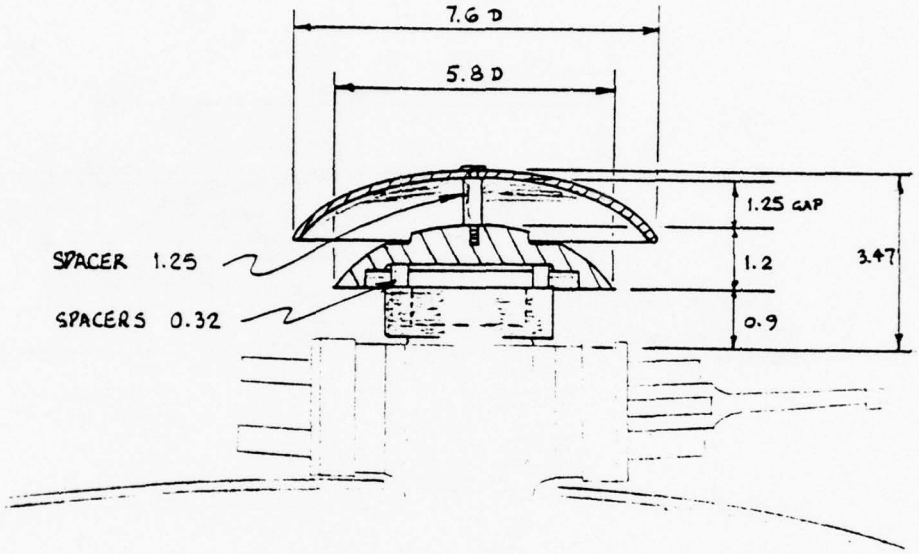

$H_{1.11.2}$ is the same as $H_{1.11.1}$, except that the four 1.27-in. spacers are replaced by a single central spacer 1.25 in. long on a larger bolt.

Figure B—39. 7.6-Inch-Diameter Open Cap With Underbody and 1.2-Inch Gap, Employing Single Supporting Post, $H_{1.11.2}$ — Runs 201, 202.

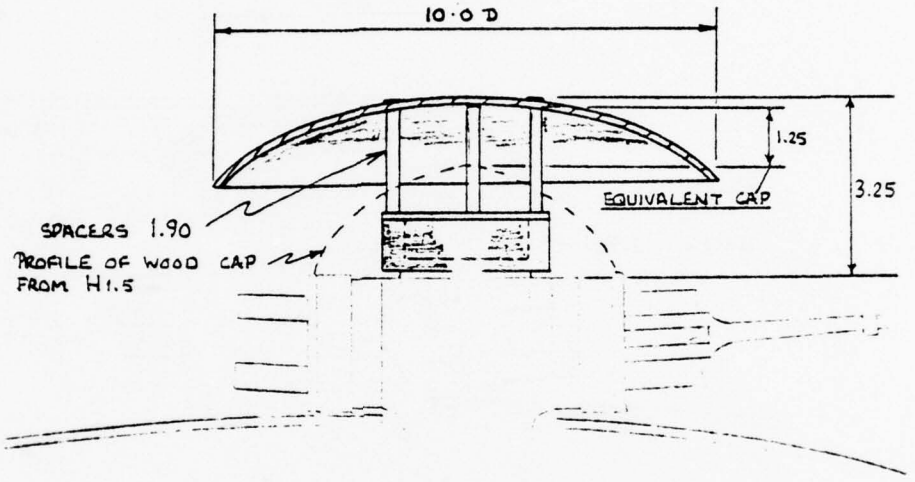

$H_{1.14.1}$ is a 10.0-in.-diam. open cap mounted above the closed instrumentation cannister at an equivalent gap of 1.25 in. (compared to $H_{1.5.2}$ without wooden underbody.

Figure B–40. 10-Inch-Diameter Open Cap Without Underbody and With Gap at 1.25 Inches, $H_{1.14.1}$ – Runs 211-215.

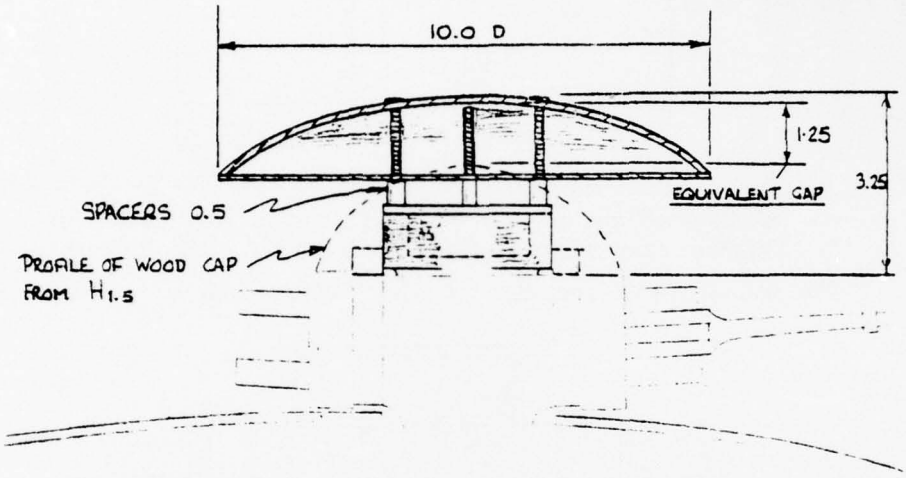

$H_{1.15.1}$ is a 10.0-in.-diam. solid hub cap mounted above the closed instrumentation cannister with the same outside dimensions as $H_{1.14.1}$.

Figure B—41. 10-Inch-Diameter Solid Hubcap With 1.25-Inch Equivalent Gap, $H_{1.15.1}$ — Run 210.

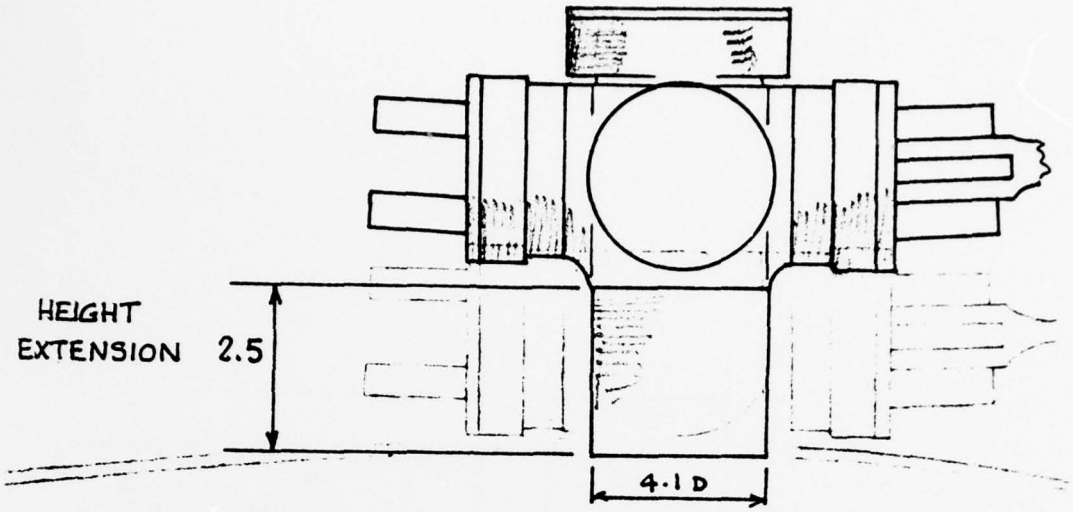

$H_{2.0}$ is the basic hub and instrumentation cannister elevated on a 2.5-in.-high extension block. Pitch links are also extended by the same amount.

Figure B–42. Basic Hub With 2.5-Inch Height Increase, $H_{2.0}$ – Runs 19, 20.

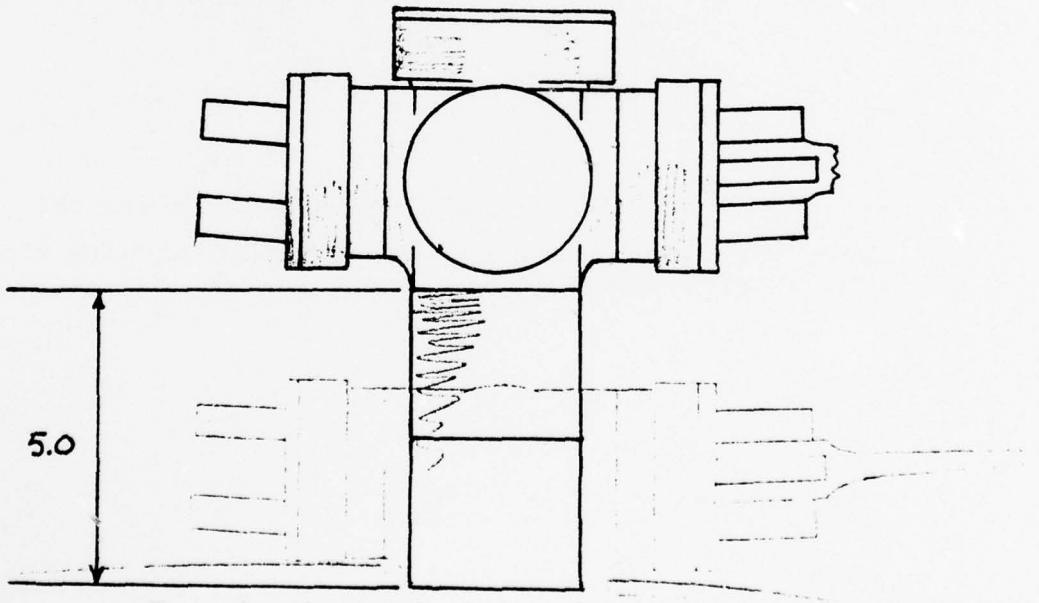

$H_{3.0}$ is the basic hub and instrumentation cannister elevated on a 5-in. extension.

Figure B–43. Basic Hub With 5.0-Inch Height Increase, $H_{3.0}$ – Runs 21, 22.

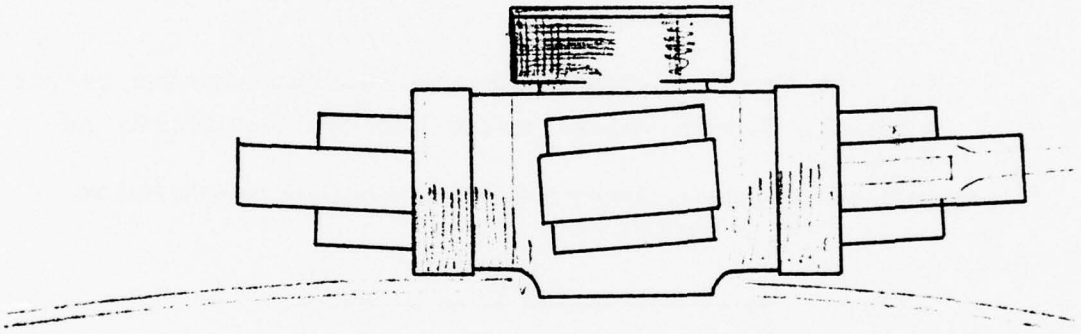

$H_{4.0}$ is a dummy hub, of wooden construction with short dummy blade shanks and the basic instrumentation cannister.

This was only tested nonrotating. It was positioned at 45° azimuth.

Figure B—44. Nonrotating Dummy Hub, $H_{4.0}$ — Runs 65-73, 78, 79.

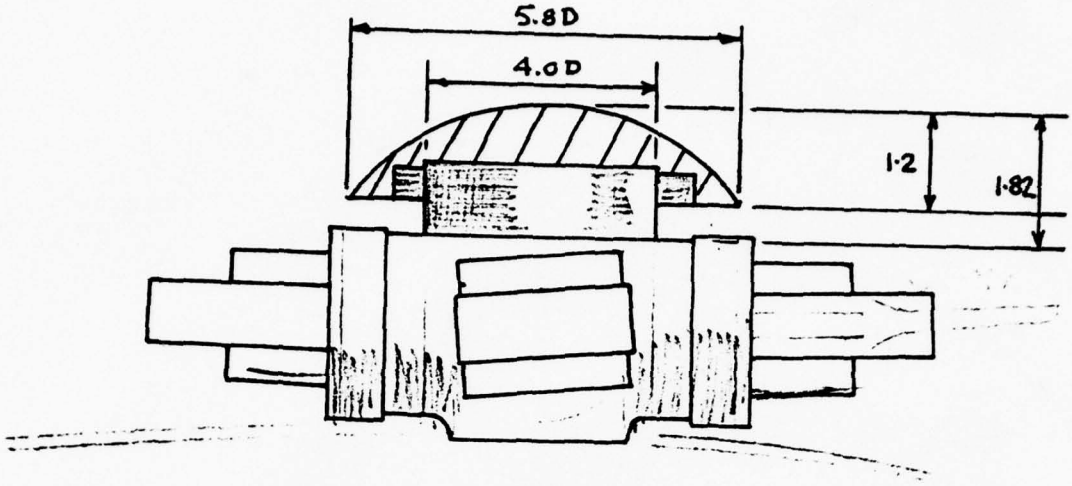

$H_{4.1}$ is the $H_{4.0}$ dummy hub and instrumentation cannister, with the 5.8-in.-diam. solid hub cap installed: as $H_{1.1}$.

Figure B–45. Nonrotating Dummy Hub With 5.8-Inch-Diameter Solid Hubcap, $H_{4.1}$ – Runs 74, 77.

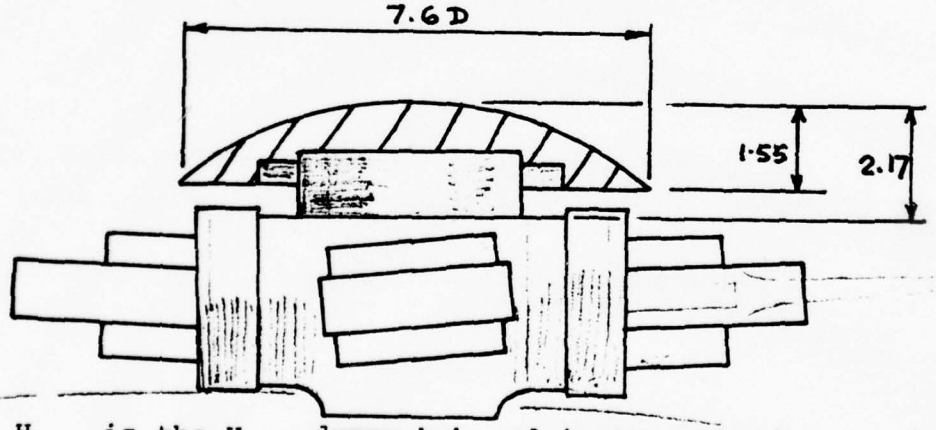

$H_{4.2}$ is the $H_{4.0}$ dummy hub and instrumentation cannister, with the 7.6-in.-diam. solid hub cap installed: as $H_{1.2}$.

Figure B–46. Nonrotating Dummy Hub With 7.6-Inch-Diameter Solid Hubcap, $H_{4.2}$ – Runs 75, 76.

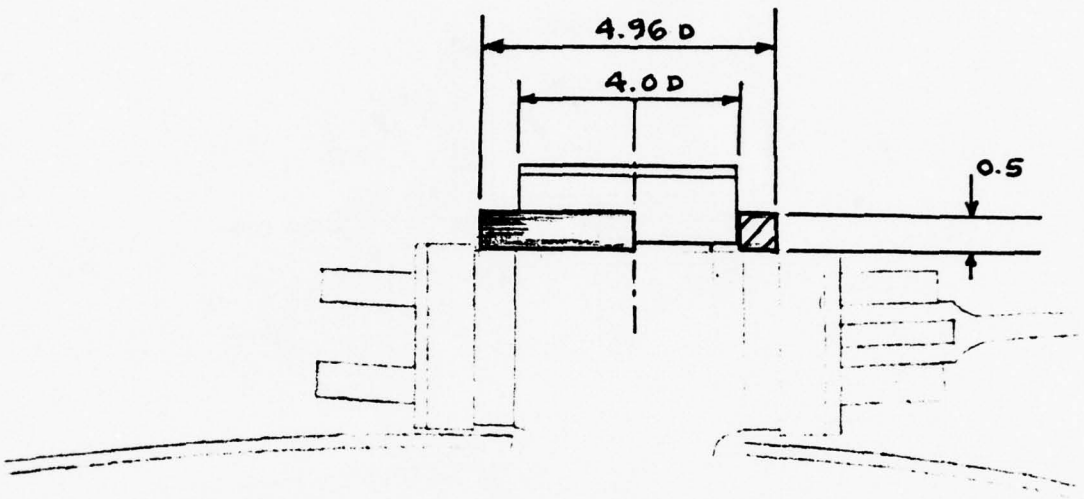

The I_1 instrumentation housing for extra rotor instrumentation used during flight test, consists of a wooden ring of square section, placed around and attached to the basic cannister, mounted flat on top of the hub.

Figure B—47. Instrumentation Housing, I, Runs 188, 189, 207-215.

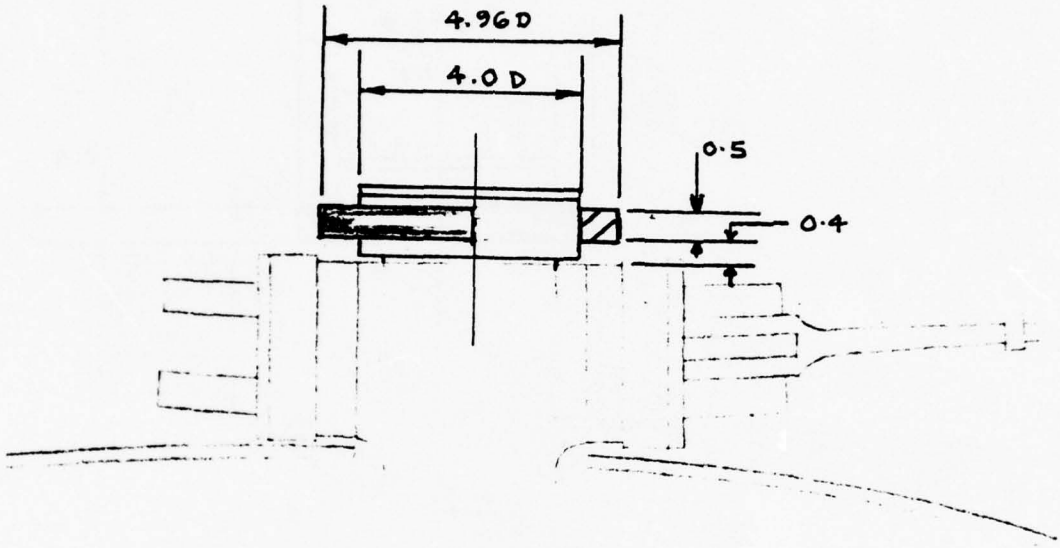

I_2 is the flight test instrumentation housing
I_1 alternately positioned, as shown.

Figure B—48. Instrumentation Ring, I_2 — Runs 194-201.

MAIN ROTOR

$M^{e\ f\ g\ h}_{a\ b\ c\ d}$ Basic UTTAS main rotor blades, with serial numbers a, b, c, d, located at azimuth positions e, f, g, h respectively at the 1/rev marker. Blades 293, 296, 297, 298, 299 are the basic model rotor blades as noted in Table B-5. Two other blades were employed briefly: a smoke blade, Serial No. 390, and a hot-film blade, Serial No. 391. These were in a developmental status and are mentioned for reference only.

$M^{e\ f\ g\ h}_{a\ b\ c\ d.1}$ Basic UTTAS blades with 0.25-inch balsa straight tip extensions. The extensions were intended to bring all blades up to the span of the smoke blade (see Figure B-49).

$M^{e\ f\ g\ h}_{a\ b\ c\ d.2}$ Basic UTTAS blades with cuffs added to the root ends as shown in Figure B-50.

PITCH ARMS
(Not illustrated)

PA_1 Soft "horseshoe" pitch arms with a measured stiffness of 6,302 lb-in./rad. These are normally used to achieve proper scaling of torsional stiffness.

PA_2 Stiff pitch arms – direct connection of pitch links to blade root fitting. These were introduced to improve simulation of flow around hub.

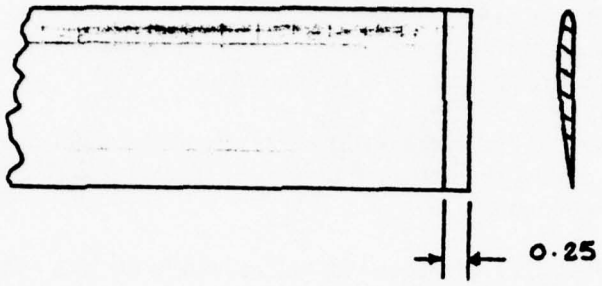

Figure B–49. Main Rotor Blades With Balsa Tips.

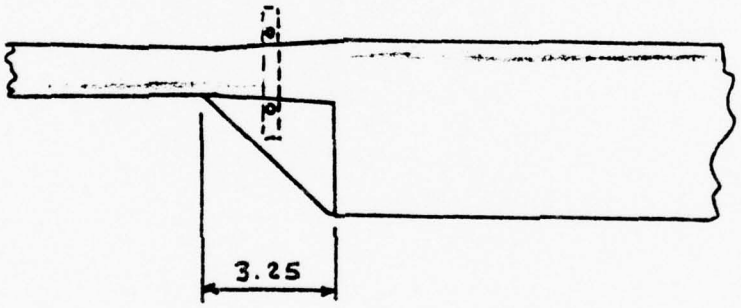

Figure B–50. Blade With Cuffs.

PYLON

$P_{1.0}$ A forward-facing pylon/nacelle fairing plus four turning vanes located aft of the hub between the nacelles, and splitter plates extending forward from nacelle intake/fuselage junction as shown in Figure B-51.

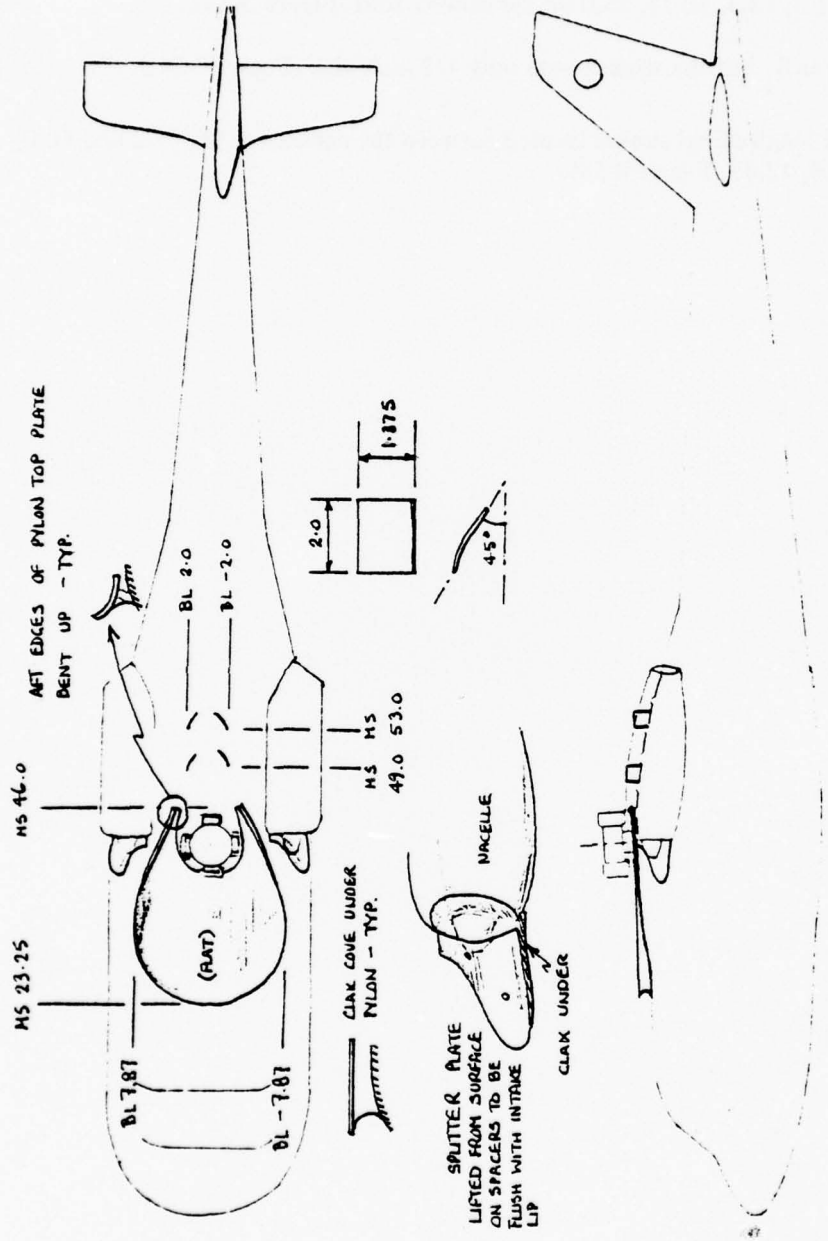

Figure B–51. Crown/Nacelle Fairing, $P_{1.0}$ – Run 152.

STRAKES

S_1 Four longitudinal strakes 1.25 and 1.75 inches high located at BL ±2.75, ±7.75 respectively on the canopy roof, as shown in Figure B-52.

S_2 Four laterally running strakes 1-1/2 inches high, 15-1/4 inches wide located at MS 11.3, 15.3, 20.75, 25.0 on the canopy roof (Figure B-53).

S_3 Same as S_1 but the strakes were only 1/2 inch high (Figure B-54).

S_4 Three longitudinal strakes located between the nacelles at MS 47.2 and 60.0, BL 0.0, ±2.47 (Figure B-55).

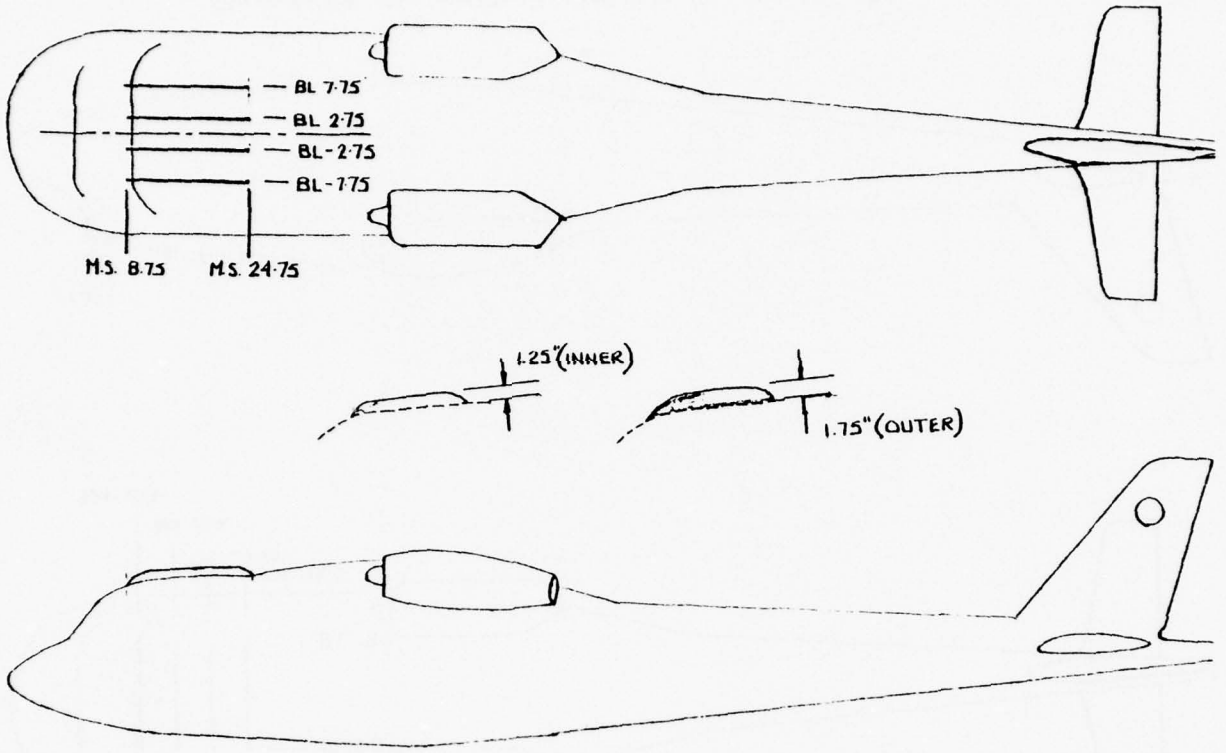

Figure B–52. Forward Crown Longitudinal Strakes, S_1 – Run 13.

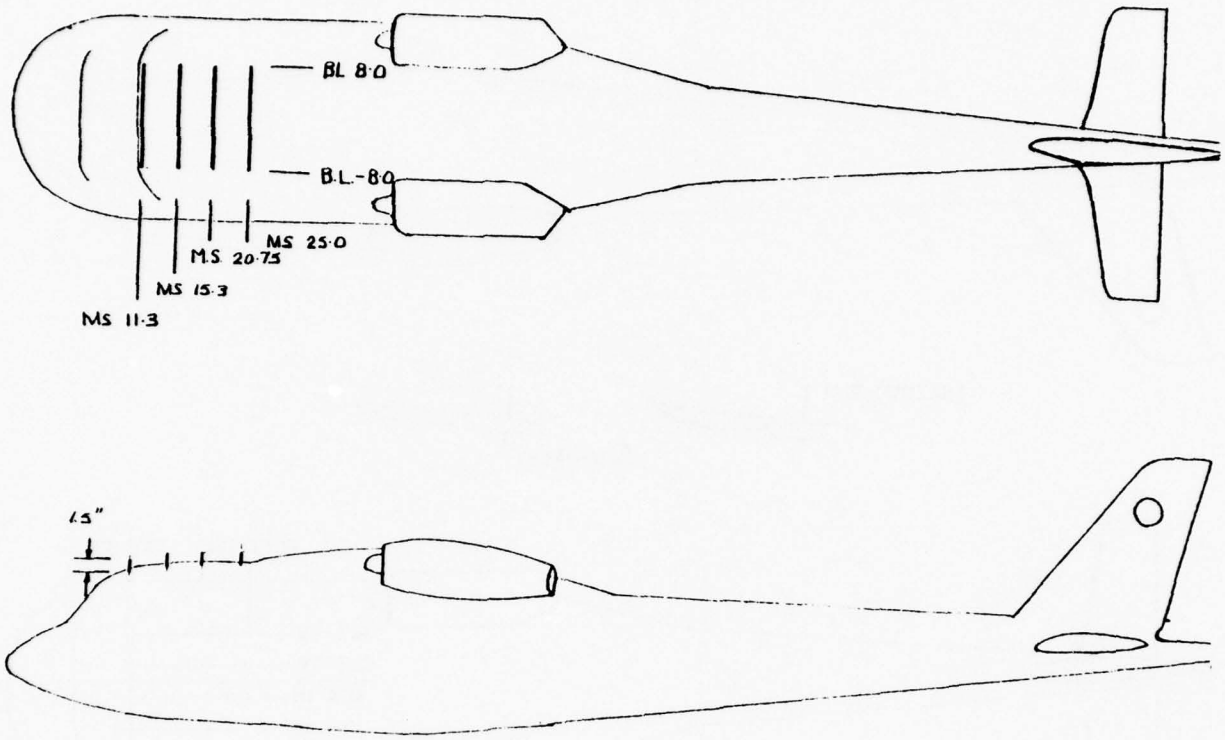

Figure B–53. Forward Crown Lateral Strakes, S_2 – Run 14.

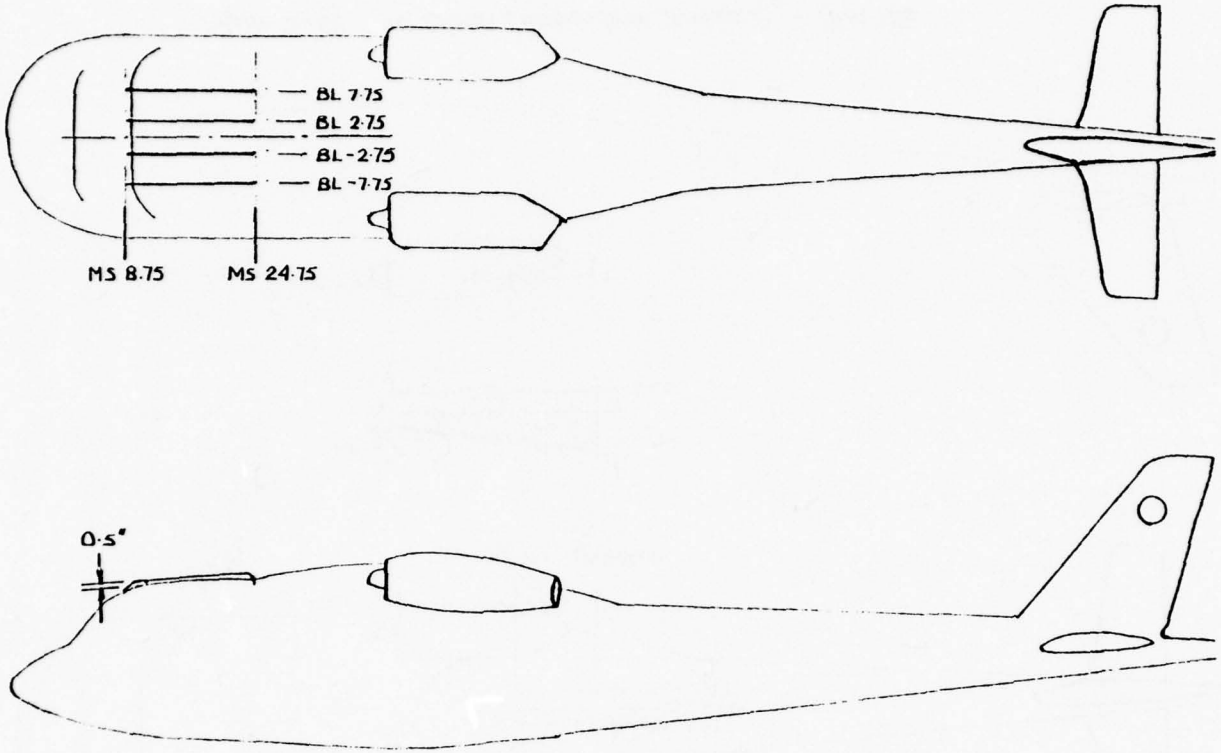

Figure B–54. Reduced-Height Longitudinal Strakes, S_3 – Runs 18, 20, 22.

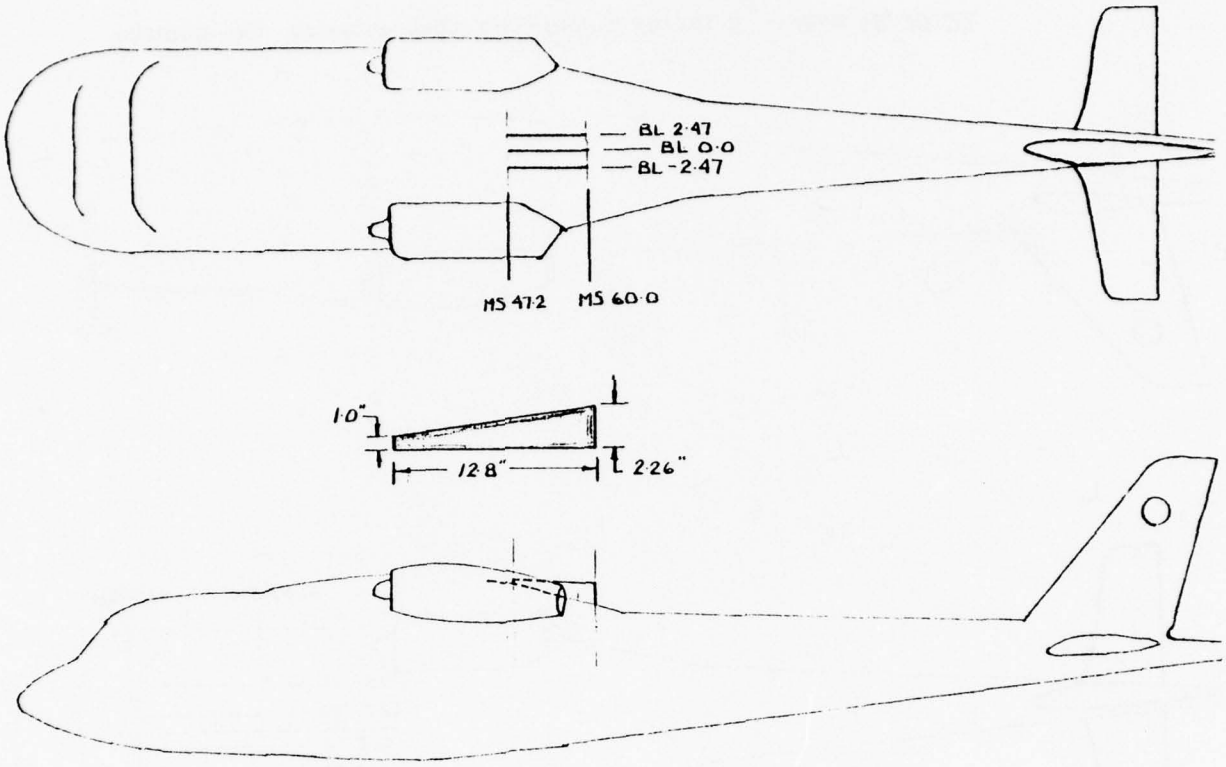

Figure B–55. Aft Crown Longitudinal Strakes, S_4 – Run 155.

VORTEX GENERATORS

VG_1 One-inch by 0.25-inch-high vortex generators on the forward crown (MS 16.5) at 20 degrees nose left to the centerline. Ten vortex generators spaced 1 inch apart (see Figure B-56).

$VG_{2.1}$ Two-inch-chord by 1.375-inch-high vortex generators located between the nacelles at 45 degrees to the flow with the leading edge toward the centerline (see Figure B-57).

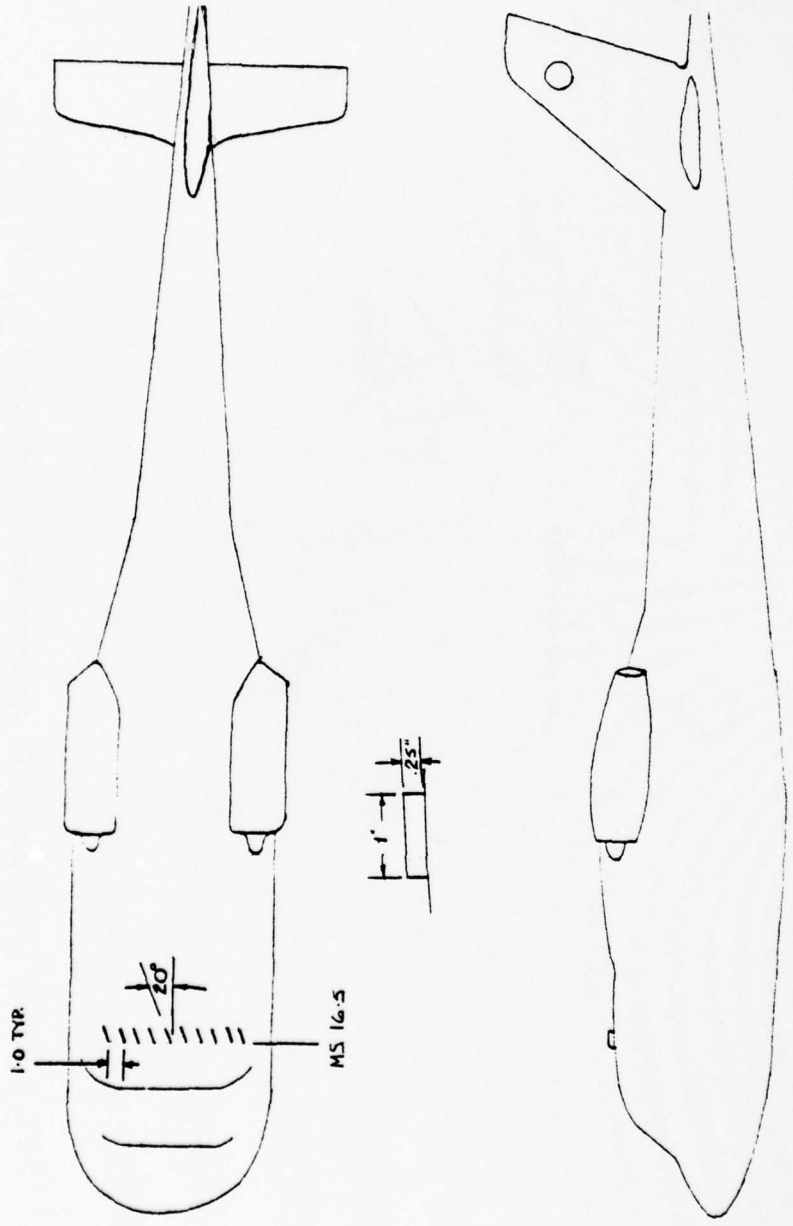

Figure B–56. Forward Crown Vortex Generators, VG_1 – Run 16.

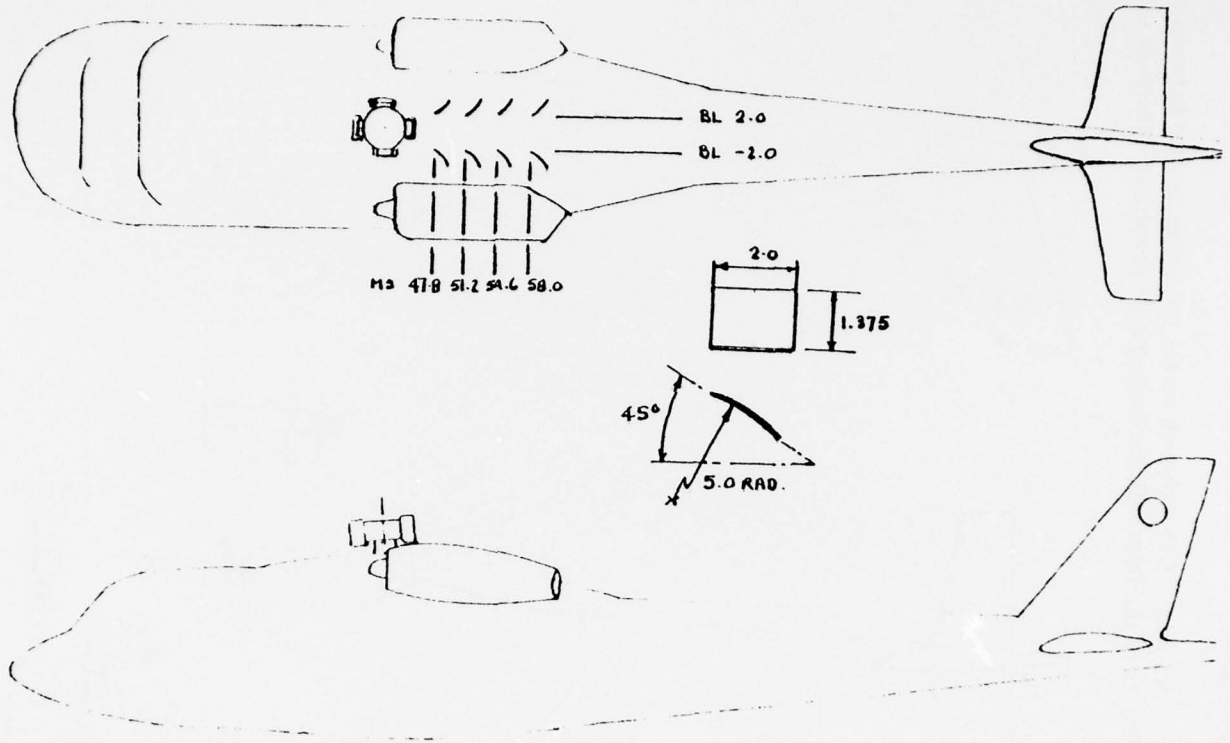

Figure B–57. Aft Crown Vortex Generators, $VG_{2.1}$ – Run 139.

WINGS

$W^{20}_{1.0}$ Stub wings attached to the nacelle cowlings, with the wing quarter-chord located at MS 43.5. They were set at 20 degrees to the fuselage waterline. The wings employed the HLH blade airfoil section and were 6 inches in chord and 4 inches in span (see Figure B-58).

$W^{0}_{2.0}$ A double-slotted flapped wing located above the tailboom at MS 69.5. It was set at 0 degrees to the fuselage waterline. Gap settings for the flaps were 0.1 inch (see Figure B-59).

$W^{0}_{3.0}$ This configuration was the same as $W^{0}_{2.0}$ except that the bottom flap was removed (not shown).

$W^{15}_{4.0}$ A stub wing added to the sides of the tailboom at MS 71.15, WL 31.69. The wings were 6 inches in chord, 8 inches in span, and set at 15 degrees to the fuselage waterline (see Figure B-60).

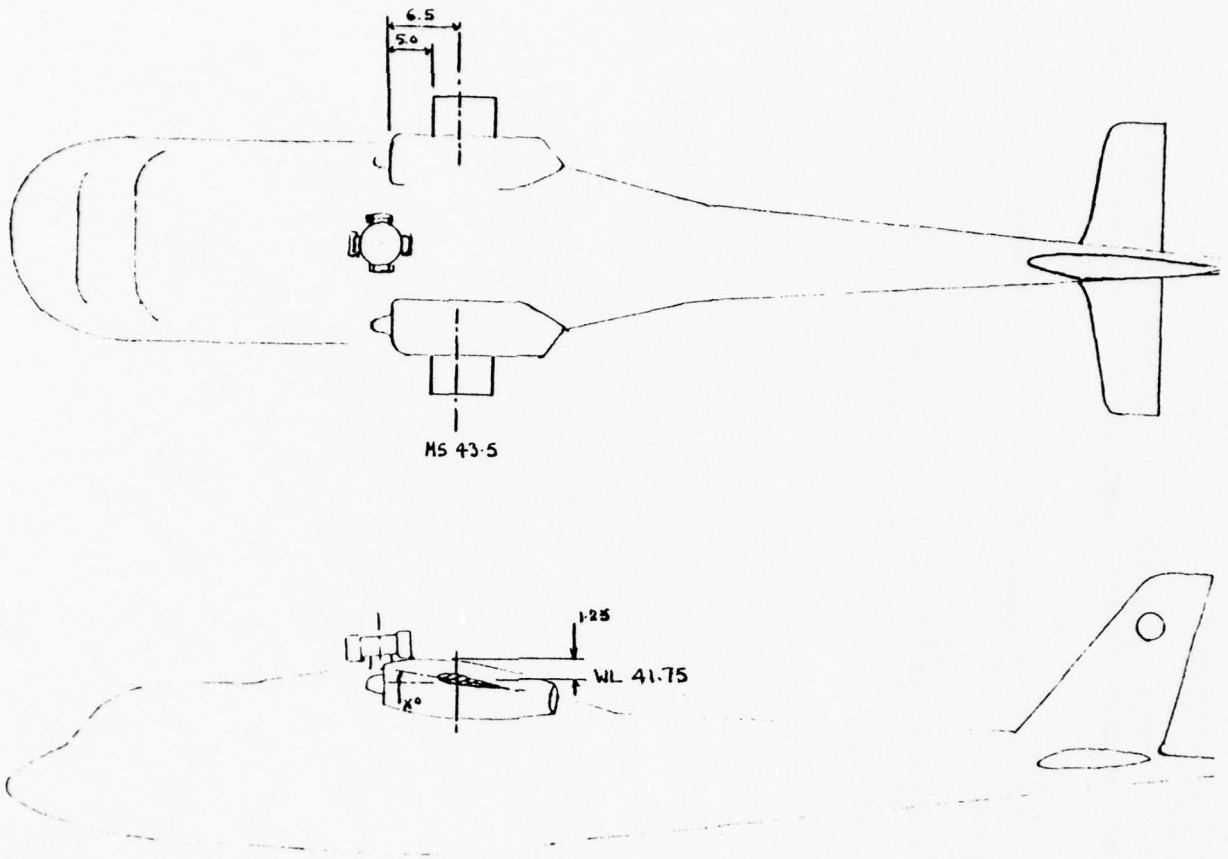

Figure B–58. Stub Wing on Nacelles, $W^{20}_{1.0}$ – Run 178.

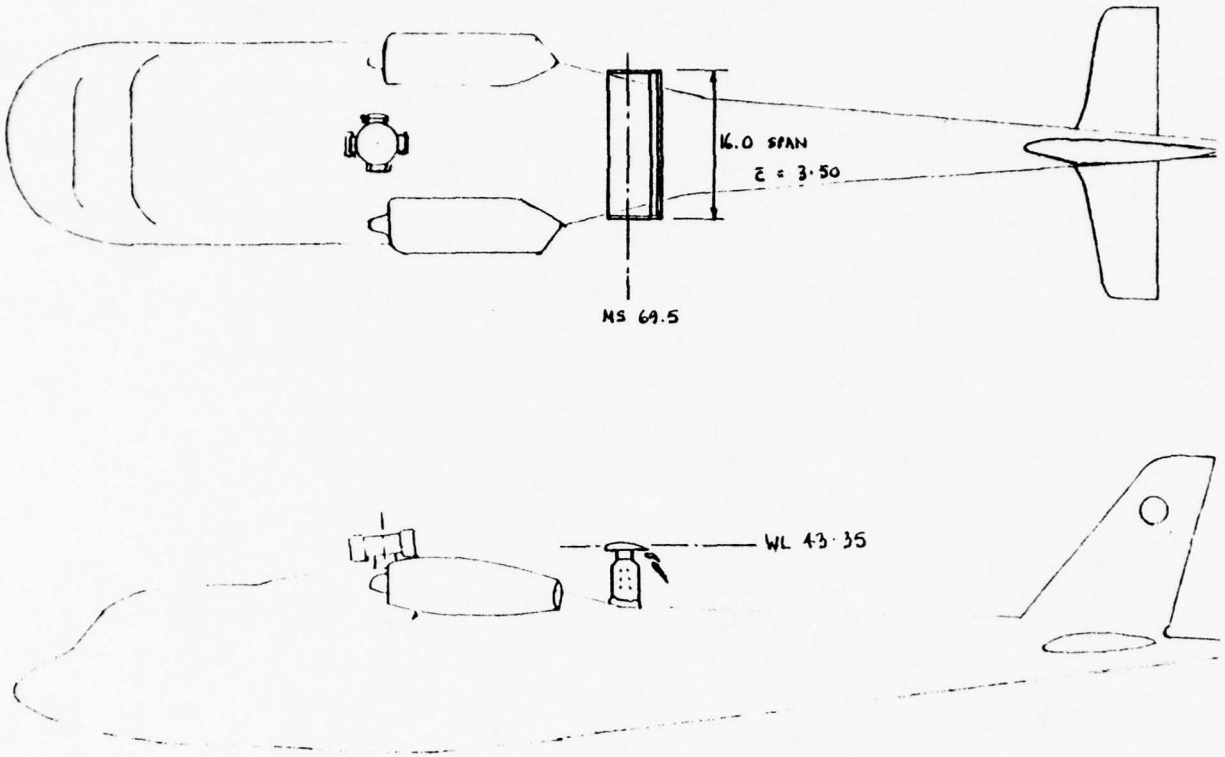

Figure B–59. Double-Slotted Flapped Wing, $W^{0}_{2.0}$ – Run 179.

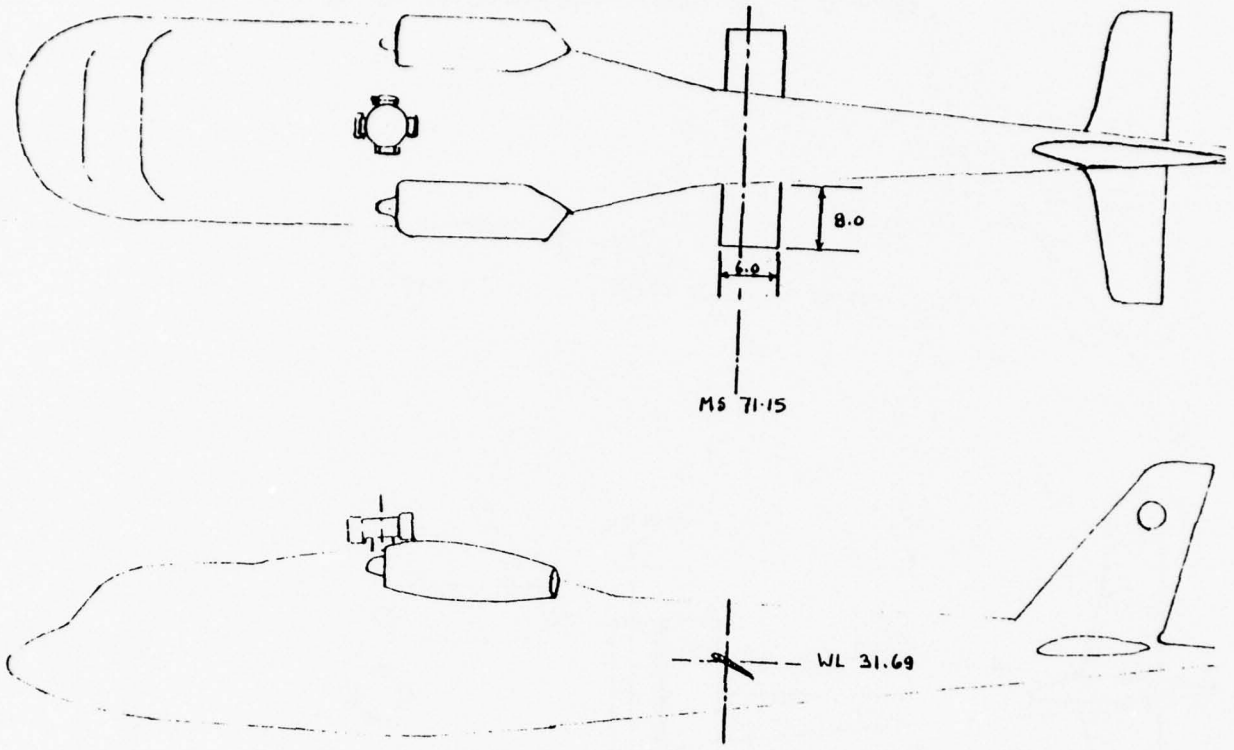

Figure B–60. Stub Wing on Tailboom, $W^{15}_{4.0}$ – Run 186.

POROUS SPOILER

X_1 A lateral spoiler located between the nacelles at MS 56.5. The spoiler was 15 inches wide and 2 inches high. One-half-inch,3/8-inch, and 1/4-inch-diameter holes were randomly spaced on the spoiler in an attempt to attenuate the lower wake frequencies (see Figure B-61).

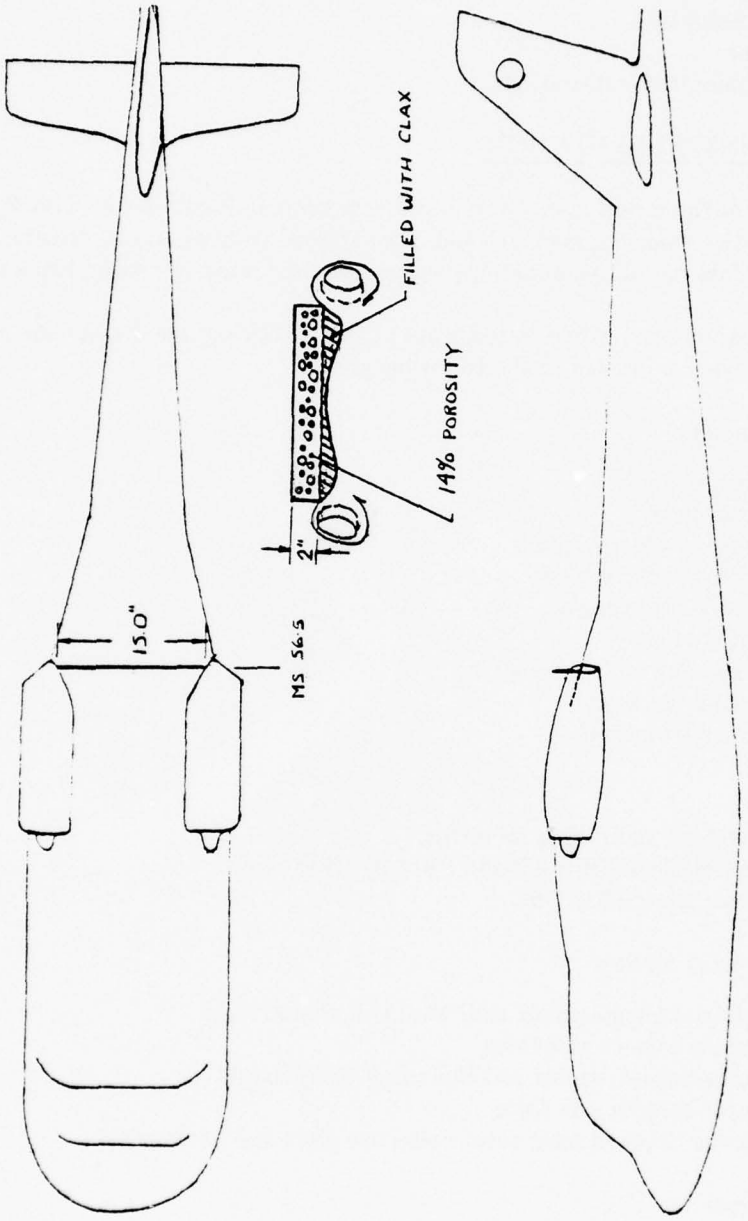

Figure B–61. Porous Spoiler, X_1 – Run 143.

INSTRUMENTATION

The model instrumentation for this test was of unusual complexity and was considered as a number of packages, used individually or in combination. These were:

Basic model, including safety-of-flight parameters
Force balances
Pressure transducers
Hot film rake
Ancillary equipment, cameras, etc.

BASIC MODEL INSTRUMENTATION

Instrumentation of the model is shown in block schematic in Figure B-62. This shows the basic package of five balances, main and tail rotor control systems, model orientation (pitch and yaw angles), lubrication system temperatures and flow rates, tail angle, blade stresses, etc.

Safety-of-flight parameters, which were always monitored by on-line display, are indicated by doubled boxes. These consisted of the following groups:

On digital meters:

Main rotor rpm
Tail rotor rpm
Main rotor collective pitch
Main rotor cyclic pitches
Main rotor blade angle
Tail rotor slider
Fuselage pitch and yaw angles
Horizontal tail angle
Inner race temperature

On scopes:

Hub pitching and rolling moments
Main rotor blade FB vs CB and FB, CB, TB vs 1/rev
Tail rotor strap FB vs CB

On peak-to-peak meters:

Total loads balance vector addition of all components
Main rotor balance side force
Tail rotor balance vector addition of all components
Tail rotor balance side force
Difference between main rotor collective pitch and blade angle

On analog meters:

Main and tail rotor air supply pressure
Lubrication system temperatures

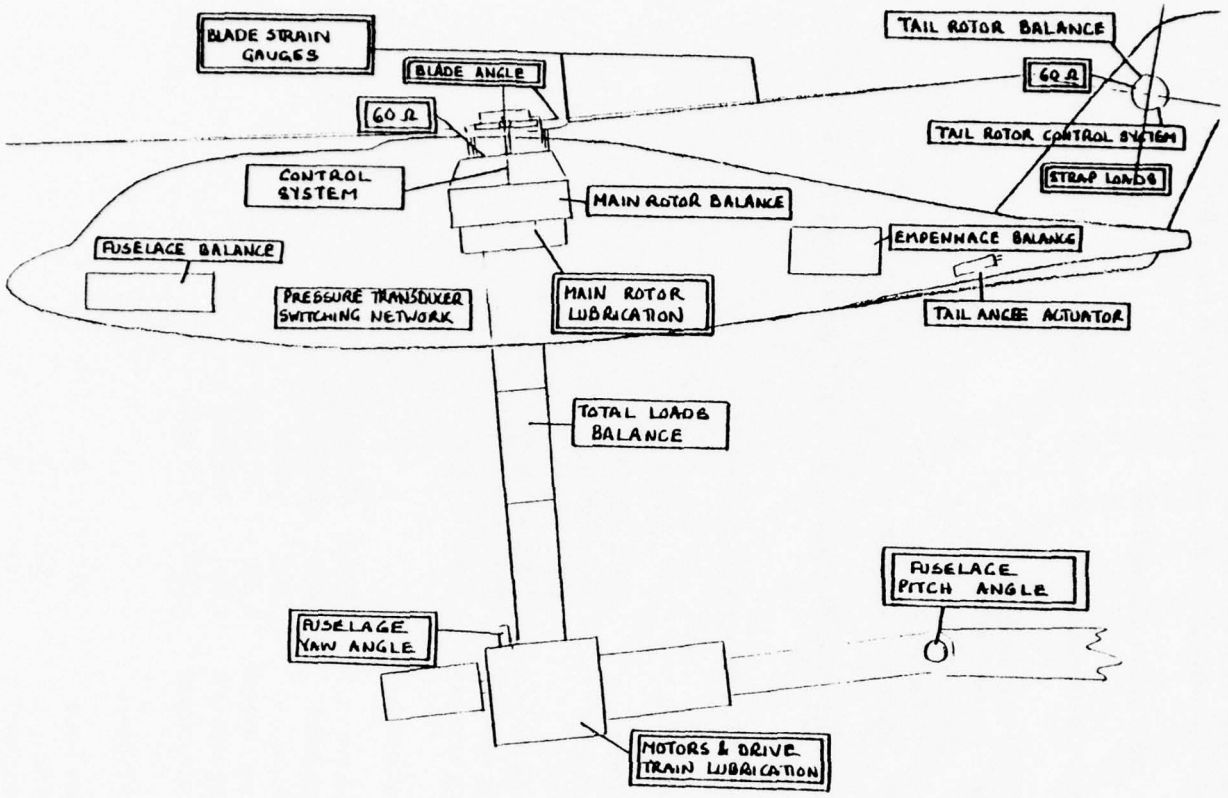

Figure B–62. Model Instrumentation.

BALANCES

Four balances are contained within the SRH system, a six-component main rotor balance, a six-component fuselage balance for measuring loads on the fuselage skins, a five-component (less axial force) balance for the empennage, and a six-component tail rotor balance. These balances and their functions are schematically portrayed in Figure B-63.

Balance locations are shown in Figure B-64.

Forces and moments measured by the individual balances are shown as follows:

Figure B-65	Total loads balance
Figure B-66	Fuselage balance
Figure B-67	Empennage balance
Figure B-68	Tail rotor balance
Figure B-69	Main rotor balance

Force and moment reference centers are indicated if different from the individual balance moment centers.

Load capabilities of the balances were as follows:

Total loads balance

Axial force	2,300 ± 800 lb
Normal force	400 ± 300 lb
Side force	400 ± 300 lb
Pitching moment	1,250 ± 417 lb-ft
Yawing moment	233 ± 125 lb-ft
Rolling moment	708 ± 167 lb-ft

Fuselage balance

Axial force	1,000 ± 950 lb
Normal force	2,000 ± 1,850 lb
Side force	500 ± 450 lb
Pitching moment	1,300 ± 1,200 lb-ft
Yawing moment	1,000 ± 950 lb-ft
Rolling moment	1,000 ± 950 lb-ft

Empennage balance

Normal force	250 ± 125 lb
Side force	250 ± 115 lb
Pitching moment	200 ± 90 lb
Yawing moment	200 ± 100 lb-ft
Rolling moment	225 ± 115 lb-ft

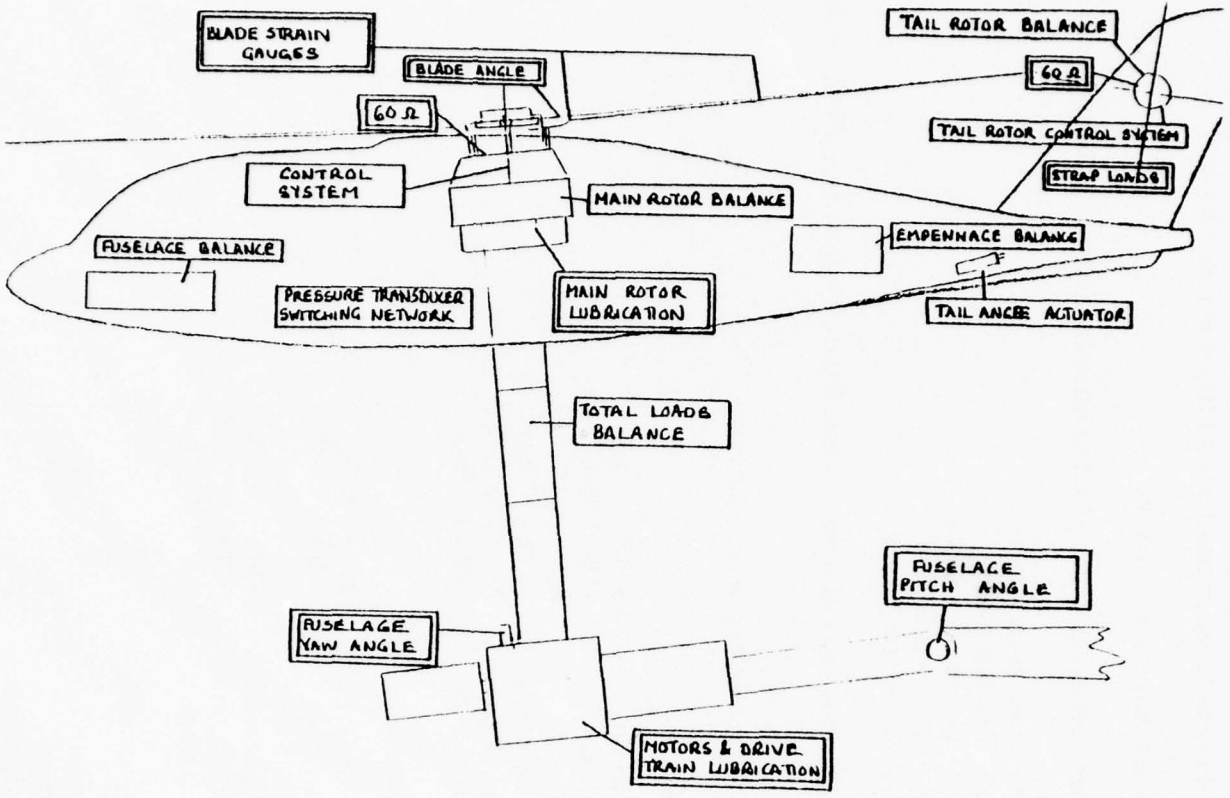

Figure B–62. Model Instrumentation.

BALANCES

Four balances are contained within the SRH system, a six-component main rotor balance, a six-component fuselage balance for measuring loads on the fuselage skins, a five-component (less axial force) balance for the empennage, and a six-component tail rotor balance. These balances and their functions are schematically portrayed in Figure B-63.

Balance locations are shown in Figure B-64.

Forces and moments measured by the individual balances are shown as follows:

Figure B-65	Total loads balance
Figure B-66	Fuselage balance
Figure B-67	Empennage balance
Figure B-68	Tail rotor balance
Figure B-69	Main rotor balance

Force and moment reference centers are indicated if different from the individual balance moment centers.

Load capabilities of the balances were as follows:

Total loads balance

Axial force	2,300 ± 800 lb
Normal force	400 ± 300 lb
Side force	400 ± 300 lb
Pitching moment	1,250 ± 417 lb-ft
Yawing moment	233 ± 125 lb-ft
Rolling moment	708 ± 167 lb-ft

Fuselage balance

Axial force	1,000 ± 950 lb
Normal force	2,000 ± 1,850 lb
Side force	500 ± 450 lb
Pitching moment	1,300 ± 1,200 lb-ft
Yawing moment	1,000 ± 950 lb-ft
Rolling moment	1,000 ± 950 lb-ft

Empennage balance

Normal force	250 ± 125 lb
Side force	250 ± 115 lb
Pitching moment	200 ± 90 lb
Yawing moment	200 ± 100 lb-ft
Rolling moment	225 ± 115 lb-ft

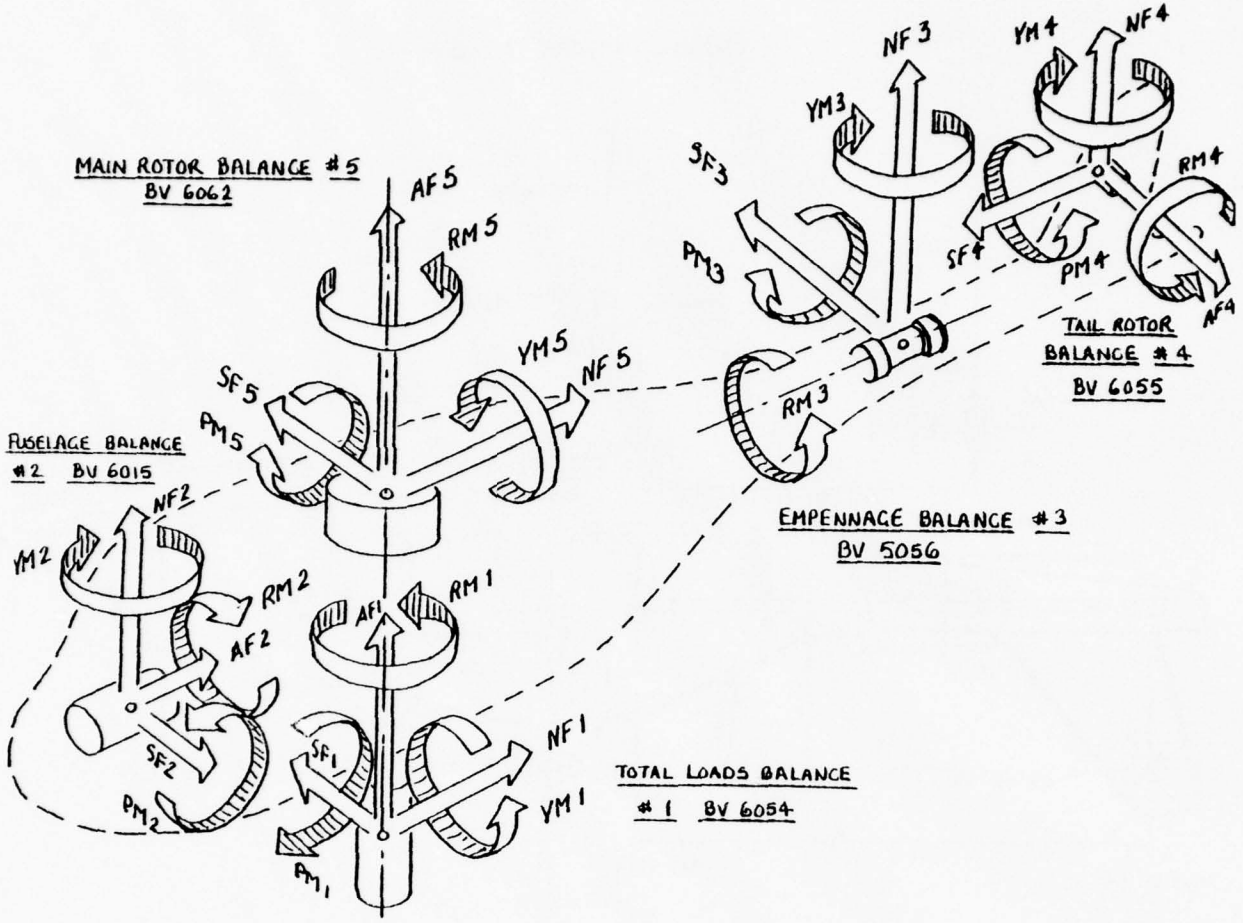

Figure B–63. Model Balances.

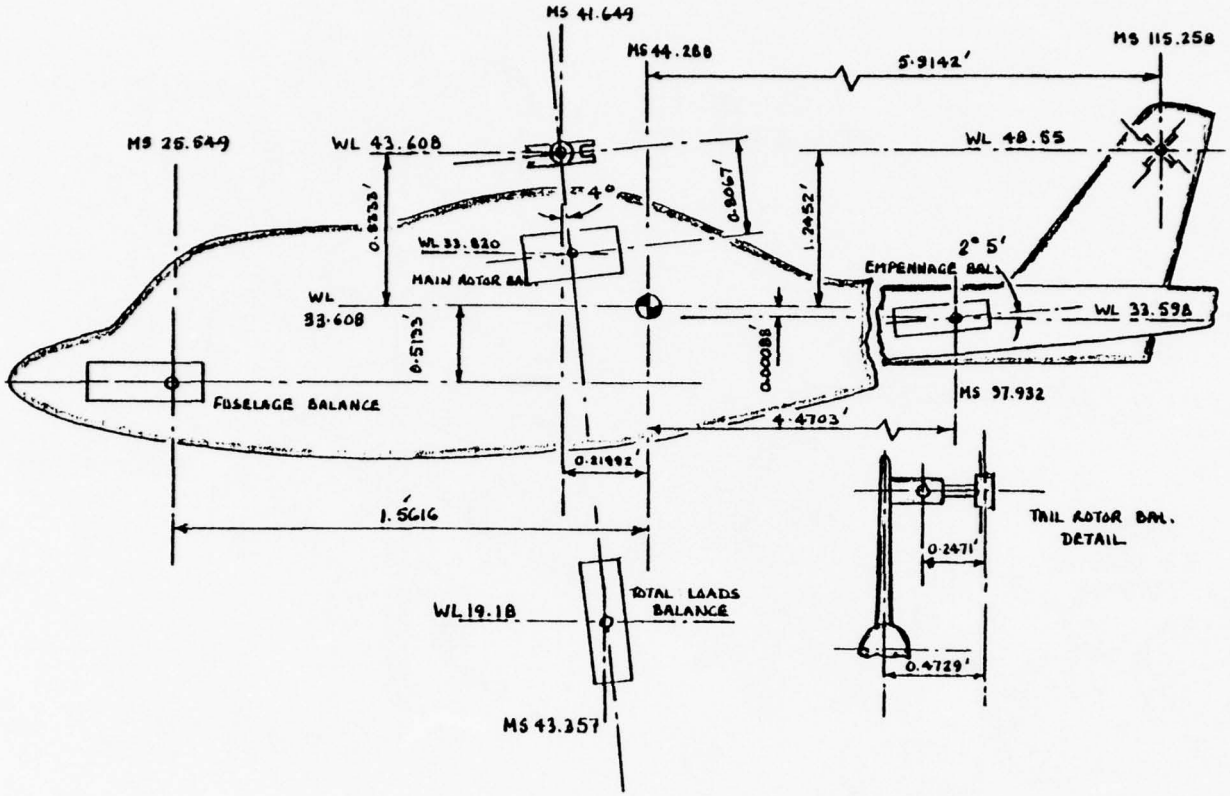

Figure B–64. Balance Locations.

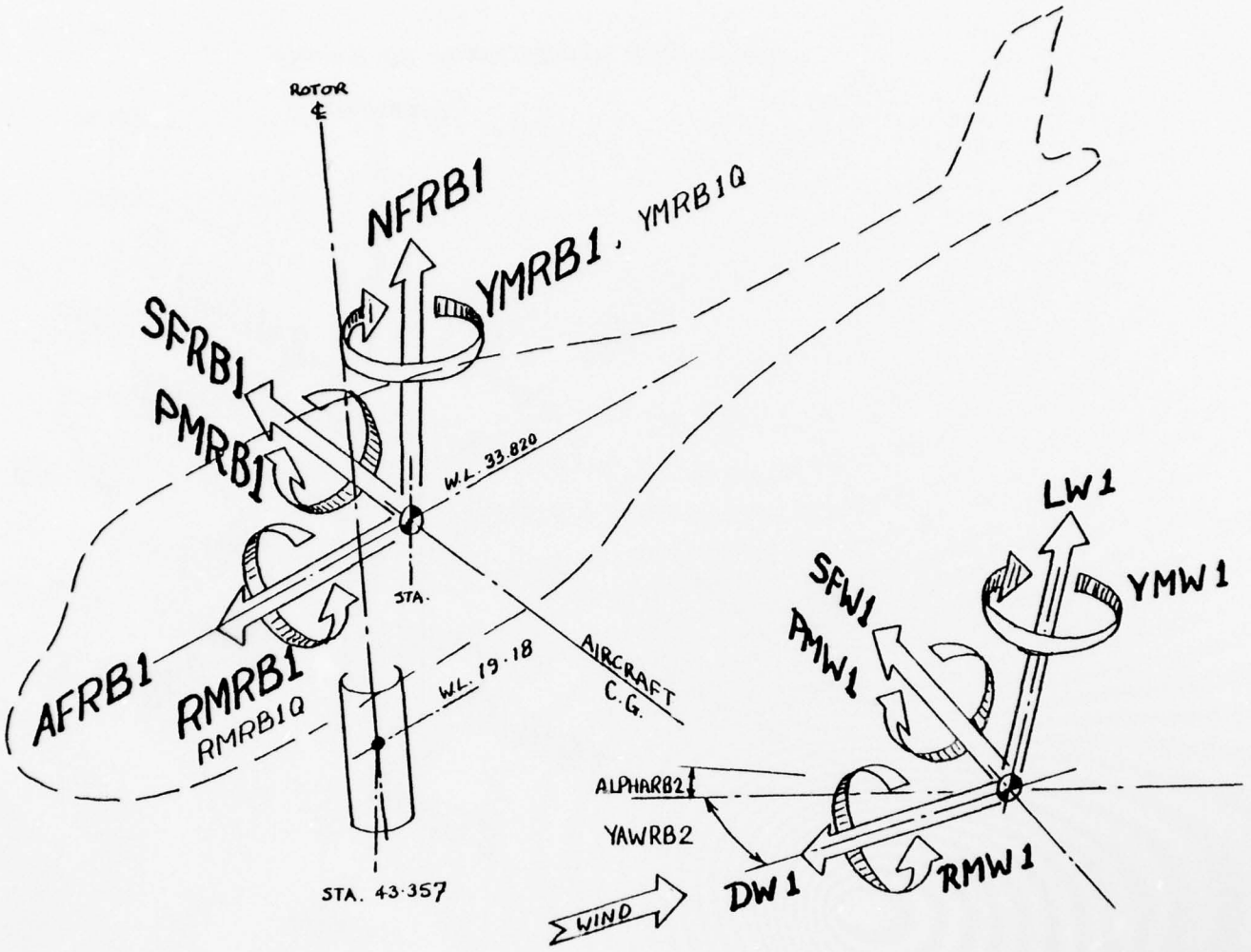

Figure B–65. Total Loads Balance Reference Axes.

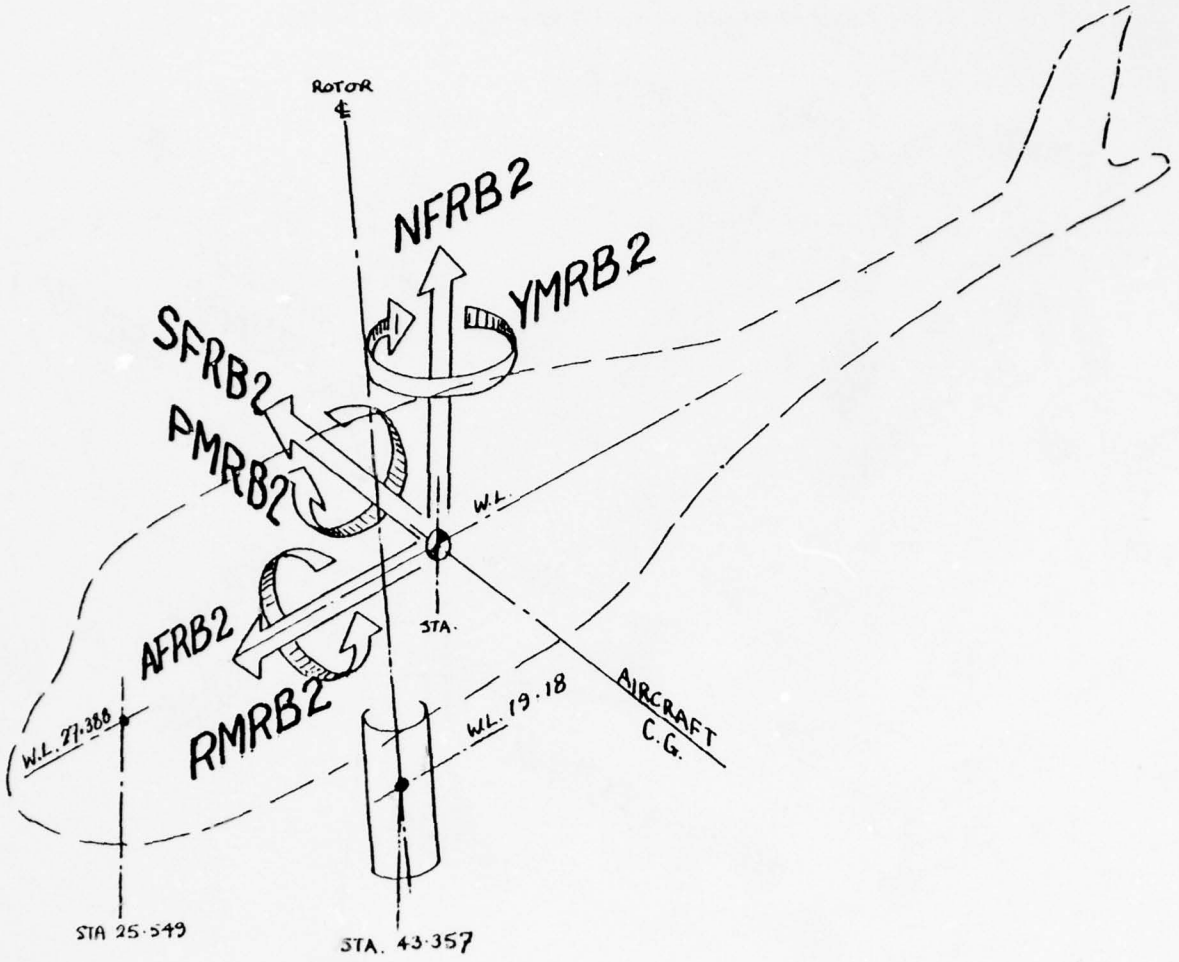

Figure B–66. Fuselage Balance Reference Axes.

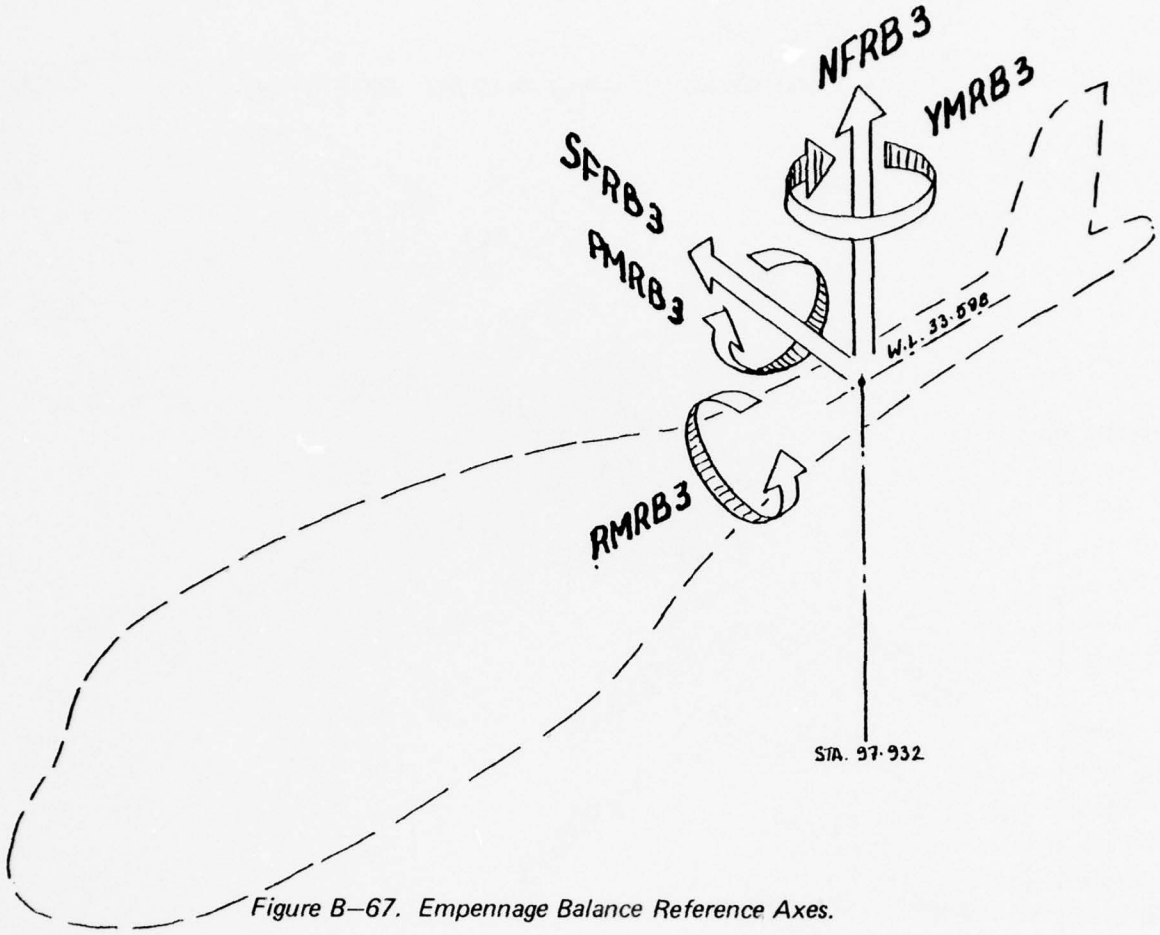

Figure B–67. Empennage Balance Reference Axes.

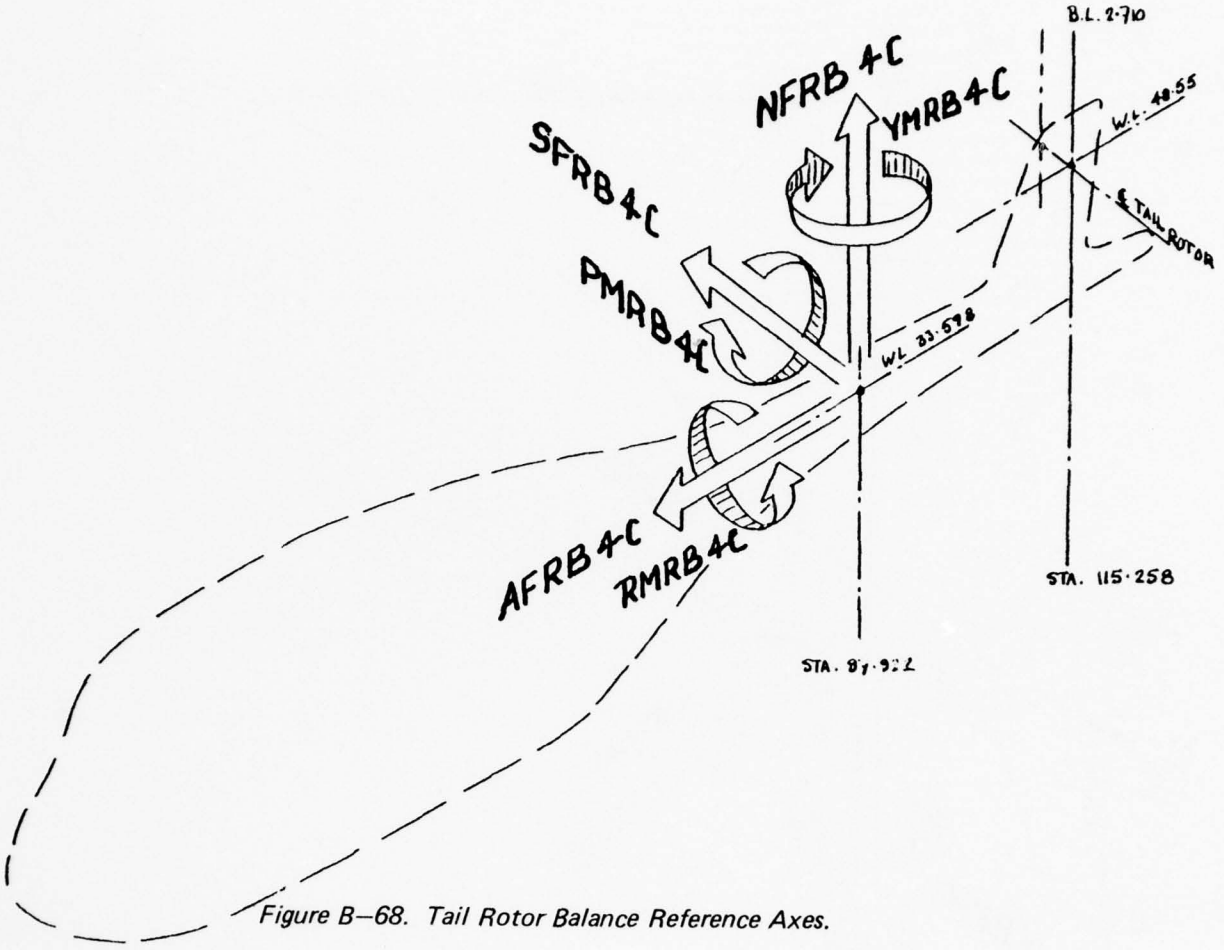

Figure B–68. Tail Rotor Balance Reference Axes.

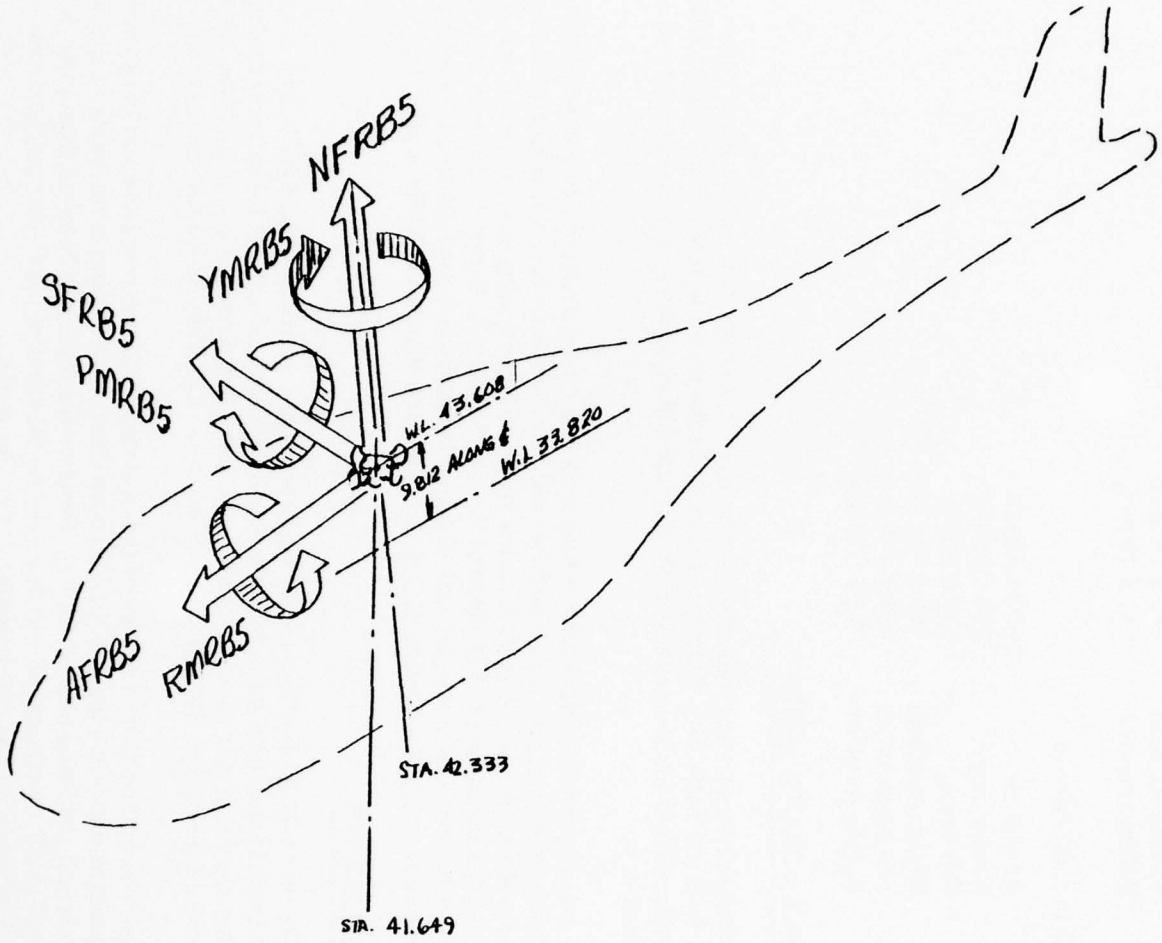

Figure B–69. Main Rotor Balance Reference Axes.

Tail rotor balance

Axial force	175 ± 50 lb
Normal force	30 ± 40 lb
Side force	30 ± 40 lb
Pitching moment	17 ± 19 lb-ft
Yawing moment	17 ± 19 lb-ft
Rolling moment	17 ± 19 lb-ft

Main rotor balance

Axial force	2,000 ± 400 lb
Normal force	250 ± 200 lb
Side force	250 ± 200 lb
Pitching moment	595 ± 455 lb-ft
Yawing moment	595 ± 455 lb-ft
Rolling moment	33 ± 0 lb-ft

PRESSURE TRANSDUCERS

Fifty-three 0.1-psi pressure transducers were fitted to fuselage skin B_2 and are shown in Figure B-70 and Table B-6. Reference pressure for the transducers was tunnel static pressure. A pressure plenum was located inside the fuselage and all transducer reference tubes were connected to it.

As the data acquisition system did not have sufficient channel capacity to sample all the transducers simultaneously, a scan address control system was used, which separately switched three sets of 18, 18, and 17 transducers for multiplexing or analog acquisition through high-speed multiplexer channels. Switching of Pressure Stations A, B, or C by the scan address unit was actuated from the model control panel, the position being indicated by a monitor voltage value – 1 volt for Section A, 2 volts for Section B, and 3 volts for Section C.

HOT FILM RAKE

The rake that held the hot film probes was assembled as shown in Figure B-71. The center probes at ±0.25 inch held split-film sensors with one oriented parallel to the rake span and the other normal to rake span and chord. This permitted measurement of two flow angles in planes 90 degrees apart. The other six sensors were single film, measuring velocity only.

The rake was supported by a system of rods and clamps that were attached to the positioning mechanism as shown in Figure B-72. The mechanism enabled remote traversing of the rake in the vertical and fore-and-aft directions. Position feedback was obtained from potentiometers in X and Y directions and was displayed on the monitor panel after computer processing in terms of model station and waterline of the rake center.

ANCILLARY EQUIPMENT

A variety of ancillary equipment was used to fulfill the data and visualization requirements.

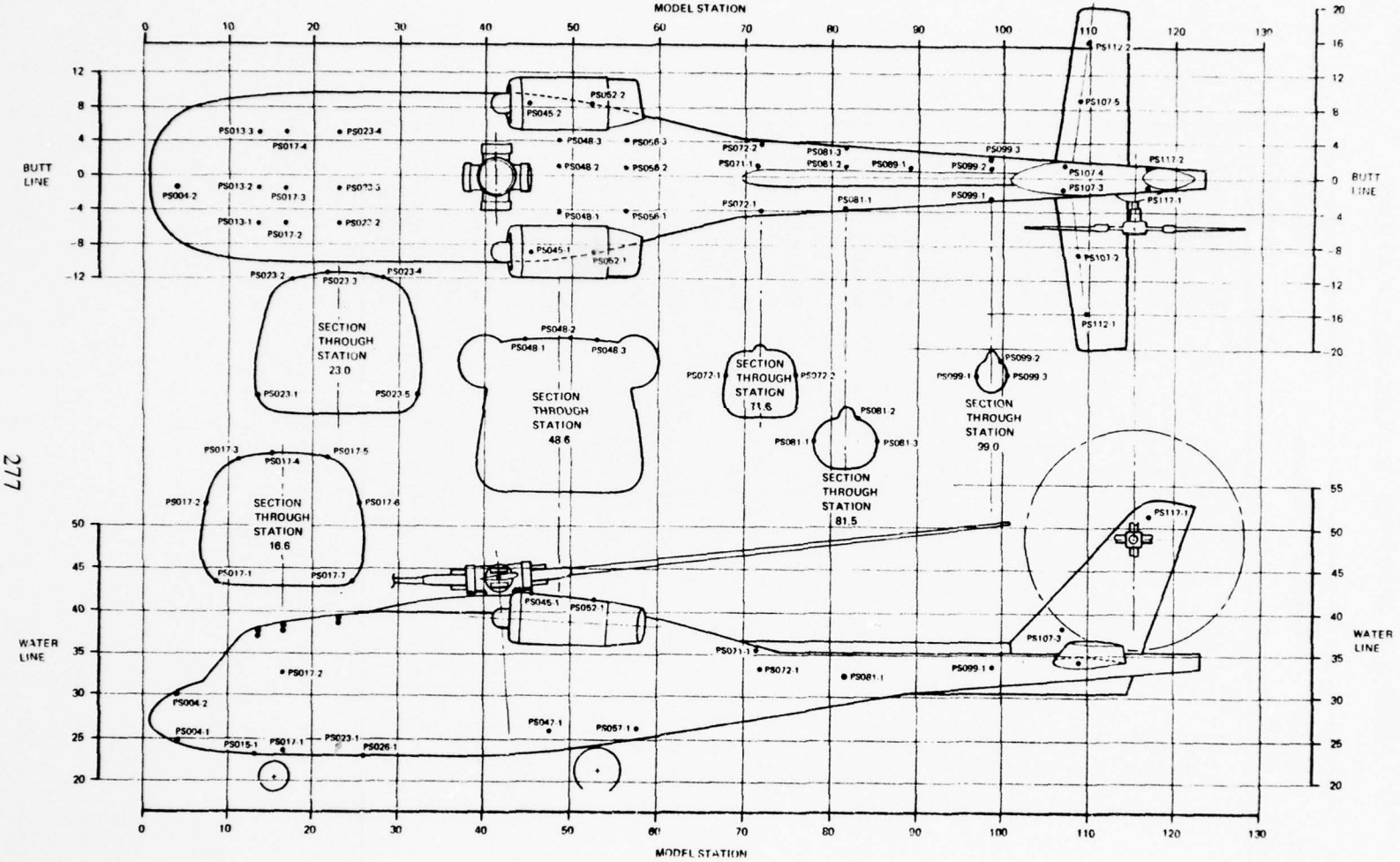

Figure B–70. UTTAS 1/4.85-Scale Model Geometry and Surface Pressure Transducer Locations.

TABLE B–6. PRESSURE TRANSDUCER LOCATIONS

Transducer Designation	Model Station	Waterline	Buttline	Location Description
PS004-1	4.0	–	–1.2	Lower Surface
-2	4.0	–	–1.2	Upper Surface
PS013-1	13.4	–	–5.3	Forward Crown
-2	13.4	–	–1.2	Forward Crown
-3	13.4	–	5.2	Forward Crown
PS015-1	13.4	–	–1.2	Lower Surface
PS017-1	16.6	24.2	–	Left Side
-2	16.6	33.4	–	Left Side
-3	16.6	–	–5.3	Forward Crown
-4	16.6	–	–1.2	Forward Crown
-5	16.6	–	5.2	Forward Crown
-6	16.6	33.4	–	Right Side
-7	16.6	24.2	–	Right Side
PS023-1	23.0	25.9	–	Left Side
-2	23.0	–	–5.3	Forward Crown
-3	23.0	–	–1.2	Forward Crown
-4	23.0	–	5.2	Forward Crown
-5	23.0	25.9	–	Right Side
PS026-1	26.0	–	–1.2	Under Surface
PS045-1	45.4	–	–8.7	Top of Nacelle
-2	45.4	–	8.7	Top of Nacelle
PS047-1	47.4	26.6	–	Left Side
-2	47.4	26.6	–	Right Side
PS048-1	48.6	–	–3.9	Aft Crown
-2	48.6	–	1.2	Aft Crown
-3	48.6	–	4.4	Aft Crown
PS052-1	52.6	–	–8.7	Top of Nacelle
-2	52.6	–	8.7	Top Nacelle

TABLE B–6. Continued

Transducer Designation	Model Station	Waterline	Buttline	Location Description
PS056-1	56.2	–	–3.9	Aft Crown
-2	56.2	–	1.2	Aft Crown
-3	56.2	–	4.4	Aft Crown
PS057-1	57.4	27.0	–	Left Side
-2	57.4	27.0	–	Right Side
PS071-1	71.4	–	1.2	Top Surface
PS072-1	71.6	28.9	–	Left Side
-2	71.6	28.9	–	Right Side
PS081-1	81.5	28.9	–	Left Side
-2	81.5	–	1.2	Top Surface
-3	81.5	28.9	–	Right Side
PS089-1	89.4	–	1.2	Top Surface
PS099-1	99.0	28.9	–	Left Side
-2	99.0	–	1.2	Top Surface
-3	99.0	28.9	–	Right Side
PS107-1	109.5	–	–8.6	Lower Surf. – Stab.
-2	109.5	–	–8.6	Upper Surf. – Stab.
-3	109.5	38.7	–	Left Side – Fin
-4	109.5	38.7	–	Right Side – Fin
-5	109.5	–	8.6	Upper Surf. – Stab.
-6	109.5	–	8.6	Lower Surf. – Stab.
PS112-1	110.3	–	–15.9	Upper Surf. – Stab.
-2	110.3	–	15.9	Upper Surf. – Stab.
PS117-1	117.0	47.7	–	Left Side – Fin
-2	117.0	47.7	–	Right Side – Fin

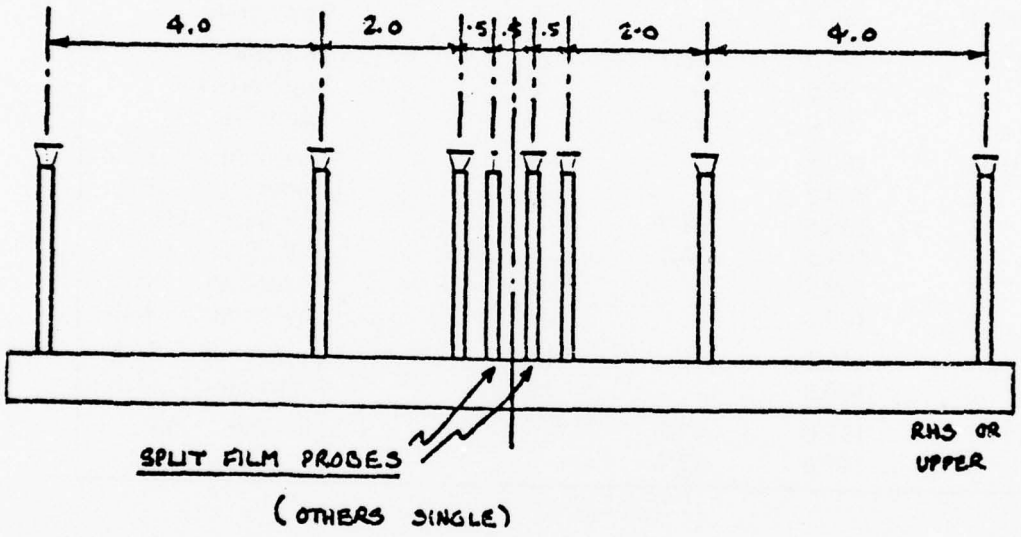

Figure B–71. Hot Film Rake Arrangement.

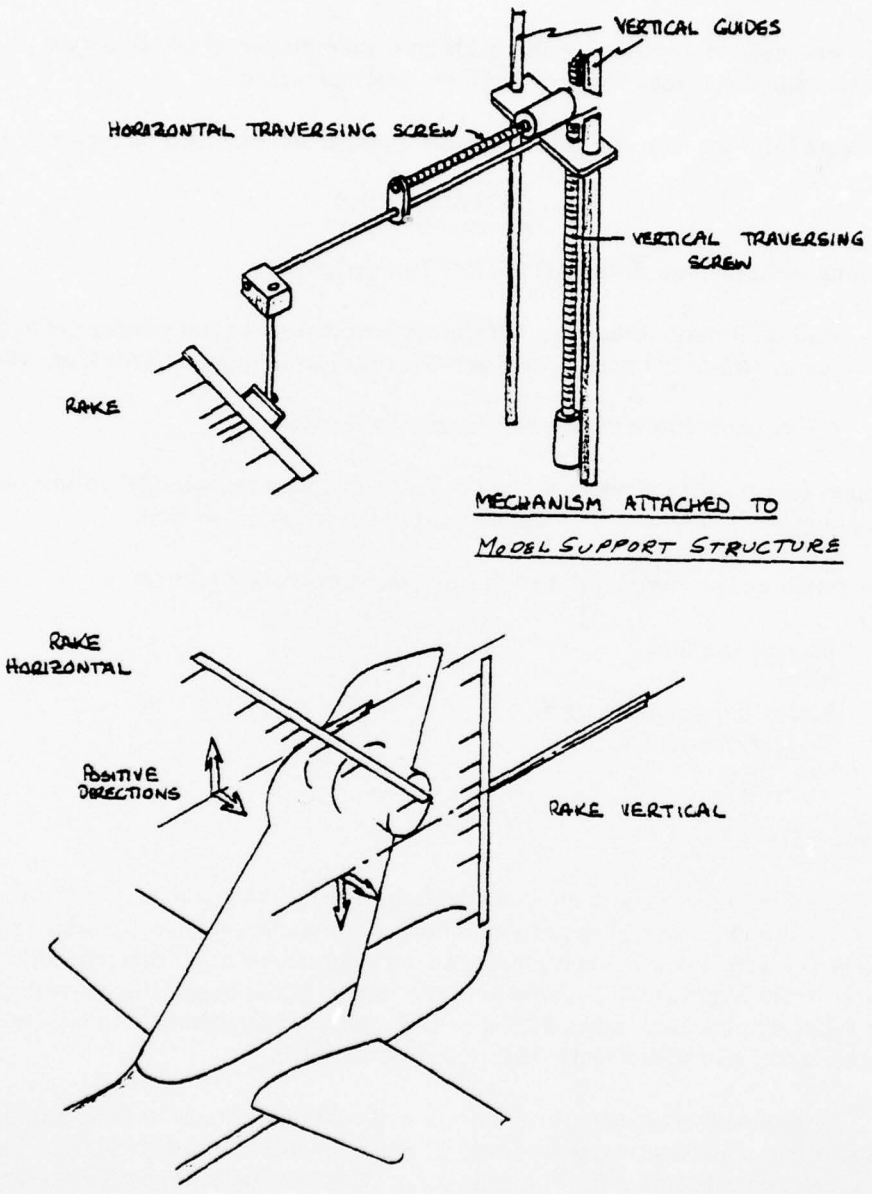

Figure B–72. Positioning the Hot Film Rake.

Flow visualization, using smoke and tufts on the model, was recorded by top- and side-mounted cameras triggered from the control room and fitted with automatic film advance. Next to each camera, TV cameras were used, their images being recorded on videotape. Smoke was produced by the combination of sulphur dioxide and anhydrous ammonia gases.

CEC and high-speed 160-in./sec recorders were used throughout the test to monitor and record analog signals from the model.

Much use was made of a spectral analyzer for on-line evaluation of hot film data. A Polaroid camera attachment was used to photograph the analyzer screen.

Hot film data from the rake and blade were conditioned and recorded on magnetic tape.

CALIBRATIONS

Calibrations performed on the model fell into two categories:

1. Full calibration prior to test of the systems that input test parameters to the model and of the systems that provide the measurement outputs from the tests.

2. Check calibrations of selected parameters during test.

This section covers the first category – work that was done during model setup and check-out. Running checks in Category 2 are covered in the following section.

Full calibration was performed in the following instrumentation groups:

1. Balance loadings
2. Angles
3. Blades and tail rotor strap
4. Pressure transducers
5. Hot films.

BALANCE LOADINGS

Figure B-73 shows the arrangement of model balances and the available fixtures for their calibration. Each balance had been rig calibrated to obtain primary sensitivities and an interaction matrix. The pretest calibration covered all components of all balances, although in most cases it was not possible to perform pure component loadings. The major portion of the balance calibration process employed the on-line computer programmed to receive as input the balance matrices and previously determined sensitivities.

Figure B-74 shows schematically the application of calibration loads to the assembled model. It is evident that a loading on one balance will also apply loads to other balances through known angles and moment arms. For example, a loading of tail rotor axial force also applies empennage balance yawing moment and side force, and total loads balance rolling moment and side force. In this way, many variations of combined loadings could be accomplished for a single setup and loads were applied directly or indirectly to all components of all balances. All loading was done using dead weights, with or without cables and pulleys.

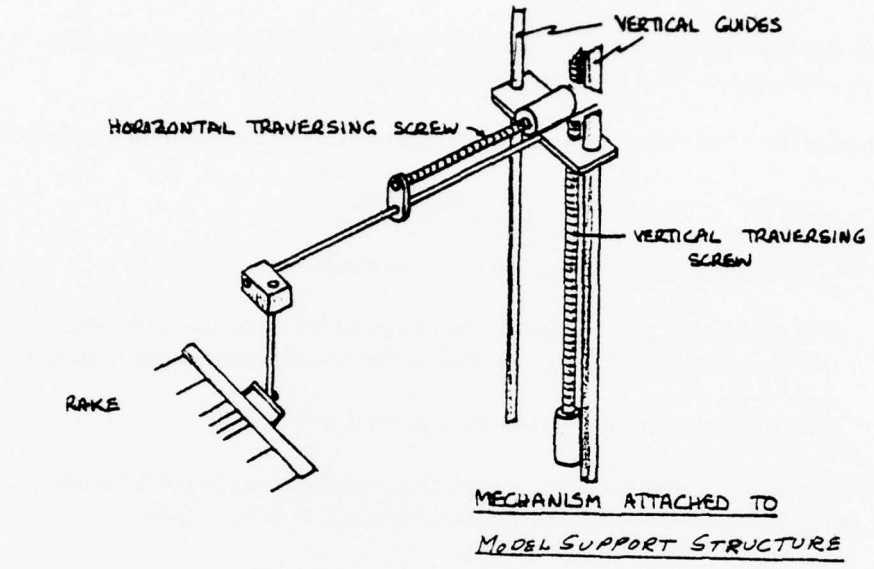

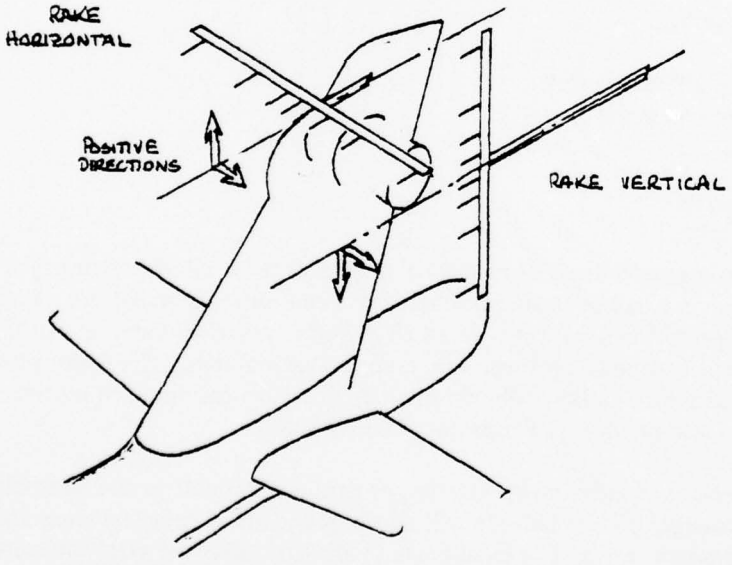

Figure B–72. Positioning the Hot Film Rake.

Flow visualization, using smoke and tufts on the model, was recorded by top- and side-mounted cameras triggered from the control room and fitted with automatic film advance. Next to each camera, TV cameras were used, their images being recorded on videotape. Smoke was produced by the combination of sulphur dioxide and anhydrous ammonia gases.

CEC and high-speed 160-in./sec recorders were used throughout the test to monitor and record analog signals from the model.

Much use was made of a spectral analyzer for on-line evaluation of hot film data. A Polaroid camera attachment was used to photograph the analyzer screen.

Hot film data from the rake and blade were conditioned and recorded on magnetic tape.

CALIBRATIONS

Calibrations performed on the model fell into two categories:

1. Full calibration prior to test of the systems that input test parameters to the model and of the systems that provide the measurement outputs from the tests.

2. Check calibrations of selected parameters during test.

This section covers the first category – work that was done during model setup and check-out. Running checks in Category 2 are covered in the following section.

Full calibration was performed in the following instrumentation groups:

1. Balance loadings
2. Angles
3. Blades and tail rotor strap
4. Pressure transducers
5. Hot films.

BALANCE LOADINGS

Figure B-73 shows the arrangement of model balances and the available fixtures for their calibration. Each balance had been rig calibrated to obtain primary sensitivities and an interaction matrix. The pretest calibration covered all components of all balances, although in most cases it was not possible to perform pure component loadings. The major portion of the balance calibration process employed the on-line computer programmed to receive as input the balance matrices and previously determined sensitivities.

Figure B-74 shows schematically the application of calibration loads to the assembled model. It is evident that a loading on one balance will also apply loads to other balances through known angles and moment arms. For example, a loading of tail rotor axial force also applies empennage balance yawing moment and side force, and total loads balance rolling moment and side force. In this way, many variations of combined loadings could be accomplished for a single setup and loads were applied directly or indirectly to all components of all balances. All loading was done using dead weights, with or without cables and pulleys.

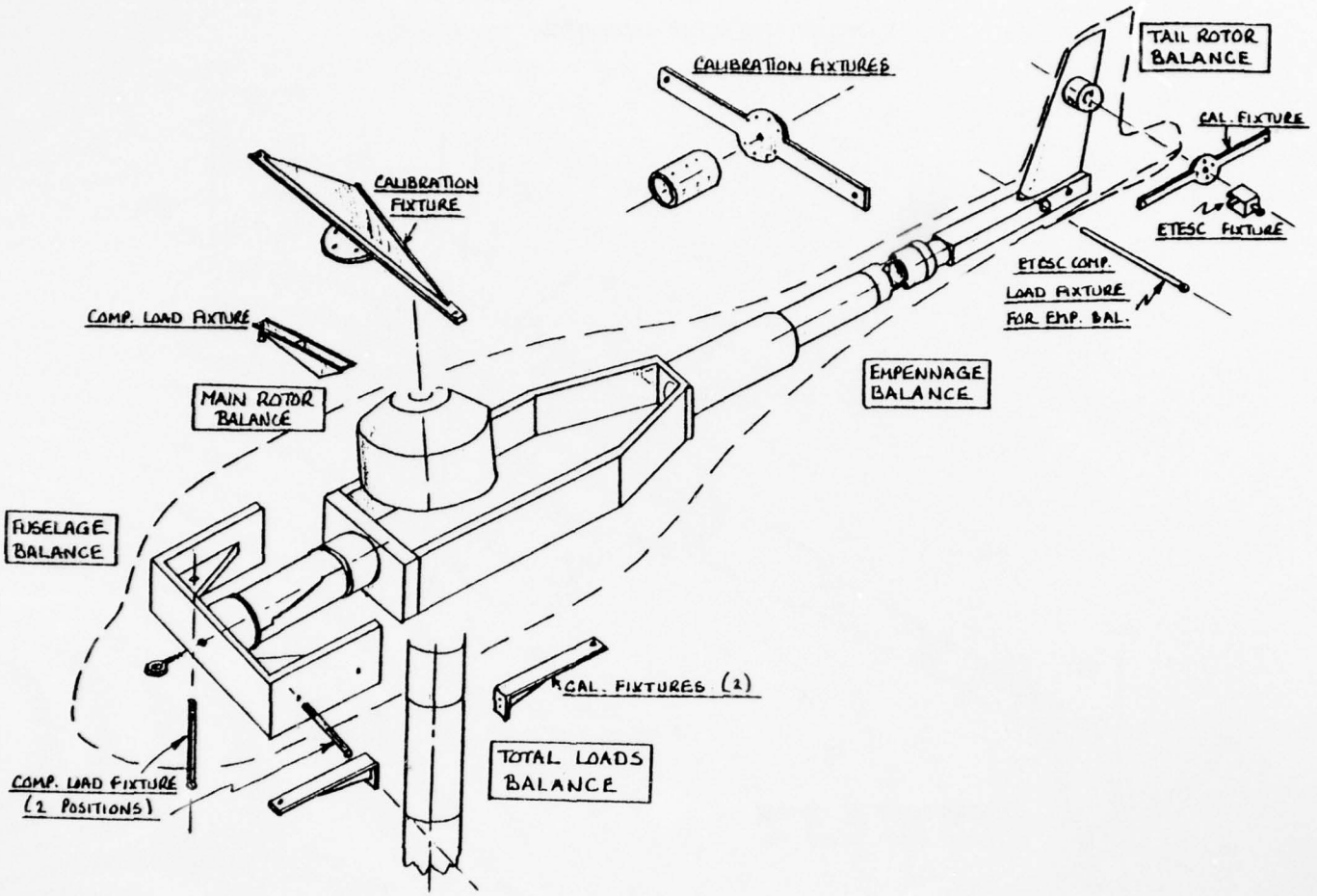

Figure B–73. Calibration and Compound Load Fixtures.

AD-A060 389 BOEING VERTOL CO PHILADELPHIA PA F/G 1/3
INTERACTIONAL AERODYNAMICS OF THE SINGLE-ROTOR HELICOPTER CONFI--ETC(U)
SEP 78 P F SHERIDAN DAAJ02-77-C-0020
UNCLASSIFIED USARTL-TR-78-23A NL

4 OF 4
AD
AO 60389

END
DATE
FILMED
1-79
DDC

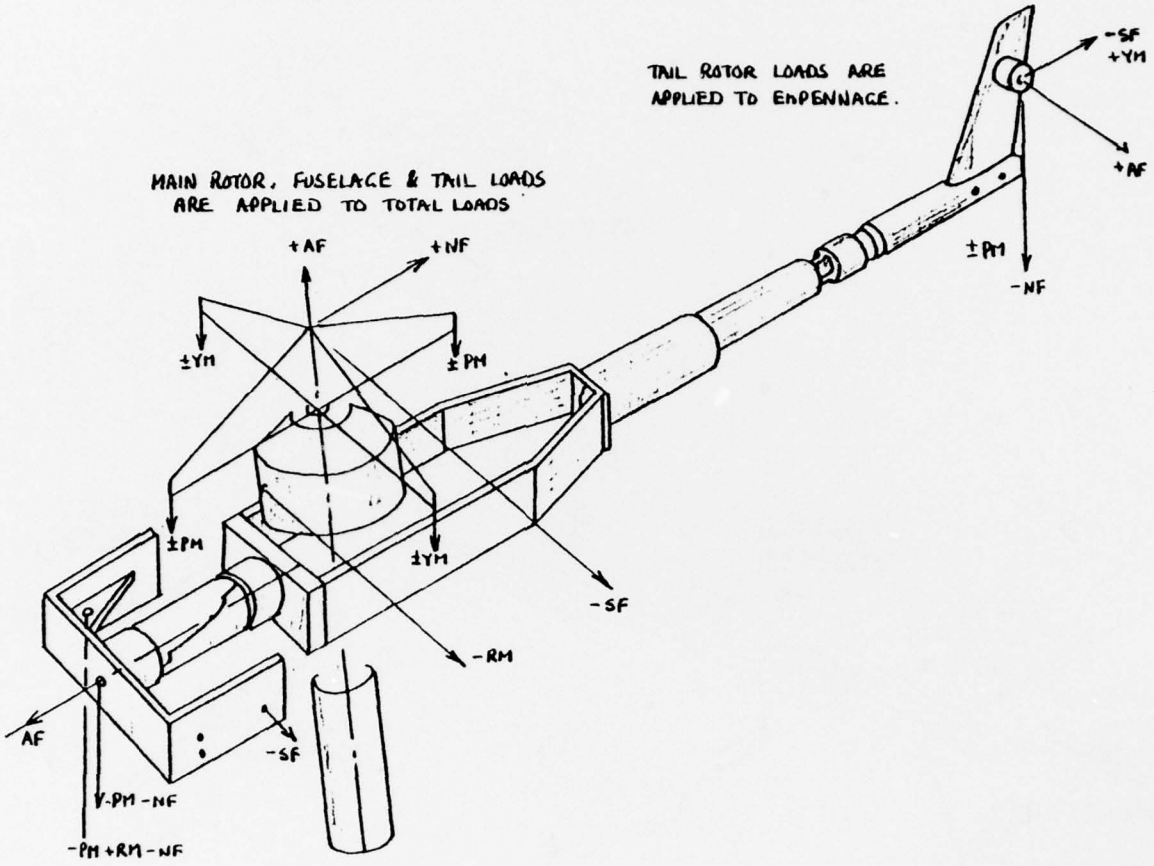

Figure B—74. Application of Calibration Loads.

ANGLES

Angles calibrated were as follows:

Fuselage pitch angle, α_F

Fuselage yaw angle, ψ_F

Horizontal stabilizer, i_H

Main rotor collective pitch, $\theta_{.75}$

Blade position, θ_o

Main rotor lateral cyclic, A_1

Main rotor longitudinal cyclic, B_1, and tail rotor slider position

BLADES AND TAIL ROTOR STRAP

Main rotor blades, Serial Numbers 296 and 298, were instrumented as shown in Figure B-75. The flap, chord, and torsion bridges measured bending strains in the minimum cross-sectional area of the blade root spar at r/R of 11.9 percent. Data were acquired by the computer and displayed in parallel on scopes for monitoring blade safety. The blades were calibrated by deadweight loading of pure moments both on the bench and on the model.

The tail rotor flexstrap was bench calibrated and checked on the model in the same way.

Friction torque of the bearings on the main rotor drive shaft introduces a small error into the total loads balance through shaft torque. The correction curve is a second-order polynomial function of rpm. This is applied directly to the rotor torque measurements and also into the total loads data reduction program.

PRESSURE TRANSDUCERS

The 53 pressure transducers fitted to the B_2 fuselage skin were individually checked and sensitivities generated at the Flight Test Calibration Lab. As installed on the model, calibration pressures were applied by using the reference tube on the back of the transducer.

HOT FILMS

The hot film probes had been calibrated individually as supplied. Check calibrations were performed on the test installation using a portable air velocity generator. This device consisted of an accurately made and aligned nozzle of 0.5-inch diameter, which was supplied with air from the 80-psi shop line. This air was filtered, expanded, and heated before passing through the nozzle, to provide a uniform stream at up to 1,000 feet per second.

Positioning of the probe in the air jet gave any desired velocity/angle calibration.

X-Y positioning of the rake was calibrated by 10- and 20-inch offsets of each traversing mechanism.

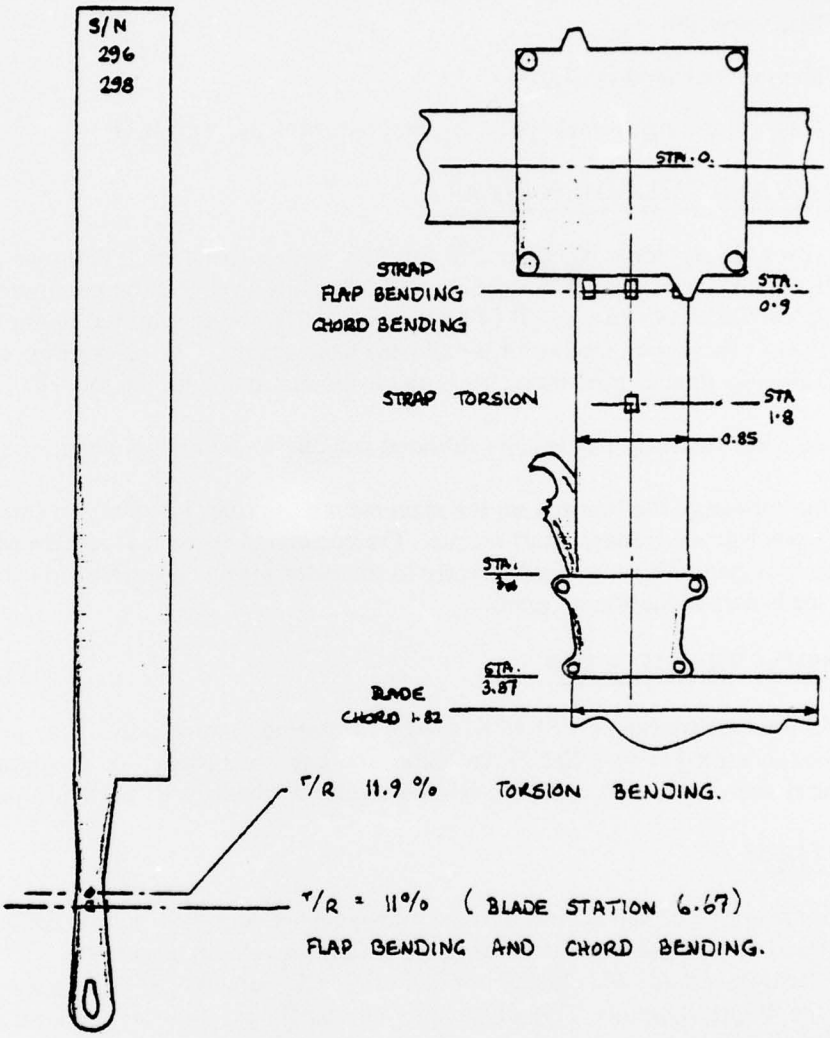

Figure B–75. Blade Instrumentation.

EQUIPMENT CHECKOUT

Checkout procedures followed for test are outlined below for the end-to-end system check and pretest checkout and shakedown.

END-TO-END SYSTEM CHECK (ETESC)

An ETESC was performed, wholly or in part, before every running shift. The purpose was to check out model parameters from the model (load, moment, angle, pressure, position, etc.) through the data acquisition system (signal multiplexing, conditioning, amplification) to the computer (monitor display and printout) and analog recording devices and displays.

Some of the items checked during the ETESC and the methods used are described in the following paragraphs.

Balance Compound Loading

Figures B-76, B-77, and B-78 show typical compound loadings that were applied to the fuselage balance, main rotor balance, and the tail rotor balance, respectively. The figures show the loading points and associated geometry for the balances, and loads measured by the loaded balance and the other affected balances.

Control Systems

Control system angles were measured on the main rotor using a small plate fixture that bolted to the weight on the blade simulating the pendulum absorber, as shown in Figure B-79. This plate served as a clinometer base as shown. For this test, the longitudinal and lateral cyclic and collective pitch angles at 75-percent radius were set to mechanical zeros (not zero hub moments or $C_T = 0$ for $\theta_{.75} = 0$).

Positions of the cyclic actuator are shown in Figure B-80. Blade position angle was used to find the $A_1 = B_1 = 0$ condition, rotating the hub around the azimuth by hand until all cyclic pitch was removed as shown by no variation of blade angle. A data point was taken, and any cyclic deviation from zero, on the printout, was removed by card input (change of calibration intercept).

Cyclic pitch amplitude was checked by positioning the pitch link of the blade, holding the clinometer over the appropriate actuator, and moving the cyclic + and −5 degrees, taking a data point at each maximum deflection. With cyclics returned to zero, the collective pitch was checked by taking data at zero and +10 degrees at 75-percent radius, accounting for blade twist from the absorber to 75-percent radius.

The tail rotor was checked by removing the pitch link from the instrumented strap, reading strap torsion bending (which was set to zero) for the resulting "flat strap" condition. The pitch link was replaced and the slider moved until zero torsion was shown. This position was defined as zero slider. Again, display and printout were zeroed. Slider deflection, displayed and printed in inches, was checked by measurement of an indicated offset of +1.0 inch.

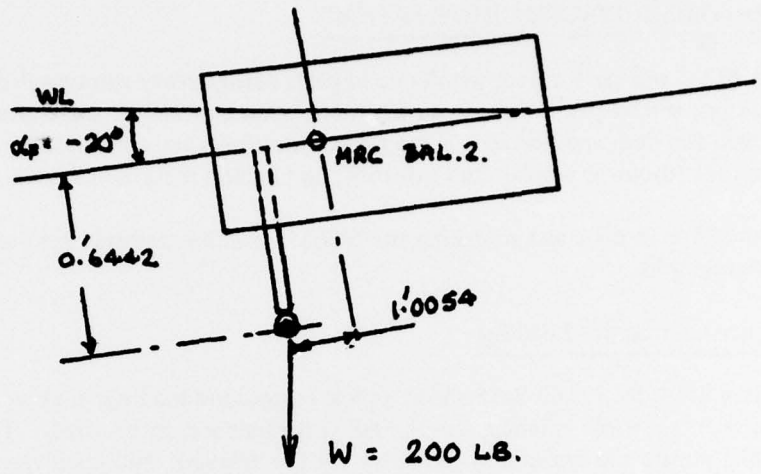


```
Fuselage Balance (#2)
   NF2  =  -187.938 lb
   AF2  =  -68.404 lb
   SF2  =       0
   PM2  =   144.887 lb ft
   YM2  =   -34.202 lb ft
   RM2  =   -93.969 lb ft

Total Loads Balance (#1)
   NF1  =   -81.348 lb
   AF1  =  -182.710 lb
   SF1  =       0
   PM1  =  -470.60 lb ft
   YM1  =    91.355 lb ft
   RM1  =    40.674 lb ft
```

Figure B–76. Typical Checkload on Fuselage and Resulting Balance Measurements.

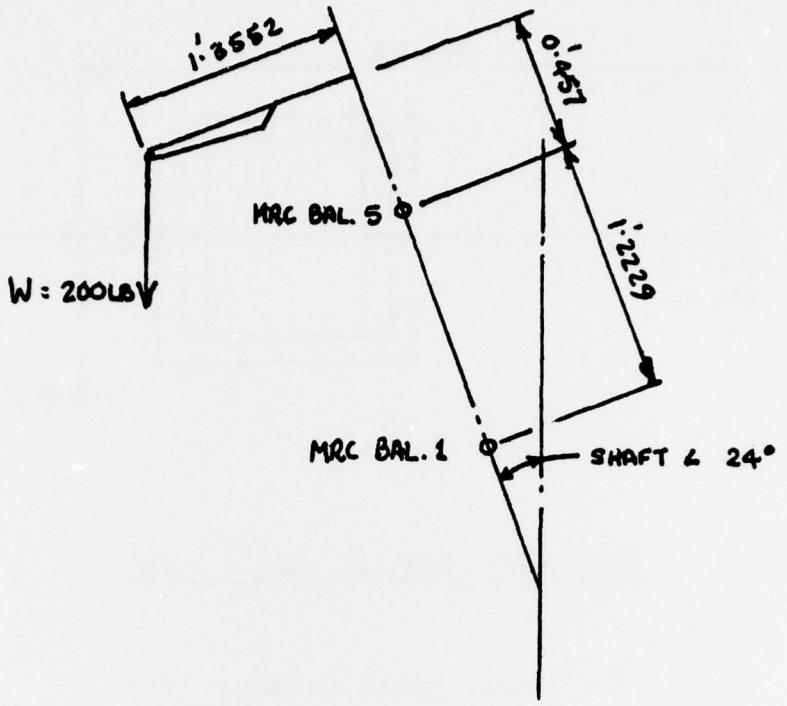

FOR ROTOR @ AZIMUTH ψ = 315° FIXTURE POSITION

Main Rotor Balance (#5)

NF5	=	-57.5 lb
AF5	=	-182.7 lb
SF5	=	-57.5 lb
PM5	=	-201.4 lb ft
YM5	=	-201.3 lb ft
RM5	=	0

Total Loads Balance (#1)

NF1	=	-57.5 lb
AF1	=	-182.7 lb
SF1	=	-57.5 lb
PM1	=	-271.7 lb
YM1	=	-271.6 lb
RM1	=	0

Figure B–77. Typical Checkload on Rotor and Resulting Balance Measurements.

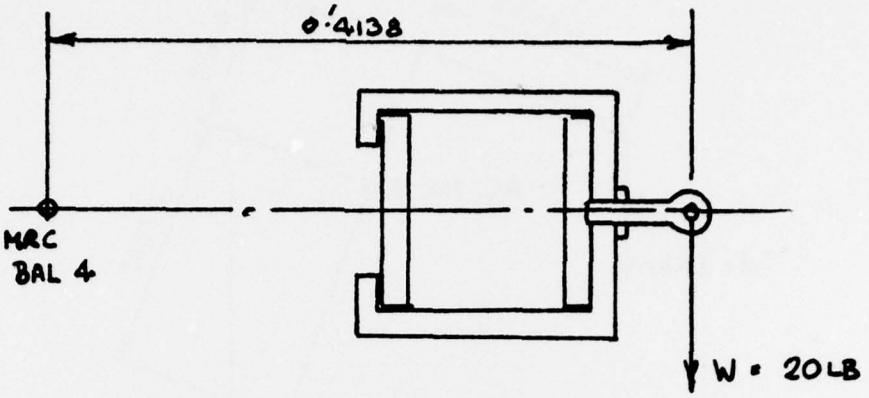

FUSELAGE ANGLE α_F = -20°

Tail Rotor Balance (#4)
NF4 = -18.8 lb
AF4 = 0
SF4 = 6.8 lb
PM4 = -7.8 lb ft
YM4 = 2.8 lb ft
RM4 = 0

Empennage Balance (#3)
NF3 = -18.5 lb
SF3 = 0
PM3 = 18.6 lb ft
YM3 = 4.8 lb ft
RM3 = -11.9 lb ft

Total Loads Balance (#1)
NF1 = -8.1 lb
AF1 = -18.3 lb
SF1 = 0
PM1 = 95.9 lb ft
YM1 = -11.7 lb ft
RM1 = -5.2 lb ft

Figure B–78. Typical Checkload on Tail Rotor and Resulting Balance Measurements.

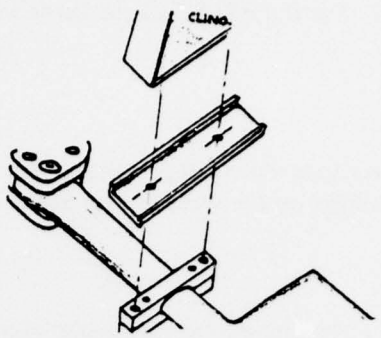

Figure B–79. Clinometer Installation for Checking Blade Pitch Angle.

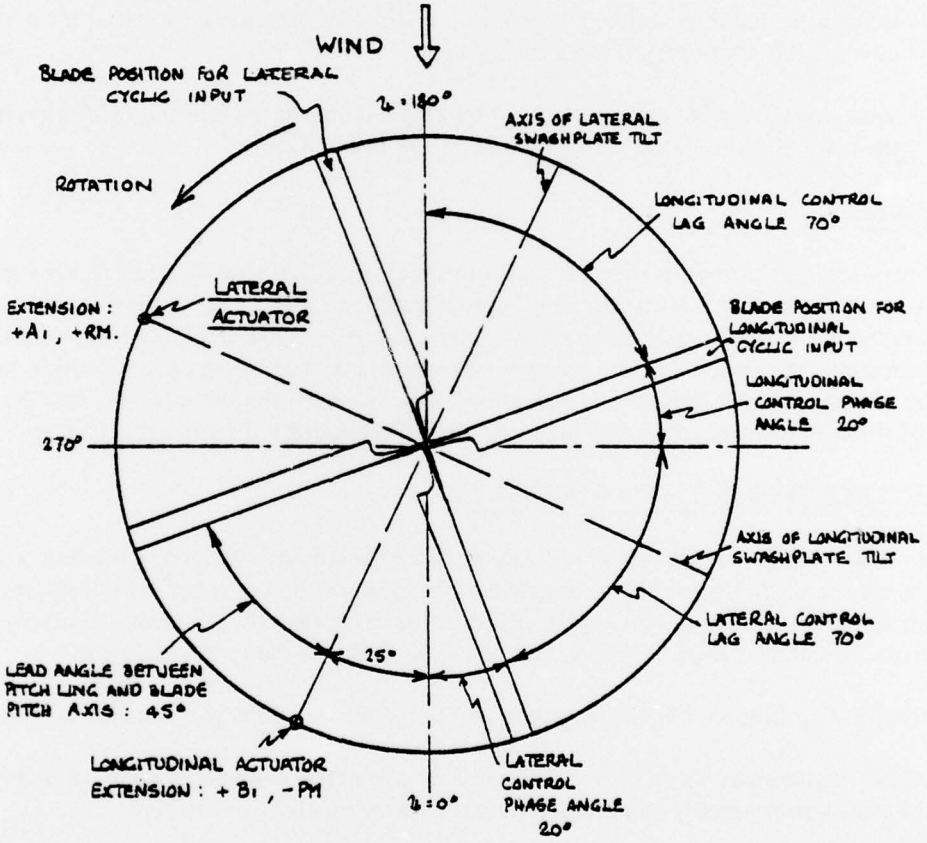

Figure B–80. Main Rotor Control System Phasing and Actuation Positions.

UTTAS-scaled blades, Serial Numbers 296 and 298, were instrumented with root flap, chord, and torsion bending bridges. For the ETESC, check loads were applied to these blades as shown in Figure B-81.

Horizontal Stabilizer

The right horizontal stabilizer spar was equipped with a flap bending bridge at BL 2.5. This was checked by hanging a weight on the stabilizer tip at the quarter chord.

Angles

Model angles were checked at two points for each parameter, comparing measured angle to printout. These were:

Fuselage angle, measured on the vertical strut reference surface (total loads balance shield) plus 4 degrees.

Horizontal stabilizer angle, measured by resting the clinometer on two pins inserted into the left stabilizer on the chord plane.

Yaw angle, checked at zero only by hanging a plumb bob from the fuselage split line at the nose, to the scribed zero yaw line on the tunnel floor.

Pressures

All pressure transducers were referenced to tunnel static, being connected to the tunnel system through manifolds in the fuselage leading to a single reference line running down the main support sting. Checking all the pressure transducers was easily and quickly accomplished by disconnecting the reference line aft of the model and reconnecting the model side to a small hand suction pump. Thus, suction on the reference side of the transducers could be applied to all of them at the same time and the same amount (normally 0.1 psi, set on a micromanometer).

PRETEST CHECKOUT AND SHAKEDOWN

Following model installation, all services were connected and checked, including compressed air supply to air motors, shop air for mist lubrication of the tail rotor drive train, main rotor drive train oil supply and scavenging, motor lubrication system, hydraulic oil supply to control system, ac and dc electrical power, and instrumentation cables and wire packs.

Calibration of all model balances, angles and pressures was done as described previously.

Auxiliary equipment was set up -- CEC recorders, spectral analyzer, smoke equipment, cameras and lights, stroboscopic equipment, videotape recorder, etc.

Safety-of-flight parameters were set up on scopes and peak-to-peak meters using specified alternating allowables.

Functioning of all flying controls and other variable parameters was checked and the available ranges matched to test envelope requirements.

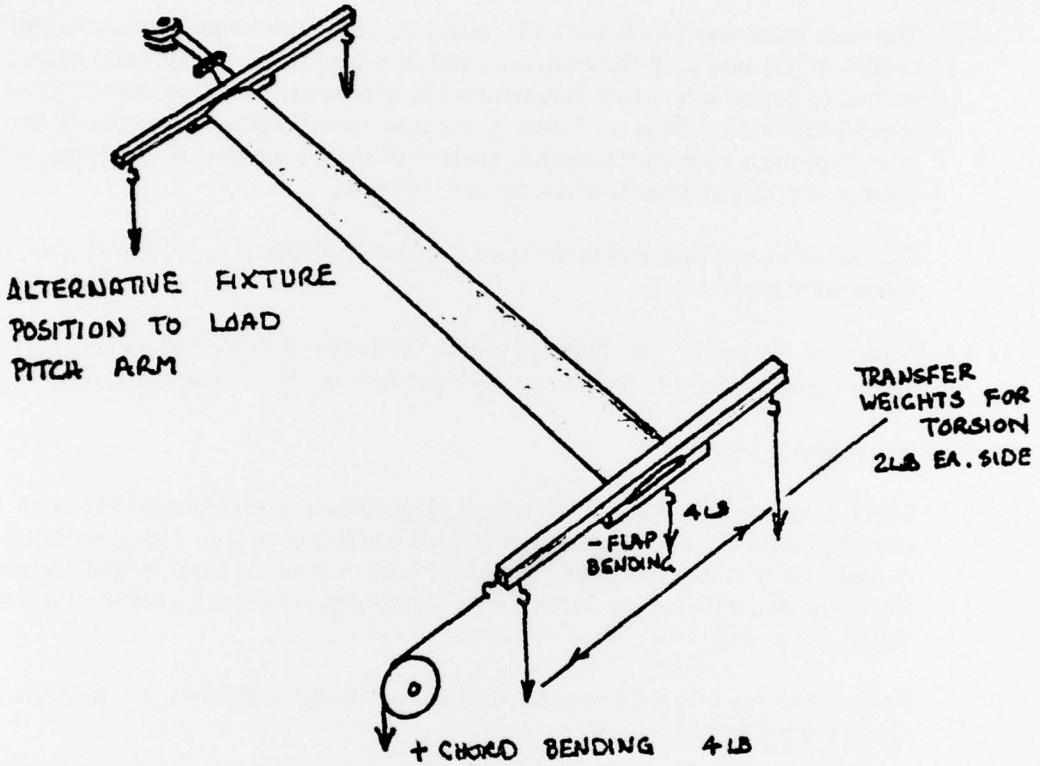

Figure B–81. Application of Checkloads to Blades.

The shakedown phase of checkout was performed with the model running, and was covered by Test Runs 0–6 (see Table B-7).

These runs were as follows:

Run 0. Balance and tracking: the main rotor blades were tracked (using pitch link length adjustments) until at a collective pitch of 10 degrees and 1,000 rpm, all blade tips, as shown by the stroboscope at 4/rev, were within a band equal to 1-1/2 blade thicknesses.

The main rotor was then balanced by attaching corrective weights to convenient locations on the hub until the alternating out-of-balance forces (main rotor balance normal force and side force) were reduced to approximately 10 percent of the allowable alternating stress, as shown by the peak-to-peak meter. Corrections were calculated using computer harmonic analysis of these components. Residual out-of-balance was almost entirely 4/rev, up to 1,500 rpm.

The tail rotor was balanced in the same way, up to 4,500 rpm. No tracking adjustments were made.

Run 1. Main rotor C_T sweep, for comparison with previous test data. The plots of C_T versus C_P and figure of merit versus C_T are shown in Figures B-82 and B-83.

Run 2. Tail rotor C_T sweep.

Run 3. Check of tail rotor exhaust air thrust. A cranked tube (see Figure B-84) was attached to the tail rotor exhaust duct and the conditions of Run 2 were repeated. A comparison of data from the empennage balance pitching moment and normal force with and without the duct showed the exhaust air to have a thrust of approximately 1.0 pound.

Run 4. Hover check run. C_T data were taken with recalibrated adjusted $\theta_{.75}$, with the fuselage skins installed.

Run 5. Standard reference run. In addition to the hover C_T checks, the parameters of earlier tests were set on the model and some tests run.

These were:

	TP.1	TP.2
Model pitch angle, α_F	2.08	−1.66
Model yaw angle, ψ_F	−14.70	−4.17
RPM, main rotor	996	999
RPM, tail rotor	4,497	4,530
Tunnel speed, knots	42.0	83.5

TABLE B–7. LIST OF TEST RUNS – PRELIMINARY CHECKOUT

Run No.	Configuration/Condition	V_{TUN} (kn)	MR/TR (rpm)	Disk Ldg (psf)	Model Angles α^o	Model Angles ψ^o	MR Ht (h/d)	Tail Rotor
0	K_1 less B_2/checkout and track and balance	0	Var/var	Var	0	0	∞	On
1	K_1 less B_2/main rotor performance hover check	0	1,433/0	Sweep	0	0	∞	On
2	K_1 less B_2/tail rotor performance hover check	0	0/4,500	0	0	0	∞	On
3	K_1 less B_2/tail rotor exhaust thrust check	0	0/4,500	0	0	0	∞	On
4	K_1/main rotor performance with fuselage shell on	0	1,433/0	Var	4	0	∞	On
5	K_1/standard reference run	Sweep	1,007/ 4,500	Per Sched	Sched	Sched	∞	On
6	K_1/continued reference run	Sweep	1,007/ 4,500	Per Sched	Sched	Sched	∞	On

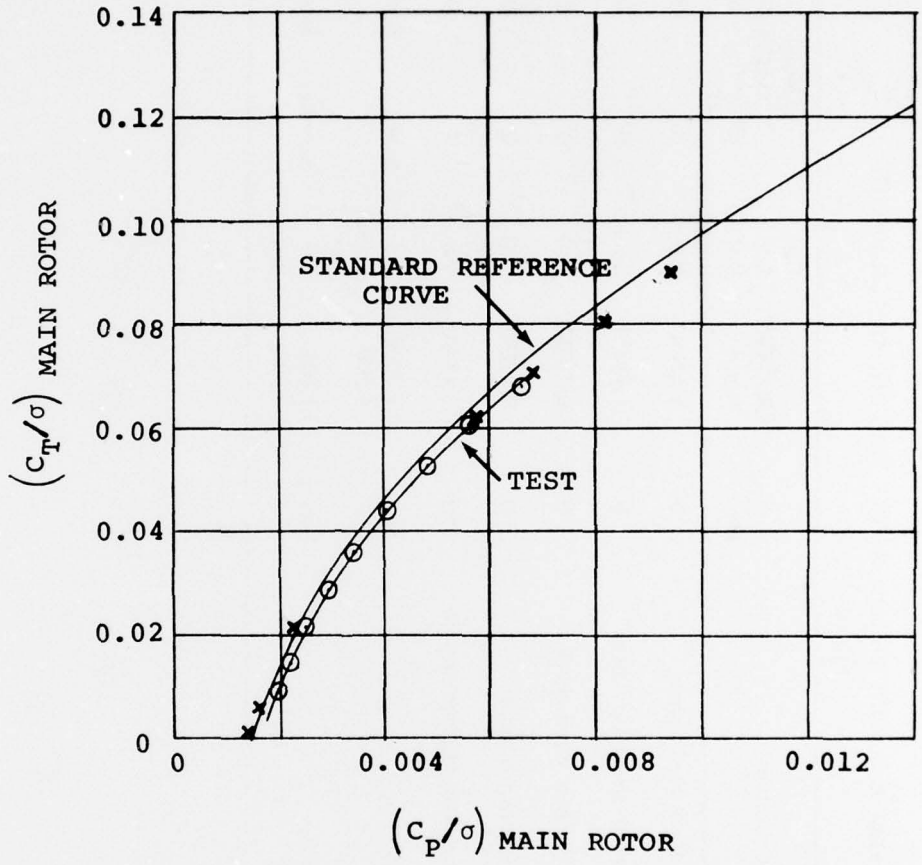

Figure B–82. Validation of Main Rotor Hover Power.

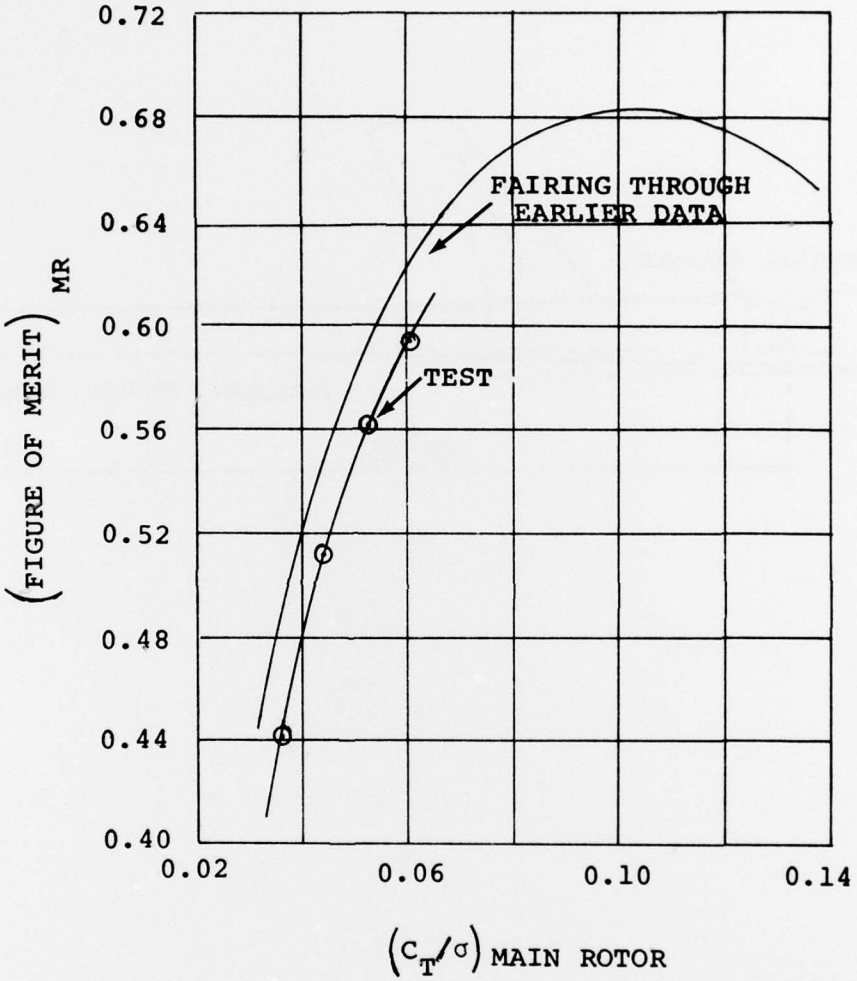

Figure B–83. Comparison of Merit to Reference.

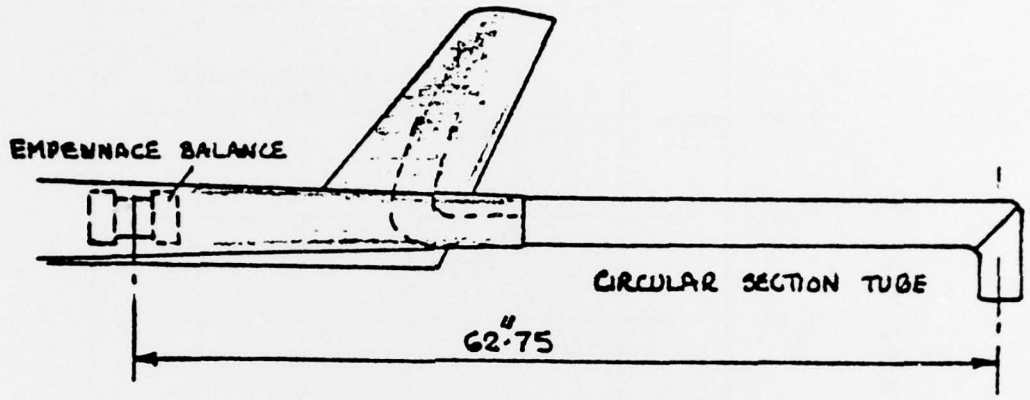

Figure B–84. Check of Tail Rotor Exhaust Air Thrust.

C_T, main rotor	0.26	0.06
C_T, tail rotor	0.036	0.023
Main rotor, A_1	−2.44	−1.13
Main rotor, B_1	+3.36	4.64
Tail angle, i_H	15.3	4.1

Comparison of balance data indicated repeatable results for the same conditions and input parameters.

10 166-78